

University of Southampton Research Repository ePrints Soton

Copyright © and Moral Rights for this thesis are retained by the author and/or other copyright owners. A copy can be downloaded for personal non-commercial research or study, without prior permission or charge. This thesis cannot be reproduced or quoted extensively from without first obtaining permission in writing from the copyright holder/s. The content must not be changed in any way or sold commercially in any format or medium without the formal permission of the copyright holders.

When referring to this work, full bibliographic details including the author, title, awarding institution and date of the thesis must be given e.g.

AUTHOR (year of submission) "Full thesis title", University of Southampton, name of the University School or Department, PhD Thesis, pagination

UNIVERSITY OF SOUTHAMPTON

FACULTY OF ENGINEERING, SCIENCE AND MATHEMATICS

Optoelectronics Research Centre

**POLARIZATION SENSITIVE OPTICAL ELEMENTS BY ULTRAFAST LASER
NANOSTRUCTURING OF GLASS**

by

Mindaugas Gecevičius

Thesis for the degree of Doctor of Philosophy

2015

UNIVERSITY OF SOUTHAMPTON

ABSTRACT

FACULTY OF ENGINEERING, SCIENCE AND MATHEMATICS

Optoelectronics Research Centre

Thesis for the degree of Doctor of Philosophy

**POLARIZATION SENSITIVE OPTICAL ELEMENTS BY ULTRAFAST LASER
NANOSTRUCTURING OF GLASS**

Mindaugas Gecevičius

In this theses I will concentrate on femtosecond laser induced modification in silica glass. One type of modification in fused silica is subwavelength nanogratings. This modification exhibits form birefringence and therefore optical elements can be fabricated based on nanogratings. The main goal of my work was development and fabrication of practical optical elements based on femtosecond laser induced nanogratings.

In order to be able to fabricate optical elements, laser induced modification had to be uniform and exhibit strong birefringence. Also fabrication speed has to be high in order to write reasonable size optical element in short time. Optimal fabrication parameters were found by studying physical and optical properties of nanogratings.

The first polarization sensitive optical element to be demonstrated was polarization converter, which transforms Gaussian beam with uniform polarization distribution into a cylindrical vector beam. Later on, polarization converters for different types of laser beams and spectral ranges were demonstrated. Properties of generated beams were measured and compared with theoretical modelling. Generated beams were also successfully exploited for material modification and results are compared with theoretical simulations.

Same converters can be also used for optical vortices generation. Unique property of such converters is that they allow tuning orbital angular momentum of photons in the light beam and therefore adjusting the torque of

the vortex beam. The important feature of this vortex generation technique is that optical angular momentum is changed without affecting intensity distribution of the laser beam. The benefits of tunable optical angular momentum were demonstrated in optical trapping experiment where silica micro spheres were trapped into a rotating ring is performed. The ability to tune the torque of the beam is proved by changing rotation speed change of the beads' ring.

Birefringence can be exploited not only for polarization control but also for phase. Half-wave retarder can induce phase delay to circularly polarized light depending on the azimuth of slow axis of the retarder. Based on that, converter for "diffraction-free" Airy and Bessel beams are fabricated. Properties of generated beams are measured and compared with theoretical simulations. Airy beam converter based on laser induced nanogratings has unique ability to generate dual Airy beam which is superposition two Airy beams accelerating in opposite direction. Generated Airy beam is also used in material modification. Self-detachment of fibre-like structure is observed from laser modified substrate which is speculated to be caused by properties of Airy beam.

Finally, an array of micro waveplates is fabricated which together with a linear polarizer and a CCD camera allows real time polarization imaging. Full state of polarization can be measured. For the demonstration, polarization distribution of cylindrical vector beams was measured.

Table of Contents

ABSTRACT.....	i
Table of Contents.....	i
List of tables	iii
List of figures	v
DECLARATION OF AUTHORSHIP.....	xix
Acknowledgements.....	xxi
Definitions and Abbreviations	xxiii
Chapter 1: Introduction	1
1.1 Motivation	1
1.2 Thesis overview.....	2
Chapter 2: Femtosecond laser material modification	5
2.1 Permanent transparent material modification	6
2.2 Self-assembled nanogratings	14
2.3 Physical and optical properties of nanogratings	22
2.4 Applications of nanogratings	26
Chapter 3: Properties of nanogratings	33
3.1 Inducing and measuring form birefringence.....	35
3.2 Pulse duration influence on nanogratings	45
3.3 Laser power, focusing conditions and fabrication speed	48
3.4 Polarization influence on laser modification	52
3.5 The lifetime of the nanogratings	67
Chapter 4: Applications of nanogratings.....	79
4.1 Introduction to the cylindrical vector beams.....	81
4.2 Cylindrical vector beams with orbital angular momentum.....	87
4.3 Cylindrical vector beams without phase modulation	102
4.4 Inducing nanogratings with CV beams	115
4.5 Beams with tuneable orbital angular momentum	122
4.6 Airy and Bessel beams converters	135
4.7 Polarization sensitive camera	152

Chapter 5: Conclusions.....	163
Appendix A.....	167
Appendix B.....	169
Appendix C.....	175
List of Publications.....	177
Bibliography.....	183

List of tables

Table 3-1 Retardance lifetime values at room temperature with its fitting parameters for all laser writing conditions.	73
Table 3-2 Scattering lifetime values at room temperature with its fitting parameters for all laser writing conditions.	74

List of figures

Figure 2-1	Schematic diagrams of different mechanisms of ionization when an electron in an atomic potential larger than the energy of photons.....	7
Figure 2-2	Dependence of threshold fluence for optical breakdown on pulse width. Image source: B. Stuart <i>et al.</i> [8].....	9
Figure 2-3	Three types of femtosecond laser induced modifications in fused silica: refractive index increase (Type 1), nanogratings (Type 2) and voids (Type 3). Image sources: (a) K. Miura <i>et al.</i> [14], (b) Y. Shimotsuma <i>et al.</i> [4], (c) E. Glezer <i>et al.</i> [15].....	11
Figure 2-4	Threshold pulse energies for different regimes of femtosecond laser induced modification in fused silica. Regime 1 corresponds to smooth refractive index modification. Regimes 2 and 3 correspond to nanograting formation. Image source: C. Hnatovsky <i>et al.</i> [16].....	12
Figure 2-5	Femtosecond laser inscription without (left) and with (right) aberration correction using adaptive optics. Top (xy) and side (xz) view of graphitic structure fabricated in diamond. The scale bar represents 5 μm . Image source: R. D. Simmonds <i>et al.</i> [22]	13
Figure 2-6	Nanograting formation dependence on the laser pulse energy. A single nano-plane could be induced by 60 nJ laser pulses. Image source: Y. Liao <i>et al.</i> [37].	15
Figure 2-7	SEM images of nanogratings formed by three different central wavelengths of the irradiated laser pulses, E: electric field of the writing laser, k: wave vector of the writing laser beam. (a): $\tau_p = 520$ fs, $E_p = 0.9$ μJ , writing speed 200 $\mu\text{m/s}$, rep. rate 500 kHz. (b): $\tau_p = 150$ fs, $E_p = 0.5$ μJ , writing speed 100 $\mu\text{m/s}$, rep. rate 250 kHz. (c): $\tau_p = 490$ fs, $E_p = 0.15$ μJ , writing speed 200 $\mu\text{m/s}$, rep. rate 200 kHz. Image source: W. Yang <i>et al.</i> [39].....	16
Figure 2-8	Nanograting period evolution predicted by plasmon interference theory. Inset shows wave vector matching diagram. Image source: Y. Shimotsuma <i>et al.</i> [4].....	18

Figure 2-9	Evolution of nanoplasma (A) formed at the ionized defects or colour centres into nanoplanes (D). Image source: R. Taylor <i>et al.</i> [43].	19
Figure 2-10	Schematic explanation of birefringence caused by nanogratings. (a) SEM image of nanogratings. (b) Nanogratings can be approximated by parallel planes with alternating refractive index which causes form birefringence. (c) Birefringence is characterized by retardance ($R = (n_o - n_e) \cdot d$) and azimuth of the slow axis (θ). (d - thickness of birefringent structure).	23
Figure 2-11	FEG-SEM, Secondary electrons images of laser tracks cross-section for each writing laser polarization. The laser parameters were: 0.5 μJ /pulse, 1030 nm, 300 fs, 200 kHz, 200 $\mu\text{m/s}$. A focusing lens of 0.5 NA was used. With the laser polarisation perpendicular (a) and parallel (b) to the scanning direction. (c) and (d) show close-ups of the nanograting and nanoplane regions respectively. Image source: J. Canning <i>et al.</i> [40]	25
Figure 2-12	(a) Microscope image of the central part of Fresnel zone plate in the crossed polarized light. (b) Phase retardation $\Delta\varphi$ of the zone plate measured with the interferometric setup. Image source: E. Bricchi [63].	26
Figure 2-13	CCD camera images of the reflection from laser written tracks. The red arrows indicate orientation of the polarization of the writing beam. The strong reflection is observed only along the electric field direction. Image source: E. Bricchi [63]	27
Figure 2-14	Spectrum of the light reflected from laser inscribed track. Two peaks can be explained by refractive index modulation with the period of 150 nm. Image source: Mills <i>et al.</i> [64].	28
Figure 2-15	Reconstruction of CGH. The highlighted areas were used for measuring the S/N. P - input beam polarization, PA - analyzer direction. (a) Reconstruction under crossed polarizers with input polarization at $\theta = 45^\circ$, (b) reconstruction under crossed polarizers with input polarization at $\theta = 2^\circ$, (c) reconstruction with parallel polarizers at 0° . Image source: D. G. Papazoglou and M. J. Loulakis [65].	29
Figure 2-16	(a) Microscope image where pseudo colors indicate the direction of the slow axis in the polarization diffraction grating. (b) The slow	

axis orientation and the corresponding phase modulation for two circular polarizations across the red line indicated in (a). The direction of the phase grating depends on the handedness of the circular polarization. (c) Grayscale map of birefringent grating phase variation measured with digital holography microscope for the linear polarization. (d) Far-field diffraction images for the incident right/left-handed circular and linear polarizations. Image source: M. Beresna *et al.* [67]..... 30

Figure 2-17 Femtosecond laser induces nanogratings and encodes information about laser fluence and polarization into material. Later information can be decoded by measuring two properties of the birefringence ($n_o - n_e$ and θ) of induced structure. 31

Figure 2-18 (Left) The Abrio image representing in false colours the recorded information in slow axis and retardance. (Middle and Right) Decoupled images of Maxwell and Newton (no additional operations on images were performed). Source: Beresna *et al.* [45]..... 32

Figure 3-1. The experimental setup..... 35

Figure 3-2 Crossed polarized microscope image femtosecond laser written map of Europe inside SiO₂ glass (a). The same structure imaged with birefringence measuring system Abrio (b). Colours indicates the azimuth of the slow axis of the birefringence. 36

Figure 3-3 Schematics of the polarized light microscope with two liquid crystal retarders (LCA and LCB) inserted in the imaging path and circular polarizer in the illumination path. α and β are the retardance of the liquid crystal plates LCA and LCB..... 37

Figure 3-4 The simulation of PolScope measurement. The dependance of measured retardance and slow axis values on real retardance value when the system is perfect (a) and when slight ellipticity is introduced into the illumination part (b). 39

Figure 3-5 Retardance and slow axis angle measurement using birefringence measurement system Abrio. (a) Retardance and slow axis distribution imaging of rectangle structures fabricated with different laser polarization and increasing laser power. Measured retardance dependence on laser power of structures written with 0° (b) and 22.5° (c) polarization. 41

Figure 3-6 (a) Schematics of setup for retardance with high magnitude measurement. The orientation of slow axis θ has to be known. (b) Retardance dependence on writing laser power measured with the setup. (c) Retardance measurement of structures having 1, 2 and 3 laser fabricated layers.	43
Figure 3-7 (a) Retardance dependence on laser power at different pulse durations. Modification threshold (b) and maximum retardance value (c) dependence pulse duration.	45
Figure 3-8. Nanogratings formation and retardance dependence on pulse duration. Structures were written with two different polarizations (blue arrows) with respect to writing direction (writing direction is horizontal).....	47
Figure 3-9. Microscopic images of femtosecond laser induced anisotropic modifications captured with a birefringence measurement system (CRi Abrio imaging system). Structures were written in two different speeds with increasing average laser power.	48
Figure 3-10 Retardance dependence of structures fabricated with 0.35 NA objective on laser intensity for two different speeds (Laser power was up to 900 mW).	49
Figure 3-11. Retardance dependence of structures fabricated with 0.16 NA lens on laser intensity for two different speeds (Laser power was up to 900 mW).	50
Figure 3-12. The dependence of retardance on pulse energy for four different polarizations of laser. Strongest difference is between 45° and -45° polarization. Writing speed of structures was $200 \mu\text{m/s}$	53
Figure 3-13. Microscopic retardance images of the structures written with various combinations of the polarization plane direction (blue), track writing direction (black) and raster scanning direction (dashed blue).	55
Figure 3-14. Microscope images of the femtosecond laser written tracks in chalcogenide, borate and phosphate glasses respectively. On the left images are taken without polarizers and the right with crossed polarizers. The highest birefringence is induced in glass with the highest photoelastic coefficient.	56
Figure 3-15. Laser induced stress birefringence in chalcogenide glass for two perpendicular linear polarizations. Grayscale images indicate the	

strength of the retardance and pseudo colors represent the orientation of birefringence slow axis (see legend). The sides of the induced tracks exhibit chevron-shaped slow axis orientation directed opposite to the writing direction (dashed lines). The width of the track is 30 μm	57
Figure 3-16. Schematic drawing describing stress and polarization geometry. The first laser written track produces chevron-shape stress (a). Grey chevrons indicate the drag of material as a result of light irradiation as sample is translated. Depending on where the next track will be written (top or bottom), polarization can be parallel or perpendicular to stress (c). Stress and polarization interaction should disappear when the distance between tracks is increased (b, d).	58
Figure 3-17. The influence of stress on the front of the laser modification. The modification front is perpendicular to the writing direction when distance between tracks is higher (a). When tracks are close to each other the modification front is tilted (b). Images were taken during laser modification.....	59
Figure 3-18. Fabrication of the polarization converter. The intensity of white light emission (due to hot plasma) during the laser fabrication oscillates as the angle between writing direction and the polarization plane changes.	61
Figure 3-19. The dependence of retardance on the separation distance between tracks for two polarizations. For the structure fabrication algorithm see the structures number 2 (a) and 3 (b) in Figure 3-13.	62
Figure 3-20. Schematic illustration of different angles between the plane of PFT and the plane of polarization or laser written line.	63
Figure 3-21. Retardance variation for two polarizations when the structure was written at different angles. The difference in the strength of birefringence is defined by the angle between the pulse front tilt and the writing direction. Separation between tracks was 3 μm , fabrication algorithm as in the structure number 2 in Figure 3-13. Arrows indicate laser writing direction (black) and the polarization plane direction (blue).....	64

Figure 3-22. Schematics explaining observed polarization dependence. For the left image, the writing direction is at 45° with respect to the pulse front tilt; whereas an electric field is oriented perpendicular or parallel to the pulse front tilt. The stronger modification is induced for the polarization parallel to the pulse front tilt. For the right image, the writing direction is perpendicular the pulse front tilt and an electric field is always at 45° to it. As a result the structures are equivalent for both polarizations..... 65

Figure 3-23. (Left) Schematic of the preparation of 25 identical samples written on fused silica glass slide. Laser tracks are indicated by solid blue arrows. (Right) Microscopic birefringence image of one sample. Colours indicate the strength of the retardance. Four different laser powers were used to write the structures and two polarizations (red arrows indicate the orientation of the polarization). 68

Figure 3-24. The retardance value decay during sample annealing at 1000° C. 69

Figure 3-25. The decay of the retardance value over time at different annealing temperatures. Structure is written with 200 mW laser power polarized parallel to the writing direction. Horizontal dashed line indicates 1/e of the retardance value R_0 at the beginning. 70

Figure 3-26. (a) Arrhenius plot of the laser induced nanograting for the lifetime of retardance value. Left inset illustrates the difference between two polarizations used for the femtosecond laser modification; right inset shows the zoomed in region of the Arrhenius plot at the room temperature. (b) Arrhenius plot of the laser induced nanograting for the lifetime of scattering value. 71

Figure 3-27 Annealing assisted control of laser induced retardance value: (a) microscopic birefringence images of laser written lines under various treatment conditions and (b) retardance value dependence on the average laser power and annealing conditions..... 75

Figure 3-28 Optical and SEM images of the cross-sectioned laser tracks before and after the annealing procedure at 900 °C for 1 hour. Annealed structures could not be imaged by SEM..... 77

Figure 3-29 Optical and SEM images of the cross-sectioned and etched (KOH, 1 mol/L, 20 °C, 24 h) laser tracks before and after the annealing procedure at 900 °C for 1 hour.	78
Figure 4-1 Spatial distribution of intensity and vector field for several spatially homogeneous SOP and CV beam modes: (a) x-polarized fundamental Gaussian mode; (b) x-polarized HG_{01} mode; (c) x-polarized HG_{10} mode; (d) y-polarized HG_{10} mode; (e) y-polarized HG_{01} mode; (f) x-polarized LG_{01} mode (vortex); (g) radially polarized mode; (h) azimuthally polarized mode; (i) linear superposition of (g) and (h).....	83
Figure 4-2 Radial polarization as superposition of orthogonally polarized HG modes.	86
Figure 4-3 (a) Schematic drawing of nanograting distribution in radial/azimuthal polarization converter for circular input polarization. (b) and (c) Distribution of electric field polarization for left-hand and right-hand circularly polarized input beam after passing through the converter.	87
Figure 4-4 The modelling of radially and azimuthally polarized vortex beams generated by quarter-wave polarization converter. Intensity and polarization distribution is modelled at the plane of the converter. The length of arrows indicates the strength instant electric field and the orientation – the direction of the polarization.	89
Figure 4-5 (a) The modelling of the propagation of radially polarized vortex beam. (b) The propagation of the same beam when linear polarizer (transmission axis is at 0° angle with the x axis) is inserted after the polarization converter.	93
Figure 4-6 Microscope images of the polarization converter in the bright field (a) and crossed polarizers (b) (circular polariser and linear polariser). The diameter of the structure is 1.2 mm. The radial lines emerging from the centre of the structure are due to finite step size in the writing process, which results in the visible segmentation of the structure. Red arrow indicates the writing laser polarization.....	95
Figure 4-7 Birefringence characterization of the structure performed with the Abrio system. The (a) and (b) images represent retardance value	

distribution with 5× (a) and 20× (b) magnification of the structure. The (c) and (d) images represents the color-coded distribution of slow axis..... 96

Figure 4-8 Measured beam profiles of second harmonic of cw Nd:YAG laser before (a) and after (b) beam converter. (c) Modelled and measured beam profile after inserting linear polarized at angles 0°, 45°, 90°, 135°. White arrows indicate the orientation of the polarizer’s transmission axis..... 97

Figure 4-9 Modelled and measured patterns of optical vortices with azimuthal and radial polarization after linear polarizer (horizontal orientation). White arrows indicate incident polarization state. 98

Figure 4-10 Propagation of radially polarized optical vortex beam through the polarization diffraction grating. Polarization diffraction grating separates beams with opposite handedness of circular polarization. 99

Figure 4-11 The modelling (a, b) and the experiment (c) of the radially polarized vortex beam propagation after passing through the polarization diffraction grating. The beam modelled in Figure 4-5 (a) propagates for 50 mm (a) or 250 mm (b)..... 100

Figure 4-12. Schematic drawings of nanogratings distribution in polarization converters. (a), (b) Converter for LG₁₀ mode beam, (c), (d) – for LG₂₀ mode beam, (e), (f) – for LG₃₀ mode beam. (a) Converter for radial/azimuthal beam generation.° 102

Figure 4-13 Modelling of intensity and polarization distributions of CV beams generated with different half-wave polarization converters. Equations describe the distribution of half-wave plates in the converters (Figure 4-12). Red arrows shows the plane of polarization of the input Gaussian beam. Green arrows indicates the orientation of the linear analyser placed after the converter and corresponding beam distributions after the analyser are modelled..... 105

Figure 4-14 The modelling of generated beams when retardance value of the converter is not exactly half-wave value..... 107

Figure 4-15 Microscopic images of small test versions of half-wave polarization converters for first and second order CV beams generation. (a,

b) Distribution of slow axis orientation, (c, d) converters are placed between crossed polarizers.....	109
Figure 4-16 (a) Half-wave polarization converter for second order CV beams (8 mm in diameter). (b) Polarization converter for first order CV beams (radial/azimuthal polarization) placed between crossed polarizers (14 mm in diameter). (c) Beam profile of input linearly polarized beam. (d) Beam profile radially polarized beam generated by the converter in (b). (e-h) The same beam after the linear analyser at angles 0°, 90°, 45° and -45°.....	110
Figure 4-17 Beam profiles of high order CV beams (i), the same beams with linear analyser (ii) and vortex beams (iii). (a)(i, iii) Profiles of linearly and circularly polarized beam before the converter. (a)(ii) 10-th order polarization converter between crossed polarizers. (b) Second order beams, (c) fifth order CV beam, (d) 10-th order CV beam.....	111
Figure 4-18 Generation of radially polarized beam at 1550 nm.....	113
Figure 4-19 SEM images of nanogratings induced by radially (a) and azimuthally (b) polarized femtosecond laser. The modelled distribution of slow axis of birefringent modifications induced by radially (c) and azimuthally (d) polarized beams. (Source for images (a) and (b): C. Hnatovsky <i>et al.</i> (2011) [106]).....	115
Figure 4-20 Modelling of the birefringent track induced by radially (a) and azimuthally (b) polarized beams moving across a sample in a sinusoidal curve.....	118
Figure 4-21 Abrio images of modifications induced by azimuthally polarized beams.	119
Figure 4-22 Modelling of disc structure fabricated with radially polarized beam: (a) perfect radially polarized beam, (b, c) beam generated with not ideal polarization converter. Not ideal polarization converter had higher than half-wave value of retardance: (b) $+0.05 \cdot \lambda$, (c) $+0.1 \cdot \lambda$. Abrio images of structure fabricated with radially polarized beam. (i) Fluence distribution, (ii) retardance distribution, (iii) slow axis orientation distribution of the modelled and measured structures.....	121
Figure 4-23 The transformation of a photon transmitted through a quarter-wave plate and S-waveplate. Linearly polarized photon passes	

through the quarter-wave plate (set at the angle θ) and acquires spin momentum depending on the θ value. (a) Photon with spin momentum $S = \hbar$ and no OAM (right-handed circularly polarized light) transmitted through the S-waveplate changes spin momentum to $S = -\hbar$ and gets $L = -\hbar$ (left handed circularly polarized left-handed optical vortex). (b) Photon with spin momentum $S = -\hbar$ (left-handed circularly polarized light) is transformed into the photon with spin momentum $S = \hbar$ and $L = \hbar$ (right-handed circularly polarized optical vortex). (c) Elliptically polarized photon with spin momentum $\langle S(\theta) \rangle$ obtains $\langle L \rangle = -\langle S(\theta) \rangle$ and $\langle S \rangle = -\langle S(\theta) \rangle$. Intensity profiles of left- and right-handed optical vortices (d), (e) and radially polarized beam (f). 125

Figure 4-24 (a) Fused silica microspheres trapping experimental setup. (b) The image of five trapped spheres forming a ring. 128

Figure 4-25 The rotation of five trapped spheres. Spheres rotates counter clockwise when polarization before the S-waveplate is right-handed circular (a) and clockwise when left-handed circular (c). Spheres do not rotate when polarization before S-waveplate is linear (b). 129

Figure 4-26 Total measured rotation angle (integral of the rotation speed) of trapped spheres at different laser trapping powers. 130

Figure 4-27 Rotation speed of trapped spheres dependence on the average orbital angular momentum of the photons at different average powers of the laser. 131

Figure 4-28 Rotation speed of trapped spheres dependence on (a) average laser power used for the trapping when $l = \pm 1$ 132

Figure 4-29 The array of nine polarization converters. Cross-polarized microscope image shows that the topological charge of converters is 4 (eight lobes). Such converter can be used in generation of optical vortex with tuneable OAM from $\langle L \rangle = -4\hbar$ to $\langle L \rangle = 4\hbar$ 133

Figure 4-30 Propagation of one dimention (1D) infinite (a) and finite (Gaussian truncated) (b) Airy beams. (c, d) Beam profiles of two dimentional (2D) finite Airy beam. After propagating the maximum of the beam shifts from the centre (d). 135

Figure 4-31 Modelled cubic 1D (a) and 2D (b) phase distribution which could be used with SLM to generate Airy beam.....	136
Figure 4-32 Schematic drawing of the birefringent optical element with 1D (a) and 2D (b) cubic slow axis distribution of the micro half-wave plates. Such optical elements work as phase element for circularly polarized light and can be used as Airy beam converter having no phase discontinuity as in Figure 4-31	138
Figure 4-33 Microscopic image of the fabricated 2D Airy beam converter between cross-polarizers (a) and quantitative birefringence microscopy image (b), where pseudo-colour represents slow axis angle. Structure size is 2×2 mm. (c) The schematics of generating Airy beam using polarization sensitive beam converter.	140
Figure 4-34 Propagation of 1D Airy beam. Arrows on the left indicates the polarization of incident Gaussian beam and arrows on the right – the polarization of generated Airy beams. Scale is in mm.....	142
Figure 4-35 Modelled propagation of 1D Airy beam with same conditions as in Figure 4-34. Scale is in mm.....	142
Figure 4-36 Experimental characterization of 2D Airy beam propagation. Arrows indicate the polarization of the input light (left-/right-handed circular polarization and linear polarization). In the case of linearly polarized input the dual Airy beam is generated...	143
Figure 4-37 Simulation of propagating dual Airy beam. (a) Dual Airy beam when the two branches have same polarization and therefore interference can be seen. (b) Dual Airy beam when the two branches are orthogonally polarized and do not interfere (Airy beam converter case).....	144
Figure 4-38 Abrio images (distribution of birefringence slow axis) of polarization sensitive Bessel beam (zero order (a) and second order (b)) converters. (c, d) Beam profiles of generated zero and second order Bessel beams, measured at different distances from the focus plane.....	145
Figure 4-39 Measured propagation of zero order Bessel beam (a) and simulation of Gaussian beam (with similar beam waist at the focus) propagation (b). Measured beam profile of Bessel beam	

(c) and modelled beam profile of Gaussian beam at 140 mm distance from the focus plane (d).	146
Figure 4-40 The scribing of the glass slide using Airy beam (a). After breaking sample to stripes (b), the fiber-like structure separates from the one side in few minutes (c). (d)-(f) The schematic drawing illustrating laser inscription, the breakage and the spontaneous detachment of the fiber-like structure.	148
Figure 4-41 (a) The SEM image of the two opposite sides of the stripe. (b) The SEM image of the heart-shape fiber-like structure detached from the stripe and left over after the fiber-like structure is removed totally from the stripe.	149
Figure 4-42 Retardance imaging of the same left over as in Figure 4-41 (b). Strong retardance near the inscribed line indicates the high accumulation of the stress which can lead to the spontaneous breakage.....	150
Figure 4-43 Visible picture of two pickup trucks in the shade (a), long-wave IR intensity image (b), and long-wave IR polarization image (c). Strong contrast in the polarization image shows advantages for enhanced target detection using imaging polarimetry. (Image source: J. S. Tyo <i>et al.</i> (2006) [156]).....	152
Figure 4-44 Poincare sphere diagram. Stokes parameters S_1 and S_2 describes the linear part of the polarization and S_3 – the circular.....	153
Figure 4-45 The basic schematic of the polarimetric camera. Before the light reaches a CCD matrix it propagates through micro waveplates array and a linear polarizer.	154
Figure 4-46 (Left) The schematic of one segment in the birefringent mask. The lines indicate direction of the imprinted nanogratings. (Right) The birefringent mask imaged in cross-polarizers (1×1 mm). The inset shows a zoomed segment of the mask.	156
Figure 4-47 Retardance dependence on the laser pulse energy when written at different polarization orientations with respect to the writing direction.	157
Figure 4-48 (a)-(f) The measurement of the polarization distribution in the radially polarized beam. (g)-(i) The transition of the circularly polarized light near the edge of the S-waveplate. (a) The image of the birefringent mask illuminated with the radially polarized	

light. (b)-(e) The distribution of the calculated Stokes parameters (S_0 , S_1 , S_2 and S_3). (f) The orientation of the linear polarization. (g) The image of the birefringent mask when it is illuminated with the circularly polarized light. (h)-(i) The distribution of the calculated Stokes parameters (S_1 and S_3). 159

Figure 4-49 The measurement of the radially polarized light and the high order cylindrical vector (CV) beam with the high resolution waveplate mask. (a), (b) The image of the mask while illuminated with the high order CV beam. (c), (d) measured polarization distribution of the radially polarized light and the high order CV beam.... 161

DECLARATION OF AUTHORSHIP

I, Mindaugas Gecevičius, declare that this thesis and the work presented in it are my own and has been generated by me as the result of my own original research.

Polarization sensitive optical elements by ultrafast laser nanostructuring of glass

I confirm that:

1. This work was done wholly or mainly while in candidature for a research degree at this University;
2. Where any part of this thesis has previously been submitted for a degree or any other qualification at this University or any other institution, this has been clearly stated;
3. Where I have consulted the published work of others, this is always clearly attributed;
4. Where I have quoted from the work of others, the source is always given. With the exception of such quotations, this thesis is entirely my own work;
5. I have acknowledged all main sources of help;
6. Where the thesis is based on work done by myself jointly with others, I have made clear exactly what was done by others and what I have contributed myself;
7. Parts of this work have been published as:

M. Gecevičius, M. Beresna, R. Drevinskas, P. G. Kazansky
Airy beams generated by ultrafast laser-imprinted space-variant nanostructures in glass
***Optics Letters*, Vol. 39, Issue 24, pp. 6791-6794 (2014)**

M. Beresna, **M. Gecevičius**, P. G. Kazansky
Ultrafast laser direct writing and nanostructuring in transparent materials
***Advances in Optics and Photonics*, Vol. 6, Issue 3, pp. 293-339 (2014)**

M. Gecevičius, R. Drevinskas, M. Beresna, P. G. Kazansky
Single beam optical vortex tweezers with tuneable orbital angular momentum
***Applied Physics Letters*, Vol. 104, Issue 23, pp. 231110 (2014)**

M. Gecevičius, M. Beresna, P. G. Kazansky
Polarization sensitive camera by femtosecond laser nanostructuring
Optics Letters, Vol. 38, Issue 20, pp. 4096-4099 (2013)

M. Gecevičius, M. Beresna, J. Zhang, W. Yang, H. Takebe, P. G. Kazansky
Extraordinary anisotropy of ultrafast laser writing in glass
Optics Express, Vol. 21, Issue 4, pp. 3959-3968 (2013)

M. Beresna, **M. Gecevičius**, P. G. Kazansky
Polarization sensitive elements fabricated by femtosecond laser nanostructuring of glass [Invited]
Optical Materials Express, Vol. 1, Issue 4, pp. 783-795 (2011)

M. Beresna, **M. Gecevičius**, P. G. Kazansky, T. Gertus
Radially polarized optical vortex converter created by femtosecond laser nanostructuring of glass
Applied Physics Letters, Vol. 98, Issue 20, pp. 201101 (2011)

Signed:

Date:

Acknowledgements

I would like to express my gratitude to the numerous individuals whose help and support assisted my professional growth during my recent years and contributed to my work presented in this theses.

Firstly I want to thank to my bachelor and PhD works supervisors. I am thankful to my supervisor in Vilnius University, Valerijus Smilgevičius, who introduced me to the research in physics. Special thanks are addressed to my PhD supervisor Peter Kazansky for leading my doctoral project and creating good atmosphere in his laboratory.

I acknowledge all the help and support from our research group members, Martynas Beresna, Costantino Corbari, Jingyu Zhang, Rokas Drevinskas and Aabid Patel. Especially I want to thank to Martynas as he helped me to learn new field and with who big part of my research was done and to Rokas for continuing some of my research I did not finish.

I am grateful to my girlfriend Yilu Xie who supported me morally during my theses writing time.

And my final appreciation is to the Engineering and Physical Sciences Research Council (EPSRC) who gave the opportunity to study in the ORC by supporting my PhD financially.

Definitions and Abbreviations

E	Electric field
w	Beam waist
γ	Keldysh parameter
ν	Frequency of light
ω	Angular frequency of light
λ	Wavelength of light
k_0	Wavenumber in vacuum
ϵ_0	Electric permittivity in free space
μ_0	Magnetic permeability in free space
c	Speed of light in free space
\hbar	Reduced Planck constant
E_g	Bandgap energy of the material
I	Laser intensity
n	Refractive index of material
n_e	Extraordinary refractive index
n_o	Ordinary refractive index
k_B	Boltzmann constant
φ	Phase
$\Delta\varphi$	Phase retardation
θ	Slow axis azimuth
ϕ	Polar angle
R	Retardance

τ	Laser pulse duration
NA	Numerical aperture
SEM	Scanning electron microscope
VP-ESEM	Variable pressure/environmental scanning electron mode
CCD	Coupled charge device
SOP	State of polarization
CV	Cylindrical vector [beam]

Chapter 1: Introduction

1.1 Motivation

Material processing of transparent materials with lasers has become a fast growing field of research and technology. The very first investigations of the laser induced material modifications followed immediately after the invention of the laser in the early sixties. Initially limited by studies of the unwanted damage caused by high laser fluences, this field sought the potential for controllable material processing. Further development of laser systems allowed focusing powerful high quality laser beams into diffraction limited spot leading to unprecedented optical intensities. As a result, the laser could serve as a unique and versatile contactless material modification tool.

The first lasers delivering sub-picosecond pulses were demonstrated in early 1970s with the advance in mode locking techniques and organic dye lasers. However, these laser sources lacked stability and power and thus were limited to applications in spectroscopy. The 1990s saw the revolution of ultrafast laser technology. The invention of new mode locking mechanisms, namely Kerr-lens mode locking [1] and semiconductor saturable absorber mirrors [2], allowed generation of stable pulse trains from solid state laser systems, which gave stability and power scalability. This was followed by first demonstrations of femtosecond laser processing in the bulk of transparent materials made by K. Hirao group, which demonstrated waveguiding structures written inside of silica glass [3].

More than decade ago another type of laser induced modification in fused silica was observed where sub wavelength nanogratings forms in laser affected volume [4]. This type of modification exhibits form birefringence which can be controlled by laser parameters. Many groups since then investigated properties of nanogratings and formation mechanism, but still there is no definite explanation on how nanogratings form. However number of application of nanogratings is growing. In this theses I will discuss about optical and physical properties of nanogratings and how it can be adjusted by changing laser parameters. Finally this knowledge leads to ability to fabricate various optical devices based femtosecond laser induces nanogratings.

1.2 Thesis overview

My thesis is divided into of three main big chapters. In **Chapter 2: Femtosecond laser material modification** I will do small literature review on femtosecond laser interaction with transparent materials and femtosecond laser induced nanogratings. **Chapter 3: Properties of nanogratings** and **Chapter 4: Applications of nanogratings** consists of my experimental work and theoretical modelling on investigation of properties of nanogratings and applications in various optical elements.

Chapter 2.1 Short review on ultrashort pulses interaction with transparent material. Mechanisms of laser induced permanent modifications are explained and different types of modifications depending on laser parameters in silica glass are introduced.

Chapter 2.2 Femtosecond laser induced nanogratings in fused silica are introduced. Possible nanogratings formation mechanism are discussed.

Chapter 2.3 Short review on physical and optical properties of nanogratings. Form birefringence on nanogratings is explained.

Chapter 2.4 Short review on application of nanogratings such as optical elements fabrication and 5D optical memory recording.

Chapter 3.1 Femtosecond laser system used in material modification experiments are introduced. Quantitative birefringence measurement system Abrio examined. Abrio system is modelled with MATLAB and results compared with experiments in order to understand the limitations of birefringence measurement as birefringence is most important property of optical elements based on nanogratings.

Chapter 3.2 Pulse duration influence on properties of nanogratings are investigated. Optimum range of pulse duration assessed in order to achieve strong birefringence of nanogratings.

Chapter 3.3 Influence on modification on other laser fabrication parameters (laser power, focusing condition, fabrication speed) is investigated. Set of laser parameters are assessed which allows fast fabrication of structures exhibiting

quarter- and half-wave retardance value at 515 nm. This leads to fast fabrication of optical elements with micro waveplates distribution.

Chapter 3.4 Polarization influence on retardance value on induced nanogratings is discussed. The influence on polarization azimuth on laser writing direction is known. However here unexpected difference between 45° and -45° to the writing direction is observed.

Chapter 3.5 Annealing of femtosecond laser induced nanogratings experiments are performed. Annealing allows estimation of the lifetime of nanogratings which is about 10^{34} years at the room temperature. Also annealing can be used to control retardance value of fabricated structures.

Chapter 4.1 Cylindrical vector beams are introduced.

Chapter 4.2 Fabrication of optical elements based on nanogratings exhibiting quarter-wave retardance value for cylindrical vector beams generation. Such converters generates cylindrical vector beams with orbital angular momentum. Theoretical modelling is performed in compared with experimentally generated beams.

Chapter 4.3 Fabrication of optical elements based on nanogratings exhibiting half-wave retardance value for cylindrical vector beams generation. Such polarization converters generates cylindrical vector beams without orbital angular momentum. Theoretical modelling is performed in compared with experimentally generated beams. Polarization converters for high order cylindrical vector beams and converters working at different wavelength were fabricated and tested. Also theoretical simulation for estimating the influence on retardance value deviation from optimum value was performed.

Chapter 4.4 Beams generated with previously discussed polarization converters are used for material modification. Theoretical modelling is compared with experimental results.

Chapter 4.5 Demonstrated that polarization converters can be used not just for polarization control in the beam but also generating optical vortices with tuneable orbital angular momentum. Optical trapping of silica micro spheres experiment was performed where tuneable torque of the beam is

demonstrated. By tuning torque of the beam, the shape of the beam stays constant.

Chapter 4.6 Converter for “diffraction-free” Airy and Bessel beams are fabricated. Generated beams are compared with theoretical simulations. Based on nanogratings Airy beam converter has unique ability to generate dual Airy beam which is superposition two Airy beams accelerating in opposite direction. Generated Airy beam is used in material modification.

Chapter 4.7 Micro waveplates array is fabricated which together with linear polarizer and CCD camera allow real time polarization imaging. Full state of polarization can be measured. For the demonstration, polarization distribution of cylindrical vector beams were measure.

Chapter 2: Femtosecond laser material modification

In this chapter I will shortly review laser mater interaction and mechanisms of permanent modifications in transparent materials. Tightly focused ultrashort pulses can reach intensities high enough to induce breakdown even in material which is transparent to the wavelength of the laser. This can happen due to nonlinear light-matter interaction and can lead to different types of modification such as refractive index increase, nanogratings exhibiting form birefringence or bubbles formation.

As the main goal of the theses is to fabricate optical elements based on laser induced nanogratings, I will mostly concentrate on nanogratings in this chapter. There are few models trying explain the formation of nanogratings under the illumination of femtosecond laser. However there is no complete explanation. Even though the exact mechanism of nanogratings formation is unknown, there are a lot of work done by different groups on physical and optical properties of nanogratings, laser parameters influence on those properties and applications.

2.1 Permanent transparent material modification

The band gap of transparent materials (mostly dielectrics) is typically much larger than the energy of a single photon of the infrared laser source. For comparison, the band gap of fused silica is about 9 eV, while the photon energy at 1030 nm wavelength is 1.2 eV. In the linear interaction regime, a photon with such energy $\hbar\omega$ is much smaller than the band gap of the material E_g and thus cannot be absorbed. If, however, the light intensity is sufficiently high, nonlinear processes can lead to the material ionization. There are two classes of such processes: nonlinear photoionization and avalanche ionization [5,6].

Photoionization refers to the direct electron excitation by an electric field of light. Depending on laser frequency and laser intensity, the photoionization can occur in the form of tunnelling or multiphoton ionization. Multiphoton ionisation tends to occur at higher laser frequencies (but still lower than the band gap) and lower laser intensities. During this process several photons are absorbed by the electron simultaneously (Figure 2-1). If the electric field is very strong (and the frequency of the laser is lower), Coulomb well binding the electron in atom, is suppressed by the electric field of the laser and the electron becomes free by tunnelling through the barrier (Figure 2-1). Normally, to know which of two, tunnelling or multiphoton ionisation, is dominant, adiabatic parameter γ , also widely referred as Keldysh parameter, is calculated [7]:

$$\gamma = \frac{\omega}{e} \sqrt{\frac{m_e c n \epsilon_0 E_g}{I}}, \quad (2-1)$$

where ω is the laser frequency, e - charge of the electron, m_e - mass of the electron, c - the velocity of light, n - refractive index of the material, ϵ_0 - permittivity of the free space, E_g - band gap of the material and I is the intensity of the laser. When the Keldysh parameter is smaller than 1.5, the tunnelling process dominates the photoionization, if it exceeds 1.5, then multiphoton process is dominant (Figure 2-1).

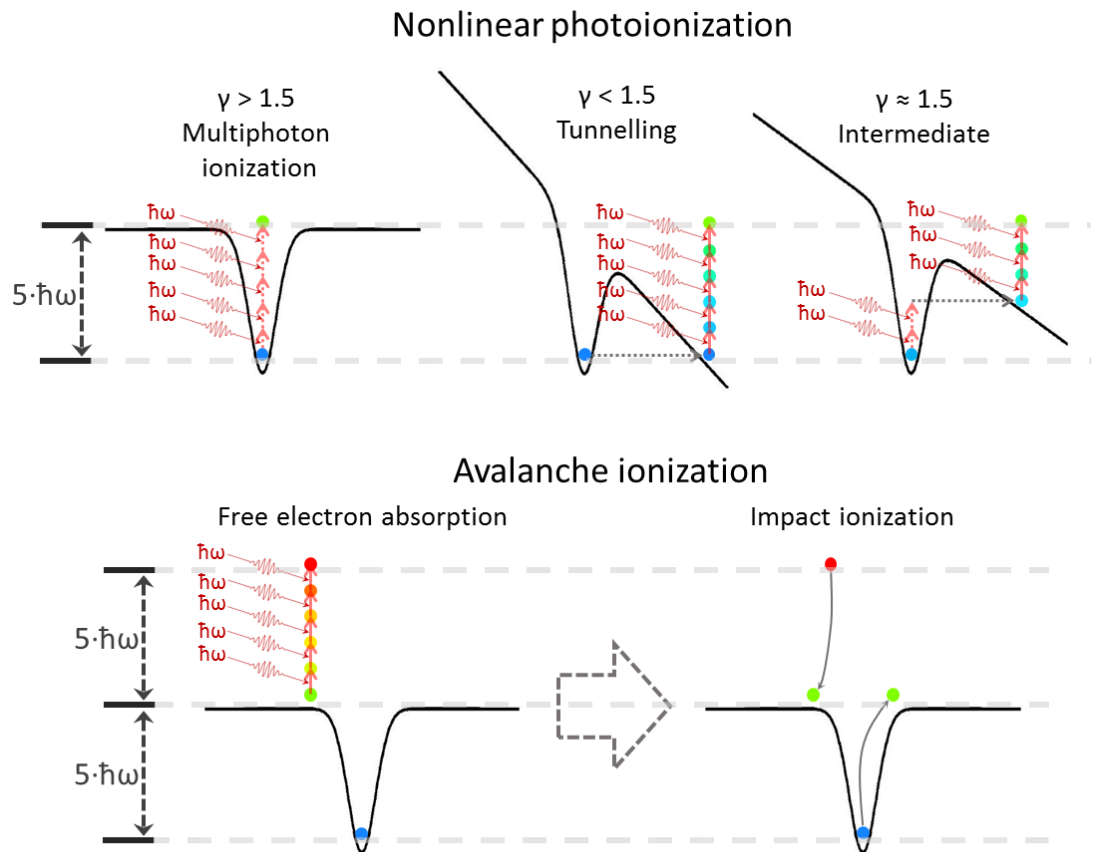


Figure 2-1 Schematic diagrams of different mechanisms of ionization when an electron in an atomic potential larger than the energy of photons.

In the multiphoton absorption regime, photoionization rate $P_{PI}(I)$ depends strongly on the laser intensity:

$$P_{PI}(I) = \sigma_k I^k \quad (2-2)$$

where σ_k is the multiphoton absorption coefficient for k -photon absorption. The electron will be excited to the conduction band if the following condition is met:

$$k\hbar\omega \geq E_g \quad (2-3)$$

The strong dependence on the intensity also means that photoionization process is more efficient for short pulses. If laser pulse gets sufficiently long

the photoionization process cannot efficiently supply the seed electrons and excitation process becomes strongly dependent on random impurities which energy levels lies close to conduction band. As a result, modification process becomes less deterministic.

When there are some electrons in the conduction band, avalanche ionisation can occur. The initial seed electrons are heated up by inverse Bremsstrahlung (free electrons are accelerated by absorbed photons) until they reach the energy of the band gap. After the electron energy exceeds that of the band gap, it can ionize, via collision, another electron from the valence band resulting in two electrons near the bottom of the conduction band (Figure 2-1) [5]. Both electrons can again absorb energy and repeat the described energy transfer cycle. The process will continue as long as the light electric field is present. The density of electrons generated through the avalanche process is:

$$\eta_{av}(t) = \eta_0 2^{w_{imp}t} = \eta_0 e^{w_{imp}t \ln 2}, \quad (2-4)$$

where η_0 is initial (seed) electron concentration and w_{imp} is the probability of the impact ionization. One can see that avalanche ionization requires the presence of seed electrons, which trigger the process and is more efficient with longer pulse durations. The source of the seed electrons η_0 depends on the material. For material with defects or some dopants initial electrons can be excited from these low lying levels via linear absorption or thermal excitation [5]. For pure dielectrics seed electrons are supplied via photoionization (for ultrashort pulses).

After laser beam passes, the excited electrons return back to their ground states and transfer part of their energy to the lattice. In order to create a breakdown in transparent dielectric material, high intensity and high fluence of light is required. High intensity is required to start photoionization and the high fluence ensures enough amount of energy per volume to cause the breakdown of the lattice. This is achieved by tightly focusing ultrashort laser beam. The heating of lattice lasts on a picosecond to nanosecond time scale.

When sufficient amount of energy is absorbed via the described mechanisms and is deposited into the material via electron-phonon coupling and defect

formation permanent damage occurs. If pulse duration is longer than a few tens of picoseconds, during the time of pulse duration, the energy from electrons is transferred to the lattice. In such situation the absorbed energy is coupled into the lattice by the thermal wave and then carried out from the focal volume by heat diffusion. In this regime required fluence (defined as integral of the laser intensity over time) for the optical breakdown threshold scales with the square root of the pulse width τ (Figure 2-2) [8]. The resulting damage is the consequence of melting and boiling of the material and therefore is spreading around the focal volume, what causes irregular shape of the damage.

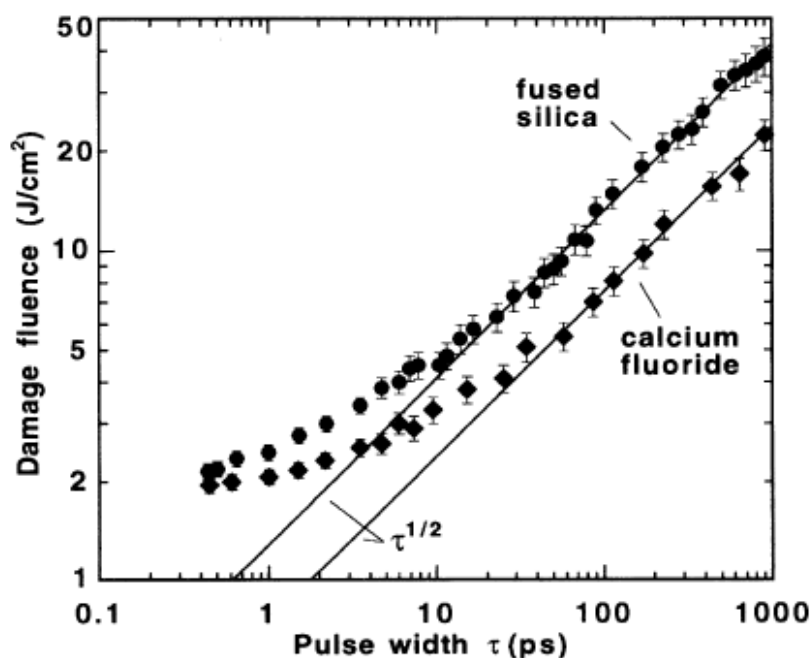


Figure 2-2 Dependence of threshold fluence for optical breakdown on pulse width. Image source: B. Stuart *et al.* [8]

There is, however, no widely accepted definition of damage threshold. Frequently the damage threshold is characterized by post-mortem optical measurements [5,9] considering the surface and bulk of the material are as the same quality. However, these two situations are quite different. First of all, the laser focus at the surface is not affected by the self-focusing and spherical aberration as for the bulk [10]. Second, the damage threshold on the surface

may greatly vary with its preparation (type of the polishing, impurities) and quality [11].

The character and mechanism of the material modification largely depends on the laser pulse duration. During laser irradiation electric field energy is absorbed by the electrons, which are excited into the conduction band. The excited electrons distribute energy between themselves via carrier-carrier scattering (10-100 fs) and also by carrier-phonon scattering (>10 ps). The first process leads to fast energy redistribution among the excited carriers, the second transfers the energy to the lattice equalizing the temperature of the electrons and the lattice. The typical timescale for the electron energy transfer to the lattice is of tens of picoseconds.

Thus if the laser pulse duration is of the same scale (~10 ps) a substantial amount of energy will be transferred to the lattice during the pulse propagation [5]. The excited lattice phonons are transferring energy into the vicinity of the laser focus by thermal diffusion. Later, the material is permanently damaged if the temperature in the affected zone becomes sufficient to melt it. As a result, strong tension gradient occurs, which leads to fracturing of the material, degrading the quality of the machined material. The damage threshold is then determined by a relative rate of energy deposition and thermal diffusion. It is known that damage threshold (given in fluence) scales as the square root of the pulse duration. However, with the development of ultrafast lasers a deviation from this law was observed with laser pulses shorter than 10 ps [9]. As it was mentioned above, mostly the damage threshold is measured for the surface in order to avoid complications related to non-linear effects such as self-focusing, dispersion and self-phase modulation. The deviation from the square root law can be explained by a rapid electron ionization mechanism. For pulses < 10 ps, thermal diffusion and electron-ion interaction take place after the laser pulse, thus the electrons can reach high temperatures, while keeping the lattice in the cold state during the laser pulse irradiation. Afterwards, the electrons release energy only to the irradiated zone, reducing heat affected zone and collateral damage in the vicinity. The permanent damage is typically related to the critical plasma concentration, when the laser irradiation is strongly absorbed by the excited electron plasma. However, recent direct measurements of the plasma concentration put this assumption under dispute. It was found that a

permanent damage can be induced even at the sub-critical plasma concentration [12,13].

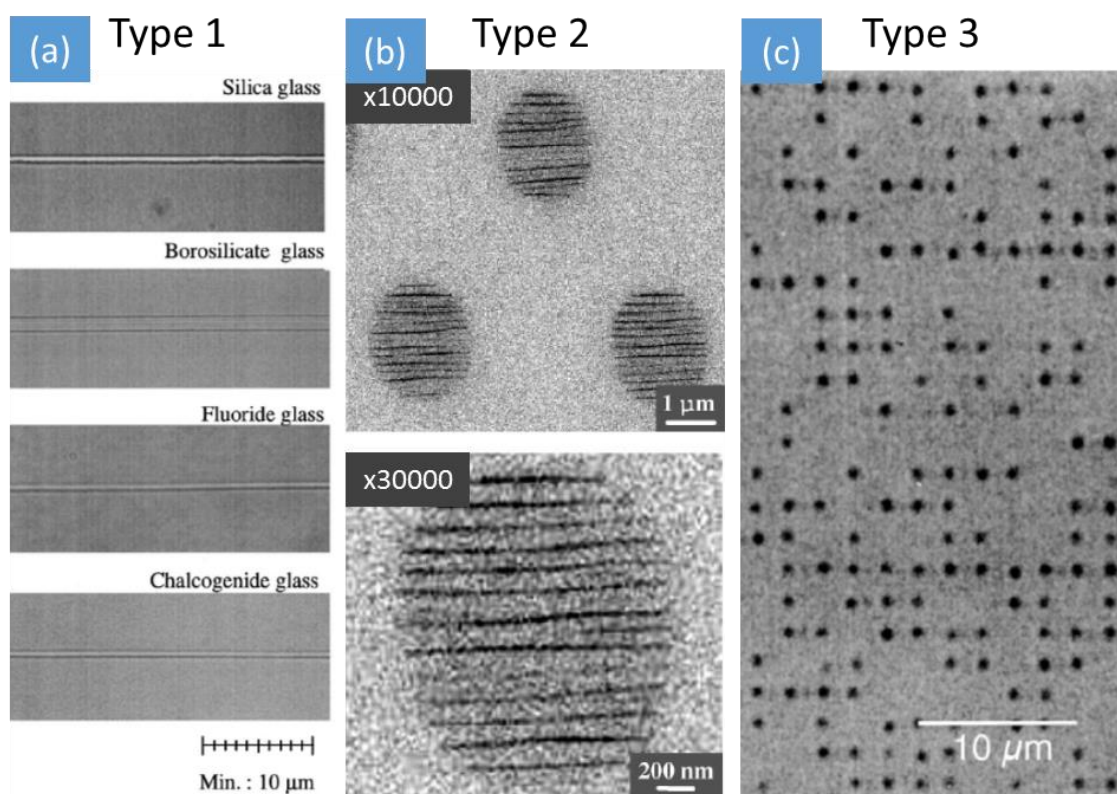


Figure 2-3 Three types of femtosecond laser induced modifications in fused silica: refractive index increase (Type 1), nanogratings (Type 2) and voids (Type 3). Image sources: (a) K. Miura *et al.* [14], (b) Y. Shimotsuma *et al.* [4], (c) E. Glezer *et al.* [15]

Depending on the fluence, femtosecond laser irradiation can produce three types of modification in the bulk of fused silica: isotropic refractive index increase (Type 1) [3,14], nanogratings (Type 2) [4] and voids (Type 3) [15] (Figure 2-3). These three types can be clearly distinguished usually for laser pulses shorter than about 200 fs [16,17] (Figure 2-4). At longer pulses nanogratings appear even at relatively low fluencies, just above a permanent modification threshold. The extensive analysis of the thresholds of these modifications for silica doped with Ge, F and P was presented by B. Pommellec *et al.* [18]. The threshold for Type 1 modification was independent on the doping and was 0.095 $\mu\text{J}/\text{pulse}$. Whereas the threshold for nanograting formation was strongly affected by dopants and varied from 0.13 $\mu\text{J}/\text{pulse}$ for

1.5% doped Ge:SiO₂ sample to 1.2 μJ/pulse for 0.3% F:SiO₂. For comparison, the threshold for pure silica was 0.31 μJ/pulse.

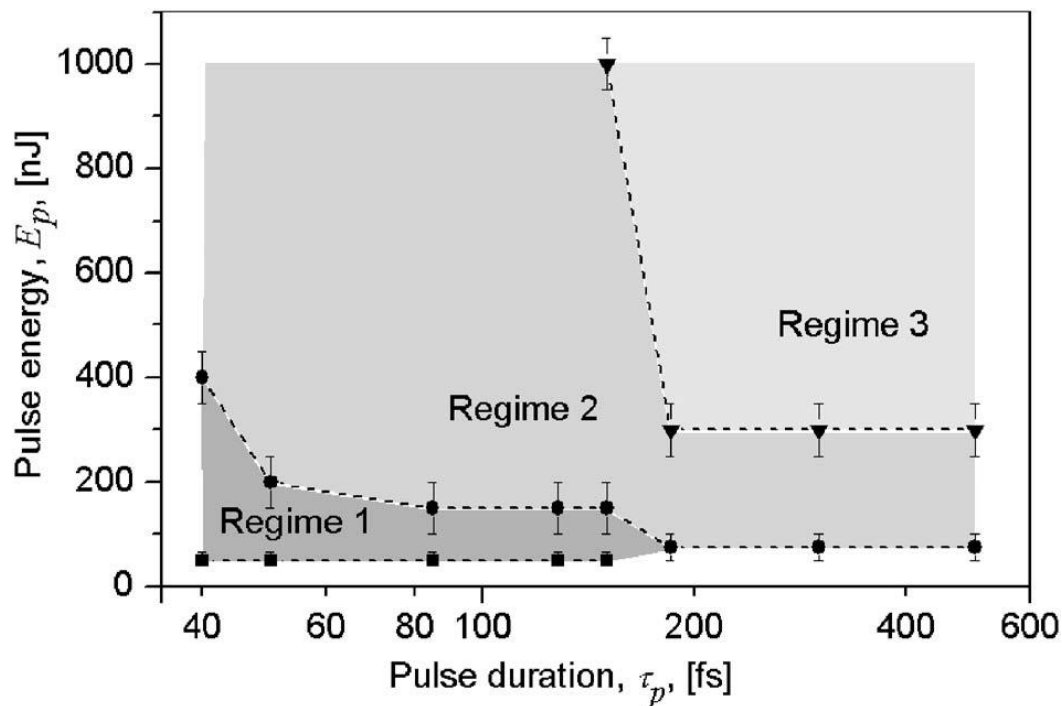


Figure 2-4 Threshold pulse energies for different regimes of femtosecond laser induced modification in fused silica. Regime 1 corresponds to smooth refractive index modification. Regimes 2 and 3 correspond to nanograting formation. Image source: C. Hnatovsky *et al.* [16].

Another important parameter for femtosecond laser direct writing is focusing conditions, which roughly can be arranged into three groups depending on the numerical aperture. The low NA regime is related to lenses with $NA < 0.1$, this gives spot size of more than 10 μm. The femtosecond laser beam weakly focused into the bulk of transparent material turns into filament below damage threshold preventing single-shot permanent structural modification [19,20]. As a result, low NA lenses are typically used for surface modification, where self-focusing is not playing a crucial role. The lenses with numerical aperture from 0.1 to 0.5 can already induce a confined permanent modification inside of transparent material. At these numerical apertures spherical aberration can strongly affect the laser beam propagation. The refractive index of fused silica is higher than air's by 0.5. The light is therefore non-uniformly refracted at the interface between the air and the material. As a result the adjacent part of the

beam is focused deeper than the central, the extending the focal spot in the propagation direction. This also effectively reduces the angular spectrum of the focused laser beam and the spot size becomes larger. The strength of this effect is increasing with numerical aperture. The refractive index mismatch can be compensated by using objectives with spherical aberration correction, immersion optics or adaptive optics methods (Figure 2-5) [21,22].

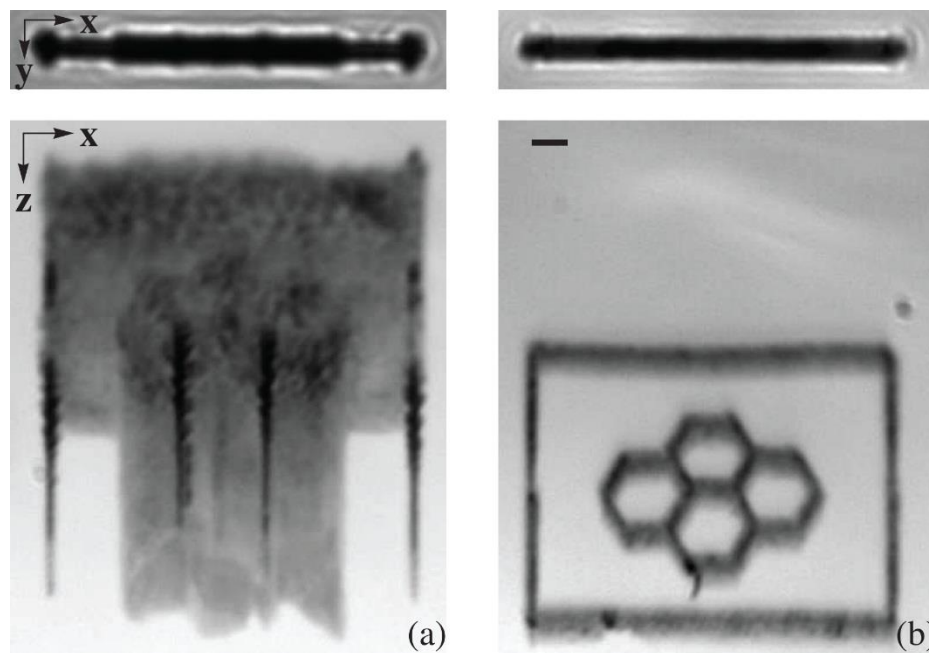


Figure 2-5 Femtosecond laser inscription without (left) and with (right) aberration correction using adaptive optics. Top (xy) and side (xz) view of graphitic structure fabricated in diamond. The scale bar represents 5 μm . Image source: R. D. Simmonds *et al.* [22]

Even larger numerical apertures ($\text{NA} > 0.9$) can be achieved with immersion oil lenses. The immersion optics not only tightly focuses the laser beam but also compensates refractive index mismatch at the surface of the sample. As a result, tightly focused femtosecond laser beam can modify material even at nanojoule energy level [23,24], i.e. an oscillator energy is sufficient to induce the permanent modification.

2.2 Self-assembled nanogratings

At higher laser fluencies smooth refractive index modification is replaced by self-organized structures. The first observation of laser induced periodic structure formation dates back to the sixties when Birnbaum reported surface ripple formation on the surface of semiconductor [25]. Since then the ripple formation was observed on virtually any material surface including dielectrics, metals and polymers. The phenomenon turned out to be rather universal; the ripples could be formed with wavelengths ranging from the mid-infrared to the blue end of the visible spectrum and from CW operating to femtosecond lasers. For normal incidence, the period of such structures is close to the wavelength of light and perpendicular to the laser beam polarization [26]. For oblique incidence and TM polarization (electric field is in the plane of incidence) the ripples occur with one of two possible periods [27]:

$$\Lambda_{gr} = \frac{\lambda}{1 \pm \sin \theta} \quad (2-5)$$

where θ is the angle of incidence and λ is wavelength of incident laser light. For TE polarization Λ_{gr} remain close to the wavelength λ . If the laser beam is moved with respect to the sample, the ripples can coherently extend over the scanned area [27].

However, ultrashort laser pulses were observed to induce two types of periodic surface structures [28]: above single pulse damage threshold – ripples with a period close to the wavelength and below single pulse damage threshold – sub-wavelength ripples with periods as small as 30 nm [29]. The period was found to increase with the number of pulses and fluence [30]. Peculiarly, such structures could be formed only after tens or even thousands of laser pulses. A subwavelength period with sharp features cannot be explained by incident and scattered wave interference.

More than decade ago, a new type of self-organization was observed inside SiO₂ glass after irradiation with an ultrafast laser [4], which was found to be responsible for femtosecond pulse induced anisotropy [31] and the propeller shape scattering reported earlier [32,33]. Under certain irradiation conditions, highly ordered subwavelength structures with features smaller than 20 nm

could be formed in the irradiated volume. As opposed to surface ripples, nanostructures inside of the material were found only for handful materials: fused silica, sapphire, tellurium oxide, ULE glass and borosilicate glasses [34–36]. From this list, fused silica is the most common material for inducing nanogratings. Several studies on nanograting formation were conducted on modified silica glasses doped with germanium, phosphorus or titanium. Nanogratings were also found in porous silica prepared from phase-separated alkali-borosilicate glass by removing the borate phase in the hot acid solution [37]. Even a single isolated nano-plane could be induced by controlling laser pulse energy, which could be used for writing nanofluidic channels (Figure 2-6 (c)). Recently, volume nanogratings was reported to continuously transform into surface ripples when the laser focus is moved out of the sample [38].

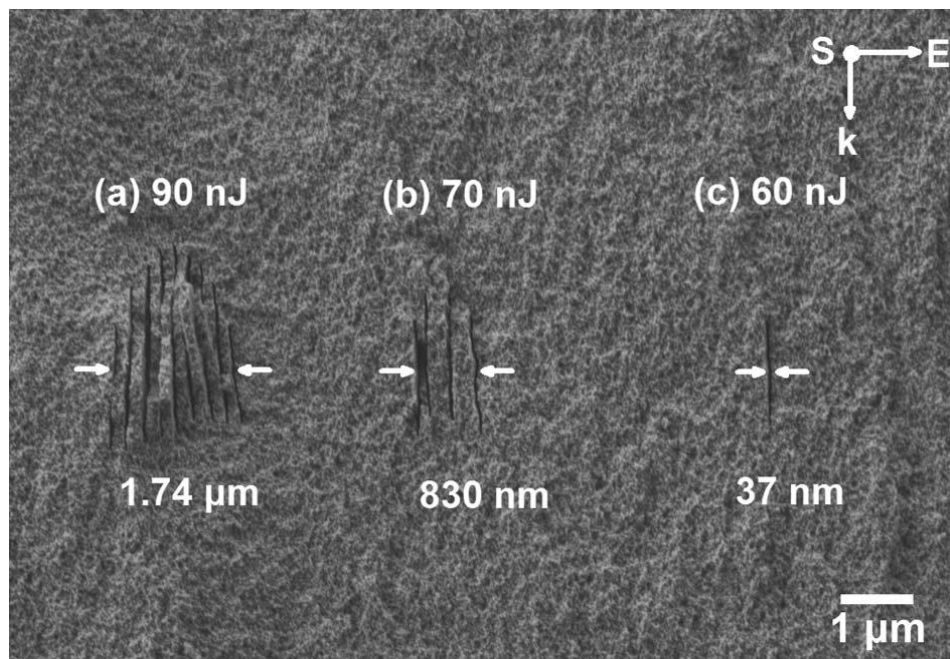


Figure 2-6 Nanograting formation dependence on the laser pulse energy. A single nano-plane could be induced by 60 nJ laser pulses. Image source: Y. Liao *et al.* [37].

Femtosecond laser induced nanogratings possess two periodicities: perpendicular to the polarization and along the light propagation direction [39] (Figure 2-7). The first grating has a period smaller than the wavelength of light, in the range of 100-300 nm depending on the experimental conditions. The

second period grows from the head of the structure to the tail with the initial period close to the light wavelength λ_0 in the material (refractive index n), i.e. λ_0/n . Recent studies suggest that the nanoplanes of the structure consists of a porous material [40] indicating possible glass decomposition during the irradiation of silica glass.

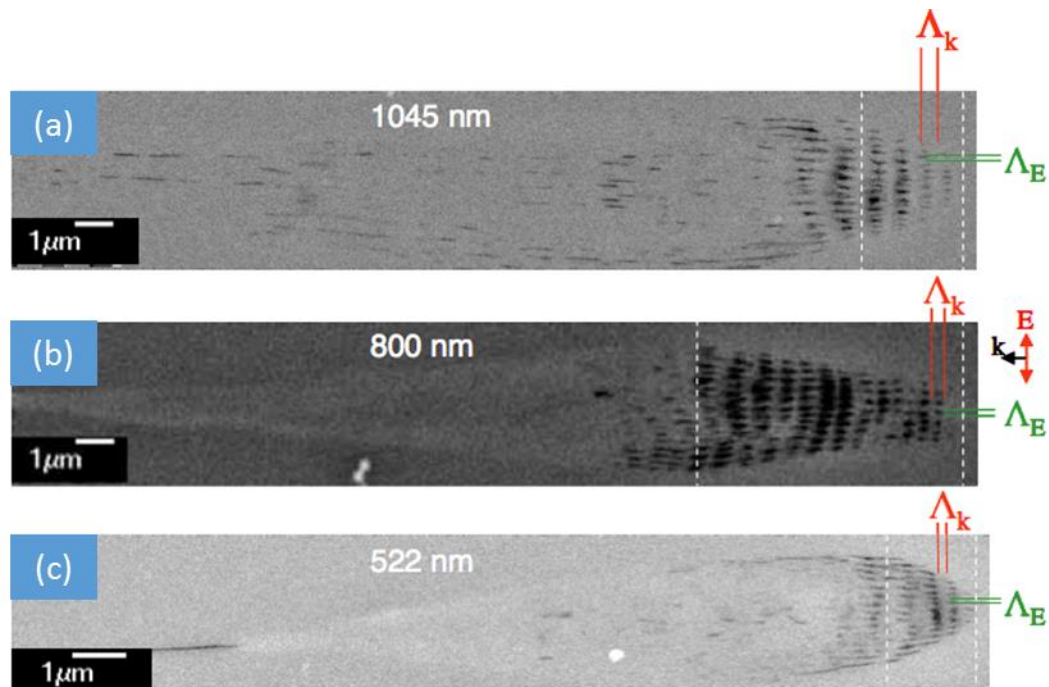


Figure 2-7 SEM images of nanogratings formed by three different central wavelengths of the irradiated laser pulses, E: electric field of the writing laser, k: wave vector of the writing laser beam. (a): $\tau_p = 520$ fs, $E_p = 0.9 \mu\text{J}$, writing speed $200 \mu\text{m/s}$, rep. rate 500 kHz. (b): $\tau_p = 150$ fs, $E_p = 0.5 \mu\text{J}$, writing speed $100 \mu\text{m/s}$, rep. rate 250 kHz. (c): $\tau_p = 490$ fs, $E_p = 0.15 \mu\text{J}$, writing speed $200 \mu\text{m/s}$, rep. rate 200 kHz. Image source: W. Yang *et al.* [39]

The theories suggested to explain nanograting formation are concentrated onto explaining the subwavelength periodicity observed perpendicular to the light propagation direction. The first model proposed for volume nanograting formation was indeed an extension of traditional surface ripple formation theory [4] and relied on the interference of the bulk electron plasma longitudinal wave with the incident light. The coupling can couple only if the plasma wave propagates in the plane of light polarization. The initial coupling

is presumably produced by inhomogeneities induced by electrons moving in the plane of light polarization. The periodic structure created due to the interference further enhances this coupling, resulting in periodic modulation of plasma concentration. Further this modulation is frozen within the material. The nanograting period can be defined from conservation of the longitudinal component of momentum:

$$\mathbf{k}_{ph} + \mathbf{k}_{gr} = \mathbf{k}_{pl}. \quad (2-6)$$

where \mathbf{k}_{ph} photon wavevector, $\mathbf{k}_{pl} = \omega_{pl}/v_{pl}$ is plasma wavevector and $\mathbf{k}_{gr} = 2\pi/\Lambda_{gr}$ is grating wavevector, with Λ_{gr} period. Explicitly the grating period can be written as:

$$\Lambda_{gr} = \frac{2\pi}{\sqrt{\frac{1}{T_e} \left(\frac{m_e \omega^2}{3k_B} - \frac{e^2 \eta_e}{3\epsilon_0 k} \right) - k_{ph}^2}}. \quad (2-7)$$

This formula predicts increase of the period with electron concentration η_e and temperature T_e . Steep increase of the period occurs when the electron concentration approaches the critical plasma density:

$$\eta_{cr} = \frac{\omega^2 \epsilon_0 m_e}{e^2}. \quad (2-8)$$

Another consequence of this model is an energy dependent nanograting period, which should grow together with pulse energy. For a period of 150 nm induced with 800 nm wavelength ultrashort laser pulses, the following conditions were found: $T_e = 5 \times 10^7$ K and $\eta_e = 1.75 \times 10^{21}$ cm⁻³ (Figure 18). Similar conditions were reported for micro-explosions induced with ultrashort laser pulses [115]. However, nanograting formation was observed even for 100 nJ laser pulses, suggesting that nanogratings can be also assembled at subcritical plasma concentrations. Also electron temperature is limited by the band gap of the material (for silica glass electron temperature should not exceed 1.1×10^5 K), the hot electrons will dissipate their energy through impact ionization.

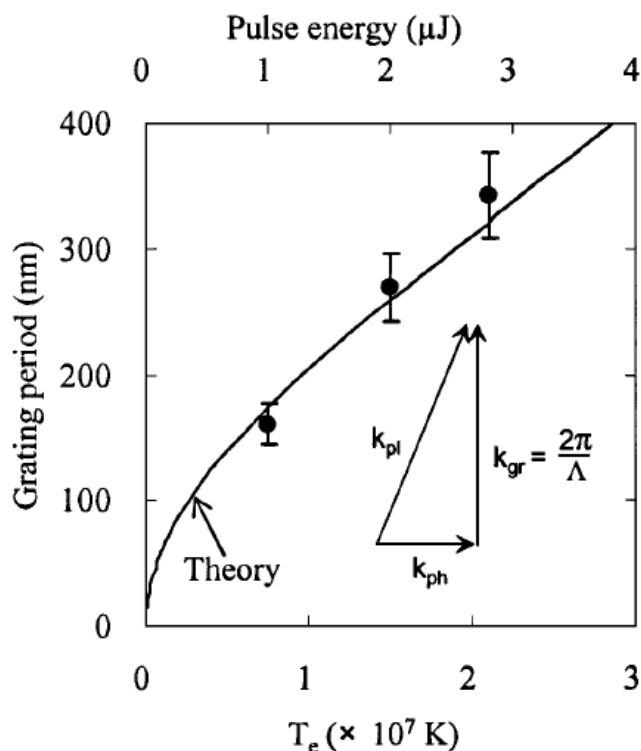


Figure 2-8 Nanograting period evolution predicted by plasmon interference theory. Inset shows wave vector matching diagram. Image source: Y. Shimotsuma *et al.* [4].

Taking these facts into account, the plasmon interference model was modified by assuming two-plasmon decay [41]. The two-plasmon decay is the parametric process where an incident laser photon splits into two plasmons (two electron plasma waves). The major difference to the previous explanation is the excitation of two bulk plasmons of about half of the photon energy. This parametric process develops when plasma concentration reaches quarter of the critical:

$$\eta_{TPD} = \frac{\eta_{cr}}{4} \sim 4 \times 10^{20} \text{ cm}^{-3}. \quad (2-9)$$

The interference between two plasmons of the same frequency propagating in the opposite directions and satisfying Cherenkov mechanism of momentum conservation can produce the periodic subwavelength modulation. An important signature of two-plasmon decay is the generation of the 3/2 harmonic, which is the result of plasma wave and incident light coupling.

The other attempt to explain the nanograting formation phenomenon was by nanoplasma formation [42]. The idea of this theory is the following. Initially, a focused ultrashort light pulse ionizes defects and colour centres leading to the formation of inhomogeneous plasma (Figure 2-9).

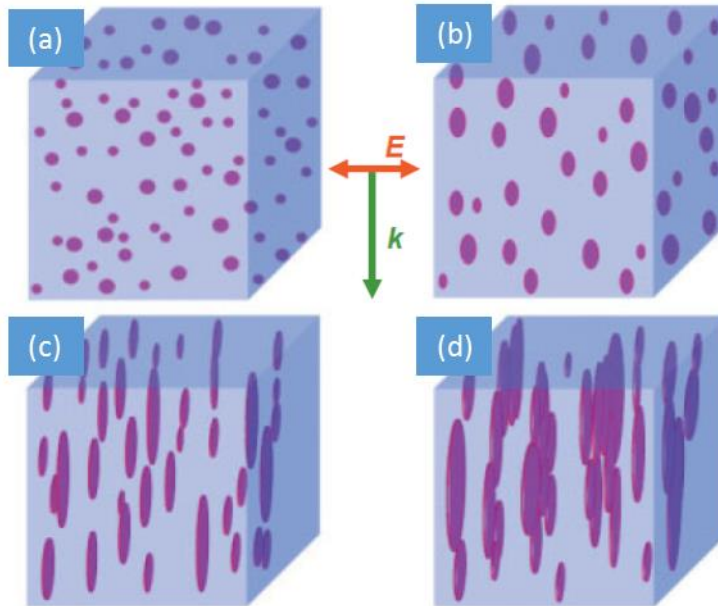


Figure 2-9 Evolution of nanoplasma (A) formed at the ionized defects or colour centres into nanoplanes (D). Image source: R. Taylor *et al.* [43].

These plasma hot-spots after multiple laser pulses can evolve into spherically shaped nanoplasma. The local field enhancement at the boundary will result in an asymmetric growth of initially spherical nanoplasma in the direction perpendicular to the laser polarization, there electric field at the poles E_{pol} and equator E_{eq} of the nanoplasma sphere will be the following:

$$E_{pol} = \frac{3\varepsilon_p E}{\varepsilon_p + 2\varepsilon_d}, \quad (2-10)$$

$$E_{eq} = \frac{3\varepsilon_d E}{\varepsilon_p + 2\varepsilon_d}, \quad (2-11)$$

there ϵ_d and ϵ_p are the real parts of the electric permittivity for dielectric medium and plasma. When the electron concentration is below critical the following condition is satisfied:

$$E_{pol} < E_{eq} \quad (2-12)$$

The electric field is enhanced at the equator leading to nanoplane formation. Further evolution of nanoplanes results in quasi-metallic waveguiding, which leads to a prediction of nanograting period equal to $\lambda/2n$, where n is refractive index of fused silica. The difficulty in this theory is that at high electron concentration when $\epsilon_p > \epsilon_d$, as a result $E_{pol} > E_{eq}$ and nanoplanes could not be formed [44].

All explanations presented above are more related to excitation of plasma and its interaction with light. Some difficulties still remain, as the plasma frequency cannot be defined as it depends on the concentration of free carriers, which is nearly zero in the absence of light and strongly varies as a function of time when the sample is illuminated with a light pulse. It is also unclear how the plasmons may be responsible for the formation of a grating in the propagation direction.

An alternative theory, which is based on attractive interaction and self-trapping of exciton-polaritons, was suggested to explain the nanograting formation [45]. It is well-known that the absorption spectra of SiO_2 are characterized by a strong exciton peak at about 10.4 eV [46,47]. In the fused silica case, the two dispersion branches of exciton-polaritons may be excited simultaneously by multiphoton absorption [45]. The interference of propagating exciton-polaritons results in formation of the polarization grating. The lifetime of exciton-polaritons is limited to a fraction of a picosecond (<300 fs) by their phonon assisted relaxation to indirect states decoupled from light [48]. The indirect excitons can be easily trapped and are essentially immobile and thus can 'freeze' the grating pattern formed by exciton-polariton interaction with light [49]. The recombination of the self-trapped excitons is accompanied by the generation of molecular oxygen due to the following reaction [40]:



where X denotes and exciton. Recently, the presence of molecular oxygen was confirmed for GeO₂ glass after femtosecond laser irradiation [50]. Nanopores of silica filled by oxygen are formed in the locations of high concentration of self-trapped excitons. Agglomerations of these nanopores form the nanograting observed in the experiments.

Each of the proposed theories is supported solely by observations made after the irradiation. It is not fully clear how nanogratings assembled in matter (while it is still excited) are imprinted afterwards. All of the presented theories consider nanogratings formation under single laser pulse irradiation. However, it is well known that nanogratings can be formed only after a sequence of laser pulses. It indicates that some sort of accumulation must take place. Direct experimental observations on nanogratings formation would definitely be of benefit to the explanation.

2.3 Physical and optical properties of nanogratings

The femtosecond laser induced nanogratings exhibit some curious properties. For instance, they are able to self-replicate over distances much larger than the spot size of the writing beam. Experiments suggest that the structure imprinted earlier provides initial “seeding” conditions during the formation of the self-organized period assembly in the adjacent region [39]. Additionally nanogratings exhibit extraordinary thermal stability and sustain the temperatures over 1000 °C [51]. On the other hand, femtosecond laser pulses with different polarization can completely overwrite previously modified regions, enabling the exploration of nanogratings as a rewritable optical medium [39,52,53].

The predominant way of characterizing nanogratings is the analysis of the structure under a scanning electron microscope (Figure 2-7). Despite its straightforwardness, the method restricts characterization of the femtosecond laser induced anisotropy to the measurements of the nanograting period. Moreover, it often requires additional post-processing efforts such as sample polishing and etching in diluted fluoric acid. The alternative, nondestructive way of characterizing the anisotropic structure is quantitative birefringence measurements, which provide information on the dependence of induced modification on writing parameters such as fluence, repetition rate, numerical aperture, etc. [31,54,55].

The effect of form birefringence, unlike intrinsic birefringence which is due to the anisotropy of oriented molecules, manifests itself due to the alignment of submicroscopic rodlets or platelets [31,56]. The light polarized parallel to the interfaces experiences a larger refractive index and as a result a phase difference for two perpendicular polarizations is acquired. The strength of the birefringence can be controlled by periodicity and material composition of the microstructure. Under a linear approximation, refractive indices of nanogratings for ordinary n_o and extraordinary n_e wave are [31]:

$$n_e = \sqrt{\frac{n_1^2 n_2^2}{f_f n_2^2 + (1 - f_f) n_1^2}}, \quad (2-14)$$

$$n_o = \sqrt{f_f n_1^2 + (1 - f_f) n_2^2} \tag{2-15}$$

where f_f - filling factor; n_1 and n_2 are refractive indices for platelets constituting the grating (Figure 2-10 (b)). One can see that

$$n_e^2 - n_o^2 = -\frac{f_f(1 - f_f)(n_1^2 - n_2^2)^2}{f_f n_2^2 + (1 - f_f) n_1^2} \leq 0, \tag{2-16}$$

i. e. the nanogratings always behave as a negative uniaxial crystal. A typical value of $n_e - n_o$ is $-(2-4 \times 10^{-3})$ [51]. For comparison, quartz crystal is a positive uniaxial crystal and refractive index difference $n_e - n_o = 9 \times 10^{-3}$.

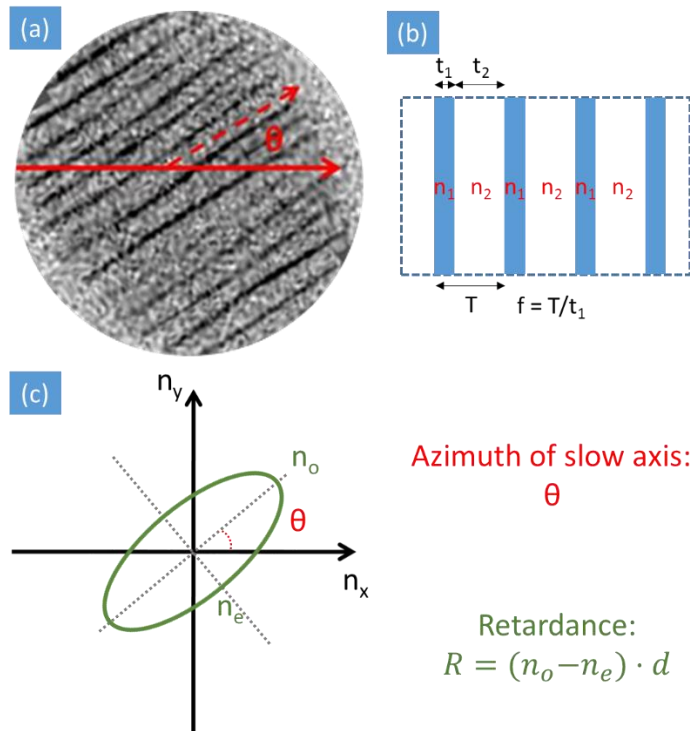


Figure 2-10 Schematic explanation of birefringence caused by nanogratings. (a) SEM image of nanogratings. (b) Nanogratings can be approximated by parallel planes with alternating refractive index which causes form birefringence. (c) Birefringence is characterized by retardance ($R = (n_o - n_e) \cdot d$) and azimuth of the slow axis (θ). (d - thickness of birefringent structure)

Birefringent modification can be characterized by two parameters: the retardance and the azimuth of the slow axis (Figure 2-10). They can be independently controlled during the writing experiment as the retardance is a function of fluence and the azimuth of the slow axis is defined by polarization.

Observation of birefringence which could be controlled by the polarization of a femtosecond IR laser beam was first reported by Sudrie *et al.* [33]. It should be noted that in these experiments the femtosecond laser induced anisotropy was reported to exhibit positive birefringence. Simultaneously, a peculiar anisotropic scattering was observed in Ge doped silica glass [32]. It was suggested that aligned subwavelength structures are responsible for this scattering. The experimental observation by Sudrie *et al.* could be explained by well-known anisotropy due to light induced anisotropic bonds rearrangement (light induced anisotropy) [57]. Knowing that the nanograting always acts as a negative uniaxial crystal these experiments do not suggest the presence of the subwavelength structure. However, this can be only error of sign made in the experiment. All further experiments confirmed the presence of negative birefringence [31]. The discovery of the nanograting produced in the bulk of the material provided an appropriate explanation for both effects [4]. Under certain conditions this type of glass modification can be an undesirable effect. As revealed from the studies of the glass modification dependence on the pulse duration, for pulses longer than ~ 200 fs a smooth refractive index increase cannot be achieved [16]. If waveguides are to be written using relatively long pulses >200 fs, they potentially can be polarization sensitive and exhibit high propagation losses due to the formation of nanogratings [58]. The problem can be at least partially solved operating the laser at megahertz repetition rates where birefringence is strongly reduced due to heat accumulation effects [59,60].

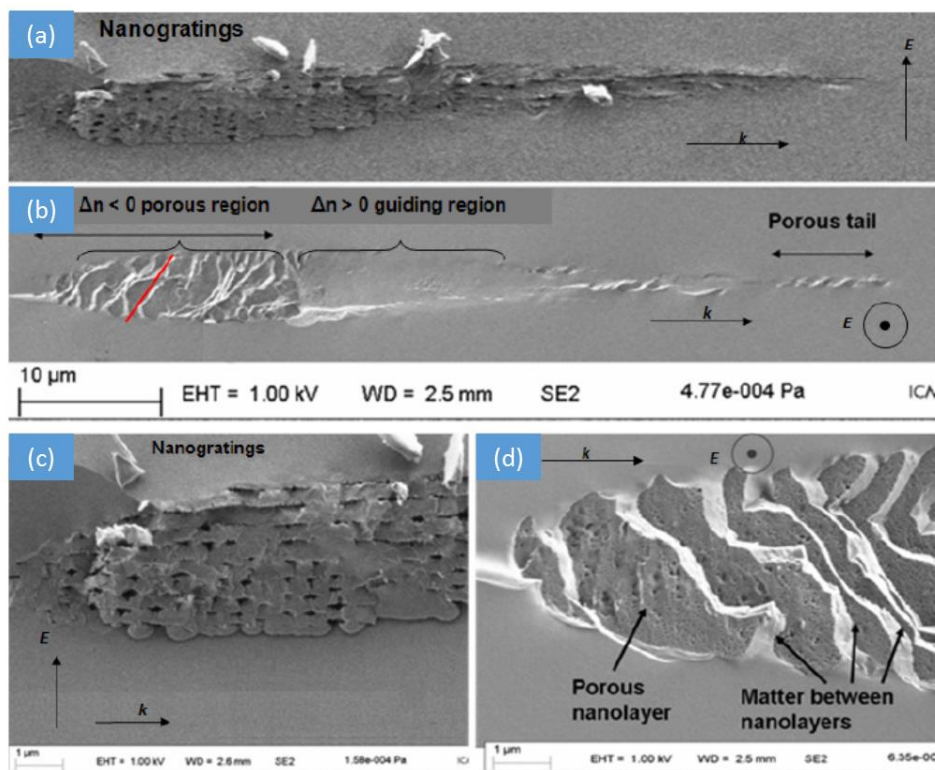


Figure 2-11 FEG-SEM, Secondary electrons images of laser tracks cross-section for each writing laser polarization. The laser parameters were: 0.5 μJ/pulse, 1030 nm, 300 fs, 200 kHz, 200 μm/s. A focusing lens of 0.5 NA was used. With the laser polarisation perpendicular (a) and parallel (b) to the scanning direction. (c) and (d) show close-ups of the nanograting and nanoplane regions respectively. Image source: J. Canning *et al.* [40]

Recent studies indicate that the nanogratings are formed by the alternation of uniform and porous glass layers [40,61] (Figure 2-11). The interior of the nanogratings was examined by cleaving the sample after laser irradiation. If the nanograting planes were parallel to the cleavage the interior structure could be observed with field emission electron microscope, which could reveal small features otherwise covered by conductive coating. The formation of nanopores is attributed to SiO_2 decomposition into $\text{SiO}_{2(1-x)} + x \cdot \text{O}_2$ under intense laser irradiation. The typical diameter of nanopores ranges from 10 to 30 nm. Small angle X-ray scattering measurements further confirmed nanoporous structure of the nanograting interior [61].

2.4 Applications of nanogratings

The peculiar optical properties of the femtosecond laser induced nanogratings allowed to implement numerous optical elements with various functionalities. Unknowingly the first diffractive optical element, the Fresnel zone plate, was fabricated in the nanogratings formation regime [62]. Nanogratings exhibits much larger refractive index change than isotropic refractive index increase. For diffractive optics the sign of refractive index does not play crucial role thus a negative refractive index change of nanogratings is well suited for this purpose. To fabricate a Fresnel zone plate it is necessary to induce a phase retardation of π between odd and even numbered Fresnel zones. This can be achieved either by modulating the thickness of the material or by modifying the index change. The femtosecond laser was used to induce refractive index change in the odd numbered Fresnel rings. The radius of fabricated zone plate was 1 mm and with 158 zones it was designed to focus light with wavelength 632.8 nm at a distance of 1 cm. In the crossed polarizers the modified areas became bright clearly indicating that the laser induced the birefringent modification. The measurements of the phase shift revealed that the laser induced modification exhibited negative refractive index change. Also phase retardation for the designed wavelength induced by a single laser scan was not π but rather $\pi/2$. The efficient zone plate thus requires multiple scanning or different focusing conditions.

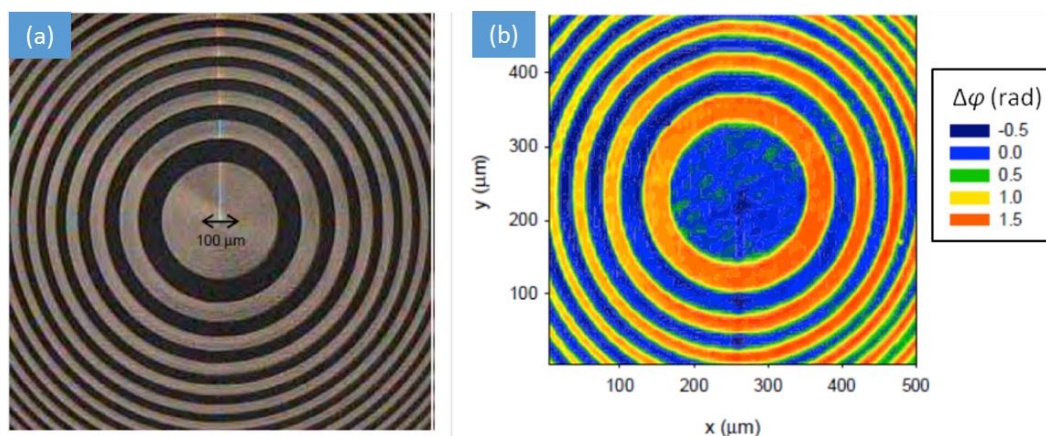


Figure 2-12 (a) Microscope image of the central part of Fresnel zone plate in the crossed polarized light. (b) Phase retardation $\Delta\varphi$ of the zone plate measured with the interferometric setup. Image source: E. Bricchi [63]

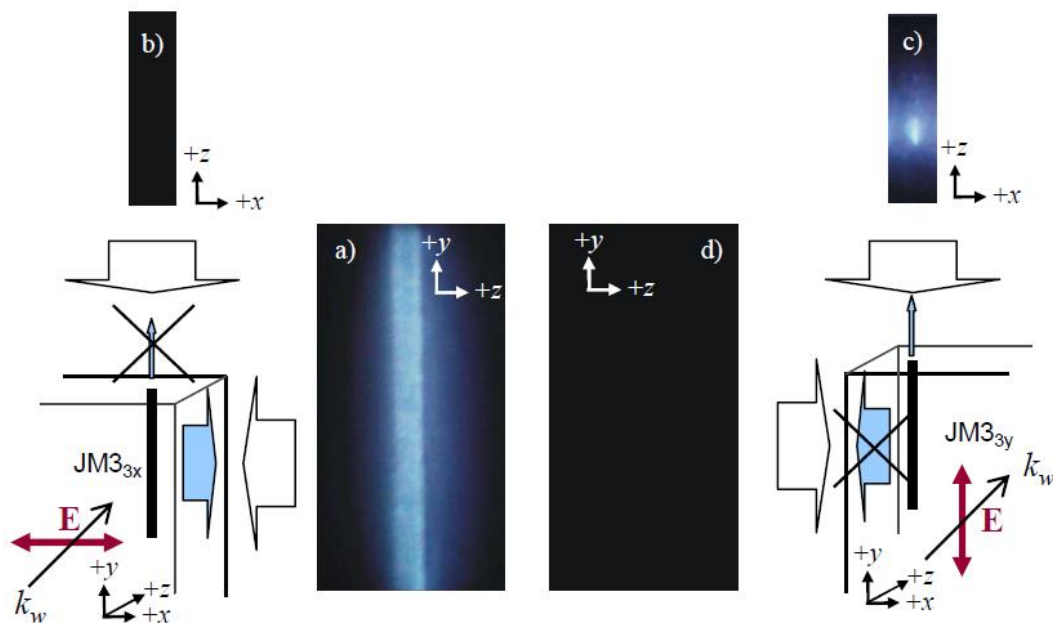


Figure 2-13 CCD camera images of the reflection from laser written tracks. The red arrows indicate orientation of the polarization of the writing beam. The strong reflection is observed only along the electric field direction. Image source: E. Bricchi [63]

Another interesting observation was anisotropic reflection [64], which at that time hinted about the presence of subwavelength nanostructures. In the experiment a series of diffraction gratings were written in the fused silica sample. After irradiation, the modified areas were inspected through the silica plate's polished edges with an optical microscope. During the inspection, the structures were illuminated with unpolarized white light. Unexpectedly, striking reflection in the blue region of spectrum could be observed (Figure 2-13). The spectral analysis revealed that that reflected light exhibited two peaks: the strongest one at 460 nm, which explains the blue character of the reflection and a weaker one at 835 nm (Figure 2-14).

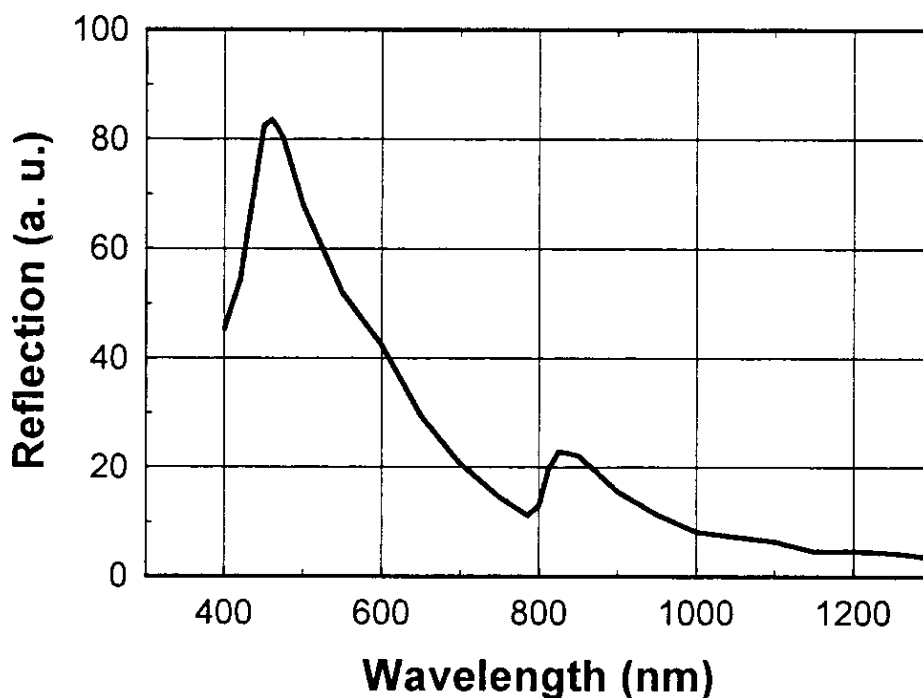


Figure 2-14 Spectrum of the light reflected from laser inscribed track. Two peaks can be explained by refractive index modulation with the period of 150 nm. Image source: Mills *et al.* [64]

A more detailed study revealed that the reflection occurred only when the viewing axis was parallel to the electric field vector and energy per pulse was above a certain threshold. The blue reflection was observed only for the birefringent modifications indicating that both phenomena are related. Indeed, the peak at 460 nm can be explained by the Bragg reflection from a modulation of refractive index with a period of 150 nm. Later on this assumption was confirmed by Shimotsuma *et al.* [4].

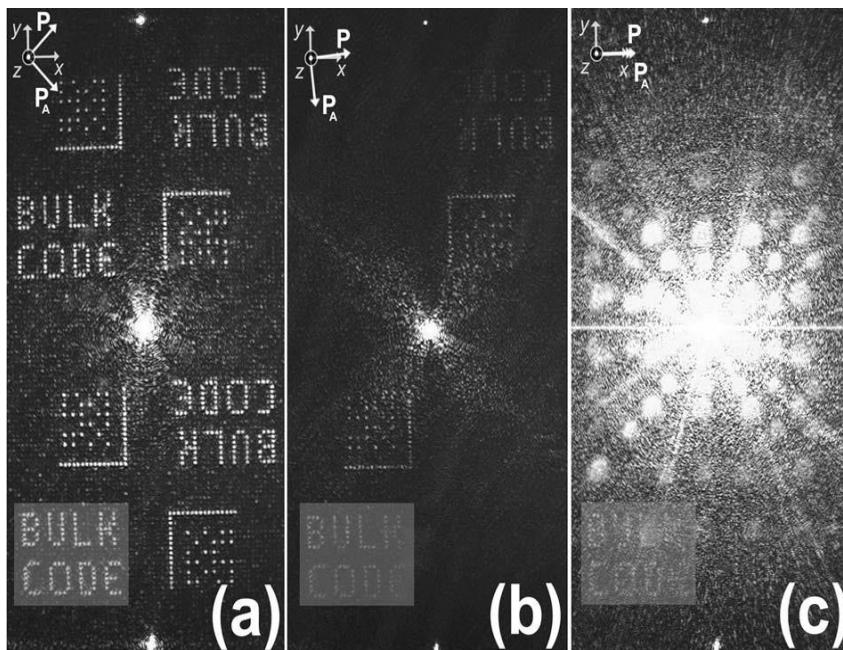


Figure 2-15 Reconstruction of CGH. The highlighted areas were used for measuring the S/N. P - input beam polarization, PA - analyzer direction. (a) Reconstruction under crossed polarizers with input polarization at $\theta = 45^\circ$, (b) reconstruction under crossed polarizers with input polarization at $\theta = 2^\circ$, (c) reconstruction with parallel polarizers at 0° . Image source: D. G. Papazoglou and M. J. Loulakis [65]

Recently several polarization sensitive optical elements were implemented exploring birefringent properties of the nanogratings. The laser structured area behaves as a waveplate of the size of a few microns. The parameters of the waveplate, retardance and orientation, are controlled by the laser power (pulse energy) and polarization. Using lenses of moderate NA (0.15-0.2) the optical elements with half-wave retardance for ~ 500 nm can be written in a single scan at a speed of several millimeters per second. Several groups demonstrated computer generated holograms (CGH) printed with self-assembled nanogratings [65,66]. The birefringence exhibited by nanogratings allows to significantly increase signal to noise ratio by at least 9 dB by polarization filtering, which suppress the undiffracted beam.

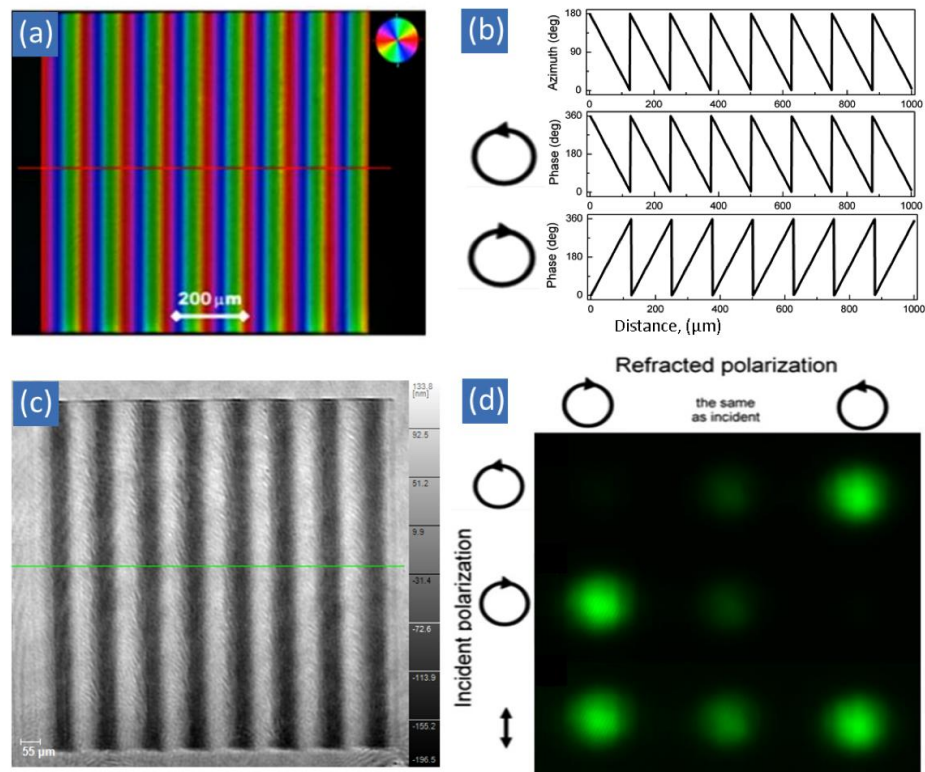


Figure 2-16 (a) Microscope image where pseudo colors indicate the direction of the slow axis in the polarization diffraction grating. (b) The slow axis orientation and the corresponding phase modulation for two circular polarizations across the red line indicated in (a). The direction of the phase grating depends on the handedness of the circular polarization. (c) Grayscale map of birefringent grating phase variation measured with digital holography microscope for the linear polarization. (d) Far-field diffraction images for the incident right/left-handed circular and linear polarizations. Image source: M. Beresna *et al.* [67]

The first demonstration of optical element based on birefringence of nanogratings was polarization diffraction grating [68]. Instead of continuous phase or amplitude modulation, polarization grating is imprinted in slow axis modulation (Figure 2-16 (a, b)). Polarization diffraction grating is sensitive to circular polarization and separates left- and right-handed circular polarization between -1 and 1 diffraction orders. The efficiency of this diffraction grating directly depends on the induced retardance [69]. The highest efficiency is at

half-wave retardance, and then all incident energy is distributed between -1 and 1 diffraction orders.

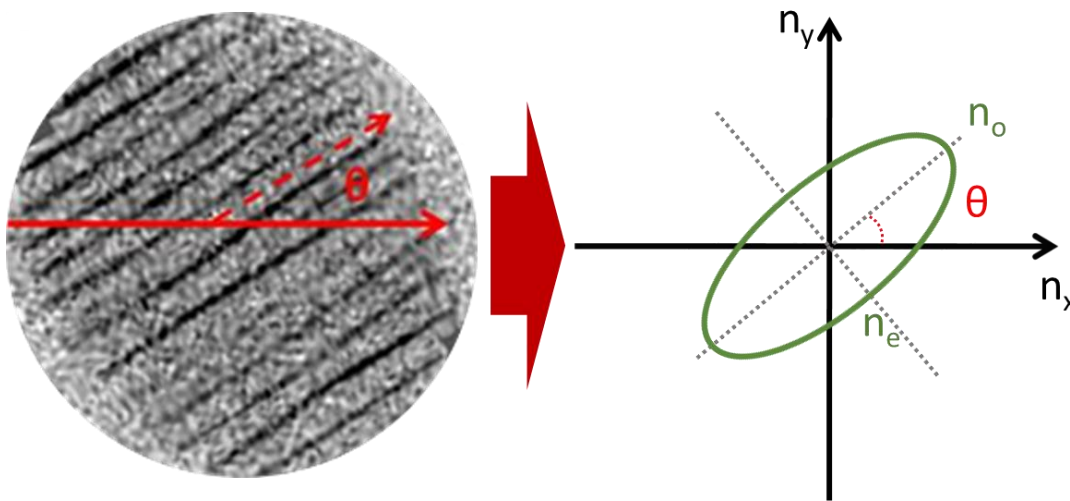


Figure 2-17 Femtosecond laser induces nanogratings and encodes information about laser fluence and polarization into material. Later information can be decoded by measuring two properties of the birefringence ($n_o - n_e$ and θ) of induced structure.

Another application of laser induced nanogratings is 5D optical memory recording. As it was mentioned above the laser induced anisotropy can be characterized by two independent parameters: retardance and slow axis orientation, which can be rewritten with successive pulse sequences (Figure 2-17). Recently, it was proposed that using these parameters optical recording can be extended beyond the three spatial dimensions [45,53,70]. The nanograting ability to withstand temperatures of 1000°C makes nanostructure based memory ideal for archiving large volume of important information. The ability to record and read several layers of information via nanogratings was demonstrated by Shimotsuma *et al.* [53,70]. During the recording procedure, number of pulse and azimuth of their polarization can independently control induced retardance and slow axis direction [53,70]. The retardance can be controlled with a precision of about 10 nm, while slow axis angle can be defined with a few degree precision. The read-out procedure was demonstrated with a quantitative birefringence measurement system Abrio (CRi Inc.), which can measure both parameters with precision of less than 1nm

and 1 degree respectively. The ability to record data simultaneously in retardance and slow axis direction was demonstrated by M. Beresna *et al.* [45]. Portraits of two prominent scientists J. C. Maxwell and I. Newton were recorded in the same physical birefringent layer. For encoding both gray-scale (256 gray levels) portraits were first matched in pixel size. The I. Newton portrait was then split into 8 layers and combined with an image of J. C. Maxwell image using a MATLAB code. Finally 8 gray-scale images were generated and each recorded with different polarization orientation by varying number of pulses with respect of pixels' gray level value. As a result the portrait of Maxwell was encoded in retardance and Newton's image was recorded in the variation of slow axis orientation. Using the Abrio microscope system, both images were successfully decoupled clearly demonstrating the potential of the proposed information recording technique (Figure 2-18).

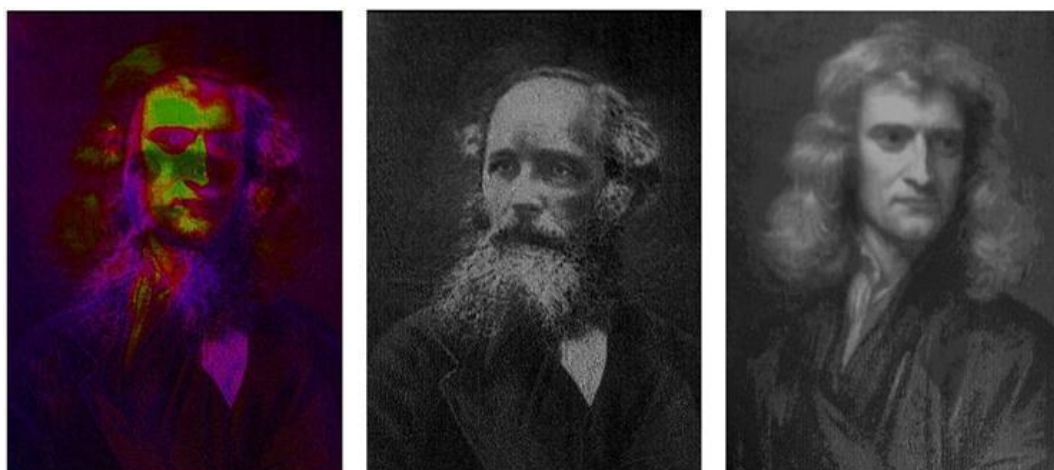


Figure 2-18 (Left) The Abrio image representing in false colours the recorded information in slow axis and retardance. (Middle and Right) Decoupled images of Maxwell and Newton (no additional operations on images were performed). Source: Beresna *et al.* [45].

Other application of the nanogratings such as optical elements for polarization distribution control of the beam, special beams generation, optical vortex with tuneable orbital angular momentum generation and real time polarization measuring will be discusses in Chapter 4.

Chapter 3: Properties of nanogratings

Femtosecond laser induced nanogratings in fused silica glass exhibits sufficient birefringence to be applicable for polarization sensitive elements. To fabricate polarization sensitive optical elements, the retardance of quarter- and half-wave value must be induced. The advantage of such elements versus conventional quarter- or half-wave plates is the ability to fabricate micro size wave plates. This also allows fabrication of optical elements comprised of micro waveplates where retardance and slow axis orientation is spatially varying. The applications of such spatially variant elements will be discussed in the following chapter.

In this chapter I will describe the dependence of nanogratings' properties on the laser parameters and how to achieve high retardance and uniformity of the birefringent structures. As the ultimate goal is fabrication of optical elements based on nanogratings, fabrication speed also has to be considered.

Our laser operates at 1030 nm wavelength, thus mostly I will address the possibility of fabricating quarter- and half-wave plates at 515 nm and 1030 nm (the first and the second harmonics of the laser). The corresponding retardance values are 128.75 nm and 257.5 nm for the 515 nm wavelength and 257.5 nm and 515 nm for the 1030 nm wavelength. However experimental results can be applied for wide range of wavelengths from 200 nm to 2 microns.

The strength of the retardance and the quality of the modification strongly depends on laser pulse duration, pulse energy, repetition rate, focusing conditions and laser scanning speed. All these parameters are strongly interconnected and must be optimised simultaneously. For example if under certain set of laser fabrication parameters we can get birefringent modification, in order to increase fabrication speed we might also need to change laser pulse duration and focusing conditions. The optimal parameters for high retardance were determined by a set of experiments.

Different laser pulse durations, repetition rates, laser energies, focusing conditions and etc. can be combined together into numerous of different sets of parameters' space. It would take long time to describe all different combinations. So as I will discuss about the influence of the variation of one

parameter, others will be fixed close to the known optimal values for polarization sensitive optical elements fabrication.

3.1 Inducing and measuring form birefringence

The experiments were performed with femtosecond laser system PHAROS (Light Conversion Ltd.) based on directly diode pumped Yb:KGW (Yb-doped potassium gadolinium tungstate) crystal. The system emits 270 fs pulses, which can be stretched to 10 ps, at a fundamental wavelength of 1030 nm. The repetition rate of laser system can vary from 10 kHz to 500 kHz. The maximum average power is 6 W.

In our femtosecond writing setup (Figure 3-1), the collimated femtosecond beam passes through a half-wave plate and a Glan polarizer (used to control average power). Polarization of the writing beam is controlled with the second half-wave plate located just before the focusing optics to avoid unwanted polarization distortion. The laser beam is focused with aspheric lenses or objectives. The sample is mounted onto XYZ linear air-bearing precise positioning stage (Aerotech Ltd.). To monitor the writing process, the sample is illuminated from the back side and the light is collected to a CCD camera.

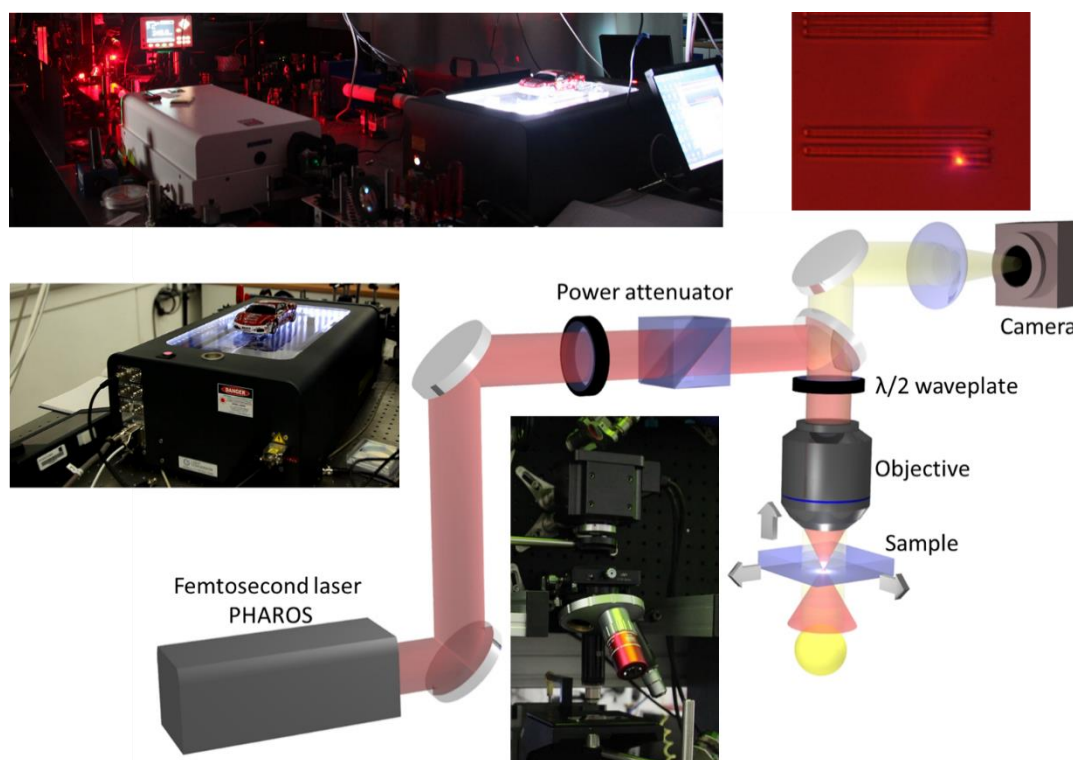


Figure 3-1. The experimental setup.

The retardance of the fabricated structures was analysed with a birefringence measurement system (CRi Abrio imaging system) integrated into the Olympus BX51 optical microscope. The example of the birefringence measurement is illustrated in Figure 3-2. The map of Europe was fabricated with the laser inside the fused silica sample where territories of different countries were fabricated with different polarization of the laser. The structure was imaged with Olympus microscope between crossed polarizers (Figure 3-2 (a)) and Abrio imaging system (Figure 3-2 (b)).

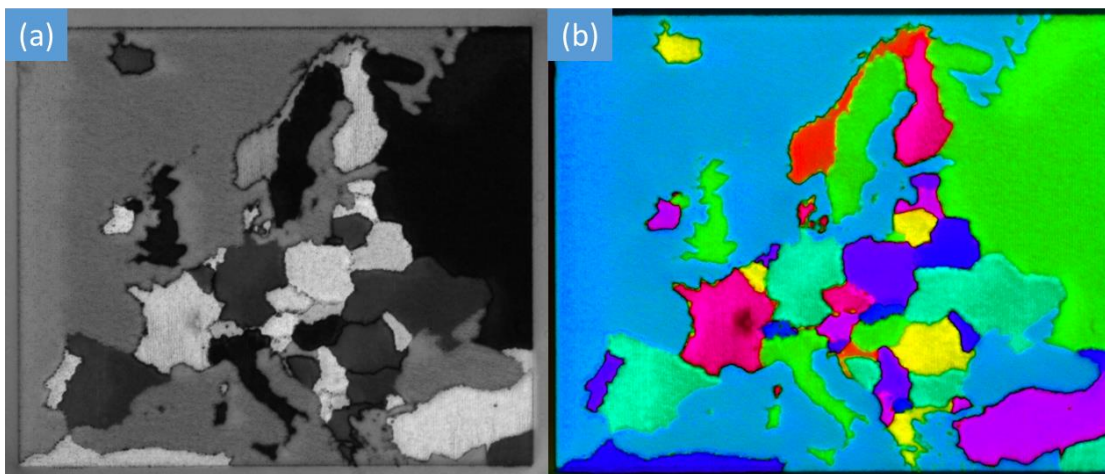


Figure 3-2 Crossed polarized microscope image femtosecond laser written map of Europe inside SiO_2 glass (a). The same structure imaged with birefringence measuring system Abrio (b). Colours indicates the azimuth of the slow axis of the birefringence.

Birefringence measurement system is based on the PolScope described in the paper by M. Shribak and R. Oldenbourg (2003) [71]. The PolScope requires monochromatic circularly polarized light. For this reason in the illumination part of the microscope a band-pass filter working at 546 nm and a circular polarizer are inserted (Figure 3-3). In the imaging part an elliptical analyser is inserted which is built from two liquid crystal retarder plates and a linear polarizer. The retardance of two liquid plates are controlled by DC field and their orientation is 45° to each other (Figure 3-3). Such configuration of two variable retarders can generate any polarization and therefore together with the linear polarizer can measure any polarization.

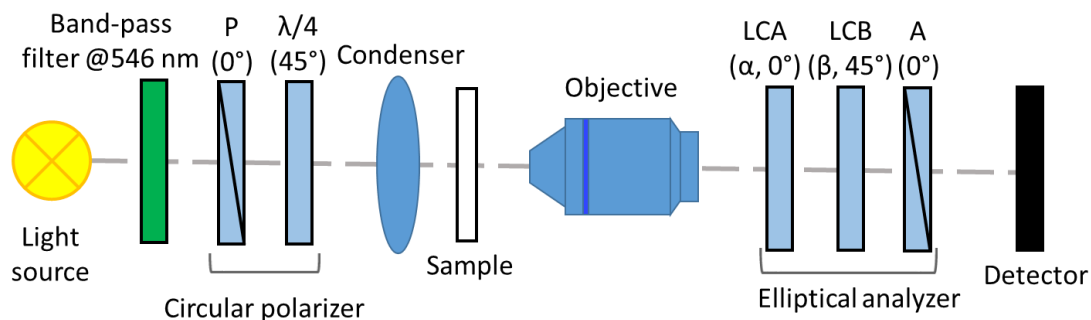


Figure 3-3 Schematics of the polarized light microscope with two liquid crystal retarders (LCA and LCB) inserted in the imaging path and circular polarizer in the illumination path. α and β are the retardance of the liquid crystal plates LCA and LCB.

The last part of the birefringence measurement system is an algorithm which allows to calculate the distributions of the retardance and slow axis. Let us define the retardance and the slow axis distributions of the analysed sample as $R(x, y)$ and $\theta(x, y)$. The intensity recorded by the detector is:

$$I(\alpha, \beta, x, y) = \frac{1}{2} I_0(x, y) \cdot [1 + \cos \alpha \sin \beta \cos R(x, y) - \sin \alpha \sin \beta \cos 2\theta(x, y) \sin R(x, y) + \cos \beta \sin 2\theta(x, y) \sin R(x, y)] + I_{\min}(x, y). \quad (3-1)$$

Here I_0 is the distribution the intensity of the light after the sample, I_{\min} - the distribution of the depolarized background arising from the imperfections of the polarizers. The α and β are retardance values for LCA and LCB retarders respectively. The measurement of retardance $R(x, y)$ and slow axis $\theta(x, y)$ direction are performed by measuring a series of intensity images for different α and β values.

Five intensity images (I_1, I_2, I_3, I_4, I_5) are generated by adding a swing value χ to the nominal values of the retarders α and β :

$$I_1(x, y) = I\left(\alpha = \frac{\lambda}{2}, \beta = \frac{\lambda}{4}\right), \quad (3-2)$$

$$\begin{aligned}
I_2(x, y) &= I \left(\alpha = \frac{\lambda}{2}, \beta = \frac{\lambda}{4} - \chi \right), \\
I_3(x, y) &= I \left(\alpha = \frac{\lambda}{2}, \beta = \frac{\lambda}{4} + \chi \right), \\
I_4(x, y) &= I \left(\alpha = \frac{\lambda}{2} - \chi, \beta = \frac{\lambda}{4} \right), \\
I_5(x, y) &= I \left(\alpha = \frac{\lambda}{2} + \chi, \beta = \frac{\lambda}{4} \right).
\end{aligned}$$

The λ is the wavelength at which the birefringence is measured and in our case it is 546 nm. The value of χ is chosen depending on the wanted dynamic range and resolution of the measured retardance. Smaller the χ , the smaller is the dynamic range and better the resolution. The maximum dynamic range is reached when the $\chi = \lambda/4$. Measured intensities are used to calculate two parameters A and B:

$$A = \frac{I_2 - I_3}{I_2 + I_3 - 2I_1} \tan \frac{\chi}{2} = \sin 2\theta \tan R, \quad (3-3)$$

$$B = \frac{I_5 - I_4}{I_5 + I_4 - 2I_1} \tan \frac{\chi}{2} = \cos 2\theta \tan R. \quad (3-4)$$

Finally the retardance and the azimuth of slow axis can be derived from Equations (3-3) and (3-4):

$$\begin{aligned}
R &= \frac{\lambda}{2\pi} \arctan \sqrt{A^2 + B^2} \\
&\text{when } I_2 + I_3 - 2I_1 \geq 0,
\end{aligned} \quad (3-5)$$

$$\begin{aligned}
R &= \frac{\lambda}{2\pi} \left(\pi - \arctan \sqrt{A^2 + B^2} \right) \\
&\text{when } I_2 + I_3 - 2I_1 < 0.
\end{aligned} \quad (3-6)$$

In the PolScope paper [71] equation for slow axis angle is given

$$\theta = \frac{1}{2} \arctan \left(\frac{A}{B} \right). \quad (3-7)$$

However this equation can be used just for angle between -45° and $+45^\circ$ to measure orientation of slow axis. In order to measure in full range of possible angles (0° to 180°), some corrections have to be made:

$$\theta = -\frac{1}{2} \operatorname{arccot}\left(\frac{A}{B}\right) + 45^\circ, \quad (3-8)$$

when $I_2 - I_3 \geq 0$,

$$\theta = -\frac{1}{2} \operatorname{arccot}\left(\frac{A}{B}\right) + 45^\circ + 90^\circ, \quad (3-9)$$

when $I_2 - I_3 < 0$.

Such a system allows the measuring of the retardance values up to $\lambda/2$. Using previous equations, modelling with MATLAB was performed which illustrates the relation between real samples retardance and slow axis angle values and what would be measured at ideal condition with the PolScope (Figure 3-4 (a)). The MATLAB code can be found in the Appendix C. Retardance value was in the interval between 0 to λ (546 nm) and slow axis angle was chosen to be 45° . As we can see, calculated values matches 'real' values until retardance reaches $\lambda/2$. From this point the retardance curve starts going down and the calculated value of retardance is $R_{calculated} = \lambda - R_{sample}$. Calculated slow axis angle rotates by the 90° and becomes -45° . This demonstrates, that when the angle of the slow axis in the measured sample is known (or at least known approximately), the retardance value can be measured up to λ value.

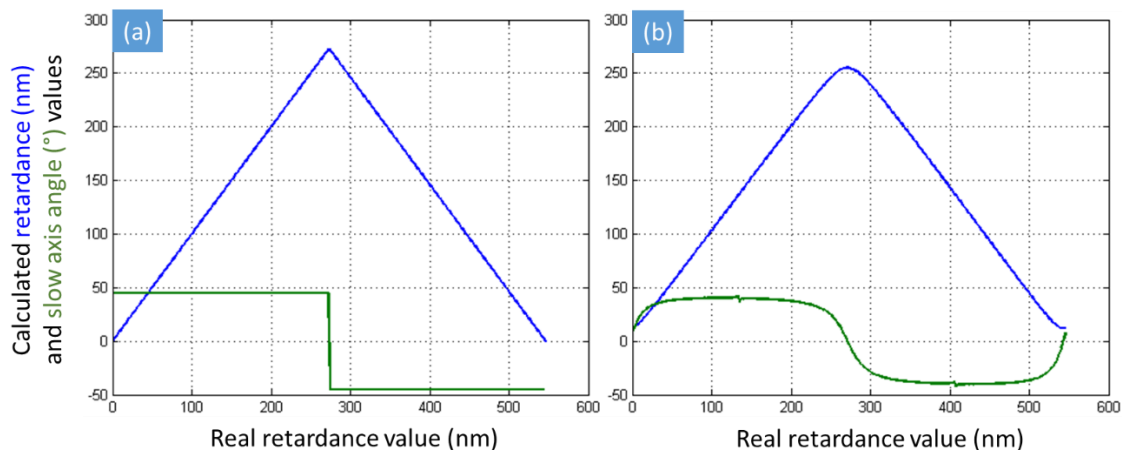


Figure 3-4 The simulation of PolScope measurement. The dependance of measured retardance and slow axis values on real retardance value when the system is perfect (a) and when slight ellipticity is introduced into the illumination part (b).

However in practice the situation is slightly more complicated. Because of misalignment or imperfections in optical elements, the dependence curve is not be as perfect as in Figure 3-4 (a). To illustrate this, the modelling was performed with slight polarization ellipticity introduced to the illumination light (Figure 3-4 (b)). The ellipticity was added by rotating the matrix of the quarter-wave plate in the circular polarizer by 4° from its original 45° . The obtained results clearly reflects the effect of system imperfections on the quality of the measurements at small retardance values and around $\lambda/2$ (Figure 3-4 (b)). Thus the reliable measurements are achievable for retardance about 20 nm smaller than $\lambda/2$ (250 nm). Also maximum measurable value would depend on the azimuth of the slow axis of the sample and even though the retardance can be uniform over sample, the variation in the azimuth of the slow axis can give variation in the measured retardance.

At small retardance values, the PolScope has background correction algorithm [71]. But it works only when the magnitude of the sample retardance and background retardance are small. Whereas for large values of retardance (close to $\lambda/2$) are measured, the background correction is neglected.

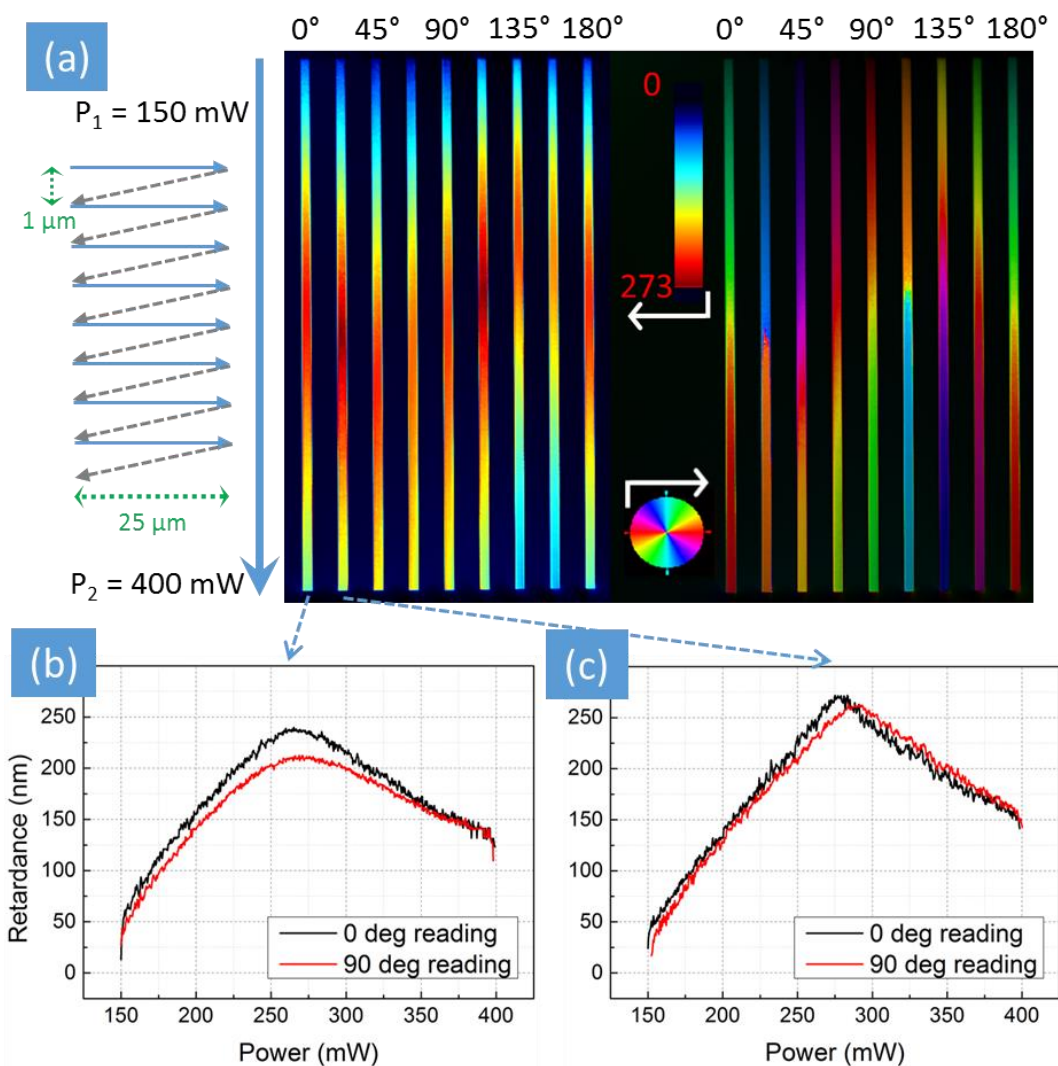


Figure 3-5 Retardance and slow axis angle measurement using birefringence measurement system Abrio. (a) Retardance and slow axis distribution imaging of rectangle structures fabricated with different laser polarization and increasing laser power. Measured retardance dependence on laser power of structures written with 0° (b) and 22.5° (c) polarization.

In order to evaluate capability of the Abrio system to measure high magnitude retardance, the rectangles with increasing power were fabricated in silica glass (Figure 3-5 (a)). The parameters of laser fabrication were following: pulse duration - 600 fs, repetition rate - 200 kHz, fabrication speed - 200 $\mu\text{m/s}$, focused with 0.16 NA lens, distance between lines - 1 μm , laser power changed

from 150 mW to 400 mW. Different rectangles were written using different laser polarization.

As we can see, measured retardance value increases with the laser power and before reaching 300 mW starts decreasing which is followed by the change of the measured azimuth of the slow axis. This is similar to the modelled data (Figure 3-4) and indicates that the retardance of the sample is still growing. However, not in all rectangles the maximum measured value reached 273 nm (which is expected as the magnitude of retardance reaches higher values than 273 nm) and the azimuth of slow axis transition is not sharp. This gives similar results as simulations with unperfected illumination (Figure 3-4 (b)).

But this is not sufficient to make a conclusion as we know that the strength of modification also depends on the polarization of the writing laser plane angle to the written line (this will be discussed later in this chapter). So the same structure was rotated by 90° and measured again. Compared results for the first and the second rectangles are in Figure 3-5 (b) and (c). We can see that measurements depend on the orientation of the measured sample. Therefore, at retardance values close to the measurement limit, the measurement depends on the orientation of the slow axis and when retardance values are higher than ~200 nm, should not be completely trusted.

Higher values of retardance can be measured using illumination source with longer wavelength. For this, custom made setup (Figure 3-6 (a)) was made using fibre laser source at wavelength 1515 nm. Theoretical limit of measured retardance in this setup is 757 nm. The orientation of slow axis θ has to be known before the measurement and only single point of the sample can be measured. Input polarization is set to 45° angle with slow axis of the sample. The detector measures power at two different orientations of the linear analyser: parallel to the input polarization P_0 and perpendicular to the polarization P_{90} . Then retardance is equal to

$$R = \text{acos}\left(\frac{P_0 - P_{90}}{P_0 + P_{90}}\right) \cdot 2\pi\lambda. \quad (3-10)$$

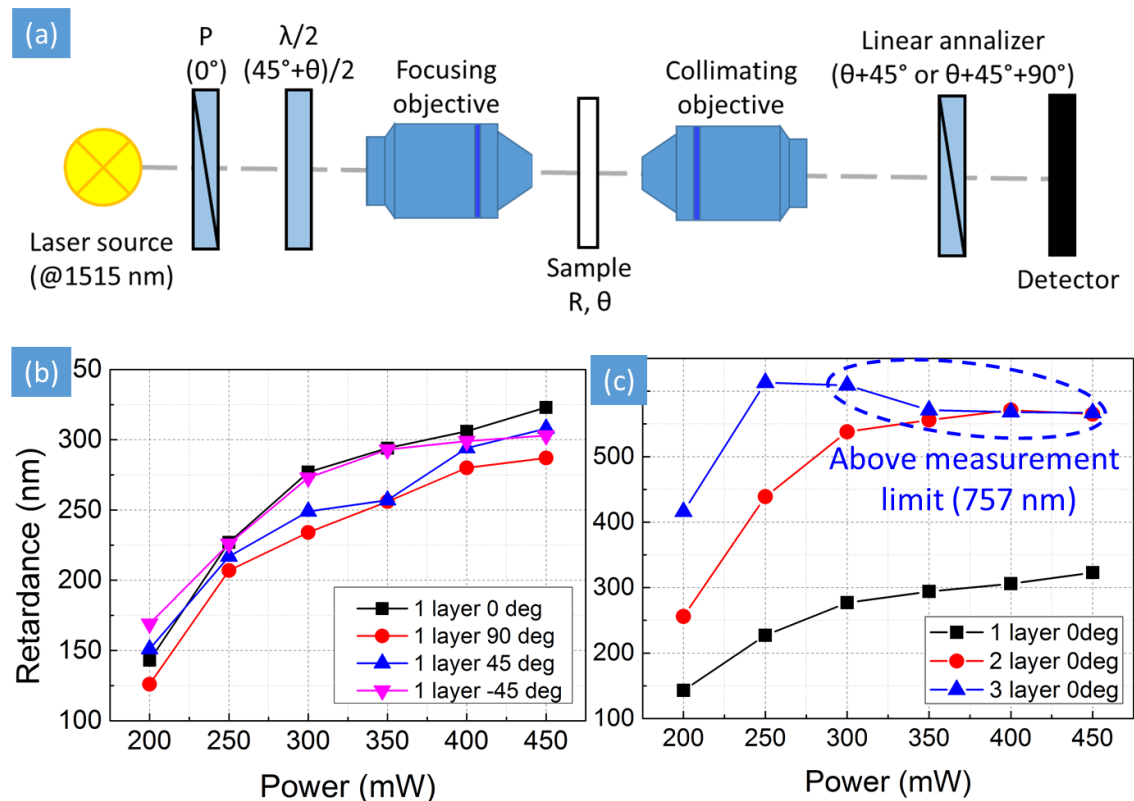


Figure 3-6 (a) Schematics of setup for retardance with high magnitude measurement. The orientation of slow axis θ has to be known. (b) Retardance dependence on writing laser power measured with the setup. (c) Retardance measurement of structures having 1, 2 and 3 laser fabricated layers.

Structures with different laser power and polarization were fabricated and measured with retardance measurement setup (Figure 3-6 (b, c)). Structures were fabricated with laser setup described earlier. The repetition rate of the laser was 200 kHz and pulse duration of the laser was stretched to 800 fs. Laser beam was focused with 0.16 NA lens. The writing speed was 2 mm/s and lines were juxtaposed with 1 μm distance. Laser power was from 200 mW to 450 mW and structures were written with four different laser polarizations (0° , 90° , 45° and -45°). In order to achieve high retardance, structure with 2 and 3 layers were also fabricated. As the thickness of one layer is around 50 μm (under the focusing conditions described above), layers were separated by 75 μm in order to avoid overlapping.

With this birefringence measurement system it was possible to measure much higher retardance values (up to ~ 750 nm) than with Abrio (PolScope). However the disadvantage is that birefringence slow axis of the sample has to be known before the measurement and in our setup the distribution of the retardance could not be measured. In order to measure retardance distribution, instead of the detector (Figure 3-6 (a)), CCD camera should be placed. With small changes it can be also used for retardance dependence on wavelength (retardance dispersion) measurements [54].

3.2 Pulse duration influence on nanogratings

In order to fabricate optical elements based on nanogratings, firstly correct set of laser writing parameters has to be found. Laser power, repetition rate, pulse duration, focusing conditions, fabrication speed define the quality of a structure and strength of retardance. Let us begin with the pulse duration.

Our femtosecond laser system has shortest pulse duration of 270 fs. However the distance between the gratings inside the pulse compressor can be changed and the pulse can be stretched up to 10 ps. In order to see the influence of pulse duration on the fabricated birefringent structure, structures with different pulse durations were fabricated and analysed with the Abrio (Figure 3-7 (a)). Laser beam was focused with 0.35 NA objective (x20 magnification) and laser written lines were juxtaposed with 1 μm distance between each other. Each line were written with increased power from 10 mW to 200 mW (similar to the structures in Figure 3-5 (a)). Repetition rate was 200 kHz and writing speed – 2 mm/s.

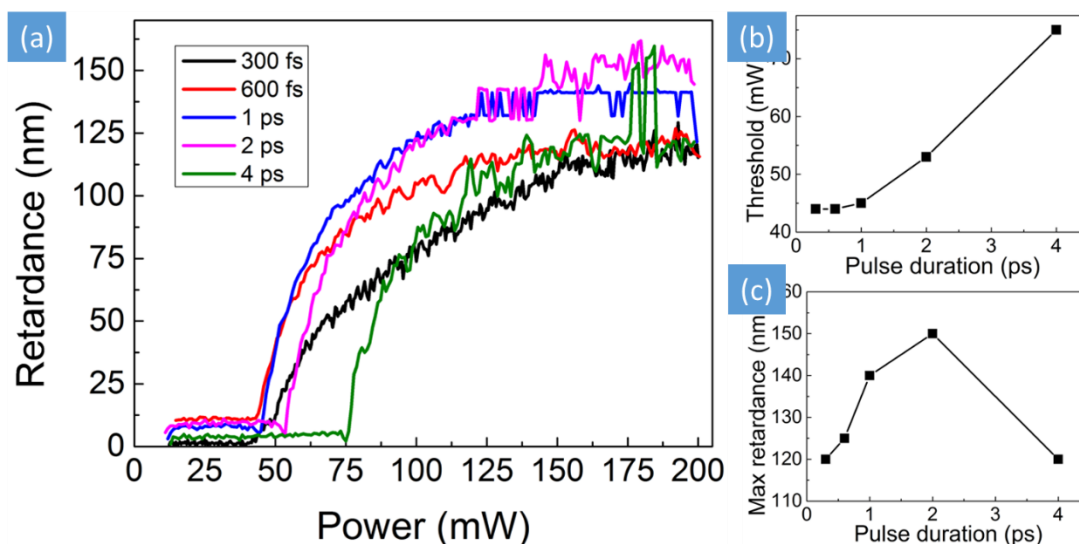


Figure 3-7 (a) Retardance dependence on laser power at different pulse durations. Modification threshold (b) and maximum retardance value (c) dependence pulse duration.

Measurement of retardance dependence on the laser power (Figure 3-7 (a)) reveals birefringent modification power threshold dependence on pulse duration (Figure 3-7 (b)). As expected, modification threshold is higher at longer pulse duration [8,72]. However up to 1 ps modification threshold is almost same and starts increasing just with longer pulse durations. When laser power increases, induced retardance also increases until it reaches certain maximum value at which it saturates (Figure 3-7 (a)). We can see that maximum retardance value also slightly depends on pulse duration (Figure 3-7 (c)). Maximum retardance increases with the pulse duration until ~ 2 ps and then starts dropping again. And third property which depends on the pulse duration is quality of the structure. Above ~ 1 ps fabricated structure become less regular which can also be noticed from the measurement curve (Figure 3-7 (a)).

From Figure 3-7, conclusion can be drawn that pulse duration should be kept below 1 ps as it gives smooth structure and modification threshold is lowest. It is known that shorter pulse duration can induce type I modification (refractive index increase) [28]. Usually pulse duration required for type I modification is below 200 fs, however other laser writing parameters are also important [72]. When higher writing speed is used or focused with lower NA lens, type I modification can be induced also with higher pulse duration.

Objective with 0.35 NA was changed with a 0.16 NA lens and other laser writing parameters were left. Rectangles were fabricated at 200 mW laser power with two laser polarizations and pulse durations from 300 fs to 800 fs (Figure 3-8). With lowest pulse duration (300 fs) nanogratings were not formed and instead we had type I modification with no birefringence. At 500 fs modification is clearly type II exhibiting scattering and strong birefringence. Between 300 fs and 500 fs we can see intermediate phase between type I and II modification. It is smoother with less scattering but has lower retardance than type II modification. At 400 fs we can also see big difference between two laser polarizations. As this modification on the boundary between two phases, we can see that polarization parallel to the writing direction gives modification closer to the type I and perpendicular - closer to type II. It shows that perpendicular polarization has lower type II modification threshold even though it has lower retardance at longer pulse durations (Figure 3-8).

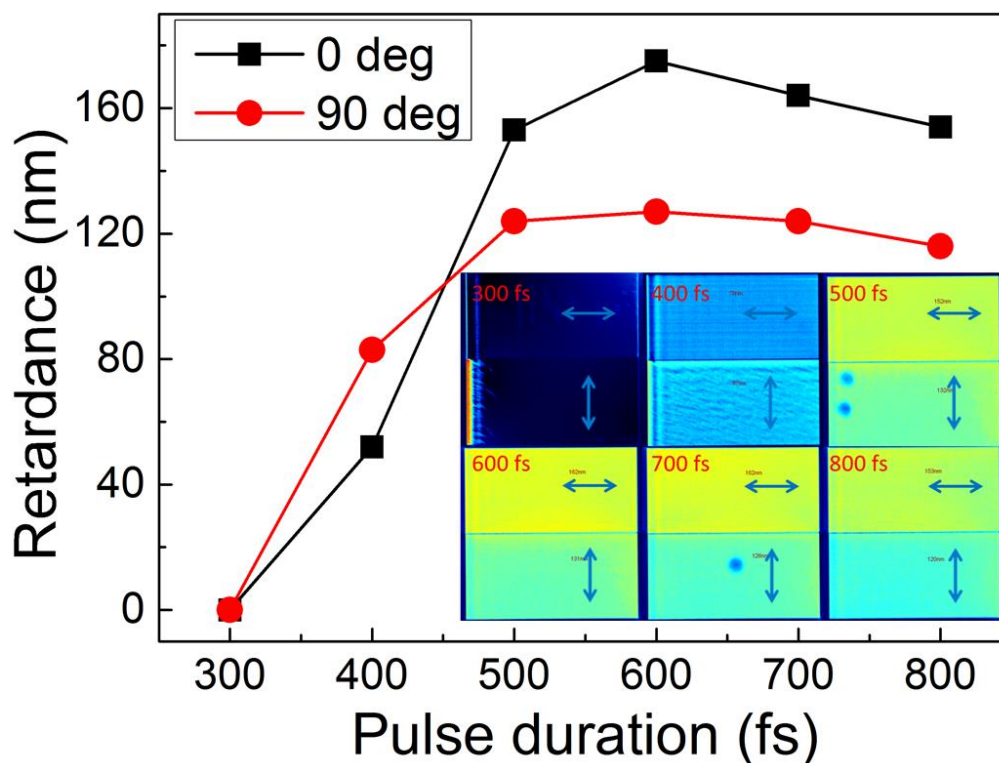


Figure 3-8. Nanogratings formation and retardance dependence on pulse duration. Structures were written with two different polarizations (blue arrows) with respect to writing direction (writing direction is horizontal).

Low writing speed would allow the formation of nanogratings at shorter pulse durations [72]. However writing speed is crucial in fabrication of optical elements. Therefore the lower boundary of pulse duration for fabricating nanogratings with different writing speeds and focusing conditions is around 500 fs. Together with previously assessed higher boundary value of pulse duration of 1 ps, we can safely choose pulse duration in the middle (700-800 fs) where type II modification will smooth with different sets of writing parameters and modification threshold is low.

3.3 Laser power, focusing conditions and fabrication speed

In previous chapter it was already demonstrated, that with increase of laser power (pulse energy), retardance increases until certain value and then saturates. However laser power has also other influence on modification such as smoothness and modification phase. Rectangles with different laser powers (40 mW - 900 mW) were fabricated at two fabrication speeds: 1 mm/s and 2 mm/s (Figure 3-9). Laser beam was focused with 0.35 NA objective and pulse duration was stretched up to 800 fs. In order to induce nanogratings, pulse density of few hundred pulses is required (number varies for different pulse energies) [83]. To have high enough pulse density for high writing speed (up to few mm/s), laser repetition rate of 200 kHz was used.

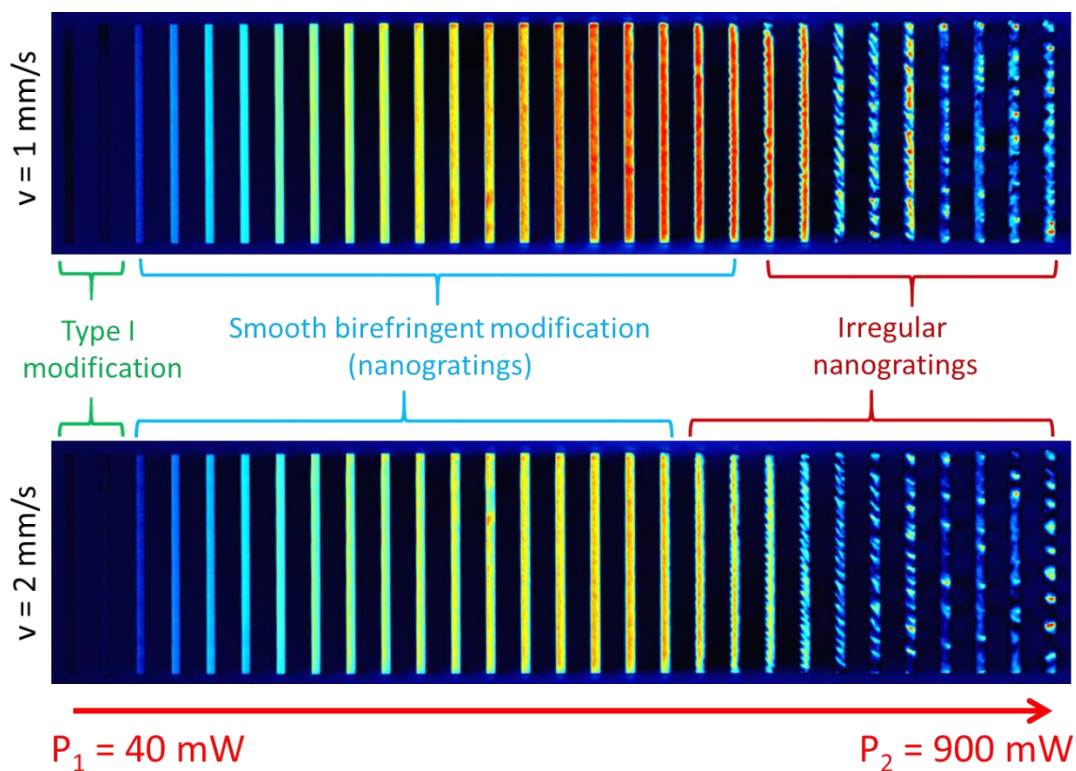


Figure 3-9. Microscopic images of femtosecond laser induced anisotropic modifications captured with a birefringence measurement system (CRi Abrio imaging system). Structures were written in two different speeds with increasing average laser power.

Fabricated structures were imaged with birefringence measurement system Abrio (Figure 3-9). Depending on laser power we can see three distinctive phases of modification. At lowest laser power, we have non-birefringent and very uniform modification exhibiting refractive index increase (Type I modification) which is barely visible. Depending on other laser parameters (focusing conditions, pulse duration, writing speed), required laser power to induce such modification can vary. For example if fabrication speed would be lower, even at lowest power (just above threshold) nanogratings would be induced. And if we have shorter pulse duration and lower NA focusing lens, even at high laser power type I modification is induced (Chapter 3.2).

With higher laser power smooth birefringent modification is induced (Figure 3-9). Retardance value increases with increase of laser power until it reaches maximum. Further increase in laser power results in strong irregularities in the structure and retardance decrease.

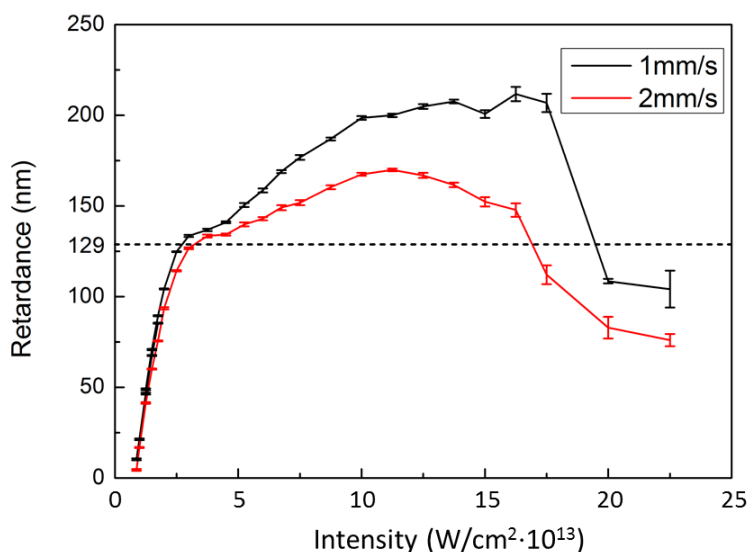


Figure 3-10 Retardance dependence of structures fabricated with 0.35 NA objective on laser intensity for two different speeds (Laser power was up to 900 mW).

Retardance measurement (Figure 3-10) reveals small difference between two fabrication speeds (1 mm/s and 2 mm/s) when laser power is below 200 mW ($5 W/cm^2 \cdot 10^{13}$). With both writing speed quarter-wave retardance value (128.75 nm) at 515 nm wavelength can be achieved. Therefore we can conclude that

that in order to fabricate quarter-wave plate (or optical element based on micro quarter-wave plates) following parameters can be used: 700-800 fs pulse duration, 200 kHz laser repetition rate, 0.35 NA objective to focus laser beam, 1-2 mm/s fabrication speed, 140 mW average laser power.

However we cannot achieve retardance as high as half-wave value (257.5 nm) at 515 nm wavelength. Even though with 1 mm/s fabrication speed higher retardance value than with 2 mm/s can be reached, it still saturates at around 200 nm. Reducing writing speed could allow reaching half-wave retardance, but that would increase time required for fabricating optical element.

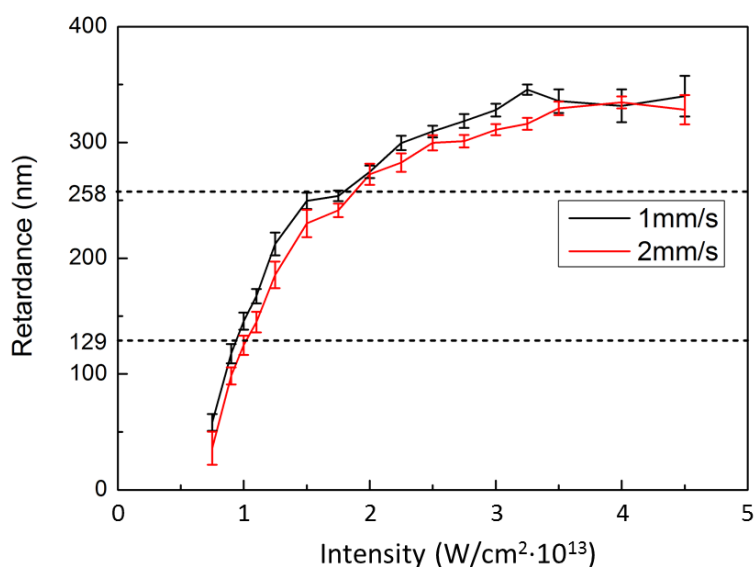


Figure 3-11. Retardance dependence of structures fabricated with 0.16 NA lens on laser intensity for two different speeds (Laser power was up to 900 mW).

Another way to increase retardance value is to focus laser beam with lower NA objective or lens. It can be explained by the fact that beam focused with lower NA lens will produce longer structure. Retardance value depends not just on birefringence ($n_o - n_e$), but also on the length of the structure (d):

$$R = (n_o - n_e) \cdot d. \quad (3-11)$$

The objective was changed with low NA lens (NA = 0.16), structures were written again and retardance measured (Figure 3-11). We can see that with

lower NA, the threshold for inducing nanogratings increased, but it became possible to reach higher retardance value. Also retardance difference for two fabrication speed is negligible.

From these results the conclusion can be made on set of laser fabrication parameters required for polarization converters based on half-wave plate: 700-800 fs pulse duration, 200 kHz laser repetition rate, 0.16 NA lens to focus laser beam, 1-2 mm/s fabrication speed, 350 mW average laser power.

3.4 Polarization influence on laser modification

Two parameters of the birefringent modification, retardance and the azimuth of the slow axis, can be controlled during the writing process as the slow axis is defined by the polarization and the retardance as a function of the laser fluence. Retardance depends also on the laser wavelength, the pulse duration and the number of pulses transmitted through the modified region [16,31,55]. However, the retardance also is affected by the orientation of the polarization plane with respect to the writing direction. As the direction of the slow axis is varied during the writing process, the angle between the laser polarization and the writing direction is changing accordingly, which couples the induced retardance with the polarization direction. The difference in modification for 0° and 90° angles of polarization with respect to the writing direction is known for metals [73]. Recently, a similar effect was reported for laser processing of dielectrics [72]. However, it is important to keep the retardance value independent on the light polarization for the fabrication of variant polarization optical elements, for applications such as polarization beam converters, polarization sensitive camera and 5D optical memory [70,74,75]. Such polarization dependence is explained by the boundary conditions. The absorption is stronger for light polarized perpendicular to the interface, as described by the Fresnel coefficients. Thus the polarization parallel to the writing direction, which is absorbed more efficiently at the front kerf, is commonly used in metal cutting. For the perpendicular polarization, the light is absorbed more efficiently at the sidewalls. As an alternative, circularly or radially polarized light is used, which is equally absorbed at the front and sidewalls of the kerf [76]. The polarization dependence also arises due to the spatio-temporal properties of the ultrashort pulse laser beam quantified by the pulse front tilt (PFT) [77,78]. The PFT produced by temporal and spatial chirps in femtosecond laser pulses [79] can lead to the quill writing [77] and the anisotropic photosensitivity phenomena [80]. When the laser pulse approaches the focal point, the beam diameter is shrinking and the pulse front tilt is proportionally increasing. Thus even negligible pulse front tilt is strongly enhanced in the vicinity of the focus.

In this chapter I will demonstrate other extraordinary anisotropic properties of the femtosecond laser writing in transparent materials. Two new types of

writing polarization dependences and related writing direction asymmetries, which are not directly connected with the boundary conditions, are observed. Characterization of the optical anisotropy induced in fused silica and germanium sulphide glass revealed the chevron-shape stress, which leads to the polarization dependence when adjacent laser written tracks are partially overlapping. Another polarization dependence, which is related to the anisotropic photosensitivity produced by the pulse front tilt, is observed for single line writing.

The experiments were performed with two different laser systems. The first was PHAROS Yb:KGW (Yb-doped potassium gadolinium tungstate) laser system (Light Conversion Ltd.) operating at 1030 nm with the pulse duration stretched from 300 fs to 800 fs using an internal pulse stretcher-compressor. The laser repetition rate was set to 200 kHz. The linearly polarized laser beam was focused with an aspheric lens (NA = 0.16) 300 μm below the surface of a fused silica sample. The polarization of the laser beam was controlled with the zero order half-wave plate placed just before the focusing optics. Writing speed was in the range from 0.2 to 5 mm/s or effectively 160-4000 pulses per dot.

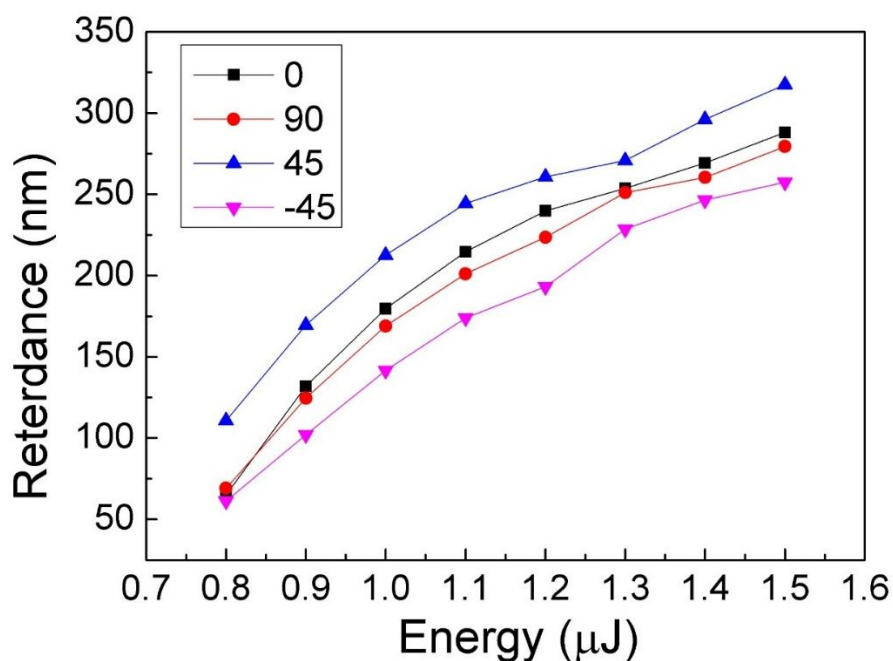


Figure 3-12. The dependence of retardance on pulse energy for four different polarizations of laser. Strongest difference is between 45° and -45° polarization. Writing speed of structures was 200 $\mu\text{m}/\text{s}$.

The separate tracks were imprinted in $\text{Ge}_{25}\text{S}_{75}$ glass with the second laser system, regeneratively amplified Ti:Sapphire laser delivering 150 fs light pulses at 800 nm wavelength and operating at 250 kHz repetition rate. The tracks were inscribed with 0.55 NA objective 200 μm below the surface at the scan speed of 200 $\mu\text{m}/\text{s}$. After the irradiation, the samples were inspected with a quantitative birefringence measurement system Abrio (CRi Inc.).

First, a set of structures was written in silica glass with four different polarization orientations with respect to the scanning direction (perpendicular, parallel and $\pm 45^\circ$). The tracks, comprising of 1×1 mm squares, were imprinted by translating the sample in the direction perpendicular to the laser light propagation. The tracks separated by 1 μm were partially overlapping (the estimated spot size was about 4 μm). The pulse energy was increased in steps from 0.8 to 1.5 μJ . All samples after irradiation exhibited strong birefringence produced by self-assembled nanostructures in the range of retardance values 50-250 nm. The retardance revealed strong polarization dependence for all pulse energies (Figure 3-12). The difference in modifications written with 0° (parallel) and 90° (perpendicular) polarization plane angles, with respect to the writing direction, could be explained by the effect of the polarization dependent Fresnel reflection at the boundaries of an induced structure [76]. The difference was also observed between $+45^\circ$ and -45° , which is unexpected and counterintuitive from the point of anisotropic laser light interaction at the boundary. Moreover, the difference for $+45^\circ$ and -45° (more than 20% of the retardance value) was stronger than for 0° and 90° (less than 10% difference at its peak). In contrast to the metal cutting, where the light polarized parallel to the writing direction is the most efficient, in our experiments we observed that the light polarized at $+45^\circ$ with the writing direction produced the highest retardance.

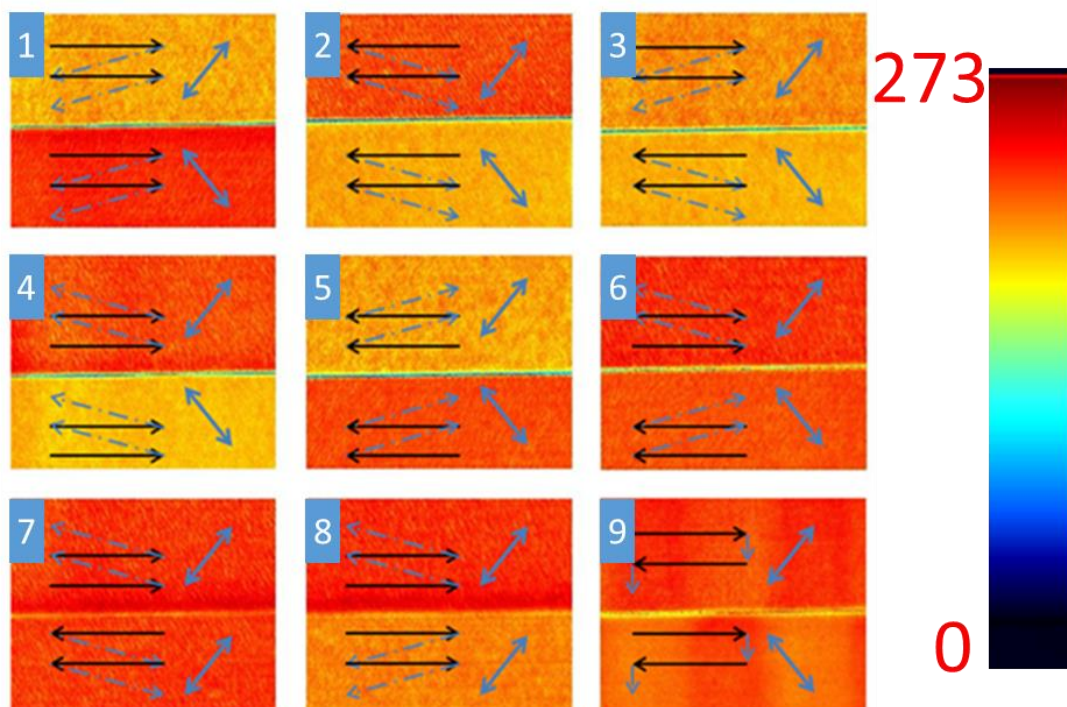


Figure 3-13. Microscopic retardance images of the structures written with various combinations of the polarization plane direction (blue), track writing direction (black) and raster scanning direction (dashed blue).

In order to understand the influence of the $+45^\circ$ polarization on the strength of the induced retardance, several squares were written with various combinations of the polarization orientation, track writing and raster scanning directions (Figure 2-7). One can clearly see that all three parameters affected the induced structures. Throughout this paper, only the strength of retardance is compared, as this parameter can be easily measured. However, the difference in obtained structures could be also observed under an optical microscope as the areas with the stronger birefringence exhibited slightly stronger scattering. Recently, Raman spectroscopy revealed higher density of 3-tetrahedra rings for the longitudinal polarization compared to the transversal polarization [81].

Very interesting case is illustrated by the structure number 8 (Figure 3-13) where two parts were written with the same angle between the light polarization and the writing direction but with the different raster scanning direction. As a result, raster scanning in one direction, from the bottom to the

top, resulted in higher retardance than for scanning from the top to the bottom.

The laser induced stress was investigated as possible reason for this phenomenon. To evaluate the effect of laser induced stress, we investigated several glasses where nanogratings are not produced and thus only stress birefringence is observed. For the stress birefringence, the relation between the retardance (R) and stress (σ) is defined as:

$$R = C_{pe} \cdot \sigma \cdot d, \quad (3-12)$$

where C_{pe} is the photoelastic coefficient, d is the thickness of the birefringent region. The larger photoelastic coefficient is, the stronger retardance is induced by stress. For the experiments, we selected glasses with different photoelastic coefficients: chalcogenide glass (germanium sulphide), borate glass and phosphate glass (Figure 3-14). The chalcogenide glass (germanium sulphide ($\text{Ge}_{25}\text{S}_{75}$)) has a photoelastic coefficient 50 times higher ($22 \cdot 10^{-12} \text{ Pa}^{-1}$) than fused silica ($0.4 \cdot 10^{-12} \text{ Pa}^{-1}$ [82]).

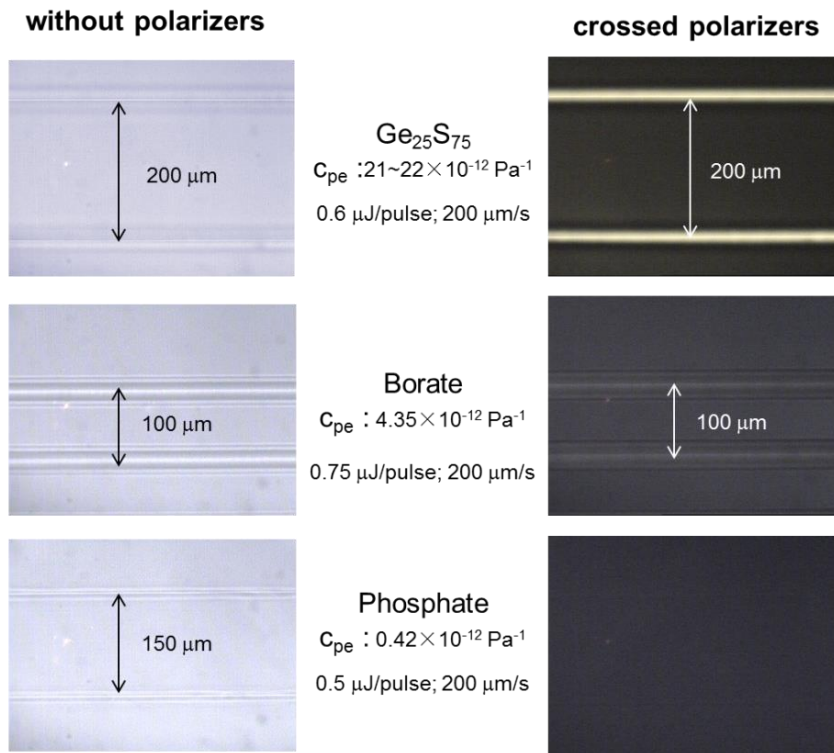


Figure 3-14. Microscope images of the femtosecond laser written tracks in chalcogenide, borate and phosphate glasses respectively. On the left

images are taken without polarizers and the right with crossed polarizers. The highest birefringence is induced in glass with the highest photoelastic coefficient.

The measured value of retardance in the chalcogenide glass was 200 nm for 0.6 μJ pulse energy. This is very close to the typical retardance values of form birefringence observed in fused silica. The subsequent thermal annealing at 310°C (glass transition temperature is 305°C) completely removed this birefringence confirming that it is induced solely by stress. Compared to chalcogenide glass, the laser exposed regions showed a much weaker birefringence in borate glass, with the C_{pe} reduced to the value of $4.35 \cdot 10^{-12} \text{ Pa}^{-1}$ (Figure 3-14). In phosphate glass, with a C_{pe} value of $0.42 \cdot 10^{-12} \text{ Pa}^{-1}$, which is about 50 times smaller than in chalcogenide glass, no birefringence was detected. We also tried measuring the stress induced birefringence in silica glass. However, the direct measurement was not possible due to strong form birefringence in this glass. Recently the stress induced by ultrashort light pulses was characterized by an indirect measurement method, where the stress has been measured via deflection of glass machined cantilevers [81]. The maximum induced stress was about 300 MPa, thus using a photoelastic coefficient for fused silica we estimate the stress-induced retardance of about 35 nm.

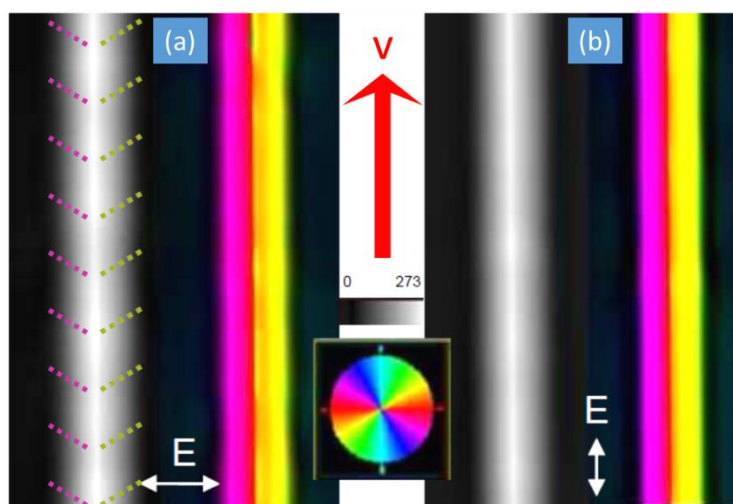


Figure 3-15. Laser induced stress birefringence in chalcogenide glass for two perpendicular linear polarizations. Grayscale images indicate the strength of the retardance and pseudo colors represent the orientation of birefringence slow axis (see legend). The sides of the

induced tracks exhibit chevron-shaped slow axis orientation directed opposite to the writing direction (dashed lines). The width of the track is 30 μm .

The slow axis distribution of imprinted tracks in chalcogenide glass revealed the presence of chevron-shaped stress along the scanning direction (Figure 3-15). The orientation of slow axis did not depend on the polarization of the writing beam confirming that the observed birefringence is related to mechanical forces exerted on the glass matrix and not to subwavelength structures. Material expansion produces stress in glass surrounding the light effected zone. The stress pattern is circularly symmetric in stationary conditions. The chevron-shaped stress distribution can be induced by multiple laser pulses delivered at a high repetition rate. We speculate that when the sample is moving the material is displaced by the thermal gradient and the front of modification is under higher strain than the back. Then the stress is annealed at the front and is frozen at the back of the modified region, leading to chevron-shaped stress distribution. It is worth to mention, that chevron-shaped structures were also observed in lithium niobate crystal [83] and on the silica glass surface [78].

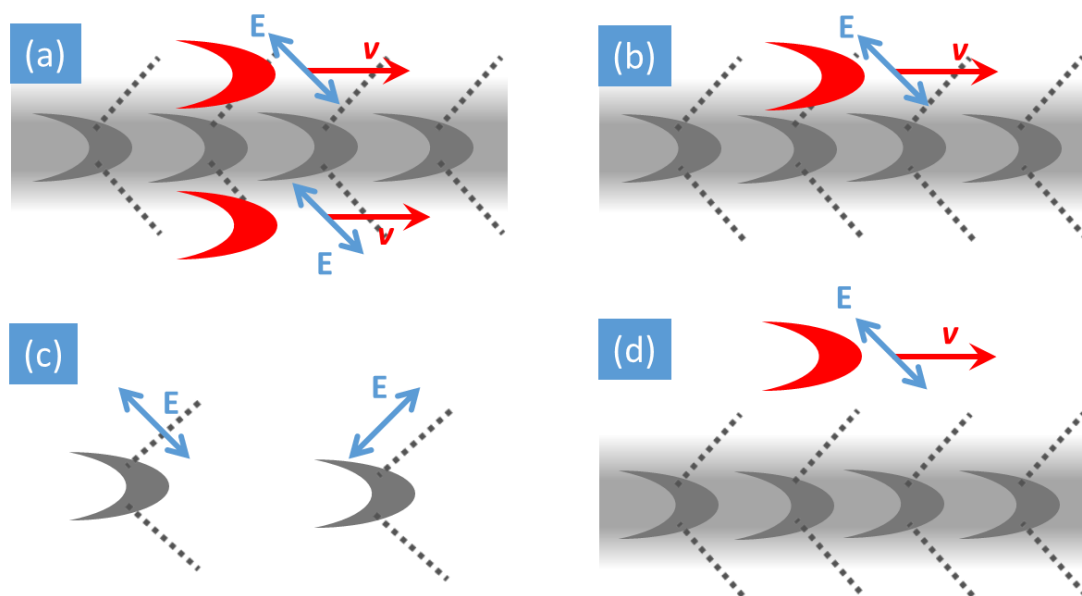


Figure 3-16. Schematic drawing describing stress and polarization geometry. The first laser written track produces chevron-shape stress (a). Grey chevrons indicate the drag of material as a result of light irradiation

as sample is translated. Depending on where the next track will be written (top or bottom), polarization can be parallel or perpendicular to stress (c). Stress and polarization interaction should disappear when the distance between tracks is increased (b, d).

If the chevron-shaped stress is indeed responsible for the observed directional dependence, the strength of the produced retardance should depend on the polarization angle with respect to the stress induced by a previous track (Figure 3-16 (a, c)). As a result, the effect should depend on the direction of the track writing and raster scanning.

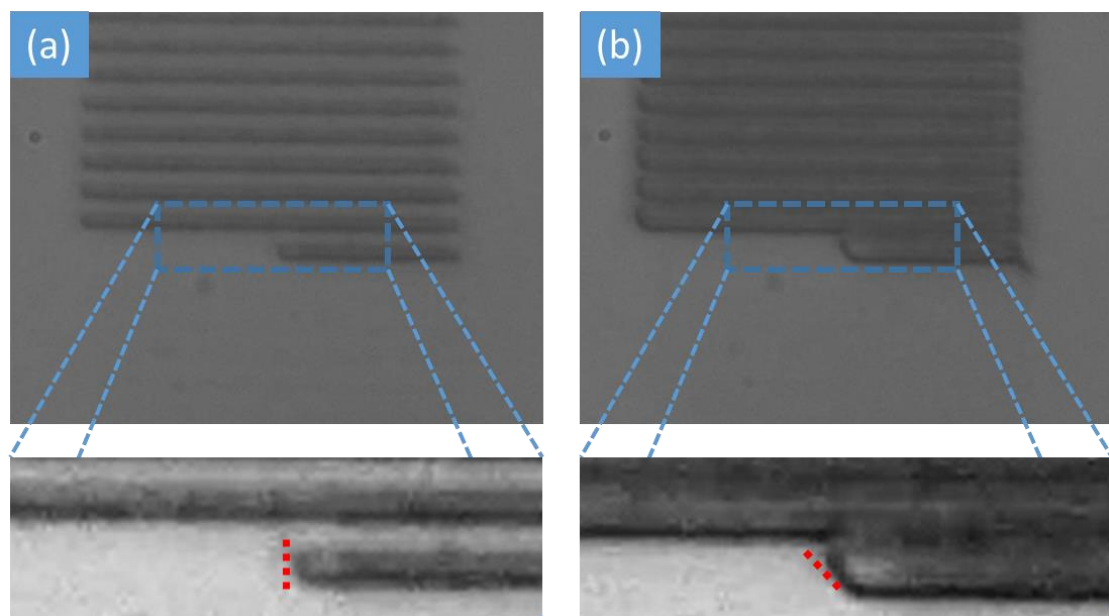


Figure 3-17. The influence of stress on the front of the laser modification. The modification front is perpendicular to the writing direction when distance between tracks is higher (a). When tracks are close to each other the modification front is tilted (b). Images were taken during laser modification.

This assumption was confirmed by images taken during the writing procedure, which reveal the influence of the induced stress on the interaction of laser irradiation with the material (Figure 3-17). When the distance between laser written tracks is sufficiently large, they can be treated as being separate (Figure 3-17 (a)). As a result, the front of the track is perpendicular to the

writing direction. In this case, the light polarized at 0° to the writing direction (perpendicular to the front) would produce stronger modification than the light polarized at 90° [72]. While the light polarized at 45° should have identical conditions as the light polarized at -45° and thus produce identical modification. If the distance between tracks is small and the track written by the laser overlaps with a region under strain, the situation is completely different. The front of the written track becomes tilted (Figure 3-17 (b)). As a result, the strongest modification is induced by polarization, which is at 45° to the writing direction and perpendicular to the front of the modification. The strength of the modification depends on the mutual angle between the polarization and the front of the modification. This observation clearly explains the observed retardance dependence on polarization (Figure 3-12).

Also in the experiment, the correlation of the strength of retardance with the angle between the laser polarization and the stress induced by the previous track (also front of modification) was observed. The retardance was much stronger for the polarization perpendicular to the induced stress (front of modification) than for the parallel. By choosing the correct scanning algorithm, the observed polarization dependence could be eliminated. For instance in the structure number 3 of Figure 3-13, the uniformity was achieved by changing the polarization orientation with the writing direction in such a way that it was always parallel to the chevron-shaped stress. The polarization dependence can be also compensated by the bidirectional raster scanning (Figure 3-13, structure number 9). However, this produces double periodicity in the imprinted structure as a result of every second track having a different birefringence than the previous one [68]. Additionally, such type of scanning is not applicable for the fabrication of certain structures such as spirals.

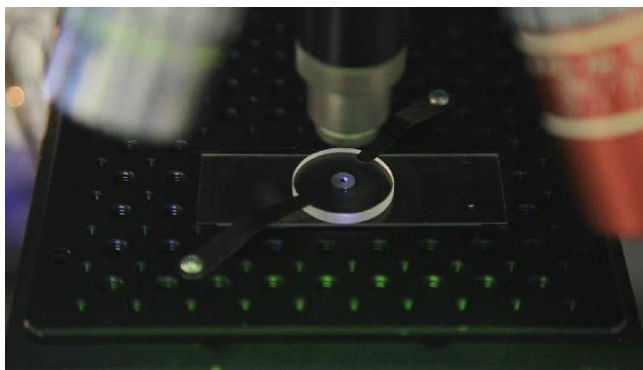


Figure 3-18. Fabrication of the polarization converter. The intensity of white light emission (due to hot plasma) during the laser fabrication oscillates as the angle between writing direction and the polarization plane changes.

The importance of the observed unusual polarization dependence can be clearly seen in the writing of the polarization converter (Figure 3-18) [74]. In this experiment, the laser beam is drawing spiral trajectories with polarization azimuth rotating in a certain manner. As the polarization plane orientation was changing with respect to the writing direction, the white light emission intensity was oscillating with the maximum (corresponding to $+45^\circ$) 5 times larger than minimum. Surprisingly, despite the relatively small retardance value difference (less than 10%), the strong corresponding variation in white light emission was observed.

As the polarization dependence is related to a previously written track, it should disappear with increasing the separation between tracks (Figure 3-16 (d)). The structures number 2 and 3 shown in Figure 3-13 were written with the distances between tracks ranging from $0.5\ \mu\text{m}$ to $3\ \mu\text{m}$. The dependence of retardance on the light polarization (the structure number 2 in Figure 3-13) disappeared at the track separation of $3\ \mu\text{m}$ (Figure 3-19 (a)). Taking into account that the estimated laser spot diameter was about $4\ \mu\text{m}$, we can assume that at $3\ \mu\text{m}$, tracks effectively do not overlap, supporting the explanation based on the stress produced by the neighboring track.

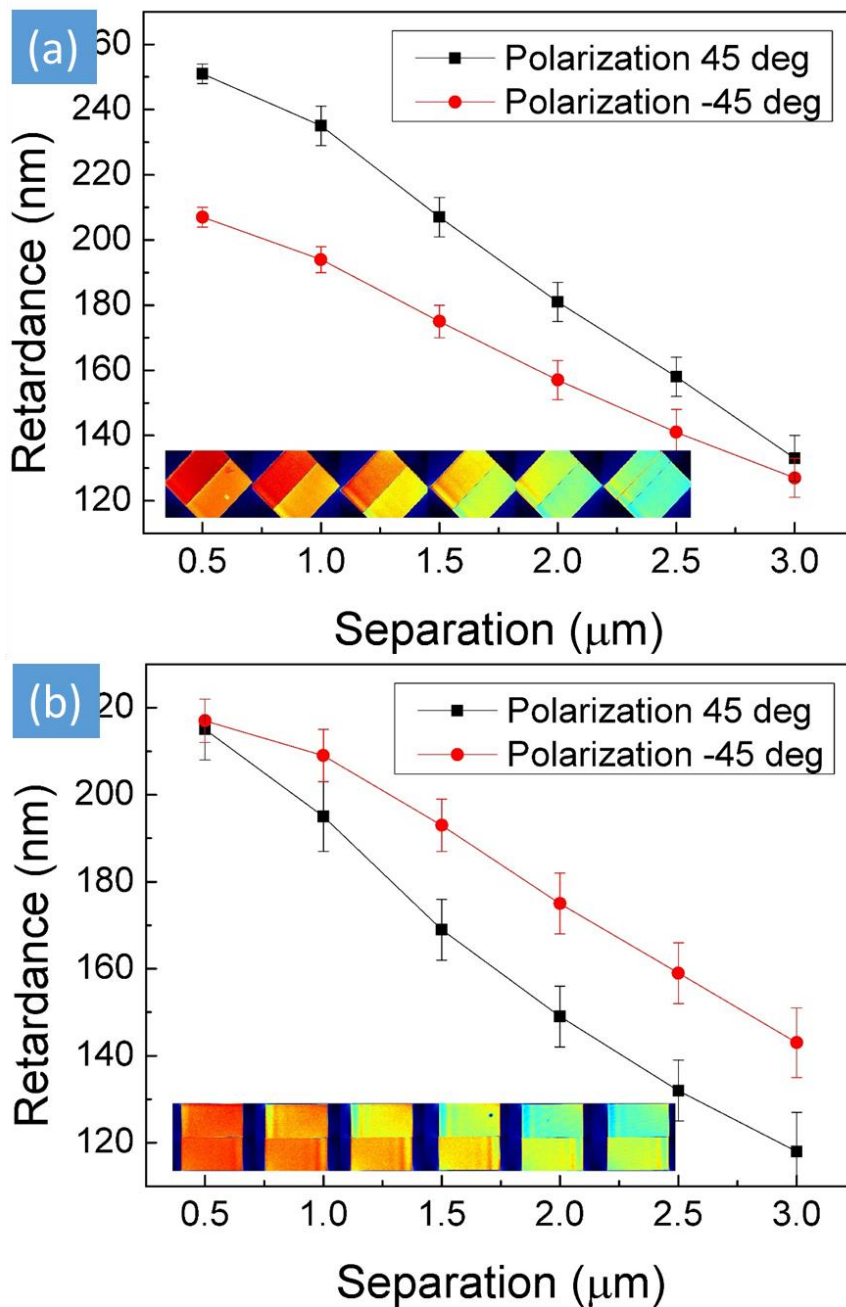


Figure 3-19. The dependence of retardance on the separation distance between tracks for two polarizations. For the structure fabrication algorithm see the structures number 2 (a) and 3 (b) in Figure 3-13.

Another type of anisotropy was observed in the structures, which did not exhibit the dependence of retardance on polarization at a small track separation (the third in Figure 3-13). Unexpectedly, at a larger track separation, the structures displayed the polarization dependence (Figure 3-19 (b)). This

indicates that the polarization-stress interaction is not the only mechanism responsible for the retardance dependence on the polarization. Indeed, the strength of modification can also depend on the angle between the pulse front tilt (PFT) and polarization [80]. The pulse front tilt can be introduced either by the angular dispersion or by the combination of spatial and temporal chirps [79]:

$$p = p_{ad} + p_{sc+\tau c} = k_0\beta + \varphi^{(2)}\nu, \quad (3-13)$$

where k_0 is a wavenumber, β - the angular dispersion, $\varphi^{(2)}$ is the group-delay dispersion and ν is the spatial frequency gradient.

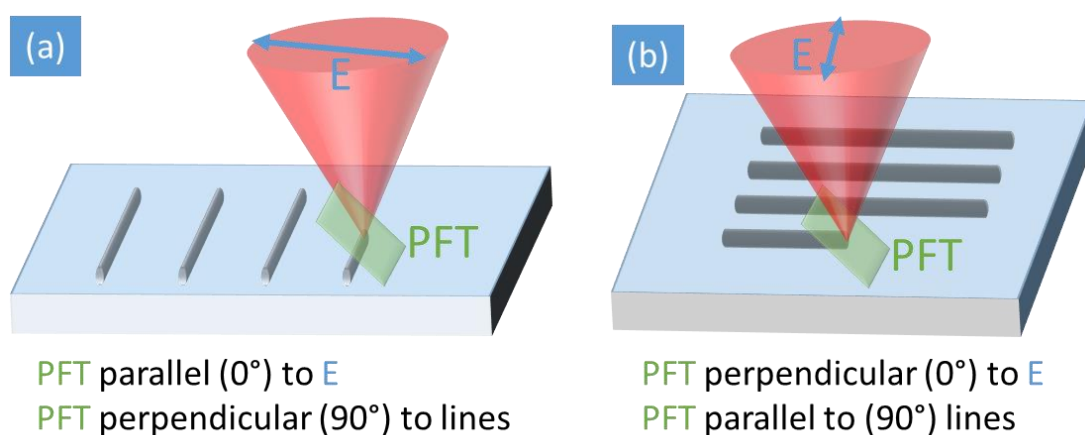


Figure 3-20. Schematic illustration of different angles between the plane of PFT and the plane of polarization or laser written line.

The pulse front tilt can be characterized by the shift of the delay axis of the FROG trace measured with a GRENOUILLE. The PFT was measured for our laser system in the horizontal (parallel to the writing direction) and vertical (perpendicular) directions for several pulse durations. At the shortest pulse duration of 250 fs, the PFT was 0.59 fs/mm and 0.18 fs/mm for horizontal and vertical axes respectively. At 800 fs, corresponding values were 0.67 fs/mm and 0.5 fs/mm. The PFT introduced by the angular dispersion does not depend on the temporal chirp. This behavior was observed for the horizontal axis, where a spatial frequency gradient was reduced by a precise pulse compressor alignment. The PFT strongly depended on the temporal chirp indicating the

presence of spatial chirp for the vertical axis. The azimuth of the PFT was controlled by adding the temporal chirp and was estimated at an angle of 37° to the writing direction for the pulse duration of 800 fs. The azimuth of the PFT plane and its relation to the polarization plane or laser written line is explained in Figure 4-20.

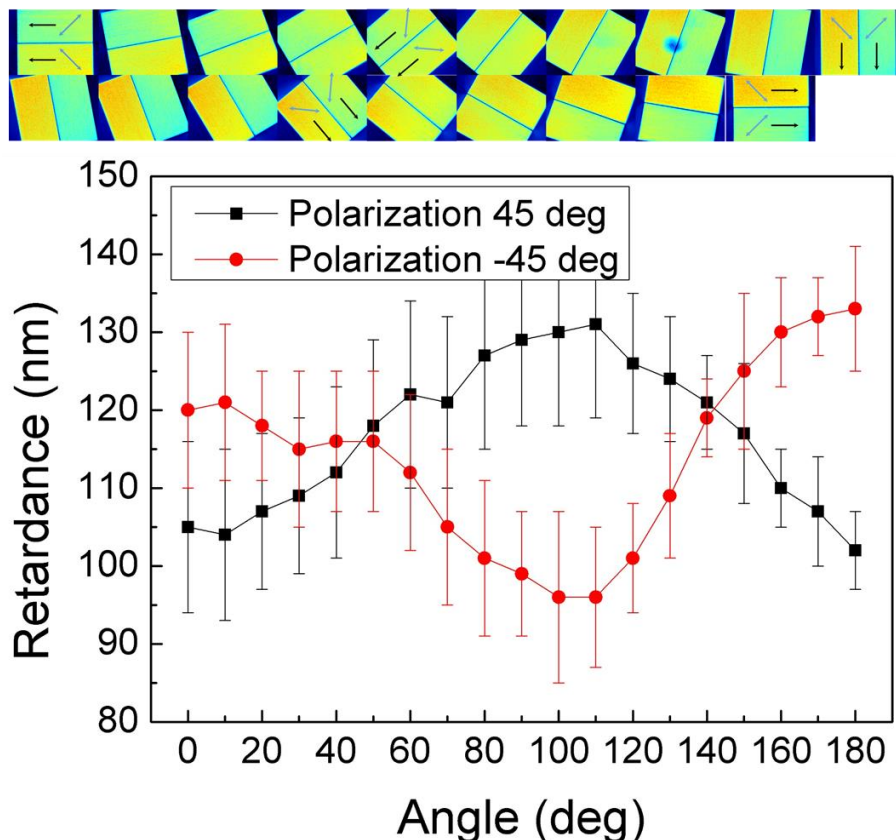


Figure 3-21. Retardance variation for two polarizations when the structure was written at different angles. The difference in the strength of birefringence is defined by the angle between the pulse front tilt and the writing direction. Separation between tracks was $3\ \mu\text{m}$, fabrication algorithm as in the structure number 2 in Figure 3-13. Arrows indicate laser writing direction (black) and the polarization plane direction (blue).

To validate this prediction, the structures (number 2 in Figure 3-13) with a $3\ \mu\text{m}$ separation between tracks were written rotating the orientation of the scanning direction (Figure 3-21). The polarization was rotated by the same angle as the writing direction keeping the same -45° or $+45^\circ$ mutual angle. The

strength of induced retardance exhibited a periodic variation with the angle of writing direction. The variation for one writing direction was shifted by π with respect to the other direction. The biggest difference was observed for approximately 90° where the pulse front tilt was at about 45° to the writing direction. The difference completely disappeared at about 45° and 135° . The explanation of this observation can be the following. The azimuth of pulse front tilt in our experiments was at about 45° to the writing setup coordinate system (Figure 3-22). If the structures were written as shown in Figure 3-22 (a), the polarization plane direction will be parallel or perpendicular to the pulse front tilt direction. It was demonstrated that the pulse front tilt leads to a stronger material modification for the polarization parallel to the pulse front tilt [80]. If the writing direction was aligned along or perpendicular to the PFT, then the polarization was always directed at about 45° to the PFT and no difference in retardance was observed (Figure 3-22 (b)). It is worth mentioning that in our experiment we also observed the quill writing effect, manifesting itself as a change in retardance strength by reversing the writing direction [77,78]. As a result of this effect, the difference in retardance was larger for polarization at 180° than at 0° (Figure 3-21). Interestingly, the PFT dependence completely disappeared when the laser written tracks were partially overlapping. All previous experiments on the pulse front tilt were performed either writing single tracks [77,78] or printing separate dots [80].

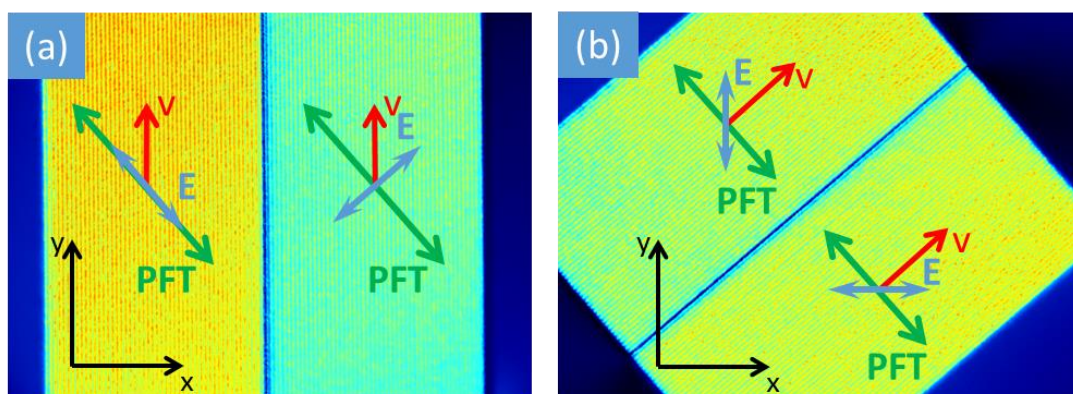


Figure 3-22. Schematics explaining observed polarization dependence. For the left image, the writing direction is at 45° with respect to the pulse front tilt; whereas an electric field is oriented perpendicular or parallel to the pulse front tilt. The stronger modification is induced for the polarization parallel to the pulse front tilt. For the right

image, the writing direction is perpendicular the pulse front tilt and an electric field is always at 45° to it. As a result the structures are equivalent for both polarizations.

In conclusion, we have demonstrated two different sources of the polarization dependence observed in femtosecond direct writing experiments. One is related to stress induced birefringence and the other is produced by the spatio-temporal distortion of the laser pulse. Stress measurement indicates that during laser writing the material is dragged by the thermal gradient and it causes chevron-shape stress distribution. Stress induced birefringence causes tilt in the front of tracks. As a result, the light polarized at 45° to the writing direction induces the highest retardance. The polarization dependence is strongly affected by the density of laser written tracks. For overlapping tracks, this dependence is mainly defined by the stress induced birefringence. The PFT is playing the major role only for separated tracks. As a result, the effect of spatio-temporal distortion can be minimized by overlapping adjacent tracks.

Stress induced retardance as high as 200 nm was observed in germanium sulphide glass because of a large photoelastic coefficient. The strength of the stress induced birefringence is very close to the values produced by self-assembled nanogratings in silica glass. The ability to control stress-induced birefringence in glasses with high photoelastic coefficients can be explored for the fabrication of birefringent optical elements such as polarization converters.

3.5 The lifetime of the nanogratings

In this chapter I will extensively analyze the thermal stability of the nanogratings by annealing laser fabricated structures at high temperature. Also the possibility of controlling the optical properties of the nanogratings by annealing is investigated.

The nanogratings are structural modifications which are known to exhibit high thermal and chemical durability. The nanoplanes have reduced refractive index (~ -0.2) which in macroscopic scale makes nanogratings birefringent (up to 10^{-2}). Close investigation on the nanoplanes reveals that refractive index is reduced because material becomes porous [40,61]. Those porous regions consist of nanovoids filled with oxygen [50] which forms during decomposition of Si-O bonds. In time such nanovoids could collapse and then the birefringence of the modification would disappear. Previous annealing experiments indicated that such modification can withstand at least 2 hours of thermal annealing at 1000°C [51] and be rewritten only with femtosecond laser pulses [52]. However, to evaluate the stability of nanovoids and the activation energy required for them to collapse at normal conditions, more thorough measurements are required.

If the thermally activated process at the room temperature is too slow to be observed, the rate of the process can be measured at high temperatures and then, using the Arrhenius law, extrapolated to the room temperature. In order to estimate the lifetime of the nanogratings, quantitatively measurable properties of the nanogratings have to be chosen. As nanogratings exhibits strong birefringence and scattering and both of them can be evaluated, the decay rate of the retardance and scattering values at high temperatures were measured.

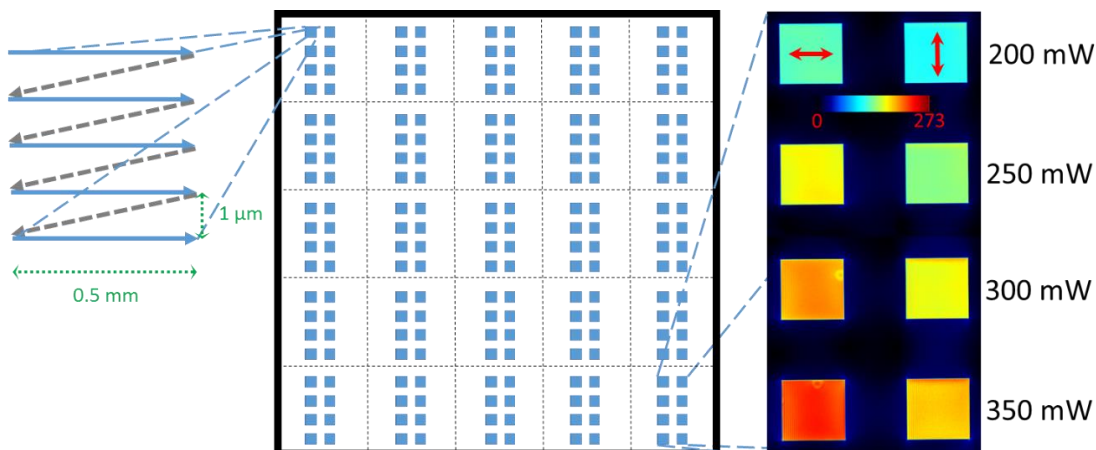


Figure 3-23. (Left) Schematic of the preparation of 25 identical samples written on fused silica glass slide. Laser tracks are indicated by solid blue arrows. (Right) Microscopic birefringence image of one sample. Colours indicate the strength of the retardance. Four different laser powers were used to write the structures and two polarizations (red arrows indicate the orientation of the polarization).

For annealing experiment, the batch of 25 samples with same conditions was fabricated with the laser on the fused silica slide (Figure 3-23). Each sample consist of 8 squares (0.5x0.5 mm) written with parallel and perpendicular polarization and laser powers from 200 mW to 350 mW (Figure 3-23). Squares were written using 0.16 NA lens by juxtaposing laser induced lines by 1 μm to each other. Laser was working at 200 kHz repetition rate and the pulse duration was stretched to 700 fs. Writing speed was 1 mm/s. After the irradiation the fused silica glass was cut into 25 identical samples for the set of different annealing parameters (temperature, time).

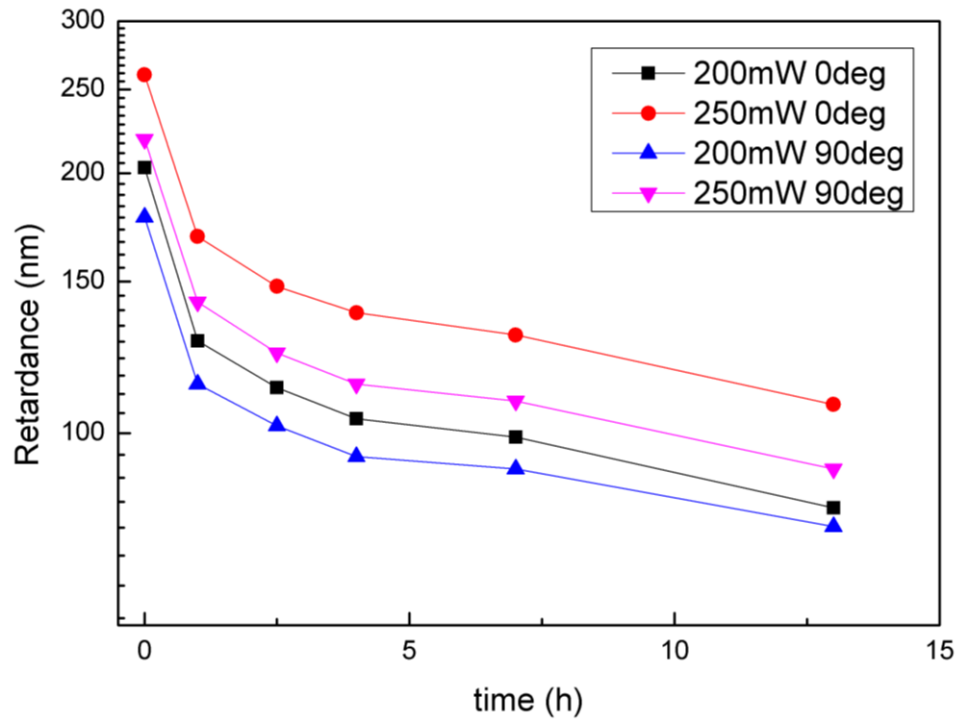


Figure 3-24. The retardance value decay during sample annealing at 1000° C.

After the annealing experiments, it was expected for the retardance value to drop exponentially regarding to the annealing time:

$$R(t) = R_0 \times e^{-t/\tau}, \quad (3-14)$$

where R - retardance value, τ - decay time. But preliminary results indicated that the retardance value drops faster at the beginning and much slower later (Figure 3-24). Samples were annealed at 1000° C for different durations of time (1 to 13 hours). After first hour retardance dropped drastically (almost 40%) and after that the decaying speed decreased. All curves in Figure 3-23 indicates that after one hour the retardance decays exponentially (in logarithmical scale curves after one hour can be easily fitted to linear dependence). It means that the decay consists at least of two independent decay processes with fast and slow decay time (τ_1 and τ_2):

$$R(t) = R_1 \times e^{-\frac{t}{\tau_1}} + R_2 \times e^{-\frac{t}{\tau_2}}. \quad (3-15)$$

The fast process can be attributed to the annealing or defects or stress as it was showed before that they can be annealed at lower temperatures [54],

whereas the slow process reflects the morphological changes of the annealed nanograting. In order to measure the decay time of nanogratings during the annealing, all 25 samples firstly were annealed at 1000° C for one hour as data from Figure 3-24 indicates that such an annealing is sufficient to erase fast decaying birefringence. The retardance values (R_0) of all preannealed samples were measured and those values were taken as a starting point of the following annealing experiment.

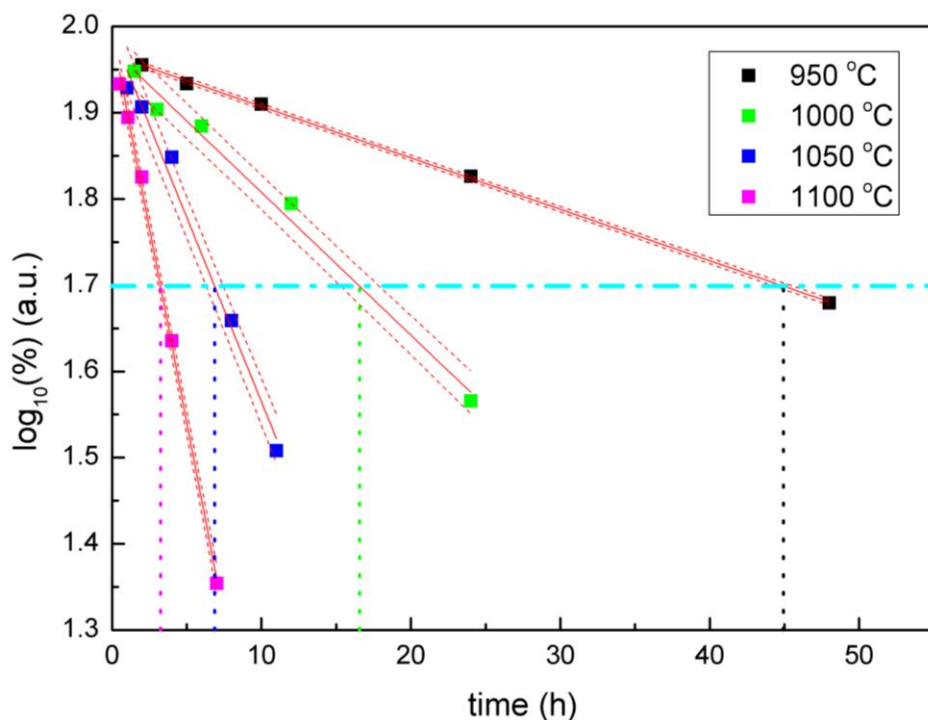


Figure 3-25. The decay of the retardance value over time at different annealing temperatures. Structure is written with 200 mW laser power polarized parallel to the writing direction. Horizontal dashed line indicates $1/e$ of the retardance value R_0 at the beginning.

The pre-annealed samples were heated at four different temperatures (950° C, 1000° C, 1050° C and 1100° C) for different time duration. The retardance measurements of one of the square (written with the laser polarized parallel with the writing direction and 200 mW power) is plotted in the Figure 3-25. The retardance values were normalized to percent the retardance value of preannealed samples ($R(t)/R_0 \times 100\%$) and plotted at logarithmic scale. For all temperatures the decay of the retardance value was exponential. For each

annealing temperature the retardance value decay time τ (the time which takes for the retardance to drop to the R_0/e value) was estimated. Knowing this time at high temperatures, the lifetime of the nanogratings at the room temperature can be extrapolated. The thermally activated decay time τ at the certain temperature can be evaluated by Arrhenius law:

$$\frac{1}{\tau} = k = A \times \exp\left(-\frac{E_a}{k_B T}\right), \quad (3-16)$$

where k is decay rate, E_a - the activation energy, A - the frequency factor, T - the absolute temperature and k_B - the Boltzmann constant.

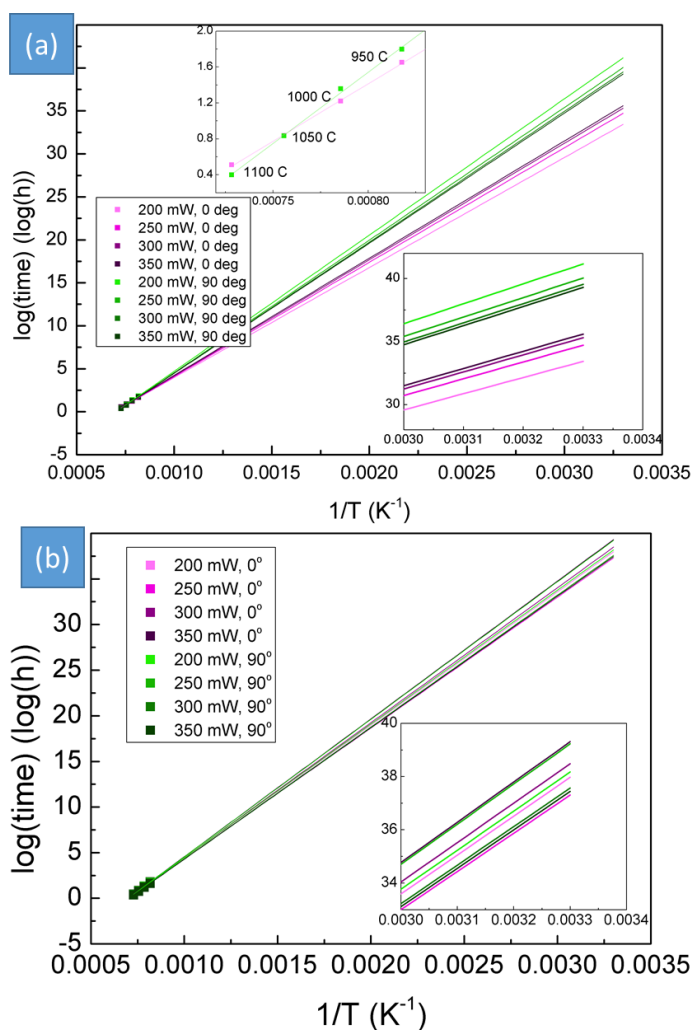


Figure 3-26. (a) Arrhenius plot of the laser induced nanograting for the lifetime of retardance value. Left inset illustrates the difference between two polarizations used for the femtosecond laser modification; right inset shows the zoomed in region of the Arrhenius plot at the room

temperature. (b) Arrhenius plot of the laser induced nanograting for the lifetime of scattering value.

The lifetimes of retardance value at the room temperature (30° C) of all 8 squares with four laser writing powers and two polarizations were extrapolated (Figure 3-26 (a)). The comparison of annealed retardance with scattering values and its extrapolation were performed. For the comparison, the scattering of the annealed samples was also measured using micro-spectroscopic system (CRAIG, Olympus BX51). No decay rate dependence on the wavelength was observed. Also, the Arrhenius plot for the scattering from 550 nm to 570 nm wavelength gives the lifetime without dependence on polarization state. Following the same procedure as for retardance, the Arrhenius plot for scattering value decay was extrapolated (Figure 3-26 (b)).

The obtained lifetime values both for retardance and scattering are significantly similar and at the room temperature were around 10^{34} years. Obviously such huge number (incomparably larger than the age of the universe) is unrealistic as the model does not take into account many external factors (temperature changes, radiation, physical impact, etc.) which could change over the long period of time. However this number tells that in practical applications we do not need to worry about the decay of the laser induced nanogratings. Also the comparison of lifetimes of different properties can provide useful information.

In the case of scattering there was no dependence on laser writing energy or polarization observed and estimated lifetimes of all 8 samples were close to the average value of $10^{34.23 \pm 0.41}$ years (Figure 3-26 (b) inset, Table 3-2). However laser power and polarization had strong influence on the lifetime of retardance value (as well as pulse duration, as structures fabricated with shorter pulse duration had shorter lifetime [70]). Depending on laser power and polarization, the predicted lifetime is in the range of 10^{29} to 10^{37} years (Table 3-1) with a clear difference for two polarizations (Figure 3-26 (a), inset). The retardance value before the annealing is higher for parallel polarization while the estimated lifetime at room temperature is at least 4 orders larger for perpendicular polarization. It shows that the strength of laser induced birefringence do not influence the lifetime of the structure. With the power increase the lifetime value for the parallel polarization increases while for

perpendicular decreases, asymptotically approaching $\sim 10^{34}$ years (similar to the lifetime of the scattering) at the room temperature (Table 3-1). As estimated average lifetimes of retardance and scattering values the same, it means that these parameters are closely related and caused by the same structural modification. Therefore, the scattering losses cannot be decreased by annealing without reducing the value of retardance.

Table 3-1 Retardance lifetime values at room temperature with its fitting parameters for all laser writing conditions.

Power (mW), polarization azimuth (°)	Retardance lifetime (year)	Activation energy (eV)	Frequency factor (MHz)
200 mW, 0°	$10^{29.49 \pm 0.66}$	2.54	0.187
250 mW, 0°	$10^{30.78 \pm 2.02}$	2.65	0.496
300 mW, 0°	$10^{31.37 \pm 0.69}$	2.69	0.689
350 mW, 0°	$10^{31.65 \pm 0.62}$	2.71	0.694
200 mW, 90°	$10^{37.23 \pm 1.37}$	3.15	38
250 mW, 90°	$10^{36.09 \pm 1.25}$	3.06	21.1
300 mW, 90°	$10^{35.59 \pm 1.34}$	3.02	14.8
350 mW, 90°	$10^{35.35 \pm 1.44}$	3.01	12.7

Table 3-2 Scattering lifetime values at room temperature with its fitting parameters for all laser writing conditions.

Power (mW), polarization azimuth (°)	Retardance lifetime (year)	Activation energy (eV)	Frequency factor (MHz)
200 mW, 0°	$10^{34.03 \pm 1.73}$	2.9	4.64
250 mW, 0°	$10^{33.36 \pm 1.37}$	2.85	2.93
300 mW, 0°	$10^{34.54 \pm 0.27}$	2.94	6.38
350 mW, 0°	$10^{35.27 \pm 0.49}$	3	9.95
200 mW, 90°	$10^{34.23 \pm 0.63}$	2.91	4.87
250 mW, 90°	$10^{35.29 \pm 0.5}$	2.99	9.63
300 mW, 90°	$10^{33.63 \pm 0.98}$	2.87	4
350 mW, 90°	$10^{33.5 \pm 0.98}$	2.86	3.9
Average 0°	$10^{34.29 \pm 0.27}$	2.92	5.27
Average 90°	$10^{34.17 \pm 0.59}$	2.91	5.21

Although the annealing cannot be used to reduce the scattering losses of the fabricated birefringent elements, it can be employed for the control of retardance magnitude. The set of lines was fabricated with the laser setup described before. Five identical samples were prepared using 700 fs pulses polarized perpendicular to the writing direction and focused in the bulk via a 0.16 NA objective lens; and using the laser power in the range of 200–400 mW. The writing speed was fixed to 0.2 mm/s. Four samples were annealed at 900 °C and 1050 °C for 1 and 4 hours while the left one was used as a non-annealed reference (Figure 3-27 (a)). The modified areas were optically characterized with the quantitative birefringence measurement system (CRi Abrio; Olympus BX51) operating at 546 nm wavelength.

Under the certain laser writing setup configuration the lowest power used in the experiment is close to the modification threshold. Therefore, the control of retardance at low values is very complicated. In order to reduce retardance, the power control alone is not enough. Other parameters such as focusing

conditions, writing speed or pulse duration should be changed. Another approach is the annealing procedure of post-fabricated birefringent element. For the processing conditions specified above, the retardance exhibited by the laser induced nanograting exceeds the value of 250 nm (above the measuring range of the Abrio). Depending on the annealing temperature and time, the retardance value was gradually reduced to ~ 60 nm (Figure 3-27 (b)). With such a process, any value down to zero can be achieved.

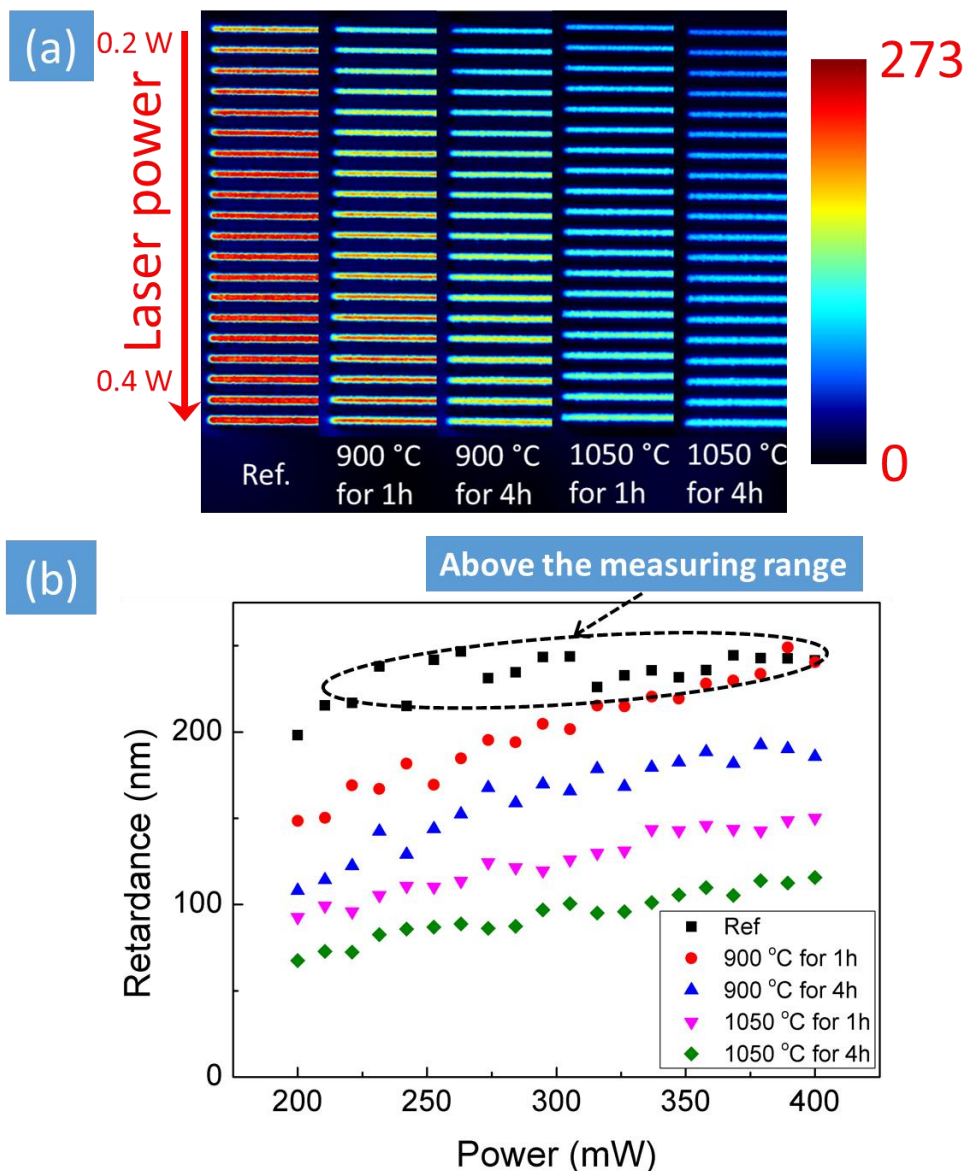


Figure 3-27 Annealing assisted control of laser induced retardance value: (a) microscopic birefringence images of laser written lines under various treatment conditions and (b) retardance value dependence on the average laser power and annealing conditions.

In order to monitor how the birefringent structure anneals at high temperatures, one side of the sample with the plane of nanogratings parallel to the written line was cut and lapped/polished in a way to reveal the cross section of nanograting. Surface imaging before and after the annealing process was performed with scanning electron microscope (SEM) Zeiss Evo ME15 (Figure 3-28). In addition, the transmission imaging was performed with optical microscope (OM) Olympus BX51 (Figure 3-28).

The study was carried out using scanning electron microscope operating in variable pressure/environmental scanning electron mode (VP-ESEM) collecting the luminescence signal by excitation-relaxation and electron-ion recombination of molecules in gaseous chamber [84]. Gas molecules are ionized via interaction with primary, backscattered and secondary electrons. After a short time, on nanoseconds scale, the excited molecules relax to the neutral ground state emitting photons. Such transition is caused by a short lifetime of the excited state and electron-ion recombination when the electrons emitted from the specimen or generated in the gas cascade are captured by ions. Due to strong electric field in the chamber, ionized gas molecules are attracted to the sample and recombined with the surface electrons mapping its insulator/conductor properties via a luminescence signal. The better insulator we have, the more electrons are built-up and the more electrons are emitted [84]. As a result, the regions with more constrained electrons in the VP-ESEM image appear brighter and vice versa.

Nanogratings were scanned with a high sub-30 nm resolution giving the grating nanoplanes as dark regions in non-annealed sample (Figure 3-28). However after the annealing at 900 °C for 1 h, the nanogratings in SEM imaging disappeared (Figure 3-28). The optical transmission images do not demonstrate the drastic change in its structure after the annealing process (Figure 3-28) as well as retardance measurements (Figure 3-26). This means that the annealing changes the modification in a way that it becomes invisible to the VP-ESEM imaging even though it barely changes optically. Knowing that the laser induced defects in SiO₂ matrix annihilate at high temperatures [54], we attribute these oxygen deficient regions as the basis for the observed surface conductivity map.

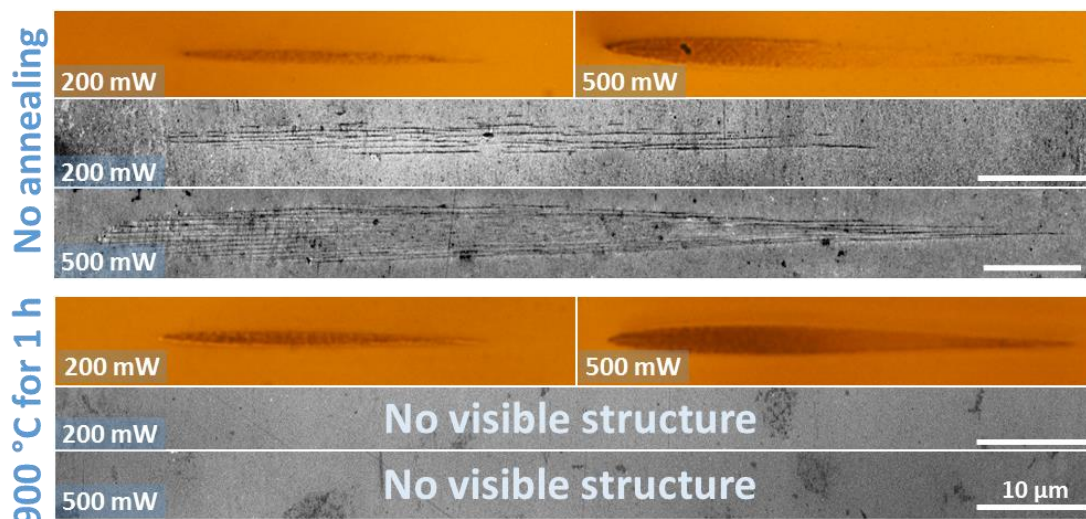


Figure 3-28 Optical and SEM images of the cross-sectioned laser tracks before and after the annealing procedure at 900 °C for 1 hour. Annealed structures could not be imaged by SEM.

To be sure that the laser induced structure remains after the annealing process, the etching procedure before SEM imaging was performed. Both the annealed and not-annealed nanogratings after 24 h etching in potassium hydroxide (KOH, 1 mol/L, 20 °C) is revealed giving the inverted conductivity map (Figure 3-29). The tendency of electrons to localize in the higher density at the surface edges of etched grooves causes the electrons build-up. Therefore, in the etched samples the nanoplanes are displayed bright and the imaging corresponds to the surface topography rather than defects mapping like in Figure 3-28. The annealed structures are less visible in comparison to the non-annealed. The ongoing etching of the annealed sample is determined by the remained $\equiv\text{Si-Si}\equiv$ defects and almost unaffected by the structural morphology [etching paper Ref.]. At the initial stage of annealing process the laser induced defects annihilate leading to the conductivity contrast and etching selectivity decrease while at the further stage the annihilation of laser induced morphological change takes part. This can also explained the retardance decay process which is composed of two independent fast and slow decay components (Figure 3-24). Fast decay component of retardance is related to the annealing of laser induced defects and the laser induced morphological change corresponds to the slow decay component.

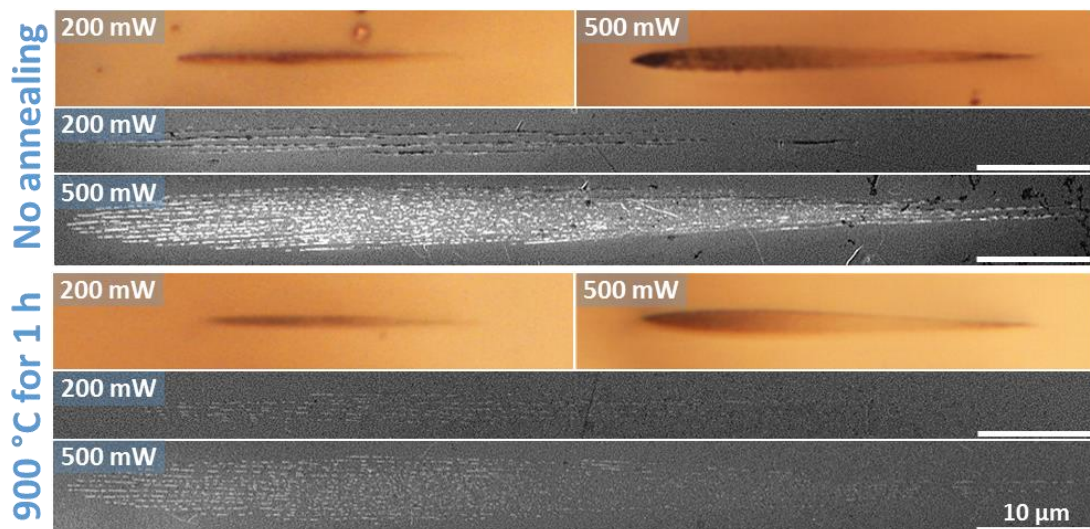


Figure 3-29 Optical and SEM images of the cross-sectioned and etched (KOH, 1 mol/L, 20 °C, 24 h) laser tracks before and after the annealing procedure at 900 °C for 1 hour.

In conclusion, by annealing laser fabricated structures, we estimated the lifetime of the laser induced nanogratings which is around 10^{34} years at the room temperature (pulse duration of the laser is 700 fs). Even though the number is too large to be realistic, it tells that modifications are extremely stable. The same estimated lifetimes of retardance and scattering values indicates that parameters closely related and annealing cannot eliminate scattering without erasing birefringence. Also we demonstrated the ability retardance control by annealing fabricated sample which has advantage over changing power during laser fabrication.

Chapter 4: Applications of nanogratings

In this chapter I will talk about application of nanogratings. In the previous Chapter it was demonstrated that femtosecond laser induced nanogratings in silica glass can exhibit strong birefringence and structures can be fabricated at high speed. This leads to ability of polarization sensitive optical elements fabrication.

Firstly I will discuss about fabrication of polarization converters for generating cylindrical vector beams. This work was started by Martynas Beresna and some parts was already discussed in his doctoral thesis [85]. However I will concentrate more on the modelling part of the beams generated by polarization converters, fabrication of the converters for higher order cylindrical vector beams converter and converters for different wavelengths. Also generated beams were used for laser modification and results will be compared with theoretical model. Next, I will demonstrate that our introduced polarization converters can be also used for optical vortices with tuneable orbital angular momentum generation which can be used in laser trapping experiments.

Birefringence can be used not only for polarization control, but also for phase control of light. Which means that optical elements based on nanogratings can be used to generate special beam instead of phase masks or SLMs. Airy and Bessel beams are generated by converters fabricated with femtosecond laser. I will compare properties of the obtained beams with theoretical modelling which will confirm good performance of converters. Also generated Airy beam is used for material modification.

And finally femtosecond laser induced nanogratings can be used for measurements of state of polarization. Micro waveplates array is fabricated and used for real time full polarization imaging.

4.1 Introduction to the cylindrical vector beams

Polarization is one of the most important feature of light. Most past research dealt with spatially homogeneous states of polarization (SOPs), such as linear, circular and elliptical polarizations. But recently there has been increasing interest in light beams with space varying SOP. One particular example is laser beams with cylindrical symmetry in polarization, the so-called cylindrical vector (CV) beams.

Recently, CV beams have attracted significant recent attention largely due to their unique properties observed under high-numerical-aperture (NA) focusing. Numerical calculations have shown that tighter focus spots can be obtained using radial polarization, a subset of CV beams, caused by strong and localized longitudinal field component [86]. Such an effect has been experimentally confirmed by several groups [87,88] and already found numerous applications in high resolution imaging such as confocal microscopy, two-photon microscopy, second-harmonic generation microscopy [89], third-harmonic generation microscopy [90] and dark field imaging [91]. Radial polarization also can be used as an ideal source for surface plasmon excitation with axially symmetric metal/dielectric structures [92], because plasmon excitation has a strong dependence on excitation polarization.

CV beam also can be used for three-dimensional focus engineering. By controlling polarization azimuthal angle φ_0 from the radial direction, it is possible to create focal field with a transverse flat-top profile [93]. Introducing pupil plane phase or amplitude mask provides additional degrees of freedom and enables extra focal field profile control and highly homogeneous field distribution in three dimensions can be generated [94]. Even more exotic focal field distributions, such as an optical “bubble” [94] or optical “needle” [95] can be generated.

There are few methods of generating cylindrical vector beams. Depending on whether the generation methods involve amplifying media, they can be categorized as active or passive. Typically, active methods involve the use of

laser intracavity devices that force the laser to oscillate in CV modes [96,97]. Major disadvantage of active generation is the need for special laser with a specific laser mode.

More convenient ways to generate CV beams is passive methods. In general, these methods convert spatially homogeneous polarization (typically linear or circular polarization) into spatially inhomogeneous CV polarizations. Typically, devices with spatially variant polarization properties are normally required. In this case, setups with a radial analyser made either from birefringent materials [98] or from dichroic materials [99] can be used to generate CV beams. Another very popular passive method employs a LC SLM (liquid crystal spatial light modulator), which enables to generate almost arbitrary complex field distribution. On the other hand, these methods require big and complicated setups, suffer high losses and, in particular, LC has low damage threshold and high price.

Converter from linear to CV polarization can be made by gluing several segments of $\lambda/2$ phase wave-plates with different discrete crystal [100]. Because of the discreteness, this type of device provides only rough spatial alignment of the polarization. With lithographic methods, form birefringence of the subwavelength gratings can be induced. The local orientation of retardance can continuously vary through lithographic patterning and good spatial alignment of polarization can be achieved [101]. However, owing to the requirement of a subwavelength period, these devices can be fabricated for far infrared but extension into the near infrared and visible would be difficult. Also this method is time consuming. Later in this chapter I will discuss about the use of femtosecond laser induced nanogratings for making polarization converters which allow generating CV beams [67,74].

The cylindrical vector (CV) beams are vector-beam solutions of Maxwell's equations that obey axial symmetry in both amplitude and phase [102,103]. Comparison of spatially homogeneous state of polarization beams (SOP) beams and CV beams are illustrated in Figure 4-1. Spatially homogeneous SOPs modes have instantaneous electric field, which may have an opposite direction due to inhomogeneous phase distribution across the beam. Typical CV beams cases

are shown in Figure 4-1 (g)-(i). When polarization of a beam is aligned in radially direction, it is called radial polarization. Similarly, azimuthal polarization is shown in Figure 4-1 (h). A linear superposition of these two modes can produce beam with even more complex polarization distribution as shown in Figure 4-1 (i).

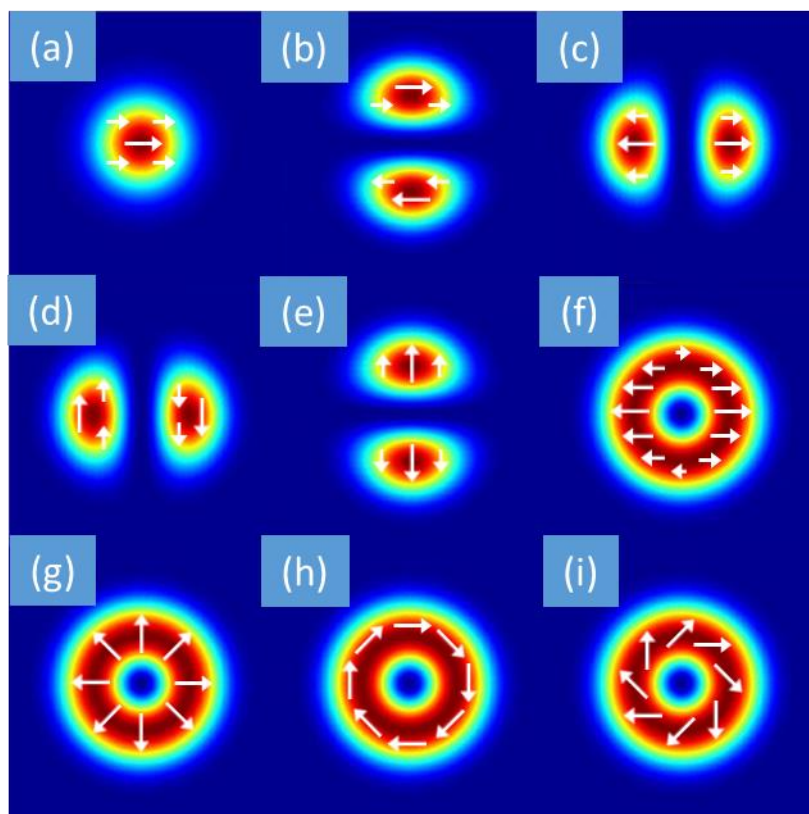


Figure 4-1 Spatial distribution of intensity and vector field for several spatially homogeneous SOP and CV beam modes: (a) x-polarized fundamental Gaussian mode; (b) x-polarized HG_{01} mode; (c) x-polarized HG_{10} mode; (d) y-polarized HG_{10} mode; (e) y-polarized HG_{01} mode; (f) x-polarized LG_{01} mode (vortex); (g) radially polarized mode; (h) azimuthally polarized mode; (i) linear superposition of (g) and (h).

The solutions for the spatially homogeneous SOP beams are obtained by solving the scalar Helmholtz equation:

$$(\nabla^2 + k^2)E = 0, \quad (4-1)$$

where k is the wave number. In Cartesian coordinates, the general solution for the electric field has a form

$$E(x, y, z, t) = u(x, y, z)e^{i(kz - \omega t)}. \quad (4-2)$$

For slowly varying envelope approximation, the Hermite-Gauss modes (HG_{mn}) solution can be obtained [103]:

$$\begin{aligned} u(x, y, z) \\ = E_0 H_m \left(\sqrt{2} \frac{x}{w(z)} \right) H_n \left(\sqrt{2} \frac{y}{w(z)} \right) \frac{w_0}{w(z)} e^{-i\varphi_{nm}(z)} e^{i \frac{k}{2q(z)} r^2}, \end{aligned} \quad (4-3)$$

where $H_m(x)$ denotes Hermite polynomials, E_0 is a constant electric field amplitude, $w(z)$ is the beam size, w_0 is the beam size at the beam waist, z_0 is the Rayleigh range, $q(z)$ is complex beam parameter and $\varphi_{mn}(z)$ is the Gouy phase shift.

The general solution in cylindrical coordinates is [103]

$$E(r, \phi, z, t) = u(r, \phi, z)e^{i(kz - \omega t)}. \quad (4-4)$$

Substituting Equation (4-4) to (4-1) and applying the slowly varying envelope approximation we get differential equation [103]

$$\frac{1}{r} \frac{\partial}{\partial r} \left(r \frac{\partial}{\partial r} \right) + \frac{1}{r^2} \frac{\partial^2}{\partial \phi^2} + 2ik \frac{\partial u}{\partial z} = 0. \quad (4-5)$$

From this equation two solutions can be found. The first solution describes Laguerre-Gauss modes (LG_{pl}) [103]

$$u(r, \phi, z) = E_0 \left(\sqrt{2} \frac{r}{w(z)} \right)^l L_p^l \left(2 \frac{r^2}{w(z)^2} \right) e^{-i\varphi_{pl}(z)} e^{i \frac{k}{2q(z)} r^2} e^{il\phi}, \quad (4-6)$$

where L_p^l is the Laguerre polynomials (l – azimuthal index, p – radial index) and $\varphi_{pl}(z)$ is the Gouy phase shift. The second solution is independent of the azimuthal angle ϕ and describes Bessel-Gauss beams [103]:

$$u(r, z) = E_0 \frac{w_0}{w(z)} e^{-i\varphi(z)} e^{i\frac{k}{2q(z)}r^2} J_0\left(\frac{\beta r}{1 + iz/z_0}\right) e^{-\frac{\beta^2 z}{2k(1+iz/z_0)}}, \quad (4-7)$$

where β is a constant scale parameter, $\varphi(z)$ is the Gouy phase shift and $J_0(x)$ is the zeroth-order Bessel function of the first kind.

Those three solutions (Hermite-Gauss, Laguerre-Gauss and Bessel-Gauss) correspond to beams with spatially homogeneous polarization. However, solution for vector beam can be found by solving full vector wave equation for the electric field [103]:

$$\nabla \times \nabla \times \vec{E} - k^2 \vec{E} = 0. \quad (4-8)$$

Consider a circularly symmetric, azimuthally polarized field [103]

$$\vec{E}(r, z) = U(r, z) e^{i(kz - \omega t)} \vec{e}_{\phi_0}, \quad (4-9)$$

where \vec{e}_{ϕ_0} is the unit vector in the azimuthal direction. $U(r, z)$ satisfies the following equation [103]:

$$\frac{1}{r} \frac{\partial}{\partial r} \left(r \frac{\partial U}{\partial r} \right) - \frac{U}{r^2} + 2ik \frac{\partial U}{\partial z} = 0. \quad (4-10)$$

There is a clear difference between the second terms of equations (4-5) and (4-10). The solution of this equation corresponds to an azimuthally polarized vector Bessel-Gauss beam [103]:

$$\begin{aligned} & \vec{E}(r, z) \\ &= -E_0 J_1 \left(\frac{\beta r}{1 + \frac{iz}{z_0}} \right) e^{-\frac{\beta^2 z}{2k(1+iz/z_0)}} \frac{w_0}{w(z)} e^{-i\varphi} e^{i\frac{k}{2q(z)}r^2} e^{i(kz - \omega t)} \vec{e}_{\phi_0}. \end{aligned} \quad (4-11)$$

Instead of the vector Bessel-Gauss solutions, in many applications simplified distribution can be used [103]:

$$\vec{E}(r, z) = A r e^{-\frac{r^2}{w^2}} \vec{e}_{r, \phi}. \quad (4-12)$$

The profile of amplitude is the same like in LG01 mode and without the vortex phase term $\exp(i\phi)$. Alternatively, CV beams can be described as a superposition of orthogonally polarized Hermite-Gauss HG_{01} and HG_{10} modes. For instance, radially polarized beam in such a way can be expressed as (Figure 4-2) [103]

$$\vec{E}_r = HG_{10} \vec{e}_x + HG_{01} \vec{e}_y. \quad (4-13)$$

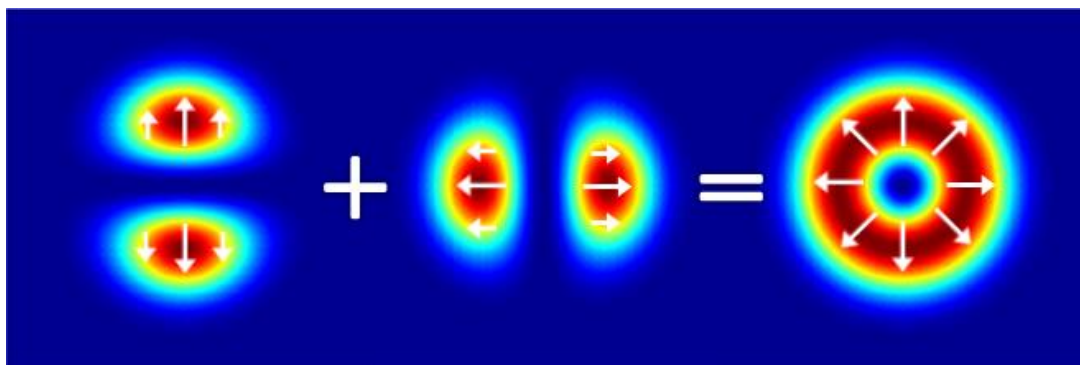


Figure 4-2 Radial polarization as superposition of orthogonally polarized HG modes.

4.2 Cylindrical vector beams with orbital angular momentum

As nanogratings exhibit form birefringence, polarization converters for cylindrical vector beams generation can be fabricated in SiO_2 glass by femtosecond laser. Polarization converters can be designed for incident beams with linear or circular polarization. Let us start from radial/azimuthal polarization converters designed for circular polarization as they require lower retardance induced by the laser (quarter-wave). In such converter, the radial or azimuthal polarization (or other polarization distribution) can be formed with a space variant quarter-wave plate with radial symmetry (Figure 4-3 (a)). Circularly polarized beam after passing through such optical element becomes radially or azimuthally polarized (depending on the handedness of the circular polarization) (Figure 4-3 (b), (c)).

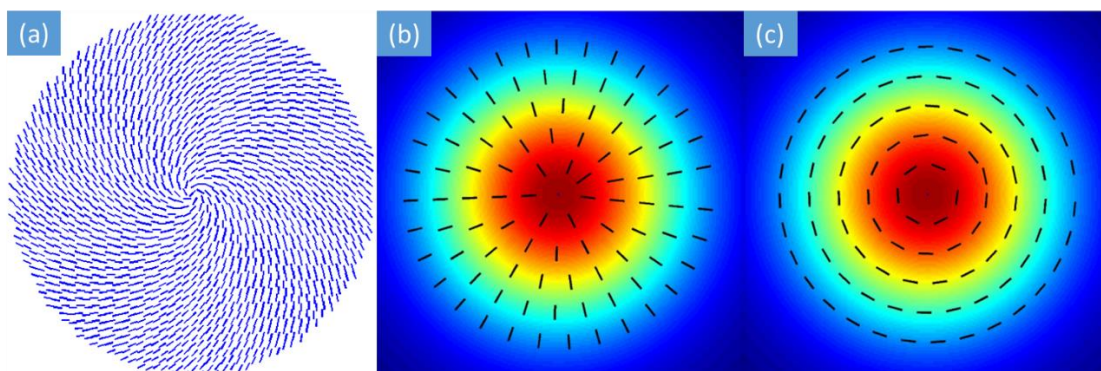


Figure 4-3 (a) Schematic drawing of nanograting distribution in radial/azimuthal polarization converter for circular input polarization. (b) and (c) Distribution of electric field polarization for left-hand and right-hand circularly polarized input beam after passing through the converter.

For the mathematical description of the polarization converter, Jones calculus can be used. To get a Jones matrix describing a space variant quarter-wave plate, we take matrix representing conventional quarter-wave plate (oriented at 0°):

$$M_q = \begin{pmatrix} 1 & 0 \\ 0 & i \end{pmatrix}. \quad (4-14)$$

and rotate it around the axis by the angle $\theta = \phi + \frac{\pi}{4}$ (ϕ is polar angle) applying rotation transformation:

$$M(\theta) = R(-\theta)MR(\theta). \quad (4-15)$$

where R is the rotation matrix

$$R = \begin{pmatrix} \cos(\theta) & \sin(\theta) \\ -\sin(\theta) & \cos(\theta) \end{pmatrix}. \quad (4-16)$$

Substituting equations (4-14) and (4-16) to (4-15) we get mathematical representation for quarter-wave polarization converter in Figure 4-3 (a):

$$M_{qwc} = \begin{pmatrix} \cos^2 \theta + i \sin^2 \theta & (1-i) \cos \theta \sin \theta \\ (1-i) \cos \theta \sin \theta & i \cos^2 \theta + \sin^2 \theta \end{pmatrix}. \quad (4-17)$$

Now let us assume that beam with left-handed circular polarization is passing through this converter. After multiplying the Jones vector describing the left handed circular polarization $Q_L = \frac{1}{\sqrt{2}} \begin{pmatrix} 1 \\ i \end{pmatrix}$ by the matrix M_{qwc} we get

$$E_{AZV} = M_{qwc}Q_L = \begin{pmatrix} -\sin \phi \\ \cos \phi \end{pmatrix} e^{i\phi} e^{i\pi/4}. \quad (4-18)$$

The first term of calculated electric field represents azimuthal orientation of polarization (Figure 4-3 (c)). The term $e^{i\phi}$ indicates the presence of orbital angular momentum $l = 1$. If the input beam has right-handed circular polarization ($Q_R = \frac{1}{\sqrt{2}} \begin{pmatrix} 1 \\ -i \end{pmatrix}$), then after the converter we have radially polarized (Figure 4-3 (b)) optical vortex with the orbital angular momentum $l = -1$:

$$E_{RadV} = M_{qwc}Q_R = \begin{pmatrix} \cos \phi \\ \sin \phi \end{pmatrix} e^{-i\phi} e^{i\pi/4}. \quad (4-19)$$

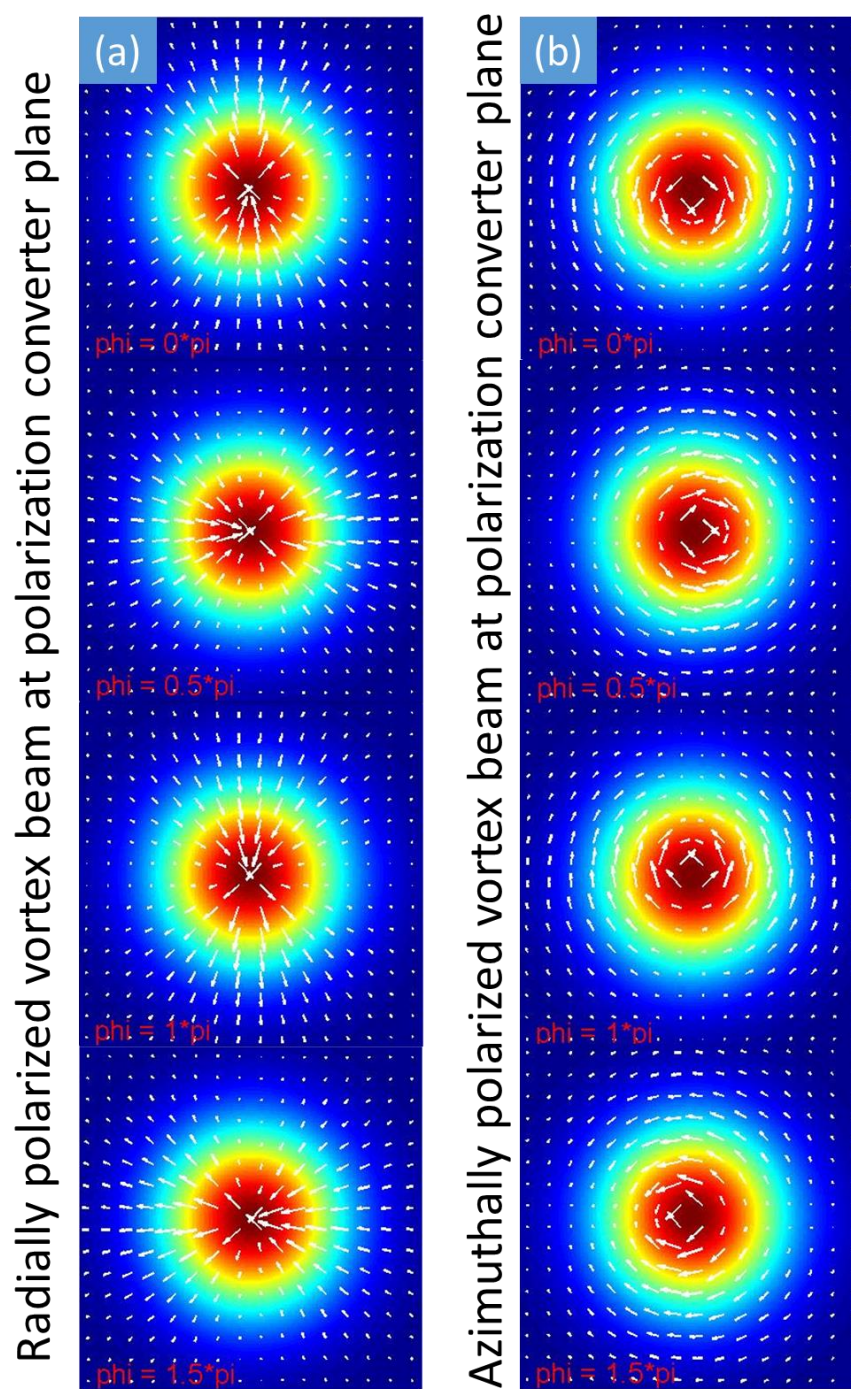


Figure 4-4 The modelling of radially and azimuthally polarized vortex beams generated by quarter-wave polarization converter. Intensity and polarization distribution is modelled at the plane of the converter. The length of arrows indicates the strength instant electric field and the orientation - the direction of the polarization.

As we can see from Equations (4-18) and (4-19), not only polarization direction is modulated of the beam by the quarter-wave polarization converter, but also the phase and therefore we get radially/azimuthally polarized optical vortex. In order to get pure radial or azimuthal polarization, half-wave polarization converter is required, which will be discussed later in this chapter.

In order to see visually the distribution of the polarization orientation and how such beams propagates, the modelling using MATLAB was performed. The basic code of the developed program can be found in the Appendix B. The circularly polarized Gaussian beam of radius $w_0 = 300 \mu m$ and wavelength $\lambda = 512 nm$, was simulated to pass the quarter-wave polarization converter. The intensity and polarization distribution was calculated at the plane of the converter (Figure 4-4).

Even though the polarization distribution is radial (Figure 4-4 (a)) or azimuthal (Figure 4-4 (b)) but due to phase helicity $l = 1$, the electric field at opposite sides of the beam are pointing at the same direction. For example in the case of pure radially/azimuthally polarized beam at any given moment, the electric vectors at opposite sides of the beam would point to the opposite directions. For this reason in the centre of the beam the direction of the electric field is undefined and therefore during the propagation the shape of radially/azimuthally polarized beam would develop to the donut-like shape. However in the case of radially/azimuthally polarized vortex beam with helicity $l = 1$ the electric field in the centre of the beam is defined (Figure 4-4). Also such beam under the tight focusing would not have z component as the pure radially polarized beam.

The propagation of the radially polarized vortex beam was modelled. For modelling the beam propagation the method called Fourier propagation was used. This method can be used for the modelling of propagation and diffraction through thin amplitude and phase elements situated in homogeneous free space.

Let us consider the propagation of field $U(x, y, z)$ along the z axis. The wavenumber of the field is $k = 2\pi/\lambda$. The 2-D Fourier representation of $U(x,$

$y, 0)$ at the initial point $z = 0$ is given in terms of its Fourier transform $A(k_x, k_y, 0)$ by

$$U(x, y, 0) = \iint_{-\infty}^{\infty} A(k_x, k_y, 0) e^{i(k_x x + k_y y)} dk_x dk_y, \quad (4-20)$$

where

$$A(k_x, k_y, 0) = \iint_{-\infty}^{\infty} U(x, y, 0) e^{-i(k_x x + k_y y)} dx dy, \quad (4-21)$$

$A(k_x, k_y, 0)$ is called the angular spectrum of $U(x, y, 0)$. Now consider the wave field at a position z :

$$U(x, y, z) = \iint_{-\infty}^{\infty} A(k_x, k_y, z) e^{i(k_x x + k_y y)} dk_x dk_y, \quad (4-22)$$

and its angular spectrum

$$A(k_x, k_y, z) = \iint_{-\infty}^{\infty} U(x, y, z) e^{-i(k_x x + k_y y)} dx dy. \quad (4-23)$$

$U(x, y, z)$ satisfies the Helmholtz equation at all points without sources:

$$\nabla^2 U(x, y, z) + k^2 U(x, y, z) = 0. \quad (4-24)$$

Substitution of equation (4-22) into (4-24) gives an equation

$$\iint_{-\infty}^{\infty} \left[\frac{d^2}{dz^2} A(k_x, k_y, z) + (k^2 - (k_x^2 + k_y^2)) A(k_x, k_y, z) \right] e^{i(k_x x + k_y y)} = 0. \quad (4-25)$$

This is true for all waves only if the integrand is zero:

$$\frac{d^2}{dz^2} A(k_x, k_y, z) + (k^2 - (k_x^2 + k_y^2)) A(k_x, k_y, z) = 0. \quad (4-26)$$

This differential equation has a solution

$$A(k_x, k_y, z) = A(k_x, k_y, 0)e^{ik_z z} = A(k_x, k_y, 0)e^{i(\sqrt{k^2 - k_x^2 - k_y^2})z}. \quad (4-27)$$

If $k_x^2 + k_y^2 < k^2$ then k_z is real and each spectrum component is just modified by a phase factor $e^{ik_z z}$. Such waves are known as homogeneous waves.

If $k_x^2 + k_y^2 > k^2$ then k_z is imaginary and that indicates that the amplitudes of such plane wave components are strongly attenuated by propagation along the z axis. Such waves are called evanescent waves.

If $k_x^2 + k_y^2 = k^2$ then $A(k_x, k_y, z) = A(k_x, k_y, 0)$ and that indicated wave propagation along direction perpendicular to z axis.

From equations (4-21), (4-22) and (4-25) we can write an algorithm to find electric field $U(x, y, z)$ by knowing it at initial point $z = 0$:

$$U(x, y, z) = F_{2D}^{-1}[F_{2D}[U(x, y, 0)e^{ik_z(k, k_x, k_y)z}], \quad (4-28)$$

where F_{2D} and F_{2D}^{-1} is 2D Fourier transform and 2D inversed Fourier transform respectively. The limits of integration in equation (26) can be limited to a circular region given by

$$k_x^2 + k_y^2 \leq k^2, \quad (4-29)$$

provided that the distance z is at least several wavelength and evanescent wave can be ignored.

The MATLAB code for the Fourier propagation can be found in the Appendix B. The intensity distribution of the radially polarized vortex beam was calculated at the different distances (0 mm, 10 mm, 25 mm, 50 mm, 100 mm, 250 mm) after the polarization converter (Figure 4-5 (a)). Also intensity profiles after inserting linear polarizer are calculated which have “s” shape. Such “s” shape

can be simple experimental clue that the cylindrical vector beam has phase helicity.

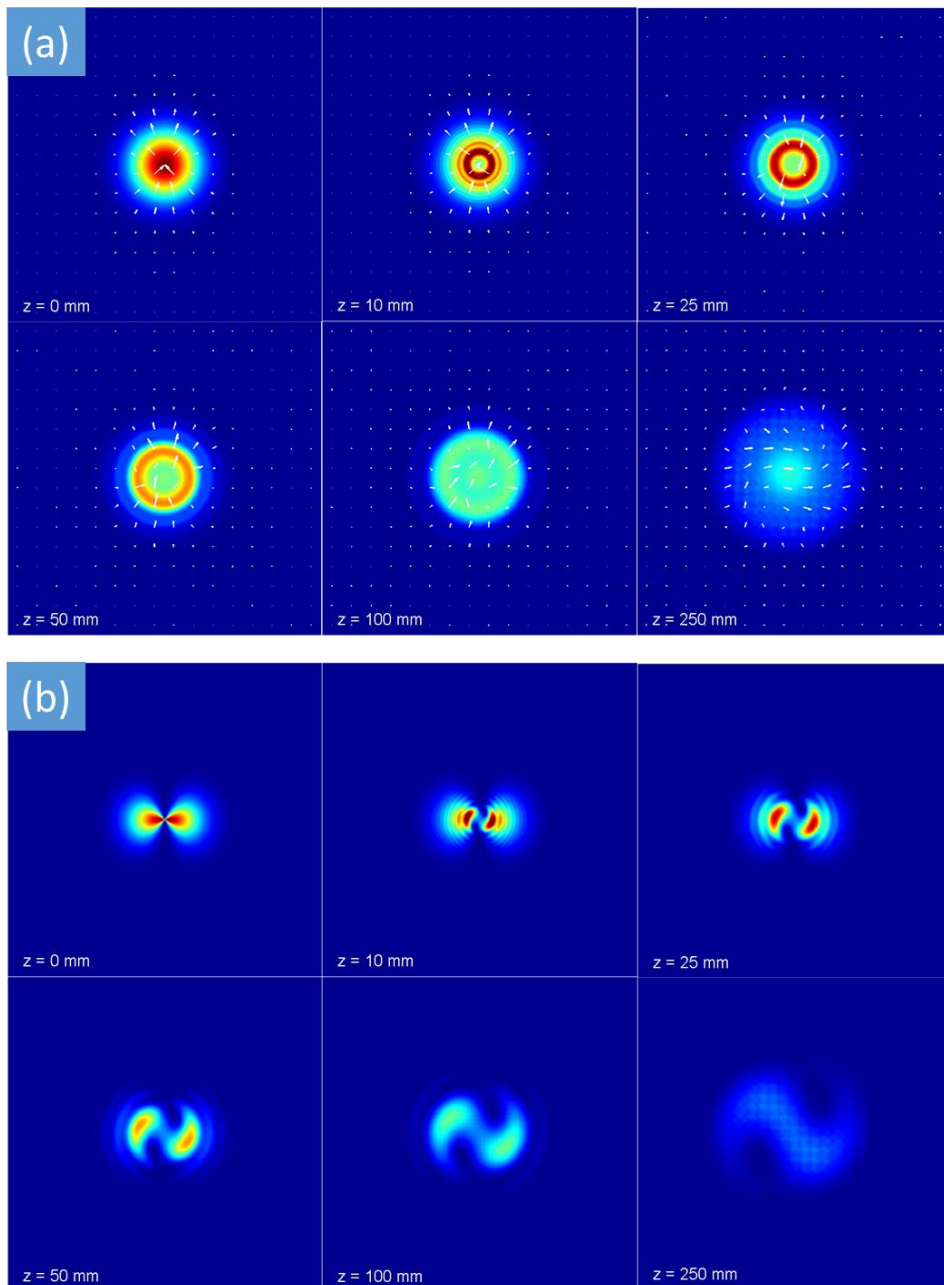


Figure 4-5 (a) The modelling of the propagation of radially polarized vortex beam. (b) The propagation of the same beam when linear polarizer (transmission axis is at 0° angle with the x axis) is inserted after the polarization converter.

The modelling shows that the shape of the beam does not develop to the eigenmode during its propagation and after some propagation the distribution of the polarization cannot be longer treated as radial. This can be explained by the fact that such beam is the superposition of two eigenmodes. Let us look again at the Equation (4-19). After some algebraic transformations, we can get the equation to the form

$$E_{RadV} = \begin{pmatrix} \cos \phi \\ \sin \phi \end{pmatrix} e^{-i\phi} = \begin{pmatrix} i(e^{i\phi} + e^{-i\phi}) \\ e^{i\phi} - e^{-i\phi} \end{pmatrix} e^{-i\phi} \quad (4-30)$$

$$= \frac{1}{2} \left[\begin{pmatrix} 1 \\ -i \end{pmatrix} e^{-2\phi} + \begin{pmatrix} 1 \\ i \end{pmatrix} \right].$$

This equation represents two circularly polarized fields with opposite handedness of circular polarization and one field of the fields has phase helicity $l = -2$. In other words this beam consists of two eigenmode beams: left handed circularly polarized Gaussian beam and right handed circularly polarized Laguerre-Gaussian beam LG_{20} (optical vortex with $l = 2$). Such definition of the beam generated by the quarter-wave polarization converter is more correct as in far field will not have radial distribution of the polarization but rather two circularly polarized beams with opposite handedness.

Now let us move to the experimental part of quarter-wave polarization converter fabrication and cylindrical vector beams generation. The fabrication of the polarization converter was performed with laser system described in the paragraph 3.1. As it was mentioned before, the optimum values for the average laser power, repetition rate and writing speed required to achieve quarter-wave retardance at 532 nm wavelength, were found to be 140 mW, 200 kHz and 1 mm/s, respectively. The distance between fabricated adjacent lines is 1 μm . The laser beam was focused 200 μm below the surface of a fused silica sample via low numerical aperture objective (Nacht, 20 \times , NA = 0.35).

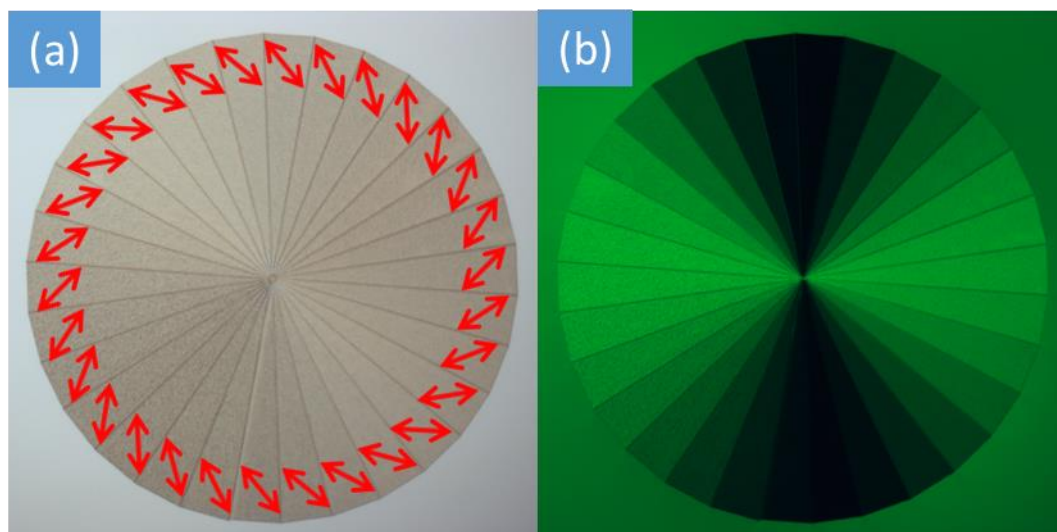


Figure 4-6 Microscope images of the polarization converter in the bright field (a) and crossed polarizers (b) (circular polariser and linear polariser). The diameter of the structure is 1.2 mm. The radial lines emerging from the centre of the structure are due to finite step size in the writing process, which results in the visible segmentation of the structure. Red arrow indicates the writing laser polarization.

The laser beam polarization angle was controlled by an achromatic half wave plate mounted on a motorized rotation stage. By controlling the angle of the half wave plate and XY stage position we could fabricate a space-variant quarter-wave plate with the geometry described by Equation (4-17). The microscopic image of fabricated structure is demonstrated in Figure 4-6 (a). The diameter of the converter was 1.2 mm and it took around 1.5 h to fabricate it. During first experiments, there was no ability to synchronize the rotation stage (rotating the half-wave plate) with the linear XYZ stage so polarization could not be changed gradually. For this reason the disc of the converter was divided into $n = 30$ segments and each segment was fabricated with different laser polarization. The difference in the azimuth of polarization for the adjacent segments is $360^\circ/n$ (Figure 4-6 (a)).

To verify presence of radial/azimuthal polarization, the converter was illuminated under a microscope with circularly polarized green light (546 nm)

and imaged under a microscope with linear polarizer (analyser) inserted at the output. The propeller shape typical for radial/azimuthal polarization was clearly observed (Figure 4-6 (b)), confirming the successful implementation of the polarization converter.

The fabricated birefringent element was also analysed with a birefringence measurement system Abrio. Measurements confirmed that the constant value of retardance (Figure 4-7 (a, b)) with a continuously varying direction of slow axis was achieved (Figure 4-7 (c, d)).

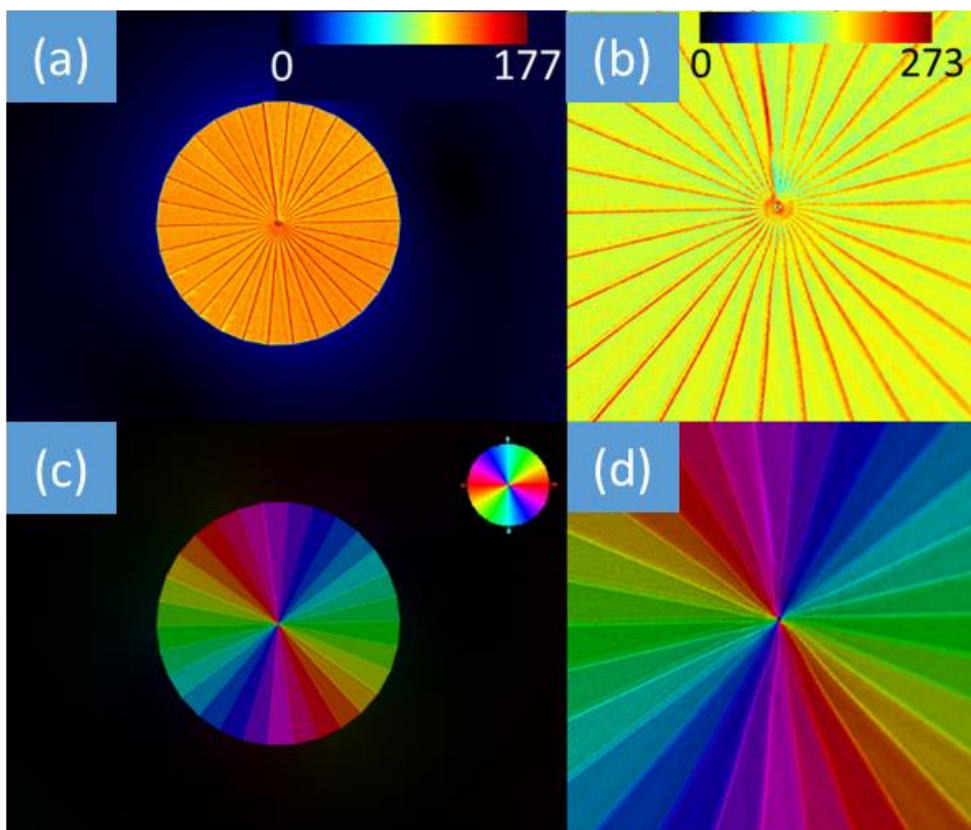


Figure 4-7 Birefringence characterization of the structure performed with the Abrio system. The (a) and (b) images represent retardance value distribution with 5 \times (a) and 20 \times (b) magnification of the structure. The (c) and (d) images represents the color-coded distribution of slow axis.

The polarization converter was also tested with second harmonic (532 nm) from a continuous-wave (cw) Nd:YAG laser (Figure 4-8 (a)). The linear polarization of the laser beam was converted into circular with a quarter-wave plate and then launched through the polarization converter. The converted beam was imaged with beam profiler (Figure 4-8 (b)). Acquired beam's profiles were similar to the modelled ones (Figure 4-5 (a)).

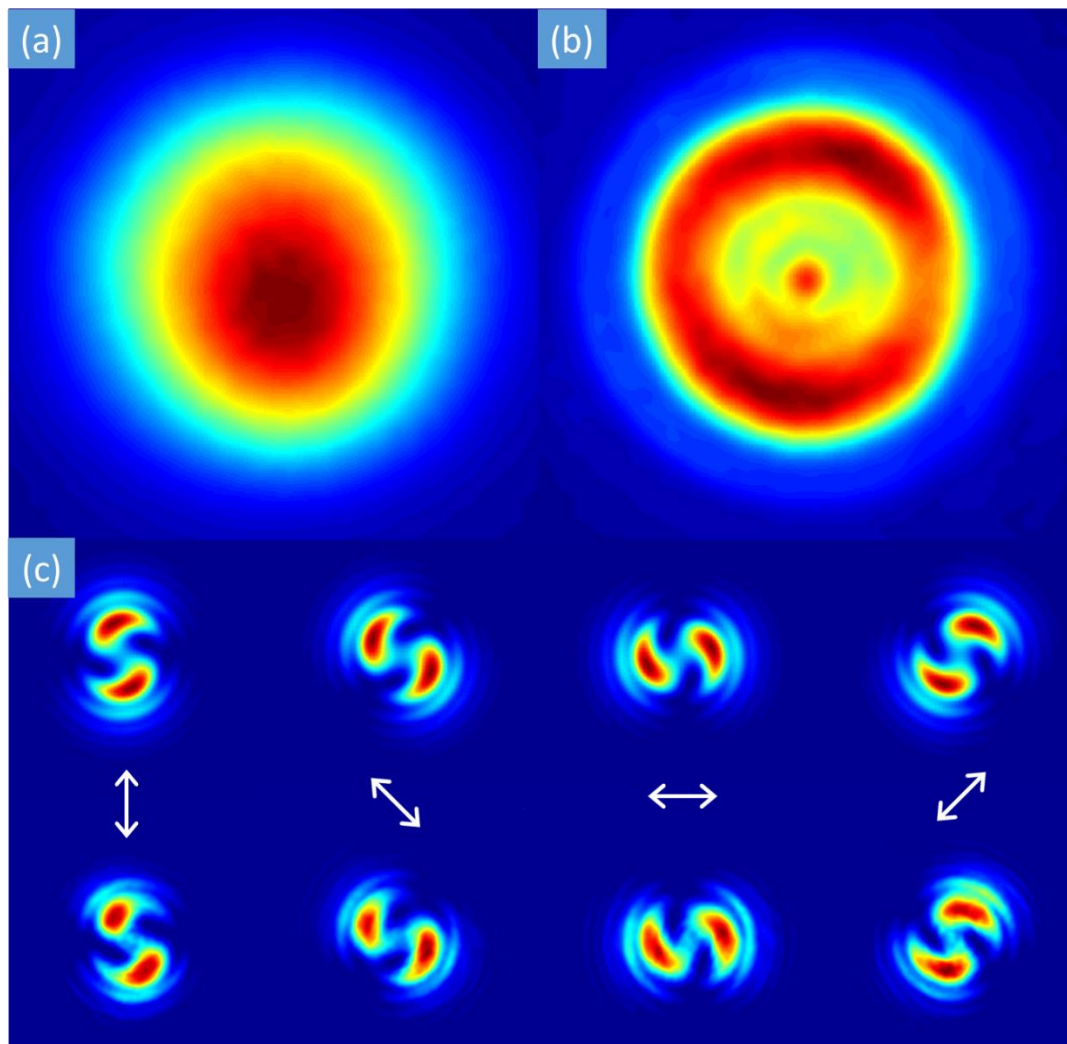


Figure 4-8 Measured beam profiles of second harmonic of cw Nd:YAG laser before (a) and after (b) beam converter. (c) Modelled and measured beam profile after inserting linear polarized at angles 0° , 45° , 90° , 135° . White arrows indicate the orientation of the polarizer's transmission axis.

To analyse converted beam, linear polarizer (analyser) was inserted after the converter. The analyser was set to four different angles (0° , 45° , 90° and 135°), at which profiles of the beam were captured (Figure 4-8 (c)). As the two lobes in the measured beams oriented in parallel to the orientation of the analysers transmission axis, this shows that the distribution of the polarization is radial. Measured beam profiles matched well with modelled ones.

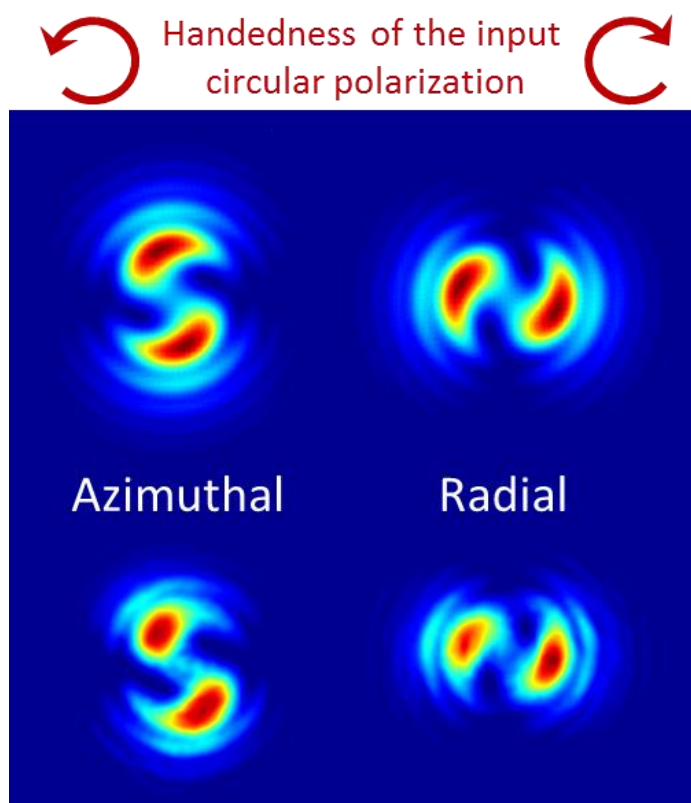


Figure 4-9 Modelled and measured patterns of optical vortices with azimuthal and radial polarization after linear polarizer (horizontal orientation). White arrows indicate incident polarization state.

In Equation (4-18) and (4-19) we can see that the handedness of the input circular polarization defines not just radial or azimuthal distribution of the polarization, but also the sign of the orbital angular momentum. The theoretical prediction of the dependence of orbital angular momentum sign on the handedness of incident circular polarization was also experimentally confirmed by comparing the radially and azimuthally polarized beams (with

linear polarizer inserted after the converter where transmission axis of the polarizer is horizontal) produced by incident left- and right-handed circular polarizations (Figure 4-9). As it was demonstrated in Equation (4-30), the beam can be separated into two circularly polarized beams (Gaussian and second order vortex beams) with opposite handedness. The linear polarizer changes the polarization of both beams to linear which allows them to interfere. The interference pattern of Gaussian beam with second order vortex beam (when they are parallel to each other) has “s” shape. The orientation of the “s” shape were changing with the handedness of the input circular polarization which indicates the change of the sign of the orbital angular momentum. In other words we can say that the converter transforms spin angular momentum of the beam to the orbital angular momentum (Spin to orbital conversion of the angular momentum [104,105]).

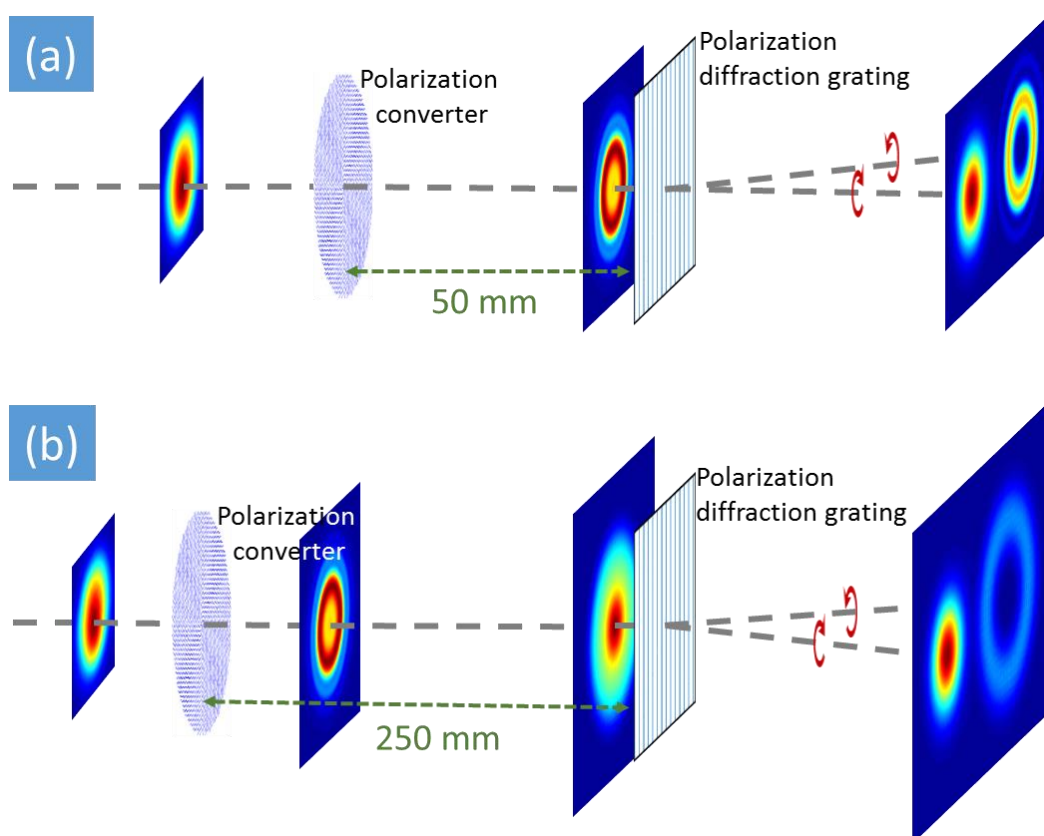


Figure 4-10 Propagation of radially polarized optical vortex beam through the polarization diffraction grating. Polarization diffraction grating separates beams with opposite handedness of circular polarization.

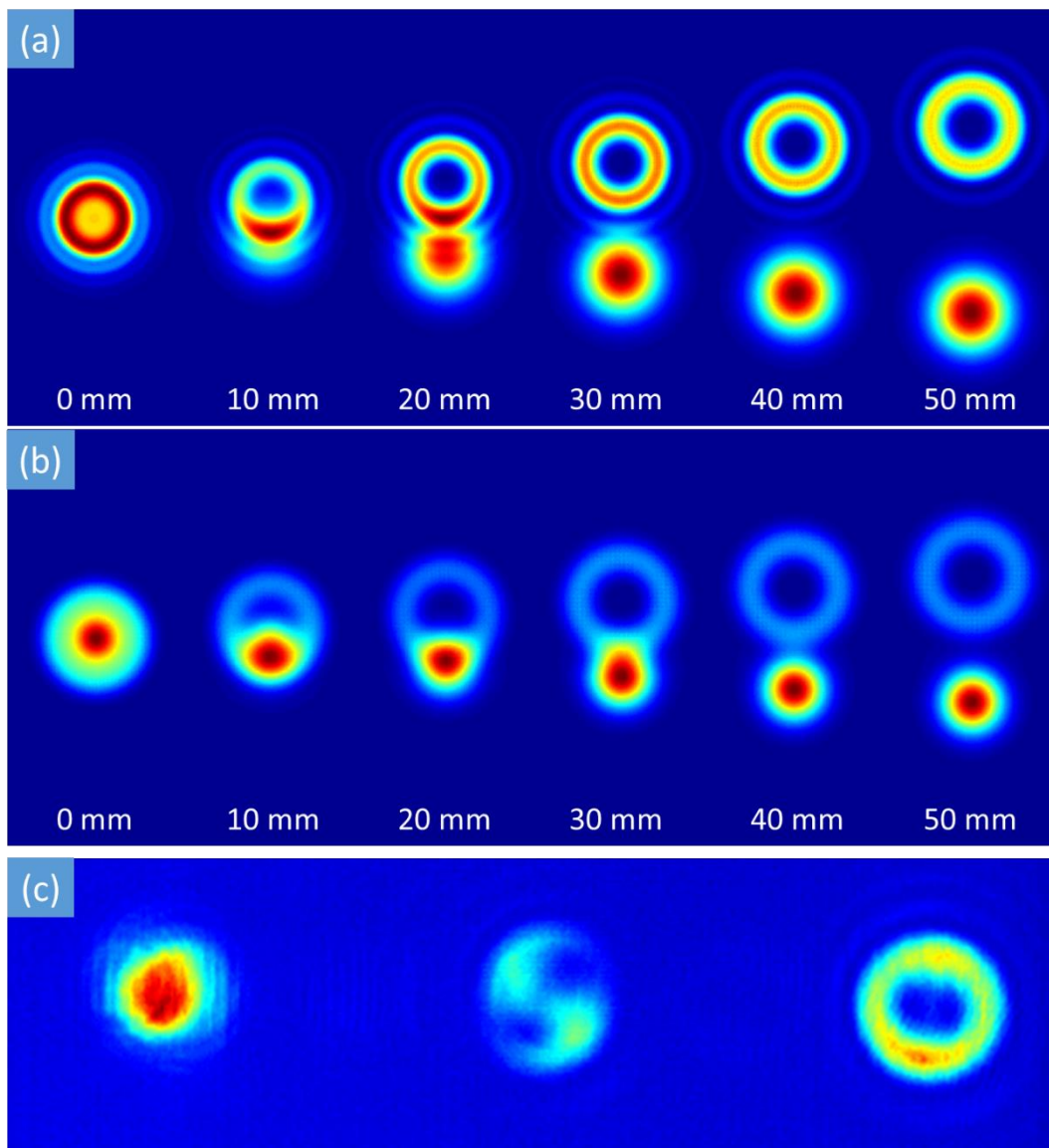


Figure 4-11 The modelling (a, b) and the experiment (c) of the radially polarized vortex beam propagation after passing through the polarization diffraction grating. The beam modelled in Figure 4-5 (a) propagates for 50 mm (a) or 250 mm (b)

Another interesting experimental verification that cylindrical vector vortex beams is superposition of Gaussian and vortex beams can be demonstrated with a polarization diffraction grating. The polarization diffraction grating is another optical element based on nanogratings, with was introduced by Beresna *et al.* [68]. This diffraction grating is sensitive to the handedness of

circularly polarized light. Light with opposite handedness is diffracted to different directions and therefore after the polarization grating the beam splits circularly polarized beams with opposite handedness.

The simulation of radially polarized vortex beam passing through the polarization grating was performed (Figure 4-10 (a, b)). The modelled beam has the same parameters as in Figure 4-5 (a). In the modelling, the polarization grating is placed 50 mm (Figure 4-10 (a)) and 250 mm (Figure 4-10 (b)) after the polarization converter. The modelled propagations of the beams after the polarization grating are in Figure 4-11 (a, b). We can see that as it was expected the beam splits in to beams: Gaussian beam and donut-like shape beam (second order vortex beam).

As it was previously demonstrated (Figure 4-5), the profile of radially polarized vortex beam changes strongly during propagation, therefore beams in Figure 4-11 (a) and Figure 4-11 (b) looks very different at the plane of the polarization grating, but in both cases after the polarization grating they split to two beams which do not change their shape during the propagation.

4.3 Cylindrical vector beams without phase modulation

Polarization converters designed for input beam with linear polarization can be more practical as they allow generating CV beams without phase helicity. In such converters spatially variant half-wave plates have to be formed. Half-wave plates are fabricated in such way that slow axis angle of the micro half-wave plates is

$$\theta = \pm \frac{l\phi}{2}, \quad (4-31)$$

where ϕ is polar angle, l is azimuthal index of the Laguerre-Gaussian mode LG_{lp} (for example in the case of radially/azimuthally polarized beam $l = 1$) (Figure 4-12).

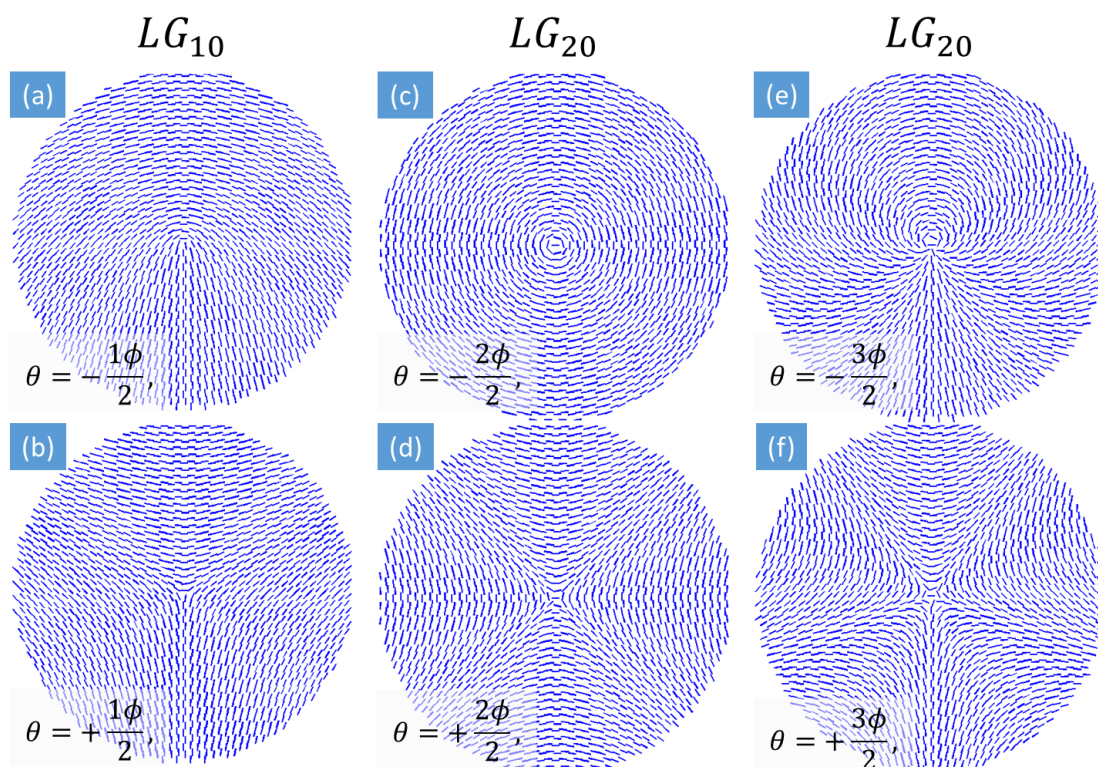


Figure 4-12. Schematic drawings of nanogratings distribution in polarization converters. (a), (b) Converter for LG_{10} mode beam, (c), (d) - for LG_{20} mode beam, (e), (f) - for LG_{30} mode beam. (a) Converter for radial/azimuthal beam generation.°

Let us start from the polarization converters designed to create radial/azimuthal polarization distribution. Firstly, it is worth to point out, that in the Figure 4-12 only converter (a) is for generation of radially/azimuthally polarized beams, even though beam generated with the converter (b) also will be LG_{10} . These two converter I will compare later. As in the previous paragraph, let us find the Jones matrix representing half-wave converter for radial/azimuthal polarization. For this we need to rotate half-wave plate matrix around the axis at angle θ (Equation (4-31)). We get much simpler equation than in the quarter-wave converter case:

$$M_{hwc} = \begin{pmatrix} \cos \phi & \sin \phi \\ \sin \phi & -\cos \phi \end{pmatrix}. \quad (4-32)$$

If we launch horizontally polarized light to converter we get radially polarized light:

$$E_{Ra} = \begin{pmatrix} \cos \phi & \sin \phi \\ \sin \phi & -\cos \phi \end{pmatrix} \begin{pmatrix} 1 \\ 0 \end{pmatrix} = \begin{pmatrix} \cos \phi \\ \sin \phi \end{pmatrix}. \quad (4-33)$$

Vertically polarized light will be converted to azimuthally polarized:

$$E_{Az} = \begin{pmatrix} \cos \phi & \sin \phi \\ \sin \phi & -\cos \phi \end{pmatrix} \begin{pmatrix} 0 \\ 1 \end{pmatrix} = \begin{pmatrix} \sin \phi \\ -\cos \phi \end{pmatrix}. \quad (4-34)$$

Any other incident linear polarization will be converted to state of polarization intermediate between radial and azimuthal.

Another useful solution emerges for incident circular polarization:

$$\begin{aligned} E_V &= \begin{pmatrix} \cos \phi & \sin \phi \\ \sin \phi & -\cos \phi \end{pmatrix} \begin{pmatrix} 1 \\ i \end{pmatrix} = \begin{pmatrix} \cos \phi + i \sin \phi \\ \sin \phi - i \cos \phi \end{pmatrix} = \begin{pmatrix} e^{i\phi} \\ -i e^{i\phi} \end{pmatrix} \\ &= e^{i\phi} \begin{pmatrix} 1 \\ -i \end{pmatrix}. \end{aligned} \quad (4-35)$$

Exponential term in equation (4-35) shows that we have vortex beam. The handedness of the input circular polarization defines the sign of orbital angular momentum. So, the half-wave converter can be used not only to get

cylindrical vector beams, but to generate optical vortices too. As well higher order converters like in Figure 4-12 (c)-(f) can be used to generate higher order optical vortices. In general, spatial distribution of half-wave plates will cause phase modulation on circularly polarized light (more applications on this will be discussed later in this chapter).

Intensity and polarization distributions of beams generated by the half-wave polarization converters which schematics are in Figure 4-12 (a, b, d) was modelled. For the modelling the same method as described in the previous paragraph was used (MATLAB code can be found in the Appendix B). In the simulation, linearly polarized Gaussian beam with radius $w_0 = 300 \mu\text{m}$ and wavelength 512 nm passed through the centre of the half-wave polarization converter and after propagating for 50 mm in the free space, the intensity and polarization distributions were calculated (Figure 4-13). Also the intensity distribution of the beams after a linear analyser is demonstrated. These simulation provides information for distinguishing the fabricated converters determining if fabricated converter produces wanted distribution of the polarization.

The linear analyser can be helpful for simple determination of the order of generated cylindrical vector beam by the polarization converter. If after the analyser the beam consists of two lobes (Figure 4-13 (a-d)), the beam has LG_{10} mode shape which corresponds to converters Figure 4-12 (a, b). Four lobes in the beam (Figure 4-13 (e, f)) means second order CV beam with LG_{20} mode shape and converters in Figure 3-14 (c, d). And in general, if the number of lobes is $2 \cdot n$ then the CV beam is n -th order and has beam shape of LG_{n0} mode.

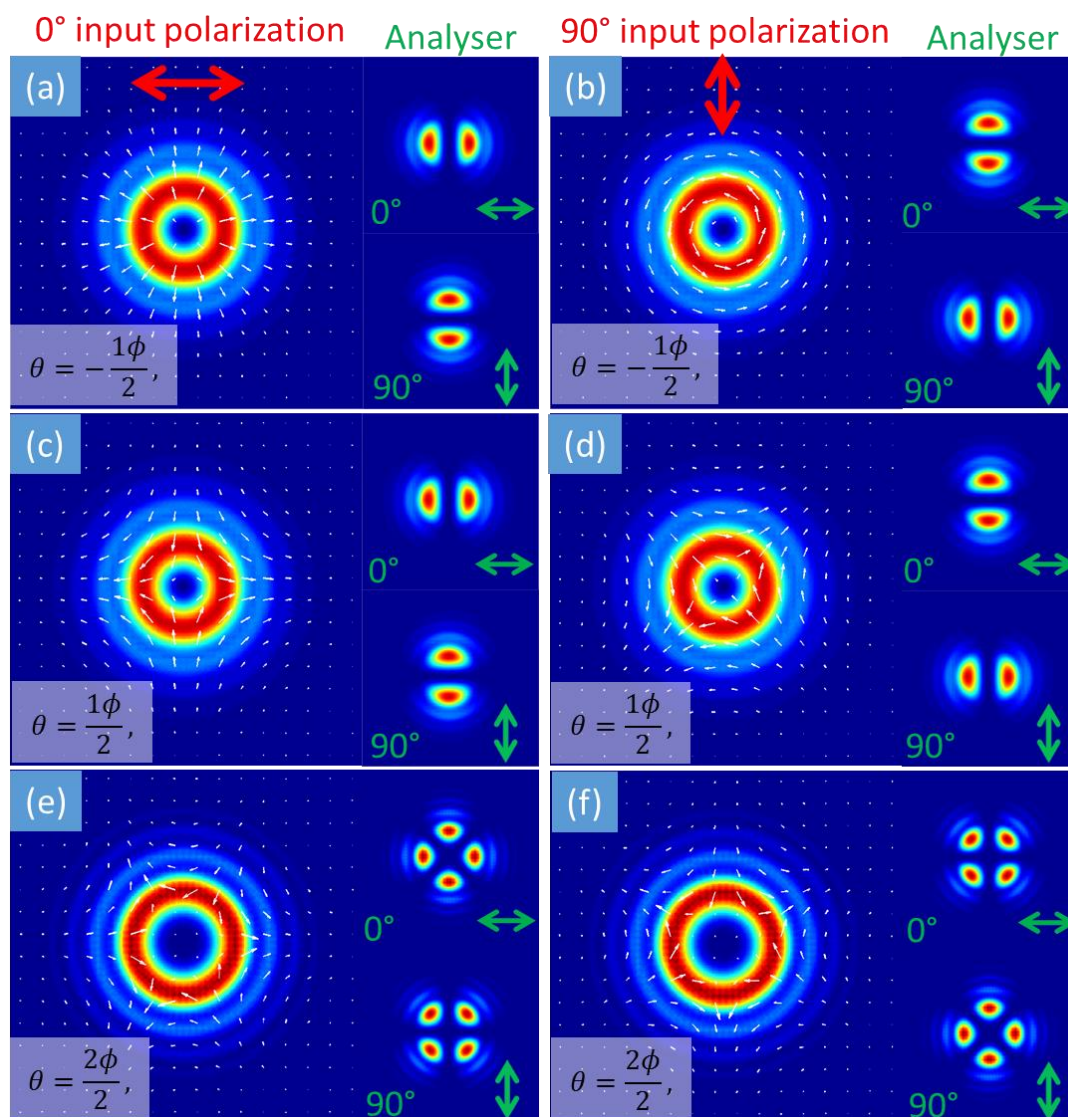


Figure 4-13 Modelling of intensity and polarization distributions of CV beams generated with different half-wave polarization converters. Equations describe the distribution of half-wave plates in the converters (Figure 4-12). Red arrows shows the plane of polarization of the input Gaussian beam. Green arrows indicates the orientation of the linear analyser placed after the converter and corresponding beam distributions after the analyser are modelled.

The polarization converter with slow axis distribution $\theta = -\frac{\phi}{2}$, generates beam with LG_{10} mode which (depending on the azimuth of the input linear

polarization) will have radial or azimuthal distribution of the polarization. Radial polarization is obtained when input light is polarized horizontally and azimuthal polarization when vertical. Obviously during the experiment the converter can be inserted into the setup not at the orientation as in Figure 4-12, but rotated. In such a case, a simple way to determine the angle of input linear polarization is to place the linear analyser after the converter. In general, to determine the distribution of linear polarization, beam profiles at four analyser angles (0° , 90° , 45° and -45°) should be acquired. But in this case it is enough to place the analyser at the fixed angle and rotate the input polarization until the orientation of two lobes in the beam will become parallel or perpendicular to the transmission axis of the analyser. If the orientation of two lobes is parallel – the distribution of the polarization is radial, if perpendicular – azimuthal.

Converters with slow axis distributions $\theta = -\frac{\phi}{2}$ and $\theta = \frac{\phi}{2}$ gives produce very similar beams. Both converter produce beams with LG_{10} mode shape. If they are used optical vortex generation (Equation (4-35)), both of them can be used in order to get orbital angular momentum $l = \pm 1$. However in vector beam case, they produce different distribution of the polarization Figure 4-13 (a-d) and only the converter $\theta = -\frac{\phi}{2}$ can produce radial/azimuthal polarization distributions. During the fabrication of the converter, it is easy to make mistake and instead of converter $\theta = -\frac{\phi}{2}$ fabricate the converter $\theta = +\frac{\phi}{2}$. Even when the fabricated converter is used in the experiment, it is not simple to notice the mistake as the beam profiles after the analyser might look the same Figure 4-13 (a-d). Therefore if the polarization before the converter will be rotated, we can align the two lobes in a parallel or perpendicular directions to the transmission axis of the analyser, but the polarization will not be radial or azimuthal. Simple way to distinguish these two converters is to rotate the analyser and check the direction of the rotating lobes. If the lobes rotates to the same direction as the analyser, the converter is $\theta = -\frac{\phi}{2}$ and it is suitable for radial/azimuthal beams generation. And if the lobes rotates to the opposite direction then the analyser, the converter is $\theta = +\frac{\phi}{2}$.

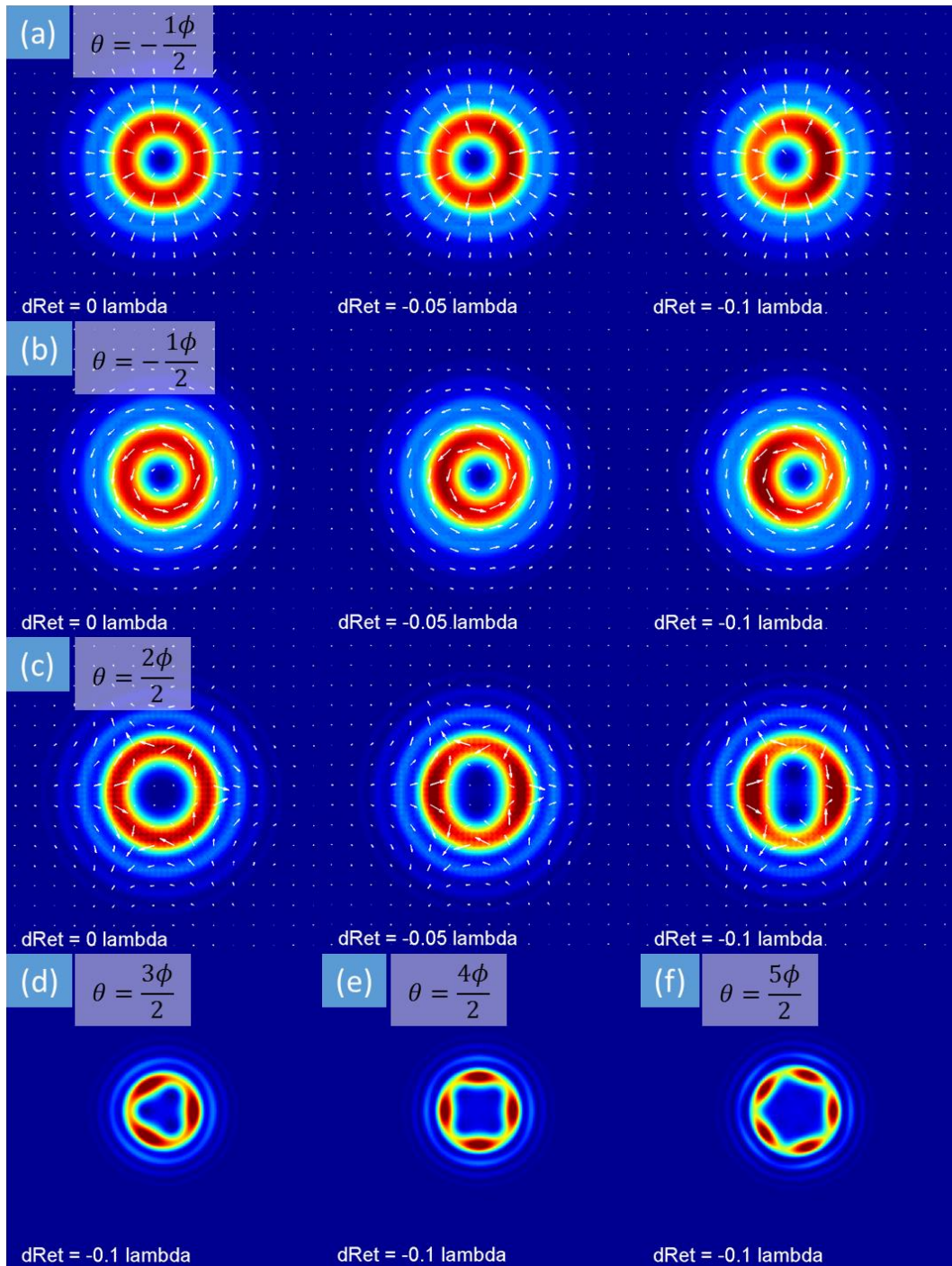


Figure 4-14 The modelling of generated beams when retardance value of the converter is not exactly half-wave value.

The conditions for generating CV beams when a fabricated converter has retardance value not exactly half-wave were also modelled. The input beam had same parameters as in previous modelling and the retardance could be altered from half-wave value. As in previous simulation, the intensity and polarization distributions were calculated 50 mm after converters (Figure 4-14). In radial and azimuthal polarization case, when retardance was reduced, the singularity in the shifted slightly from the centre (opposite sides for radial and azimuthal case) and intensity on the one side of the beam is larger than on the other (Figure 4-14 (a, b)). Even when the deviation from the half-wave value is as high as 0.1λ (53 nm in this case), the distribution of the polarization stays same.

In the case of second order CV beam, when the retardance value deviates from half-wave, the singularity splits into two and they move to the opposite sides of the beam (Figure 4-14 (c)). And again the distribution of the polarization is barely affected. Analogically in the cases of third, fourth and fifth order CV beams, singularities splits into 3, 4 and 5 parts and instead of circular shape of the beam, form triangle, square and pentagonal shape of the beam (Figure 4-14 (d-f)).

Now let us move to the experimental part of fabrication and testing of the half-wave polarization converters. Quarter-wave converter was fabricated in 30 segments where each of them had a different polarization. Due to the segmentation of the converter, radial lines with larger retardance (because of the overlapping) were emerging from the centre. In order to avoid the radial lines, segmentation of the slow axis distribution and improve the quality of the converter, the fabrication algorithm for half-wave converter was improved.

The rotation of the half-wave plate was synchronized with XYZ stages movement. The XYZ stage was programmed to move the sample at constant speed in XY plane in the trajectory of Archimedean spiral with $1 \mu\text{m}$ step. The rotational stage was rotating the half-wave plate to have the laser polarization as in Equation (4-31).

For half-wave polarization converter fabrication, optimum values for the pulse energy, repetition rate and writing speed required to achieve half-wave retardance at 532 nm wavelength, were found to be 1.75 μJ , 200 kHz and 2 mm/s, respectively. Beam was focused through 10 \times singlet lens (NA = 0.16). The polarization of laser beam was controlled with achromatic half wave plate to imprint space variation of half-wave plate. Microscope images of first and second order small testing versions of converters can be found in Figure 4-15. As the Abrio system cannot measure the orientation of the slow axis when the value of the retardance is close to 250 nm (Chapter 3.1), converters with lower value of retardance were fabricated in order to measure the distribution of slow axis (Figure 4-15 (a, b)). Converters with half-wave value of the retardance were placed between crossed polarizers (Figure 4-15 (c, d)). These images demonstrate that wanted distribution of slow axis angle and value of retardance were achieved.

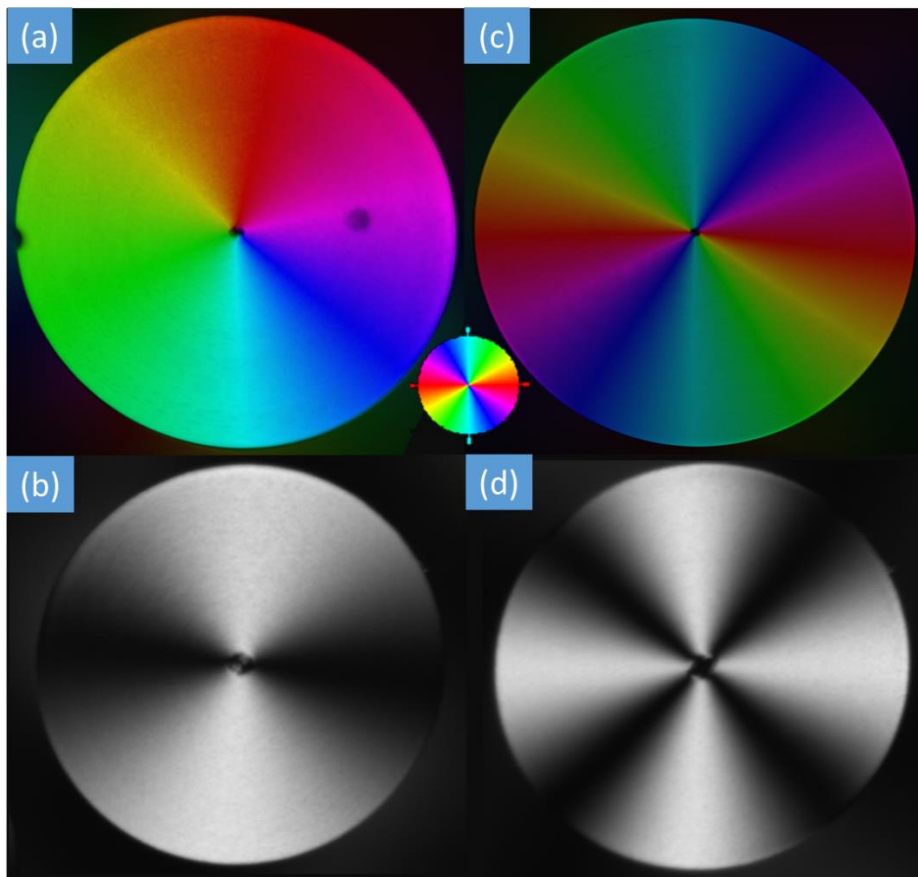


Figure 4-15 Microscopic images of small test versions of half-wave polarization converters for first and second order CV beams generation. (a, b) Distribution of slow axis orientation, (c, d) converters are placed between crossed polarizers.

After testing converters were analysed under the microscope, large size converters (6 mm in diameter and larger) were fabricated (Figure 4-16 (a, b)). As the speed of fabrication is 2 mm/s and distance between lines is 1 μm , to fabricate one 6 mm diameter size converter takes around 4 hours.

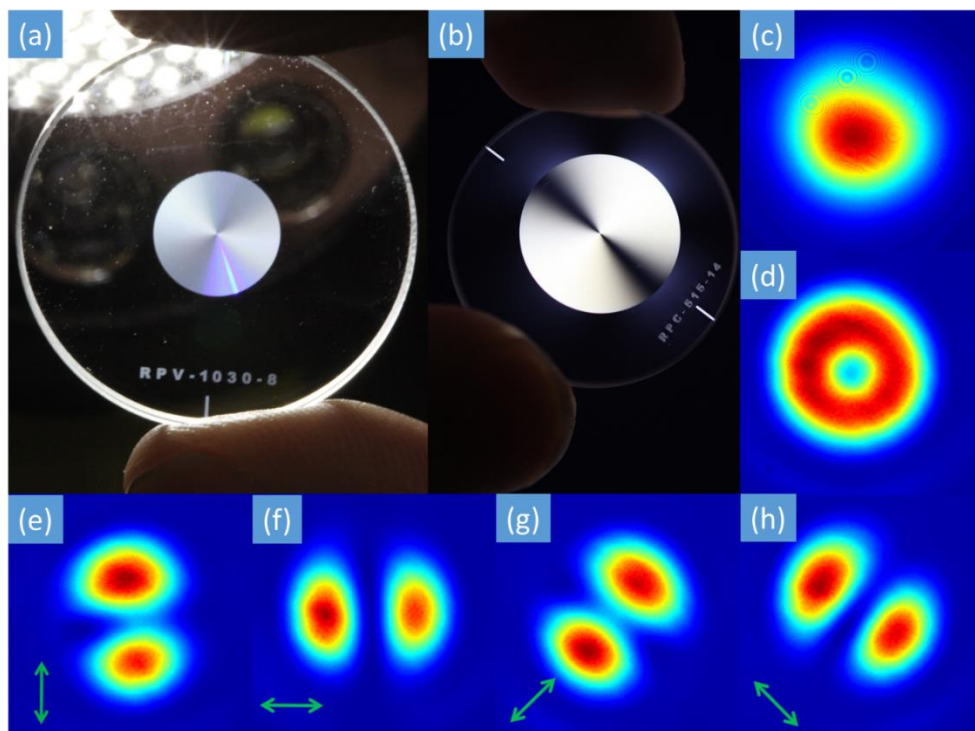


Figure 4-16 (a) Half-wave polarization converter for second order CV beams (8 mm in diameter). (b) Polarization converter for first order CV beams (radial/azimuthal polarization) placed between crossed polarizers (14 mm in diameter). (c) Beam profile of input linearly polarized beam. (d) Beam profile radially polarized beam generated by the converter in (b). (e-h) The same beam after the linear analyser at angles 0° , 90° , 45° and -45° .

Firstly the polarization converter of first order was tested. Fabricated converter was examined with similar experimental setup as quarter-wave converter. Linearly polarized laser beam ($\lambda = 532 \text{ nm}$) (Figure 4-16 (c)) was launched through the converter (Figure 4-16 (b)) to generate radially polarized beam (Figure 4-16 (d)). Measured intensity distributions of generated radially polarized beam and the same beam after the linear analyser (Figure 4-16 (e-f)) are in good agreement with modelled beam profiles Figure 4-13 (a).

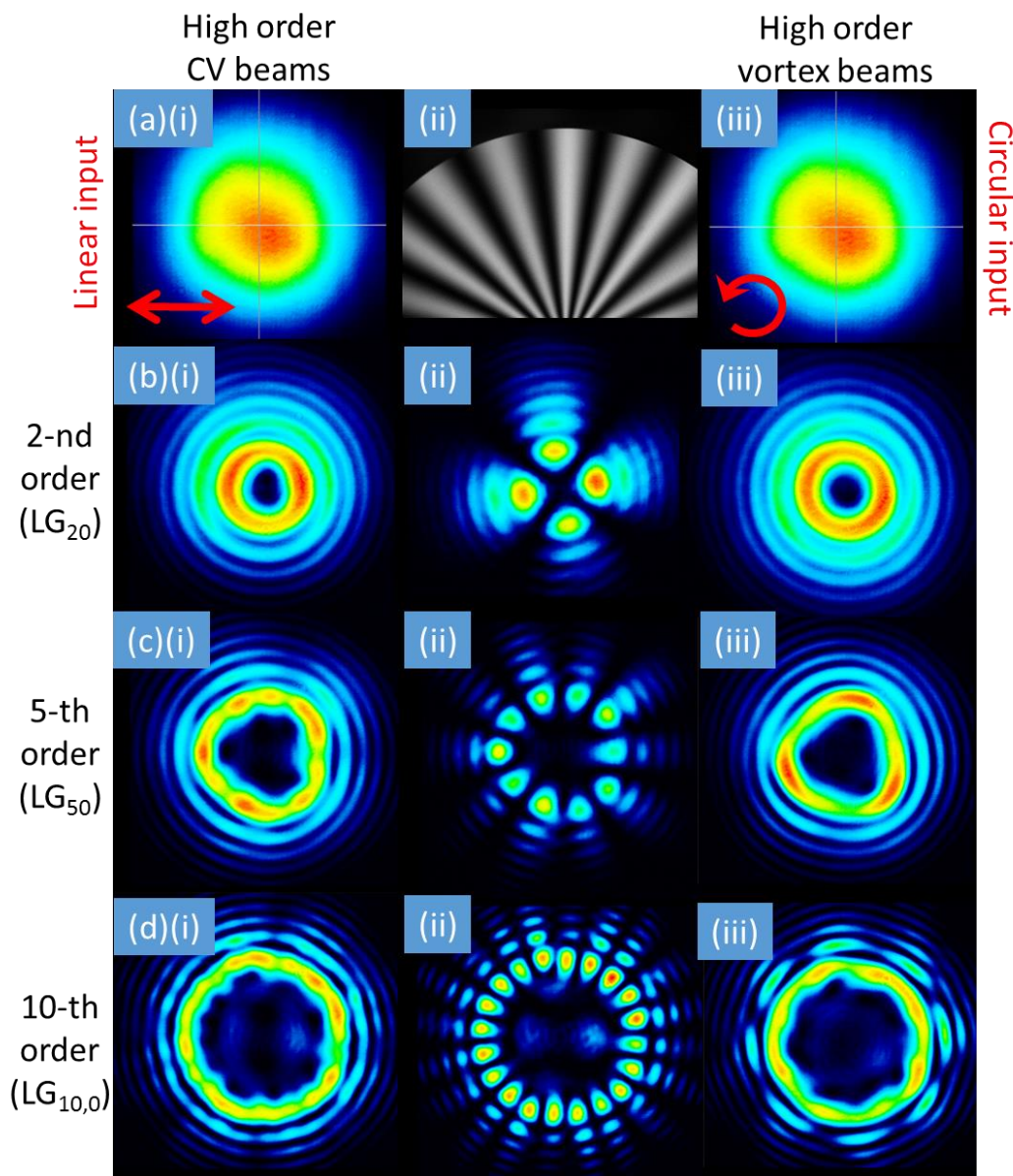


Figure 4-17 Beam profiles of high order CV beams (i), the same beams with linear analyser (ii) and vortex beams (iii). (a)(i, iii) Profiles of linearly and circularly polarized beam before the converter. (a)(ii) 10-th order polarization converter between crossed polarizers. (b) Second order beams, (c) fifth order CV beam, (d) 10-th order CV beam.

Also high order polarization converters were tested. The microscope image of the 10-th order polarization converter placed between crossed polarizers is in Figure 4-17 (a)(ii). High order CV beams were produced with linearly polarized Gaussian beams entering polarization converters (Figure 4-17 (i)) and high

order optical vortices in the case of circular polarization (Figure 4-17 (iii)). Even though the intensity distributions of the beams were not as perfect as in theoretical modelling, the polarization had expected distributions (Figure 4-17 (ii)).

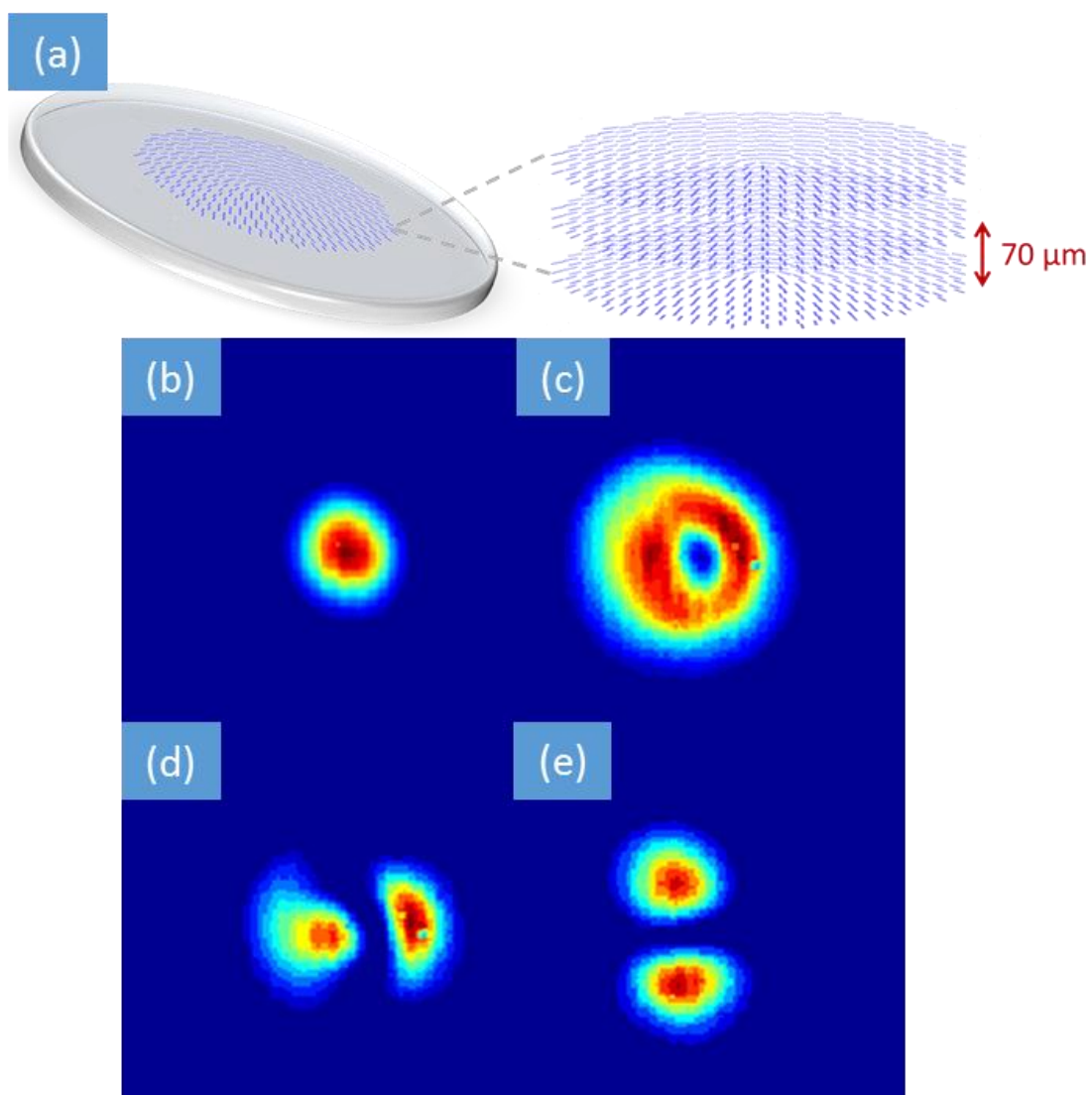


Figure 4-18 Generation of radially polarized beam at 1550 nm.

Polarization converters for different wavelength can be fabricated by adjusting the value of retardance using different laser power. However it is difficult to achieve more than 300 nm of retardance (Figure 3-6). The other way to fabricate converter with high retardance is to write few layers (Figure 4-18 (a)).

Then for example converter for 1030 nm can be fabricated with the same parameters as for 512 nm by adding two layers.

Polarization converter for generating radially/azimuthally polarized beams working at 1550 nm was fabricated by adding three layers separated by 70 μm (Figure 4-18 (a)). The parameters for fabrication were the same as for 515 nm converter. The converter was tested with continuous wave fibre laser working at 1550 nm (Figure 4-18 (b, e)).

Due to scattering, the transmission of polarization converters working at 515 nm is around 50%. Scattering losses strongly depends on the wavelength (Rayleigh scattering $\sim 1/\lambda^4$). For this reason, two-layered converted working at 1 μm has more than 80% transmission and the transmission of three-layered converter working at 1.5 μm is more than 95%.

4.4 Inducing nanogratings with CV beams

Linearly polarized femtosecond laser beams induce nanogratings with uniform distribution of nanogratings orientation, which is perpendicular to the polarization. As in cylindrical vector beams the polarization has certain distribution, the orientation of induced nanogratings also will have non-uniform distribution. For example, radially polarized light will induce azimuthally distributed nanogratings. Nanogratings induced by radially and azimuthally polarized femtosecond laser was reported for first time by C. Hnatovsky *et al.* (2011) [106] (Figure 4-19 (a, b)). As expected, radial polarization induced azimuthally distributed nanogratings (Figure 4-19 (a)) and azimuthal polarization – radially (Figure 4-19 (b)).

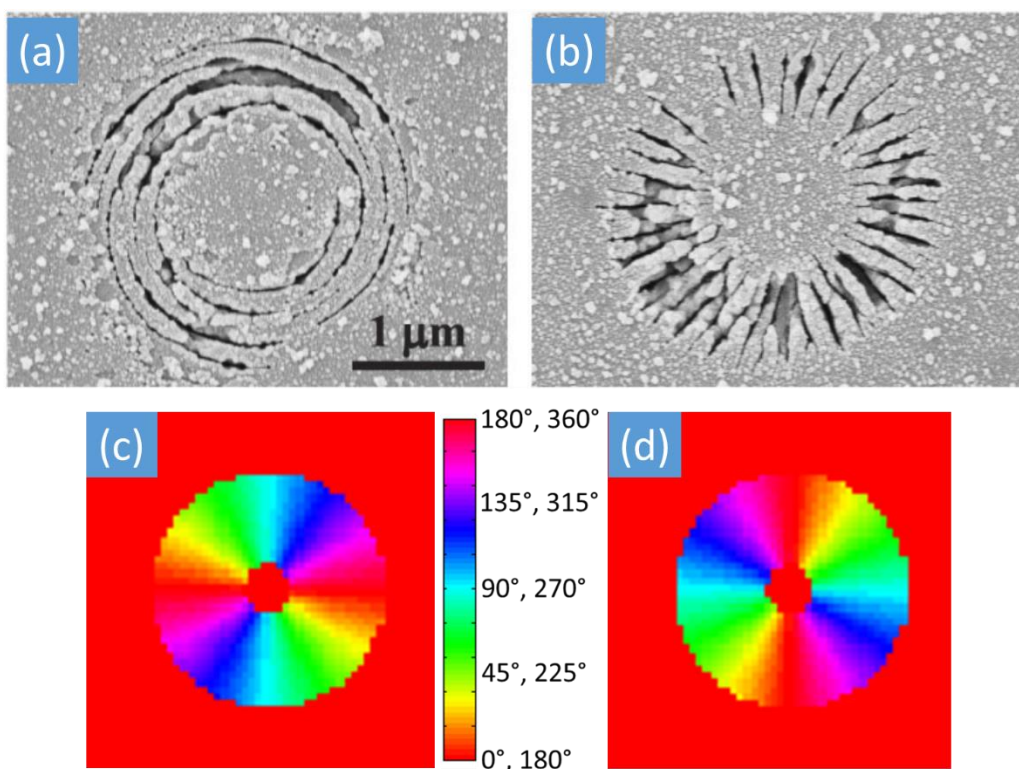


Figure 4-19 SEM images of nanogratings induced by radially (a) and azimuthally (b) polarized femtosecond laser. The modelled distribution of slow axis of birefringent modifications induced by radially (c) and azimuthally (d) polarized beams. (Source for images (a) and (b): C. Hnatovsky *et al.* (2011) [106])

As it was mentioned earlier, another method of investigating nanogratings is measuring their optical properties such as birefringence. As nanogratings always form in the direction perpendicular to the laser polarization and the slow axis of form birefringence is perpendicular to the nanogratings, it is easy to predict the distribution of slow axis if the distribution polarization is known. In Figure 4-19 (c, d) it is demonstrated the slow axis distribution if the birefringence of structures in Figure 4-19 (a, b) would be measured.

However, when the line or multiple overlapping lines are fabricated with radially or azimuthally polarized beam, situation becomes more complicated. The modelling of induced birefringence by radially or azimuthally polarized laser was performed. The algorithm of modelling and the assumptions made for the modelling described in the following.

Firstly, the matrix $M(n \times m)$, describing the distribution of birefringence of the material, was created. Each element in the matrix M is Jones matrix $m_{i,j} = J$ which at the beginning is set to be identity matrix:

$$M_{n,m} \begin{pmatrix} J_{1,1} & \cdots & J_{1,m} \\ \vdots & \ddots & \vdots \\ J_{n,1} & \cdots & J_{n,m} \end{pmatrix}; \quad m_{i,j} = J = \begin{pmatrix} 1 & 0 \\ 0 & 1 \end{pmatrix}. \quad (4-36)$$

This means, that at the beginning the uniform and non-birefringent space is described. Next, the matrix describing CV beam with certain intensity and polarization distribution is generated. The size of the beam is much smaller to compare to the space described by the matrix M , so that beam could be moved. Then the beam is placed at the certain coordinates of the matrix M and each pixel of the beam is affecting one pixel in the matrix M .

Now let us take single pixel of the matrix M and the pixel of the beam which affecting it. Depending on the intensity and the orientation of the polarization of the certain pixel of the modelled beam, the Jones matrix for describing retarder can be constructed:

$$R(\theta, \Delta\varphi) = \begin{pmatrix} \cos^2 \theta + e^{i\Delta\varphi} \sin^2 \theta & (1 - e^{i\Delta\varphi}) \cos \theta \sin \theta \\ (1 - e^{i\Delta\varphi}) \cos \theta \sin \theta & \sin^2 \theta + e^{i\Delta\varphi} \cos^2 \theta \end{pmatrix}, \quad (4-37)$$

where θ is slow axis angle and $\Delta\varphi$ is phase retardation. The orientation of slow axis θ is parallel to the laser polarization θ_{laser} : $\theta = \theta_{laser}$. The assumption that the magnitude of retardance has linear dependence on the laser intensity I_{laser} is made: $\Delta\varphi = kI_{laser}$. Also certain threshold for the modification exists. This assumption is not valid under high intensities, when the value of retardance starts saturating, but it is correct under lower intensities (Figure 3-5). Therefore, depending on the laser intensity and polarization we get we get Jones matrix:

$$R(\theta_{laser}, I_{laser}) = \begin{pmatrix} \cos^2 \theta_{laser} + e^{ikI_{laser}} \sin^2 \theta_{laser} & (1 - e^{ikI_{laser}}) \cos \theta_{laser} \sin \theta_{laser} \\ (1 - e^{ikI_{laser}}) \cos \theta_{laser} \sin \theta_{laser} & \sin^2 \theta_{laser} + e^{ikI_{laser}} \cos^2 \theta_{laser} \end{pmatrix}. \quad (4-38)$$

Now the elements of the matrix M (the matrix describing the medium) affected by the laser can be recalculated:

$$J' = R(\theta_{laser}, I_{laser})J. \quad (4-39)$$

The procedure can be repeated again and again by placing new beams at the same or other coordinates. As new pulses can be placed on top on already modified region in the matrix M, two more assumptions has to be made: overwriting of previous slow axis orientation is possible, each pulse brings the same amount of the retardance to the modified region. The first assumption about overwriting nanogratings is correct [53]. However the second assumption does not include saturation of the retardance value and the fact that certain amount of pulses is required for inducing nanogratings. The algorithm could be improved by taking into the account the saturation of the retardance and the amount of fluence required to start inducing nanogratings, however it would bring too many unknown variables to the algorithm.

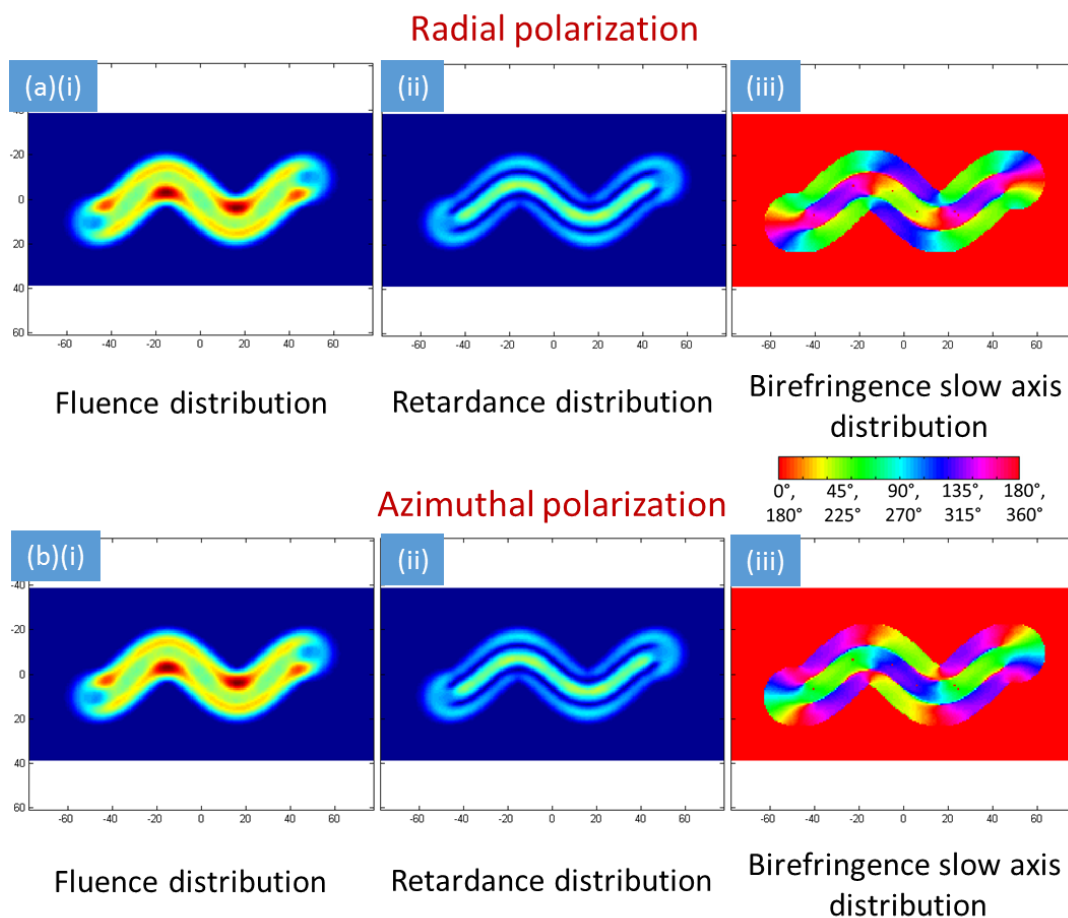


Figure 4-20 Modelling of the birefringent track induced by radially (a) and azimuthally (b) polarized beams moving across a sample in a sinusoidal curve.

Firstly, the modification induced by the laser beam moving in sinusoidal curve was modelled (Figure 4-20). Radially or azimuthally polarized beam (around $20\ \mu\text{m}$ in diameter) was moved with $2\ \mu\text{m}$ step. Laser fluence distribution (Figure 4-20 (i)) and laser induced retardance distribution (Figure 4-20 (ii)), as it could be expected, were the same for both, radial and azimuthal, polarization. Fluence distribution image shows minimum in the centre of the curve and two maximums at the edges. This can be explained by zero intensity in the donut-like shape beam. Interestingly, the retardance calculation shows almost opposite result than fluence: maximum in the centre and two minimums close

to the edge. The distribution of slow axis (Figure 4-20 (iii)) had 90° difference for radial and azimuthal polarizations. We can see that the central maximum of the curve has different colour (slow axis orientation) that edges and the colour also depends on the writing direction. This can be explained by the overwriting of the nanogratings: as the beam is mover across the sample, just the end of the beam can record the information of the polarization and the front is overwritten. As during the overwriting of the birefringence the magnitude of retardance not necessarily increases (for example, if rewritten with perpendicular polarization, the value of retardance will decrease), it can also explain the difference between modelled fluence and retardance distributions.

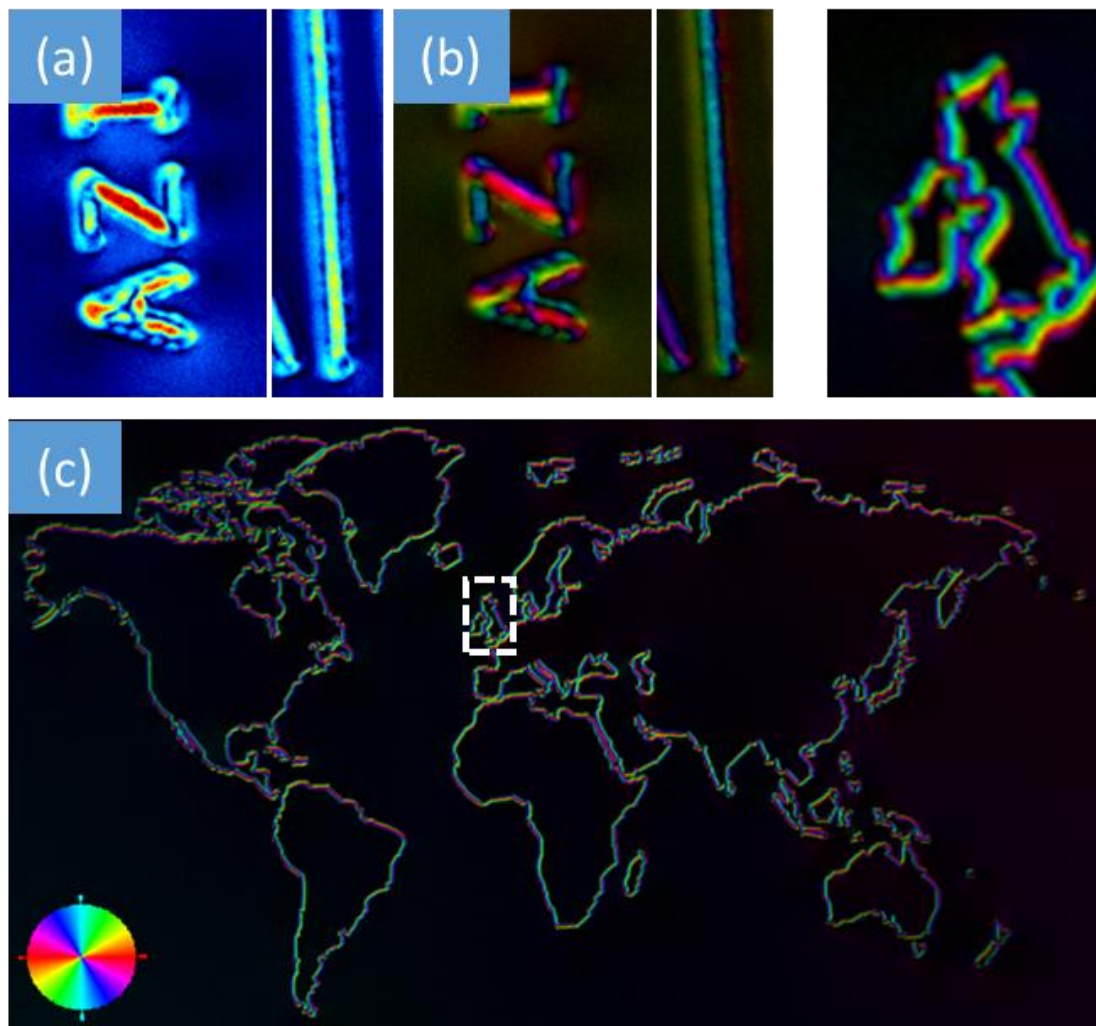


Figure 4-21 Abrio images of modifications induced by azimuthally polarized beams.

Experimental results (Figure 4-21) are in good agreement with the modelling. Lines and curves were written with azimuthally polarized beam and fabricated structures were investigated with Abrio system. The retardance image of the single line (Figure 4-21 (a)) shows maximum in the centre of the line and two minimums near the edges (which is exactly as it was predicted by the modelling). In the image of slow axis distribution (Figure 4-21 (b)) indicates that the centre of the line has different slow axis orientation than sides and also by looking at the fabricated letters we can see slow axis orientation dependence on the writing direction. Laser calligraphy is demonstrated in (Figure 4-21 (c)), where properties of laser induced structure depends on the writing direction.

More complicated situation is in the case of fabrication of multiple overlapping lines (Figure 4-22). This time not just front of the beam is overwriting the modification, but also new line is partially overwriting previously written one. The simulation of radially polarized laser beam moving in a spiral trajectory ($2\ \mu\text{m}$ step) and fabricating disc like structure was performed. Slow axis distribution of the modelled fabricated structure (Figure 4-22 (a)(iii)) is similar to the 2nd order polarization converter (Figure 4-15 (c)) or polarization converter for radially polarized vortex beam (Figure 4-7 (c)). However due to multiple overwriting, the value of induced retardance is low (Figure 4-22 (a)(ii)). In a case of not perfect beam (generated with polarization converters with retardance $0.55 \cdot \lambda$ and $0.6 \cdot \lambda$) retardance distribution of fabricated structure becomes not smooth and slow axis distribution also changes (Figure 4-22 (b, c)). The comparison of experimental results (Figure 4-22 (d)) with the modelling, indicates, that laser beam was not perfect.

Simulation shows that radially polarized beam could be used for fabrication of polarization converters with certain birefringence distribution. However the technique would be very sensitive to the beam quality and it might be difficult to induce high retardance values.

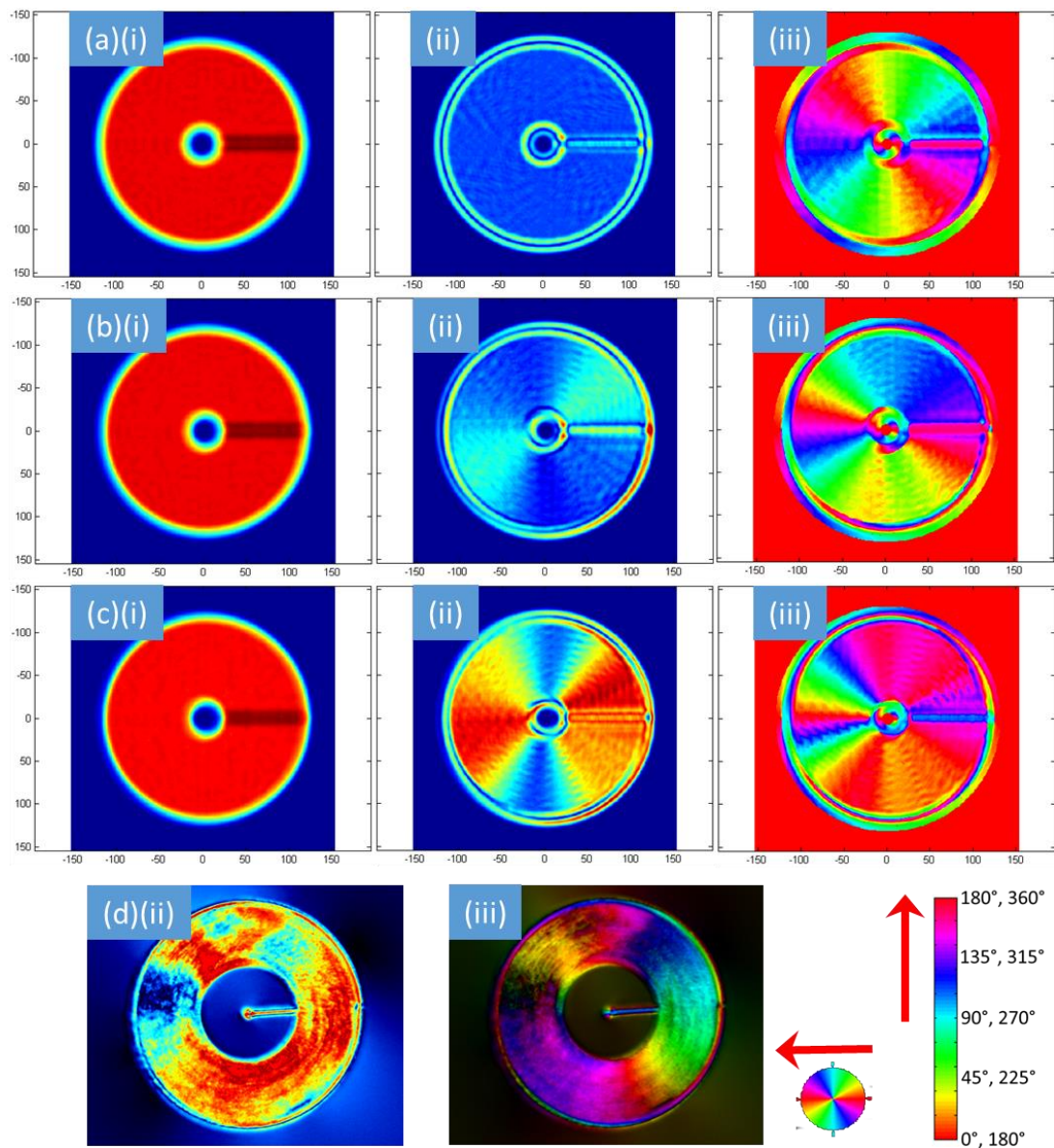


Figure 4-22 Modelling of disc structure fabricated with radially polarized beam: (a) perfect radially polarized beam, (b, c) beam generated with not ideal polarization converter. Not ideal polarization converter had higher than half-wave value of retardance: (b) $+0.05 \cdot \lambda$, (c) $+0.1 \cdot \lambda$. Abrio images of structure fabricated with radially polarized beam. (i) Fluence distribution, (ii) retardance distribution, (iii) slow axis orientation distribution of the modelled and measured structures.

4.5 Beams with tuneable orbital angular momentum

The optical trapping of microscopic transparent objects has been demonstrated almost three decades ago [107]. Since it was shown that the gradient force can be used in three-dimensional manipulations, the technique has become attractive for numerous fields in physical and biomedical sciences [108–112]. The photon carries linear and angular momentum that can be transferred to the illuminated objects. Angular momentum of a photon is comprised of spin angular momentum (SAM) [113] and orbital angular momentum (OAM) [114]. SAM is associated with the polarization of the light which is always intrinsic [115]. It can be used to rotate absorbing or birefringent particles along their axis [116–119]. Whereas OAM comes from the azimuthal phase variation of the beam. It was demonstrated that the beam with helical phase $\phi = l\varphi$, where φ is phase, ϕ is polar angle and l is positive or negative integer number, possess well-defined OAM with $l\hbar$ [114]. Such beams, frequently referred as optical vortices, enables the rotation of transparent non-birefringent particles [120] and the rotation can be both extrinsic or intrinsic [115]. The ability to tune angular momentum adds an extra degree of control to optical systems and has applications ranging from atomic manipulation [121,122] to quantum information processing [123,124].

The transfer of total angular momentum to the trapped particles can be accomplished in several ways. Some methods involve beams without orbital momentum when the intensity distribution or the linear polarization of the beam is actively rotated in order to torque objects [119,125,126]. By changing the state of polarization, the average spin momentum of the photon is changed and therefore the rotation speed of the particle can be controlled [117,118,127]. Furthermore, without introducing elliptical or linear polarizations the transferred torque might be tuned by two counter-propagating waves of orthogonal circular polarization [126,128,129].

The control of OAM is more complicated. The change of wavefront helicity affects the geometry of the beam: the higher is $|l|$, the larger is diameter of the beam. As a result, the angular momentum of the beam can be defined either by the shape of the beam or by the photon density what make the approach

limited for the task that requires constant gradient of the intensity and tunable angular momentum. OAM of the beam can be controlled using a spatial light modulator by generating and superimposing two optical vortices with opposite handedness [130] or generating fractional vortices [131]. However, the polarization of two vortices is the same and leads to interference fringe pattern while in partial vortices case the beam does not have symmetric donut shape. Other approach introduces azimuthal phase gradients in holographic ring [132]. However, this method is limited with the range of rotation speed that is quantized and possess azimuthal intensity gradient variations.

In this section I will discuss about an alternative method of generating optical vortices with gradually controlled OAM which do not have previously mentioned limitations. For this we used first order half-wave polarization converter. As CV beam converters discussed previously in this chapter already became commercial products, from now in this section I will call them by their commercial name S-waveplate [133]. Usually it is used to generate beams with radial/azimuthal polarization distribution. It is also known that such a structure can be exploited to generate optical vortices [67,134]. Here I will demonstrate the continuous control of an orbital angular momentum by controlling the spin angular momentum of the light before the S-waveplate. I will also show that it does not affect the shape of the beam and can be used as an optical tweezer with tunable torque.

Before I demonstrated that when the polarization of the input beam before the S-waveplate is circular, we get optical vortex at the output. If left-handed (right-handed) circularly polarized light is transmitted through the S-waveplate, right-handed (left-handed) circularly polarized right-handed (left-handed) optical vortex is generated:

$$E_{RV} = M_S \begin{pmatrix} 1 \\ i \end{pmatrix} = \begin{pmatrix} \cos \phi + i \sin \phi \\ \sin \phi - i \cos \phi \end{pmatrix} = e^{i\phi} \begin{pmatrix} 1 \\ -i \end{pmatrix} \quad (4-40)$$

$$E_{LV} = M_S \begin{pmatrix} 1 \\ -i \end{pmatrix} = \begin{pmatrix} \cos \phi - i \sin \phi \\ \sin \phi + i \cos \phi \end{pmatrix} = e^{-i\phi} \begin{pmatrix} 1 \\ i \end{pmatrix} \quad (4-41)$$

Each photon of circularly polarized light carries a spin angular momentum of $S = s\hbar$, where $s = \pm 1$. So, the polarization of light is the macroscopic

representation of a SAM carried by photons. In the case of optical vortices, the optical momentum is contributed by OAM with $L = l\hbar$. Positive l corresponds to right-handed optical vortex and negative to left-handed. We can see that the S-waveplate changes the photon spin momentum S and transfers OAM to the photon:

$$S_{out} = -S_{in}, \quad (4-42)$$

$$L_{out} = -S_{in}. \quad (4-43)$$

where S_{in} and L_{in} are SAM and OAM before and L_{out} is OAM after S-waveplate.

The electric field of any linearly or elliptically polarized light can be expressed as the superposition of left- and right-handed circular polarizations. This means that in the case of elliptically polarized input at the output of the S-waveplate two optical vortices will be generated. They would have opposite handedness circular polarization and opposite handedness of the helical phase. Overall, the effect of the S-waveplate on the photon can be expressed as:

$$(\alpha|\uparrow\rangle + \beta|\downarrow\rangle)|0\rangle \xrightarrow{S\text{-waveplate}} \beta|\uparrow, R\rangle + \alpha|\downarrow, L\rangle, \quad (4-44)$$

where $|\uparrow\rangle$ and $|\downarrow\rangle$ are up and down spin state of the photon, $|R\rangle$ and $|L\rangle$ are right and left orbital state of the photon. The coefficients describing the state of orbital angular momentum are the same as for spin state of the photon entering the S-waveplate (Figure 4-23 (c)). It means it is enough to know the coefficients of the spin state of the input photon and therefore average OAM transferred to the photon depends on the angle of the quarter-wave:

$$\langle L_{out}(\theta) \rangle = -\langle S_{in}(\theta) \rangle. \quad (4-45)$$

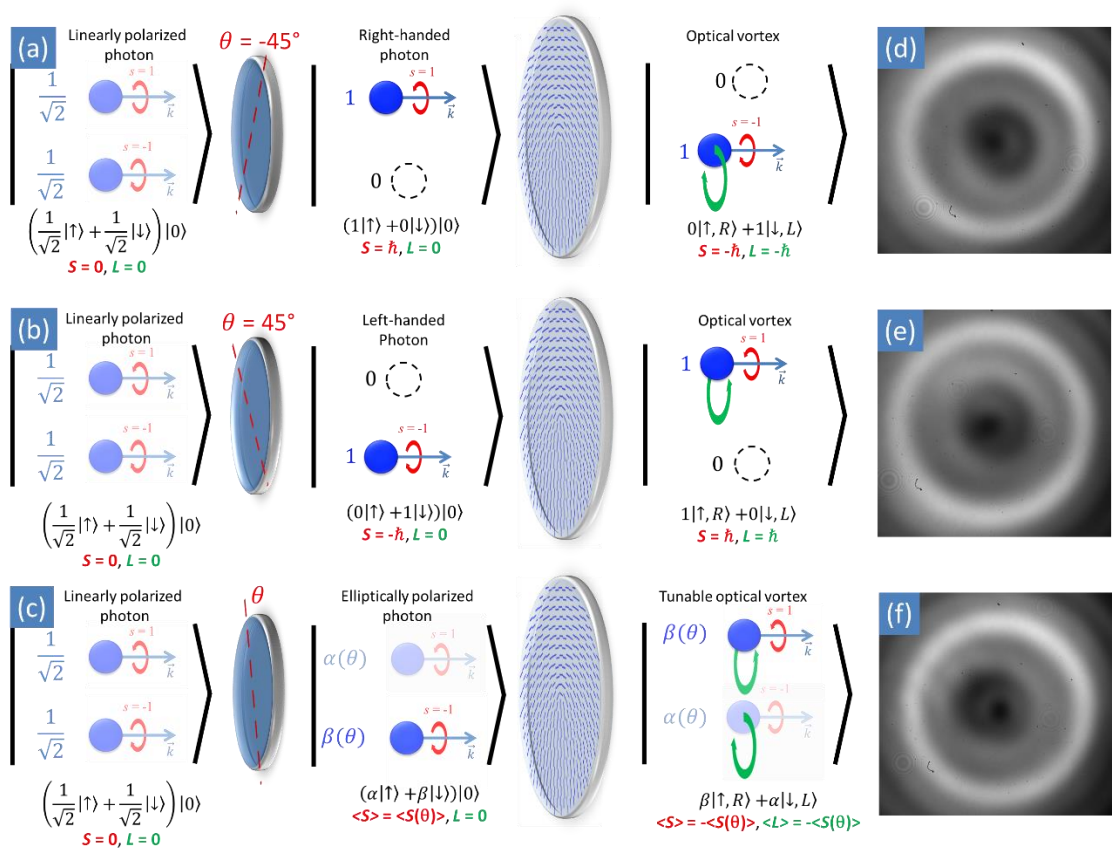


Figure 4-23 The transformation of a photon transmitted through a quarter-wave plate and S-waveplate. Linearly polarized photon passes through the quarter-wave plate (set at the angle θ) and acquires spin momentum depending on the θ value. (a) Photon with spin momentum $S = \hbar$ and no OAM (right-handed circularly polarized light) transmitted through the S-waveplate changes spin momentum to $S = -\hbar$ and gets $L = -\hbar$ (left handed circularly polarized left-handed optical vortex). (b) Photon with spin momentum $S = -\hbar$ (left-handed circularly polarized light) is transformed into the photon with spin momentum $S = \hbar$ and $L = \hbar$ (right-handed circularly polarized optical vortex). (c) Elliptically polarized photon with spin momentum $\langle S(\theta) \rangle$ obtains $\langle L \rangle = -\langle S(\theta) \rangle$ and $\langle S \rangle = -\langle S(\theta) \rangle$. Intensity profiles of left- and right-handed optical vortices (d), (e) and radially polarized beam (f).

In the case of linearly polarized input light when the spin momentum of the photons is zero, the output is radially or azimuthally polarized light when the orbital momentum is zero.

Now we need to determine the SAM relationship with the angle of quarter-wave plate which transforms linearly polarized light to elliptically polarized light at the first part of the beam conversion. The electric field can be described as

$$E_E = a_L(\theta) \begin{pmatrix} 1 \\ i \end{pmatrix} E_0 + e^{i\Delta\Phi} a_R(\theta) \begin{pmatrix} 1 \\ -1 \end{pmatrix} E_0 \quad (4-46)$$

where θ is the angle of the quarter-wave plate, $\Delta\Phi$ is the phase difference between two polarizations. The photon spin state is:

$$|\chi\rangle = a_L(\theta)|\downarrow\rangle + a_R(\theta)|\uparrow\rangle, \quad (4-47)$$

and same for intensities:

$$I_E = k_L(\theta)I_0 + k_R(\theta)I_0 \quad (4-48)$$

The expectation value of a spin can be evaluated by

$$\begin{aligned} \langle S \rangle = \langle \chi | S | \chi \rangle &= \left\langle \begin{pmatrix} a_R(\theta) \\ a_L(\theta) \end{pmatrix} \middle| \hbar \begin{pmatrix} 1 & 0 \\ 0 & -1 \end{pmatrix} \middle| \begin{pmatrix} a_R(\theta) \\ a_L(\theta) \end{pmatrix} \right\rangle \\ &= \hbar(|a_R(\theta)|^2 - |a_L(\theta)|^2) = \hbar(k_R(\theta) - k_L(\theta)). \end{aligned} \quad (4-49)$$

After some algebraic operations $k_L(\theta)$ and $k_R(\theta)$ can be expressed by the simple trigonometric functions. In order to do that we multiply linearly polarized electric field by quarter-wave plate matrix (Q), left/right handed circular polarizer (L/R) and find the intensity of the final electric field. The expression for $k_L(\theta)$ is following:

$$\begin{aligned} E_L(\theta) = LQ \begin{pmatrix} 1 \\ 0 \end{pmatrix} &= \frac{1}{2} \begin{pmatrix} 1 & -i \\ i & 1 \end{pmatrix} \begin{pmatrix} \cos^2(\theta) + i \sin^2(\theta) \\ (1-i)\cos(\theta)\sin(\theta) \end{pmatrix} \\ &= \frac{1}{2} \begin{pmatrix} (\cos(\theta) - \sin(\theta))(\cos(\theta) - i \sin(\theta)) \\ (\cos(\theta) - \sin(\theta))(\sin(\theta) + i \cos(\theta)) \end{pmatrix}, \end{aligned} \quad (4-50)$$

$$k_L(\theta) = \frac{\langle E_L | E_L \rangle}{I_0} = \frac{1 - \sin(2\theta)}{2}. \quad (4-51)$$

Applying the same for $k_R(\theta)$ we get

$$k_R(\theta) = \frac{\sin(2\theta) + 1}{2}. \quad (4-52)$$

Now we can see that the dependence of the spin value on the orientation of quarter-wave plate is

$$\langle S \rangle = \sin(2\theta) \hbar. \quad (4-53)$$

If we launch elliptically polarized light through S-waveplate, we will get the superposition of two optical vortices with opposite topological charges. The ratio between these vortices will be same as the ratio between opposite circular polarizations at the input with the elliptically polarized light. The average OAM of the photon transferred by the S-waveplate is

$$\langle L(\theta) \rangle = -\langle S \rangle = -\sin(2\theta) \hbar. \quad (4-54)$$

As a result the average OAM value per photon can be not just integer number but any real number in the range $[-1 \ 1]$ and it can be controlled by simply rotating quarter-wave plate.

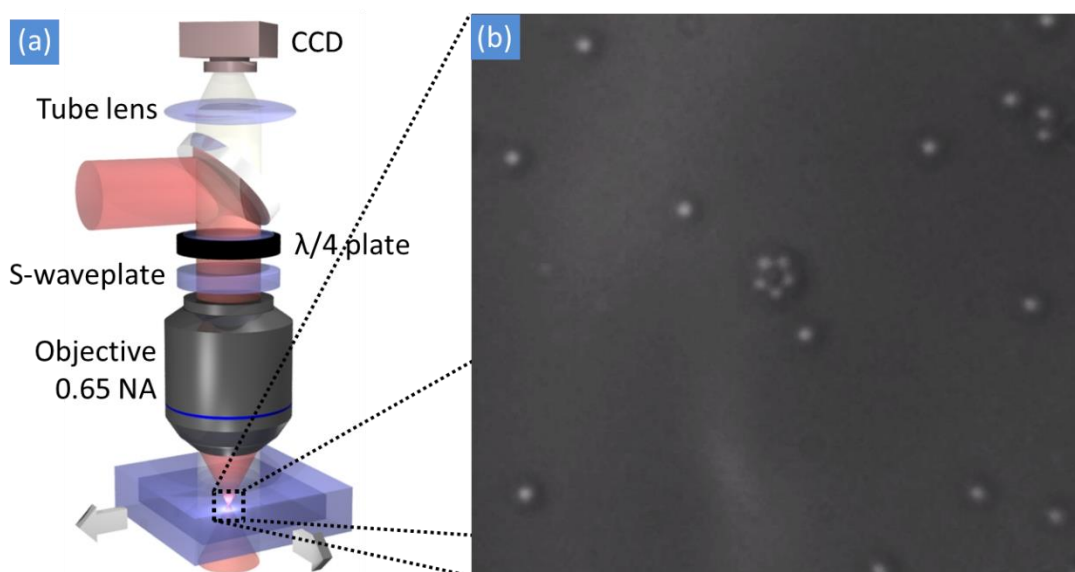


Figure 4-24 (a) Fused silica microspheres trapping experimental setup. (b) The image of five trapped spheres forming a ring.

In order to experimentally verify the control of the OAM we set up an “optical tweezers” for the trapping of fused silica spheres ($1\ \mu\text{m}$ size) dispersed in aqueous solution. The experiment was performed with femtosecond laser operating at $\lambda = 1030\ \text{nm}$, described in Chapter 3.1. To avoid the damage of silica spheres, the pulse duration was stretched from 270 fs to 14 ps and the repetition rate was set to the maximum (500 kHz). At these conditions the laser system was working as close to continuous wave regime as possible. The polarization of the laser beam was controlled by the quarter-wave plate mounted on the motorized rotational stage. After the quarter-wave plate the laser beam passed through the S-waveplate and was focused with 20x microscope objective (0.65 N.A.) into the cell filled with colloidal glass beads (Figure 4-24 (a)). The imaging was implemented by illuminating the sample with white light and recorded using CCD camera (Figure 4-24 (b)).

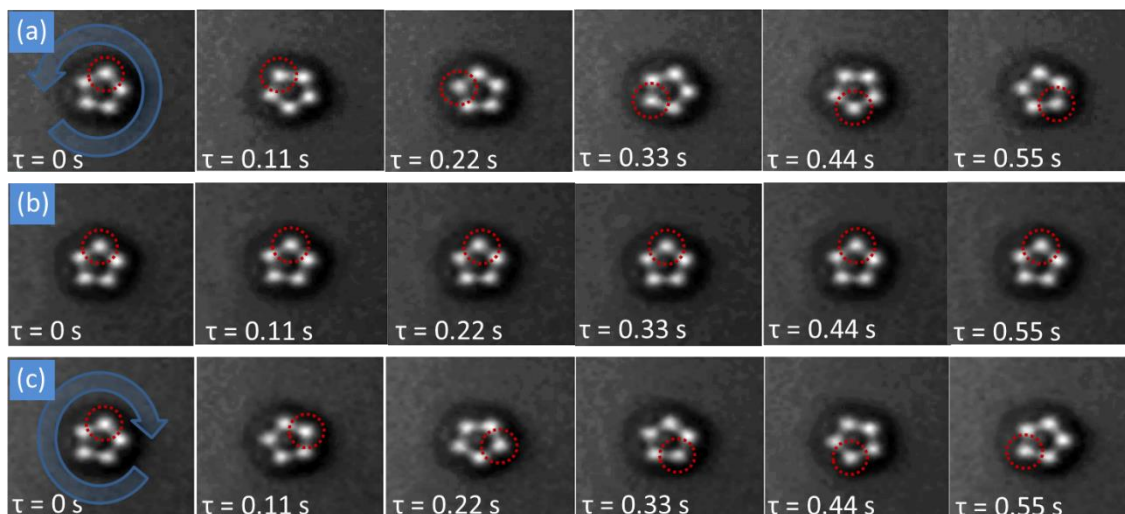


Figure 4-25 The rotation of five trapped spheres. Spheres rotates counter clockwise when polarization before the S-waveplate is right-handed circular (a) and clockwise when left-handed circular (c). Spheres do not rotate when polarization before S-waveplate is linear (b).

In the experiment five SiO_2 beads were trapped by the optical vortex forming a ring. When the angle of the quarter-wave plate was set to 45° (right handed circular polarization), spheres started rotating counter clockwise (Figure 4-25 (a)) what indicates left handed optical vortex ($l = -1$), as it was shown in Equation (4-41). By rotating quarter-wave plate by 90° we changed the handedness of polarization and the trapped particles instantly switched the direction of the rotation (Figure 4-25 (c)). When the quarter-wave plate was at 0° (i.e. we have linear polarization) the OAM of the beam vanished (Equation (4-54)) and the bead ring stopped rotating (Figure 4-25 (b)).

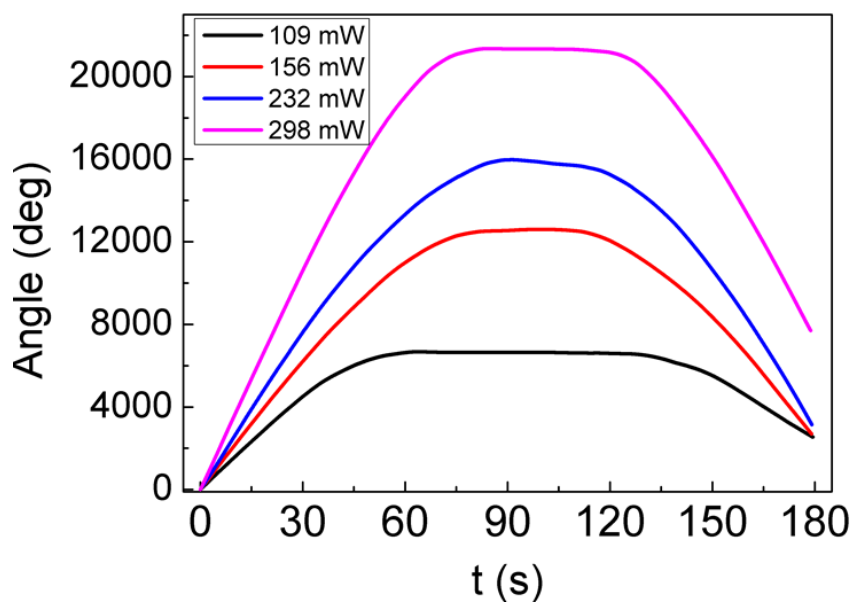


Figure 4-26 Total measured rotation angle (integral of the rotation speed) of trapped spheres at different laser trapping powers.

In order to measure the rotation speed of the ring and its dependence on the beam photons OAM, the quarter-wave plate was rotated with a constant angular speed of 0.5 deg/s from 45° to -45° . The rotation of the trapped particles was recorded for 180 seconds (Figure 4-26). As the rotation speed of the quarter-wave plate was kept constant, at any given time the angle of the wave plate is known: $\theta(t) = 45^\circ - 0.5^\circ \cdot t$, where the OAM can be calculated from Equation (4-54).

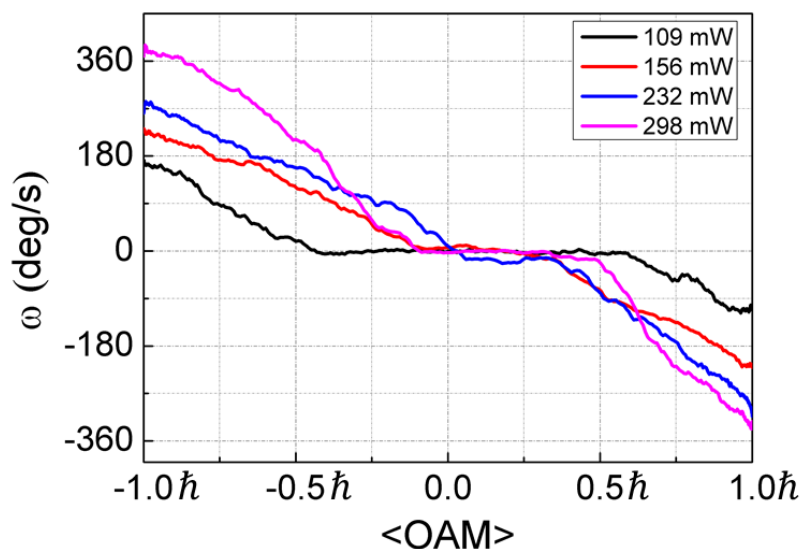


Figure 4-27 Rotation speed of trapped spheres dependence on the average orbital angular momentum of the photons at different average powers of the laser.

The rotation speed of the ring was calculated by comparing adjacent frames n and $n+1$. The frame $n+1$ was rotated by the angle $\Delta\theta$ and estimated the matching factor:

$$\chi_n(\theta)^2 = \sum_{i,j} (a_{n,i,j} - a(\Delta\theta)_{n+1,i,j})^2. \quad (4-55)$$

The lower the χ^2 , the more two frames match. In order to find the rotation angle between two frames, the minimum of the function $\chi(\theta)^2$ must be found. To make it safe, the rotation angle is defined in the range of $\Delta\theta = -36^\circ \div 36^\circ$. Adding the rotation angles between frames, the total rotation angle dependence on time is calculated. Then the dependence of trapped spheres rotation speed on OAM and laser average power is calculated (Figure 4-27).

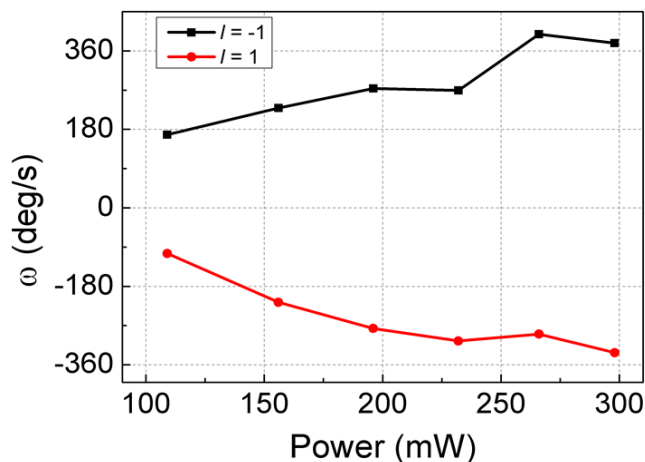


Figure 4-28 Rotation speed of trapped spheres dependence on (a) average laser power used for the trapping when $l = \pm 1$.

The lowest average power sufficient for trapping silica beads was 109 mW corresponding to the lowest rotation speed of about 90 deg/s when $l = \pm 1$ (Figure 4-28). Below this threshold the laser power was insufficient to keep particles in the ring. It means that if we control the rotation speed by changing average power of the laser, we cannot reduce the rotation speed below the certain value without letting particles free. But by changing the OAM of the beam we can transfer any lower than maximum value of torque to the particles by keeping the same trapping potential. When the OAM is approaching low values, the rotation stops earlier than it reaches zero due to the friction force and it causes zero speed plateau (Figure 4-27). In order for the vortex beam to rotate the beads, the rotation force has to be higher than the friction force. The width of the plateau depends on the laser power as the higher power means more photons and larger OAM per beam at the same average OAM per photon. Also there is noticeable asymmetry in rotation speeds at the positive and negative OAM. Figure 4-28 shows that the asymmetry is reducing with the increase of the laser power. It gives a clue that the force causing the asymmetry is small and does not depend on the laser power and at higher laser powers becomes over dominated the rotation force of the beam. Such a force could be preferential friction force which strength depends on the

rotation direction and could be caused by small imperfections of silica beads or small dusts.

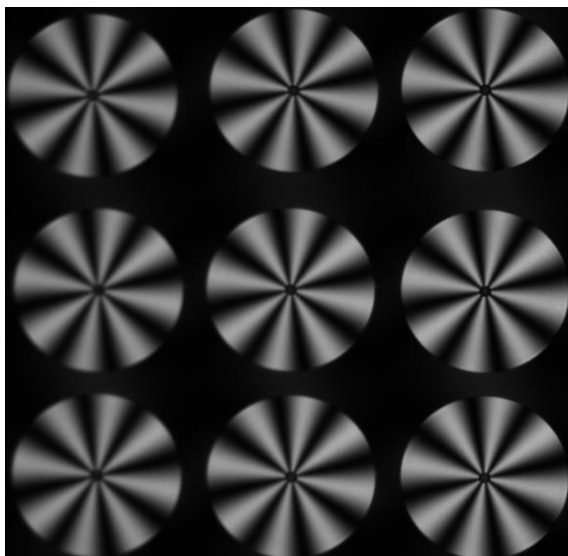


Figure 4-29 The array of nine polarization converters. Cross-polarized microscope image shows that the topological charge of converters is 4 (eight lobes). Such converter can be used in generation of optical vortex with tuneable OAM from $\langle L \rangle = -4\hbar$ to $\langle L \rangle = 4\hbar$.

In this demonstration the optical vortex together with OAM also had SAM. As the particles were transparent and non-birefringent, SAM did not have any effect on them. On the other hand, if it is necessary to have the angular momentum consisting only of OAM, quarter wave plate inserted after the S-waveplate would eliminate SAM from the beam.

As it was demonstrated in Chapter 4.3, this method of generating tunable optical vortices is not limited by topological charge 1 (Figure 4-17). Polarization converters can be written with higher topological charge n and therefore the average OAM of the transformed photons can be in a range from $\langle L \rangle = -n\hbar$ to $\langle L \rangle = n\hbar$. The fabrication technique also allows the production of array (Figure 4-29) of converters which enables trapping of more than one set of particles at the same time. Vortices with tunable OAM allows high control of rotation of any type of material and can be used for biomedical applications

measuring not only linear but also rotational elasticity of bio-objects such as DNA molecules [109].

4.6 Airy and Bessel beams converters

Wave packets that remain invariant during the propagation are called “diffraction-free” beams. Strictly speaking, such beams have to be infinite in space and carry infinite power. For these reasons they can propagate any distance without spreading. In practice, as the light beam has a certain finite power, as a result the diffraction eventually occurs. However, the rate of the diffraction is considerably slower compared to Gaussian beam. The best known example of “non-diffracting” wave is Bessel beam, first demonstrated in 1987 [135]. Other examples include higher order Bessel beams, Mathieu beams [136,137] and waves based on parabolic cylinder functions [138].

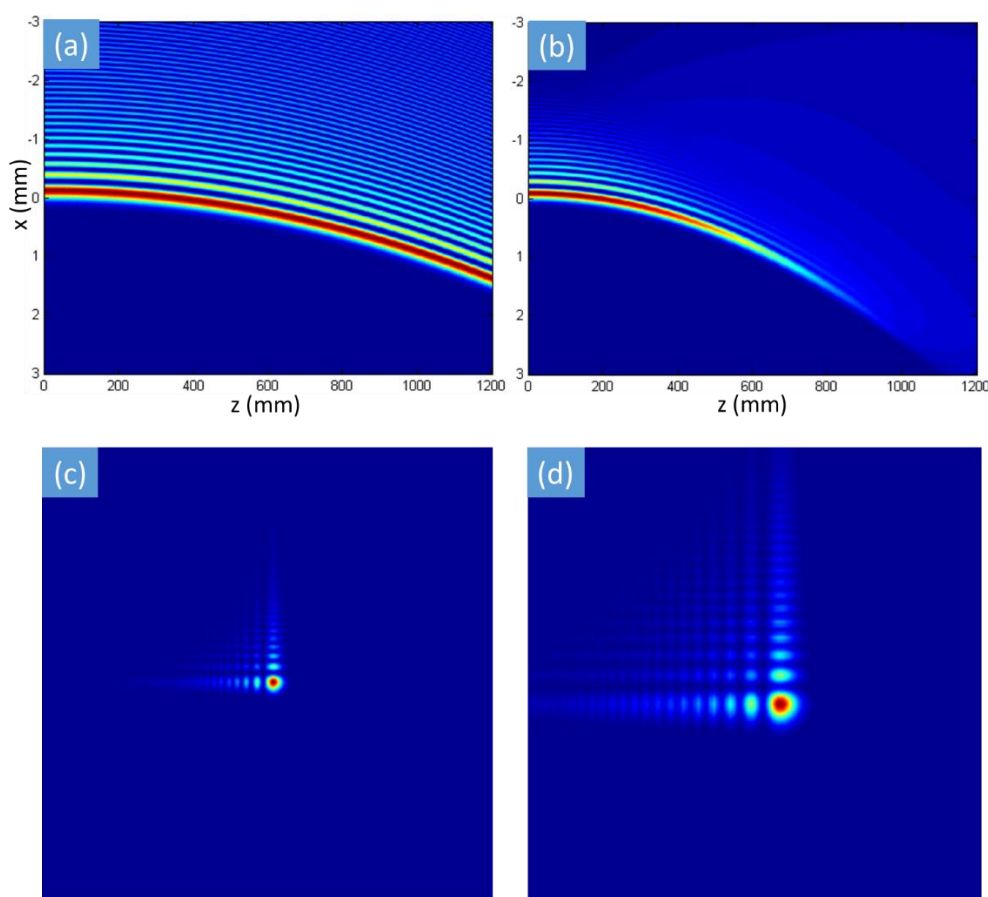


Figure 4-30 Propagation of one dimension (1D) infinite (a) and finite (Gaussian truncated) (b) Airy beams. (c, d) Beam profiles of two dimensional (2D) finite Airy beam. After propagating the maximum of the beam shifts from the centre (d).

Another recently explored class of “diffraction-free” wave packets are Airy beams. The first Gaussian truncated optical Airy beams were experimentally demonstrated by Siviloglou *et al.* [139]. The envelope of such beams is described by a truncated Airy function. The most interesting attribute is their ability to freely “accelerate” in the transverse direction even in the absence of any external potential (Figure 4-30). As others “non-diffracting” beams, Airy beam should have infinite power in order to be really “diffraction-free” (Figure 4-30 (a)). In real beams, Airy function has to be truncated, but they still preserve most of features of infinite Airy beams (Figure 4-30 (b)). Similarly to the Bessel beams, Airy beams also exhibits “self-healing” properties [140]. It was shown to be significant in optical micro-manipulation of small particles [141], the generation of curved plasma channels [142], supercontinuum generation [143] and laser micromachining [144]. Also, as Airy function is the unique one-dimensional non-spreading solution of Maxwell equation [145], “non-dispersing” pulses in linear regime can be implemented [146,147].

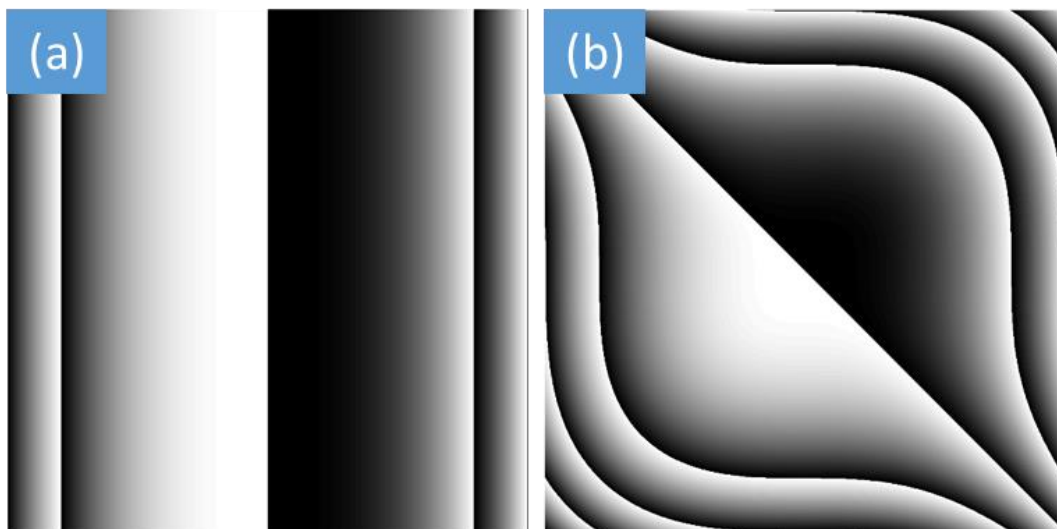


Figure 4-31 Modelled cubic 1D (a) and 2D (b) phase distribution which could be used with SLM to generate Airy beam.

The generation of the Airy beam is based on the fact that the angular Fourier spectrum of an exponentially truncated Airy function is a Gaussian beam with a

cubic phase modulation [145]. In this context, in order to generate Airy beams, the cubic phase (Figure 4-31 (a), (b)) must be imprinted into the Gaussian beam and the angular Fourier transformation implemented by a converging lens. Several methods were proposed to generate optical Airy beams. The straightforward way to control the phase of the beam and add the cubic phase modulation into it is to use spatial light modulator (SLM) [139]. This method is useful when properties of the beam is adjusted dynamically during the experiment [148]. However, this process requires delicate and expensive setup, which does not tolerate high laser powers. Additionally the phase is wrapped inducing high scattering losses. Alternatively, Airy beams can be generated using cubic phase masks [142,143], three-wave mixing process in an asymmetrically modulated quadratic non-linear optical media [149], or by exploiting optical aberrations induced by tilting a simple spherical lens [150]. But these methods also suffer from certain drawbacks. For example, the fabrication of phase mask requires expensive lithography techniques giving the wrapped phase; asymmetric poling for nonlinear Airy beam is limited to 1D beam generation and lens tilting requires extremely precise alignment.

Here I present a simple and effective way of generating Airy beams by exploiting femtosecond laser fabricated beam converter which is based on laser induced nanogratings in fused silica glass [151]. As it was mentioned in previous chapter, nanogratings due to their form birefringence can control not only the state of the polarization. Half-wave retarder, which is possible to achieve by single layer of laser induced nanogratings [54], can also control the phase of the circular polarization.

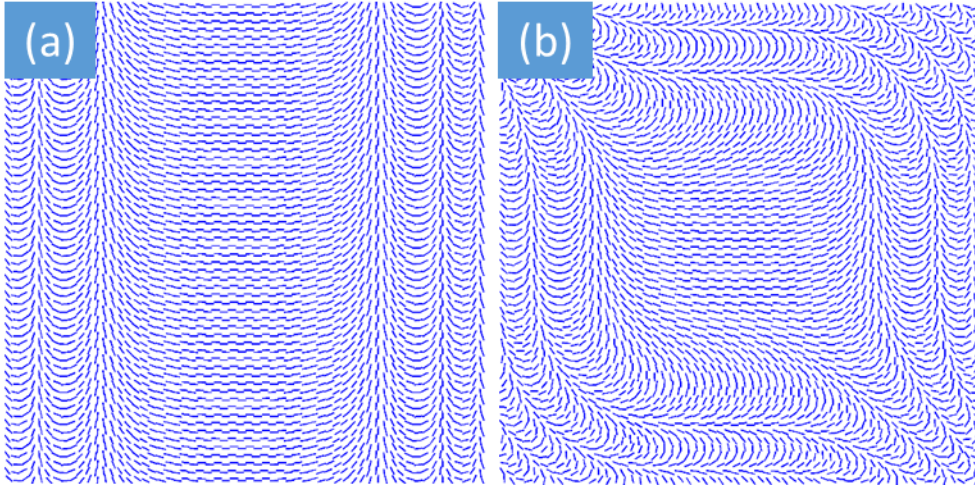


Figure 4-32 Schematic drawing of the birefringent optical element with 1D (a) and 2D (b) cubic slow axis distribution of the micro half-wave plates. Such optical elements work as phase element for circularly polarized light and can be used as Airy beam converter having no phase discontinuity as in Figure 4-31.

This effect can be described using Jones calculus. Multiplying half-wave plate Jones matrix M with Jones vector for the left-handed circular polarization, we obtain:

$$M(\theta) \begin{pmatrix} 1 \\ i \end{pmatrix} = \begin{pmatrix} \cos 2\theta & \sin 2\theta \\ \sin 2\theta & -\cos 2\theta \end{pmatrix} \begin{pmatrix} 1 \\ i \end{pmatrix} = e^{2i\theta} \begin{pmatrix} 1 \\ -i \end{pmatrix} \quad (4-56)$$

where θ is the angle of the half-wave plate slow axis. The second term of the product indicates that the handedness of polarization flips from the right- to left-handed. The first term shows the phase delay which depends on the orientation of half-wave plate ($\phi=2\theta$). Thus depending on the angle of slow axis, the transmitted light can acquire phase from 0 to 2π . The arbitrary phase element can be produced using phase truncation as for typical diffraction element design. In order to have optical element with cubic phase distribution

$$\varphi(x, y) = \left(\frac{x}{a}\right)^3 + \left(\frac{y}{a}\right)^3, \quad (4-57)$$

the azimuth of the half-wave plate slow axis must be modulated as following:

$$M\left(\frac{1}{2}\left(\frac{x}{a}\right)^3 + \frac{1}{2}\left(\frac{y}{a}\right)^3\right)\begin{pmatrix} 1 \\ i \end{pmatrix} = e^{\left(\frac{x}{a}\right)^3 + \left(\frac{y}{a}\right)^3} \begin{pmatrix} 1 \\ -i \end{pmatrix}. \quad (4-58)$$

Such birefringent structure (Figure 4-32) does not have discontinuity and will not suffer from scattering caused by the phase discontinuity that the SLM has (Figure 4-31). Moreover, the structure is polarization sensitive as the left-handed circular polarization input would give opposite sign of the phase shift compared to the right-handed:

$$M\left(\frac{1}{2}\left(\frac{x}{a}\right)^3 + \frac{1}{2}\left(\frac{y}{a}\right)^3\right)\begin{pmatrix} 1 \\ -i \end{pmatrix} = e^{-\left(\frac{x}{a}\right)^3 - \left(\frac{y}{a}\right)^3} \begin{pmatrix} 1 \\ i \end{pmatrix}. \quad (4-59)$$

Thus the same optical element introduces different phase shift for different circular polarizations. As a result, polarization diffraction grating can be implemented, where the light diffraction is controlled by the handedness of polarization [68]. The same principle can be found in optical vortex converters where the polarization handedness defines the sign of topological charge [67].

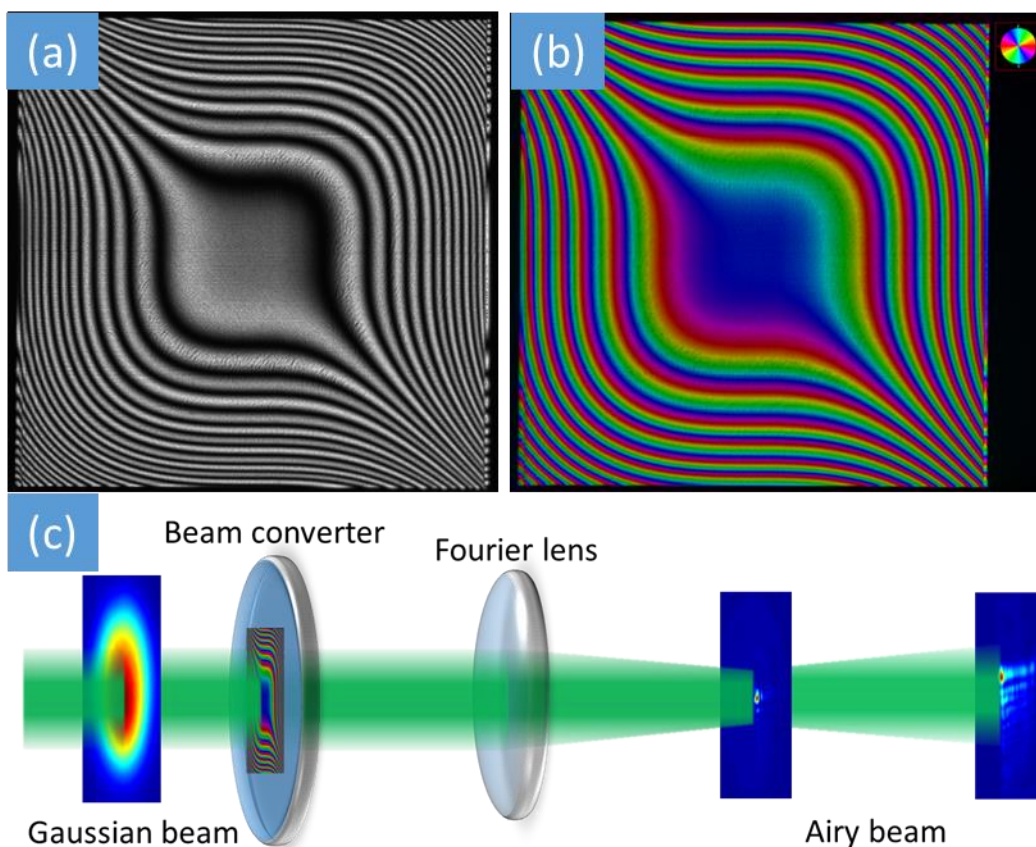


Figure 4-33 Microscopic image of the fabricated 2D Airy beam converter between cross-polarizers (a) and quantitative birefringence microscopy image (b), where pseudo-colour represents slow axis angle. Structure size is 2×2 mm. (c) The schematics of generating Airy beam using polarization sensitive beam converter.

Two 1D and 2D Airy beam converters were fabricated. The structures were imprinted with the femtosecond laser (described in Chapter 3.1) operating at 1030 nm and delivering pulses stretched to 800 fs at 200 kHz repetition rate. The pulse energy was set to 0.75 μJ . The light beam was focused via a $\times 10$ (0.16 NA) aspheric lens into a fused silica plate 300 μm below the surface. The control of the incident beam polarization azimuth was performed with an achromatic half-wave plate mounted into a motorized rotation stage. The sample was placed onto a three-axial translation stage. Structure of 2×2 mm size was fabricated at 2 mm/s laser writing speed. Nanogratings written under

these conditions induce retardance of ~ 257 nm, which corresponds to half wave for 515 nm wavelength.

The structures were fabricated by juxtaposing laser tracks leaving $1 \mu\text{m}$ distance between adjacent tracks. The translation stages were moving at the constant speed and the rotational stage controlling the half-waveplate was programed to have an angle

$$\theta = \frac{1}{4} \left(\left(\frac{(x - x_0)}{a} \right)^3 + \left(\frac{(y - y_0)}{b} \right)^3 \right), \quad (4-60)$$

where the coordinates of the laser beam are (x, y) and the coordinates of the center of structure is (x_0, y_0) . The angle is expressed in degrees. In 2D converter case $a = b = 700 \mu\text{m}$ and in 1D case $a = 300 \mu\text{m}$, $b = \infty$.

Fabricated converters were investigated under the Olympus BX51 microscope and the quantitative birefringence measurement system (CRi Abrio) (Figure 4-33 (a, b)). The sample was illuminated with 546 nm light. Cross polarized imaging (Figure 4-33 (a)) indicates that the retardance is close to the half-wave at the 546 nm and the slow axis orientation image (Figure 4-33 (b)) shows the cubic distribution of the orientation.

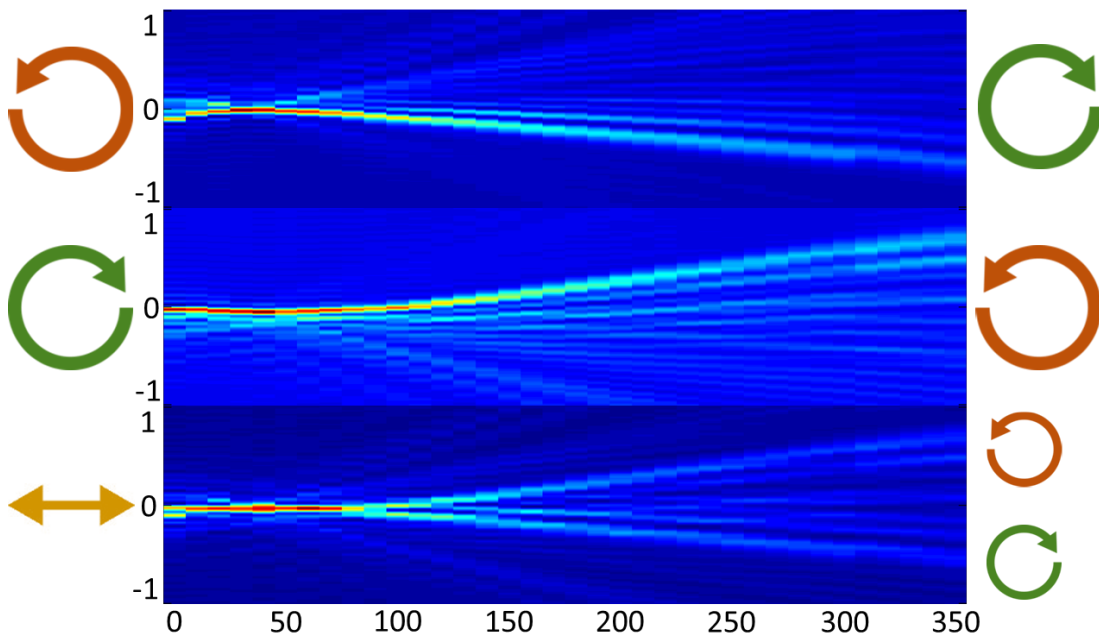


Figure 4-34 Propagation of 1D Airy beam. Arrows on the left indicates the polarization of incident Gaussian beam and arrows on the right - the polarization of generated Airy beams. Scale is in mm.

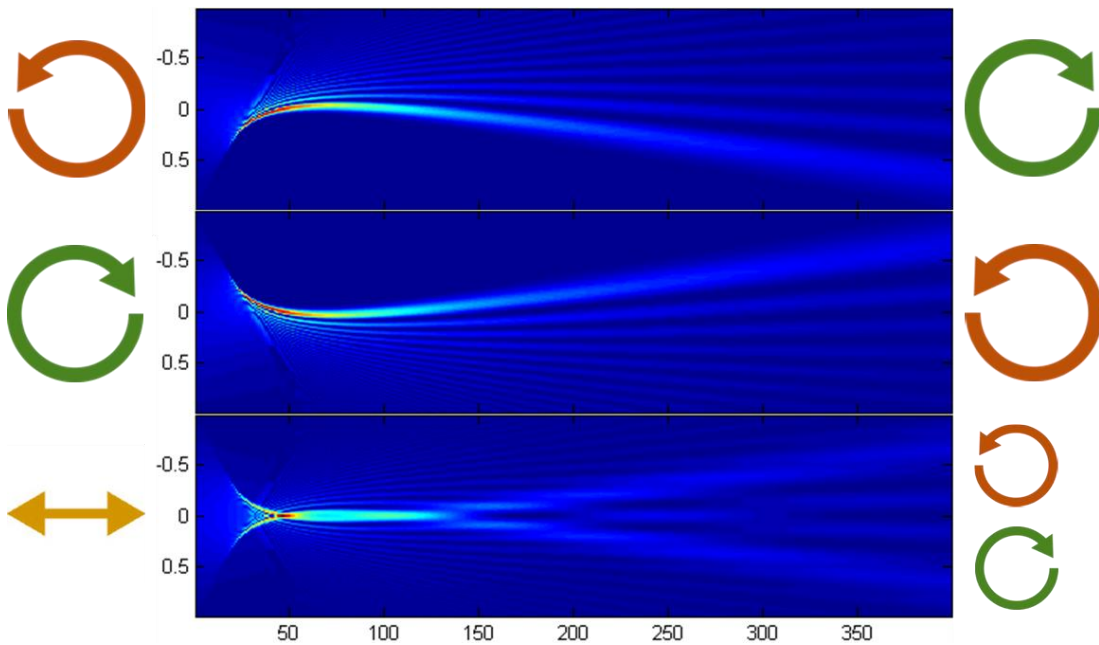


Figure 4-35 Modelled propagation of 1D Airy beam with same conditions as in Figure 4-34. Scale is in mm.

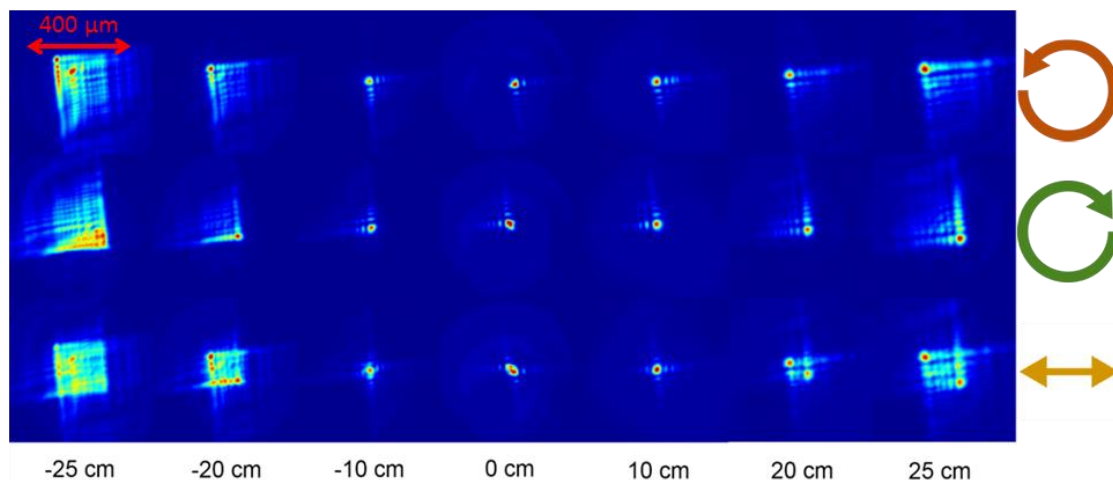


Figure 4-36 Experimental characterization of 2D Airy beam propagation. Arrows indicate the polarization of the input light (left-/right-handed circular polarization and linear polarization). In the case of linearly polarized input the dual Airy beam is generated.

The Airy beam was generated by launching an Ar⁺-ion laser (515 nm) beam through the imprinted structure and a converging lens (Figure 4-33 (c)). The beam profiles at different distances were taken with a CCD camera mounted on the optical rail (1D – Figure 4-34, 2D – Figure 4-36). In the vicinity of the Fourier lens, bended caustics of the laser beam can be clearly seen indicating successful conversion of Gaussian laser beam into finite energy Airy beam. For the comparison, the simulation of 1D Airy beam generation with Airy beam converter and propagation can be found in Figure 4-35. As it was discussed above, the phase modulation added by the converter depends on the handedness of the circular polarization. As a result, we can see that the acceleration direction is opposite for the different input polarizations (the first and the second row in Figure 4-34, Figure 4-35 and Figure 4-36). While the linear polarization can be described as a superposition of two circular polarizations, the superposition of two Airy beams is generated (the third row in Figure 4-34, Figure 4-35 and Figure 4-36).

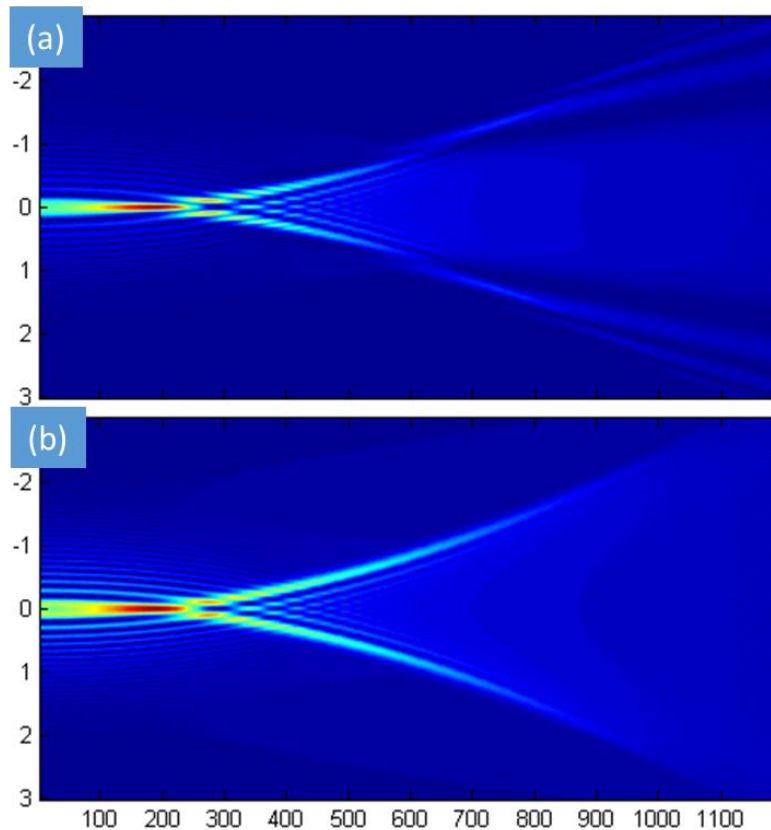


Figure 4-37 Simulation of propagating dual Airy beam. (a) Dual Airy beam when the two branches have same polarization and therefore interference can be seen. (b) Dual Airy beam when the two branches are orthogonally polarized and do not interfere (Airy beam converter case).

The branches of the dual beam have the opposite handedness circular polarizations, therefore they do not interfere (Figure 4-37). Using dual beam it is easy to measure the deflection angle at a certain distance just by taking a single beam profile, as it can be calculated by measuring distance between the two branches. For example in our case (Figure 4-34) after 30 cm propagation, the deflection angle is 0.15° . The power ratio for two branches is controlled by changing the ellipticity of the input beams' polarization similarly to a simple polarization grating [68]. The dual Airy beam was described theoretically before and was claimed to have better self-regeneration properties [152]. In

our case beam is different when two branches have orthogonal states of polarization. Such beam could give an extra advantages to the previously mentioned Airy beam trapping [141] and curved plasma channels generation experiments [142]. Also it gives possibility to generate dual Airy pulse overlapping just at a certain time.

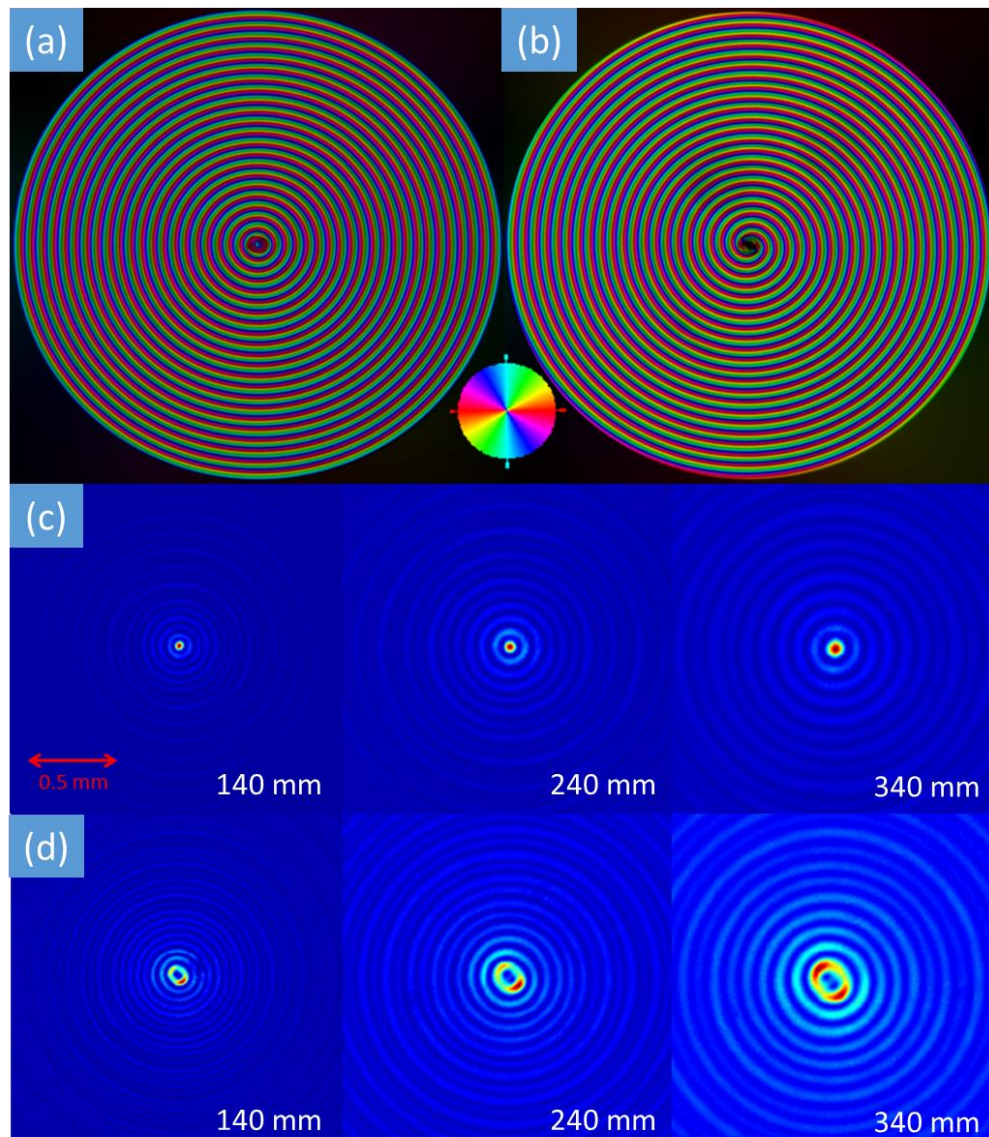


Figure 4-38 Abrio images (distribution of birefringence slow axis) of polarization sensitive Bessel beam (zero order (a) and second order (b)) converters. (c, d) Beam profiles of generated zero and second order Bessel beams, measured at different distances from the focus plane.

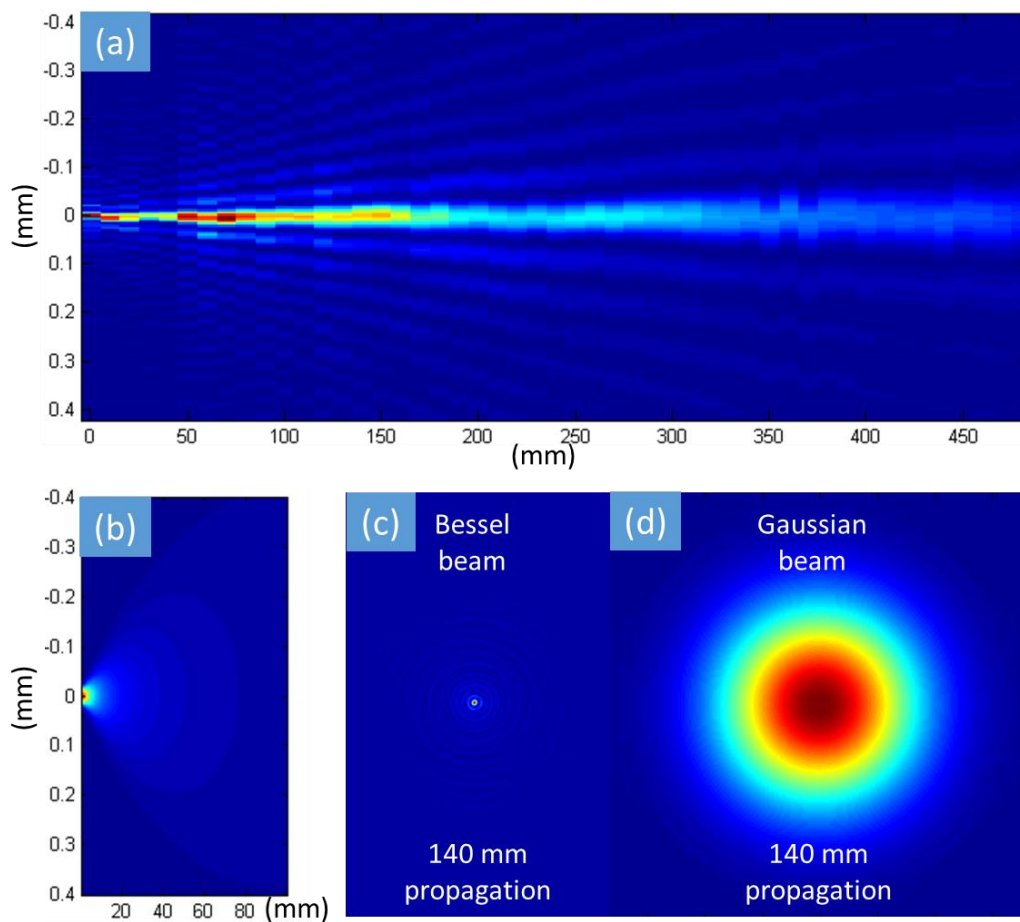


Figure 4-39 Measured propagation of zero order Bessel beam (a) and simulation of Gaussian beam (with similar beam waist at the focus) propagation (b). Measured beam profile of Bessel beam (c) and modelled beam profile of Gaussian beam at 140 mm distance from the focus plane (d).

Nanogratings ability to control the phase of circularly polarized light can be used for other beams generation too. Basically any manipulation of light, which requires manipulation of the phase, can be implemented with converter based on nanogratings. The second demonstration of beam converter based on nanogratings is Bessel beam converter. As in Airy beam converter's case, firstly we need to find the phase distribution required for Bessel beam converter. Typically zero order Bessel beams are generated by focusing Gaussian beam with axicon lens. The phase of axicon has the distribution of

$$\varphi(r) = \tan((n - 1)\alpha) \cdot 2\pi \cdot r, \quad (4-61)$$

where r is polar coordinate, n – refractive index of the glass, α – the angle of the axicon. Higher order Bessel beams have phase helicity which means that the phase of the converter depends also on polar angle ϕ :

$$\varphi_l(r, \phi) = \tan((n - 1)\alpha) \cdot 2\pi \cdot r + l\phi, \quad (4-62)$$

where l is the order of Bessel beam. Other steps of fabricating Bessel beam converters are the same as for Airy beam converters.

Zero and second order Bessel beam converters for 515 nm were fabricated. Abrio images show the wanted distribution of birefringence slow axis (Figure 4-38 (a, b)). Right-handed circularly polarized laser beam (Ar⁺-ion laser, 515 nm) was launched through the converters and beam profiles at different distances were measured (Figure 4-38 (c, d)). Beam profiles had the specific features attributed to Bessel beams. The centre of the second order beam did not have a perfect ring shape (Figure 4-38 (d)) as it would be expected from the vortex beam. This was probably caused by the retardance value of the converter not being exactly half-wave (Figure 4-14 (c)).

The propagation of generated zero order Bessel beam was compared with the propagation of Gaussian beam (Figure 4-39). The radius of Bessel beam in the focus was not larger than 10-15 μm . As the pixel size of the beam profiler is 4.65 μm , it is hard to measure precisely. After 0.5 m propagation, the diameter of the beam increased only around 5 times (Figure 4-39 (a)). For comparison the propagation of Gaussian beam (20 μm radius) was simulated with MATLAB (Figure 4-39 (b)). Also profiles of measured Bessel beam and simulated Gaussian beam 140 mm after the focus are compared (Figure 4-39 (c, d)). This illustrates the ability of generated Bessel beam to suppress diffraction for long distance.

High damage threshold of birefringent converters allows exploiting them for laser material processing. To demonstrate the applicability of the Airy beam converter, we performed laser machining using 2D Airy beam. The non-diffractive nature and “self-healing” properties of Airy beams enable cutting of reasonably thick samples in a single pass [144]. Recently, a 70 μm thick diamond and silicon slides were successfully cut with Airy beams generated using spatial light modulator producing beveled surface edge. Substantial interest emerged using lasers for a thin glass cutting in consumer electronics [153,154]. The curved caustics of Airy beam could help improving quality of the cut where the beveled edge would smooth out sharp corners of the glass plate minimizing possibility of cracking.

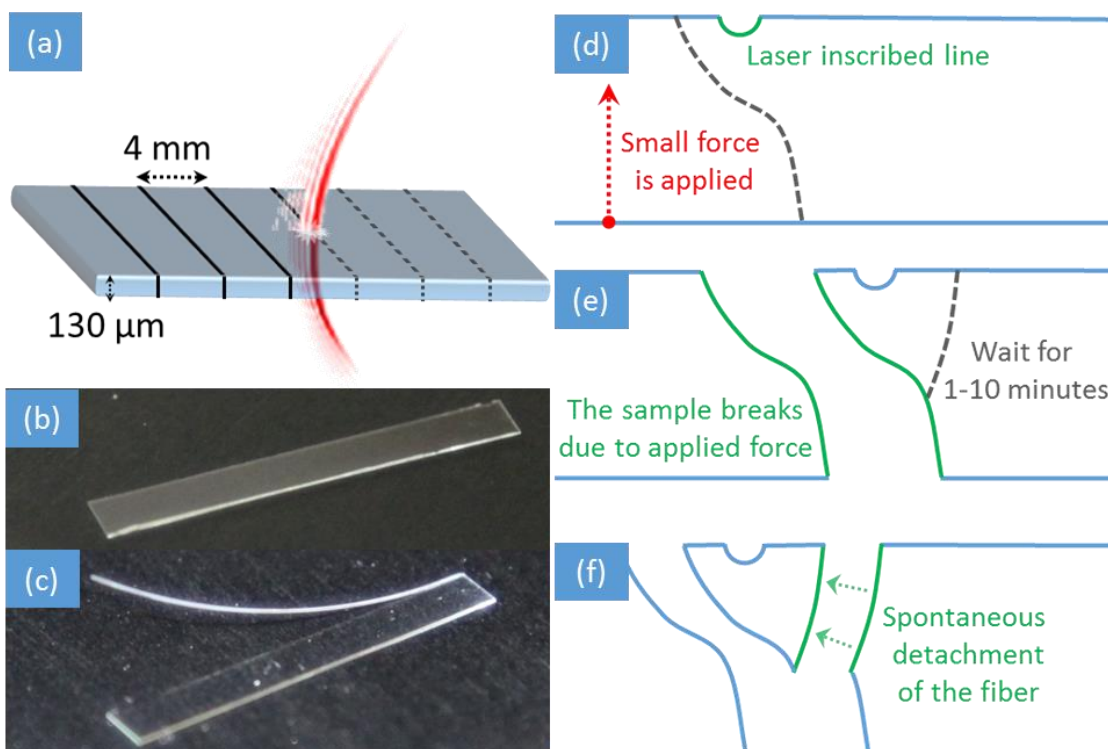


Figure 4-40 The scribing of the glass slide using Airy beam (a). After breaking sample to stripes (b), the fiber-like structure separates from the one side in few minutes (c). (d)-(f) The schematic drawing illustrating laser inscription, the breakage and the spontaneous detachment of the fiber-like structure.

For the laser cutting experiments 130 μm thick borosilicate microscope cover slide was chosen (Figure 4-40 (a)). The laser power was set to 2 W at 200 kHz repetition rate and 300 fs pulse duration. Since the fundamental wavelength of the laser is 1030 nm, the new beam converter was fabricated. In order to have half-wave retardance at 1030 nm, two overlapping birefringent layers were imprinted.

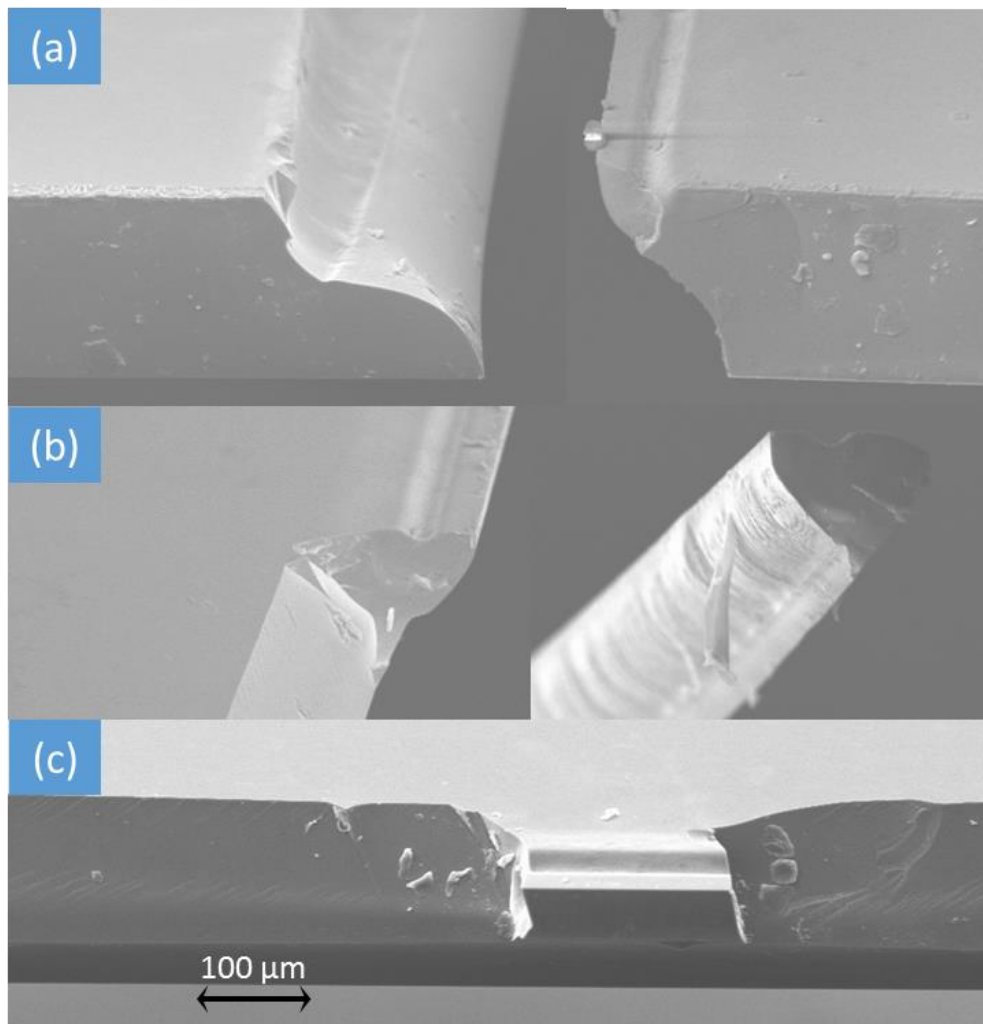


Figure 4-41 (a) The SEM image of the two opposite sides of the stripe. (b) The SEM image of the heart-shape fiber-like structure detached from the stripe and left over after the fiber-like structure is removed totally from the stripe.

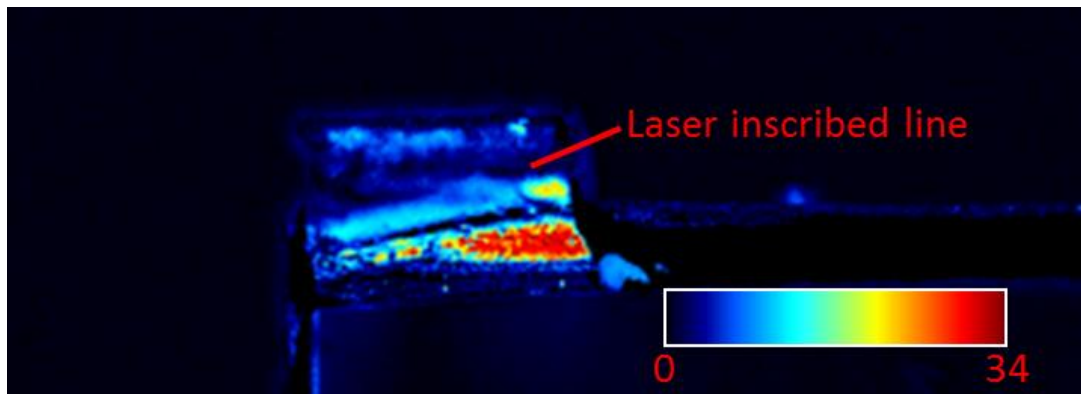


Figure 4-42 Retardance imaging of the same left over as in Figure 4-41 (b). Strong retardance near the inscribed line indicates the high accumulation of the stress which can lead to the spontaneous breakage.

The Airy beam was focused with 0.16 NA lens and the sample translated with 2 mm/s speed. In comparison to Mathis *et al.* [144], the sample in our experiment was thicker operating at lower number of pulses, longer pulse duration and less tight focusing conditions. As a result, the laser fluence was not sufficient to cut through the sample, but sufficient enough for scribing the sample (Figure 4-40 (d)).

After the processing experiment, small force was applied to break the substrate into the 4 mm stripes (Figure 4-40 (b)). If applied force has the direction as indicated in Figure 4-40 (d), it is enough a small touch to induce the breakage. On the other hand, if the sample is broken from the opposite side, it requires much larger force and mostly causes the asymmetric fractures. SEM images (Figure 4-41 (a)) reveal that the sample breaks along with the ~ 20 μm distance from the inscribed line. The schematics in Figure 4-40 (e) illustrate the shape of the produced crack.

Curiously we noticed that after leaving the separated glass stripes for few minutes, a thin fibre-like structure spontaneously detached from one side of the stripe (Figure 4-40 (c, f)). The separation was taking place in 1 to 10 minutes after breaking the sample. When the fibre separation process is

started, it takes 20-30 s to stand apart over the almost whole length of stripe. Due to the laser inscribed line, the cross-section of the fibre-like structure has the shape of a heart (Figure 4-40 (f), Figure 4-41 (b)). It always was observed only on one side of the stripe, which means it has to be related to the asymmetry of the Airy beam. The asymmetry of the Airy beam causes asymmetric stress distribution after the modification and therefore sample always breaks on one side of the modification rather than over the modification (Figure 4-40 (e)). On the other side of the inscribed line the stress is accumulated (Figure 4-42) which leads to spontaneous detachment of the fibre-like structure (Figure 4-40 (f)). Such a process could be a way of simple fabrication of cantilevers. Even though the fibre-like structure is not smooth (Figure 4-41 (b)), where the surface roughness could be removed by heating it [155].

In summary, exploiting the ability of femtosecond lasers to imprint birefringent modification inside fused silica glass, Airy and Bessel beam converters were fabricated. It was demonstrated the generation of 1D and 2D Airy beams and zero and second order Bessel beams. Converters are polarization sensitive which allows the generation of a dual Airy beams where two Airy beams with opposite acceleration directions propagates together. Thin glass laser scribing with Airy beam is demonstrated and as an outcome a simple way of cantilever fabrication is proposed.

4.7 Polarization sensitive camera

The primary physical quantities associated with an optical field are intensity, wavelength, coherence and polarization. The human eye and the majority of imaging devices are sensitive only to the first two parameters: intensity and wavelength. While spectral properties can give information about the material, polarization provides information on surface features, shape, shading and roughness. Adding to the imaging devices ability to detect polarimetric information could enhance contrast and reveal new details of the observed object. For instance birefringence, which is exhibited by various materials such as organic substances and crystals, could only be revealed by polarimetric analysis.

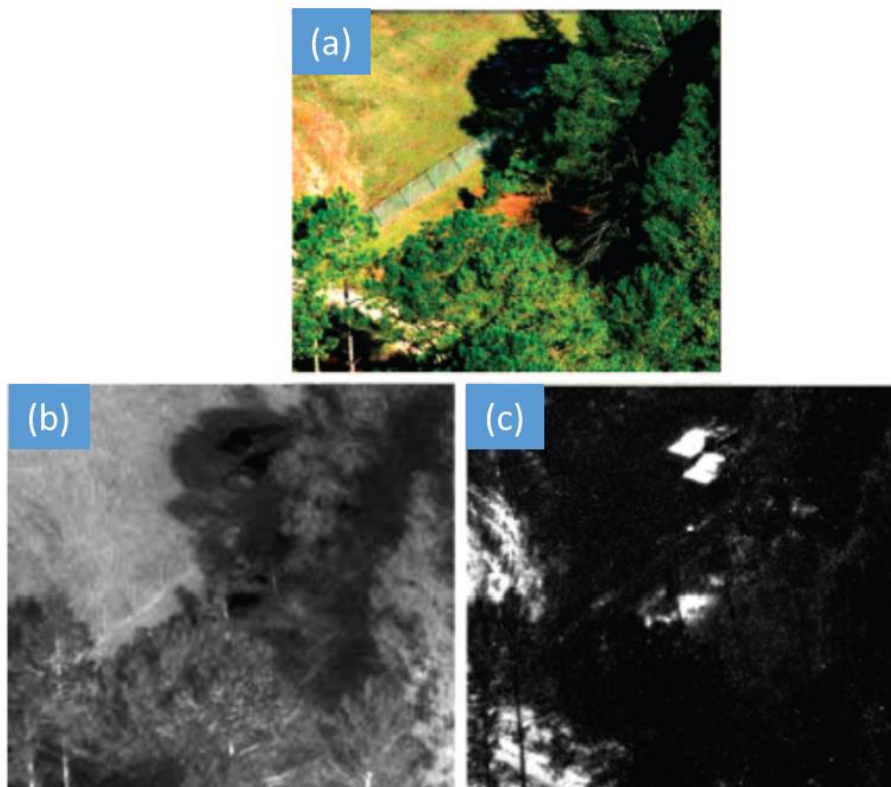


Figure 4-43 Visible picture of two pickup trucks in the shade (a), long-wave IR intensity image (b), and long-wave IR polarization image (c). Strong contrast in the polarization image shows advantages for enhanced target detection using imaging polarimetry. (Image source: J. S. Tyo *et al.* (2006) [156])

Polarimetric imaging can be an important tool in medicine. A number of biological tissues are known to be birefringent and polarimetric imaging can reveal some tissue structures that are not perceptible in standard optical imaging techniques [157–159]. It can be used for eyes tomography [160,161] or for detection of cancer in its early stages [162,163]. This technique can also help to detect radiation reflected from unnaturally smooth man-made objects (Figure 4-43) [156].

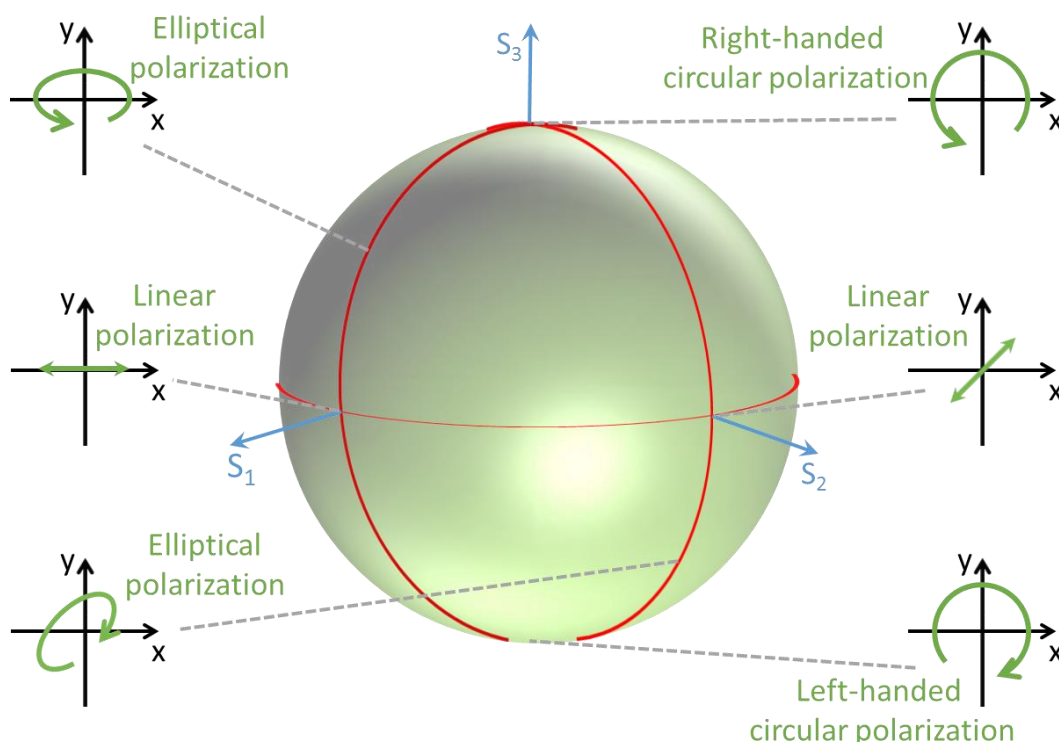


Figure 4-44 Poincaré sphere diagram. Stokes parameters S_1 and S_2 describes the linear part of the polarization and S_3 – the circular.

The full description of polarization can be achieved by measuring four Stokes parameters: S_0 , S_1 , S_2 and S_3 . Combination of these four parameters can describe the degree of the polarization and any point on the Poincaré sphere, i.e. any state of the polarization (Figure 4-44). Additionally, simple mathematical analysis can provide the information on birefringence, depolarization, and dichroism of the observed material. Normally, the Stokes

parameters are retrieved from multiple intensity images, which are analyzed using certain computational algorithms [71,164]. However, this approach can be applied only for imaging of static objects as full polarization information requires at least three measurements. Whereas real time characterization of polarization parameters requires instant acquisition of polarimetric data [156,165]. The solution to this problem can be the polarization analog of the Bayer mask, which allows instantaneous capturing of the polarization information [166,167]. The idea behind this approach is to measure all Stokes parameters simultaneously on a microscale level. Therefore, single image will provide full polarization information at the expense of the spatial resolution. However, standard polarizing elements, especially wave-plates, cannot be easily shrunk to the size of several microns and then assembled into a single mosaic element. Despite the polarizer matrix can be fabricated by spin coating and subsequent photolithographic processes, stacking three layers of polarizers to obtain a complete matrix is a relatively complex process [166].

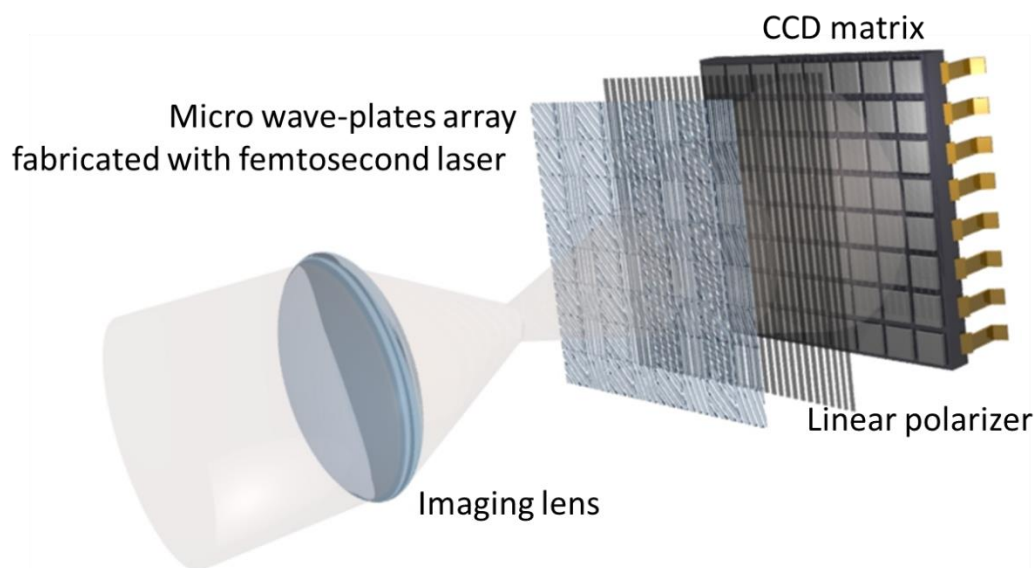


Figure 4-45 The basic schematic of the polarimetric camera. Before the light reaches a CCD matrix it propagates through micro waveplates array and a linear polarizer.

Alternatively, photolithography can be used for making micro-polarizers and wave-plates with subwavelength nanostructures [168,169]. Although this process can be successfully applied to devices operating in the infrared, the structure period for the visible would be around 200 nm, which complicates the fabrication process. An alternative approach is based on ultrafast laser induced nanostructuring [4,67]. This technique allows imprinting self-assembled nanostructures with periods down to 200 nm, which exhibit form birefringence [31]. Here we demonstrate technology based on femtosecond laser nanostructuring, which allows printing waveplates with dimensions of a few microns into the transparent material and permits single step fabrication of a compact polarization analyzer, converting an ordinary CCD or CMOS camera into a polarimetric data imaging device.

As it was mentioned above, a birefringent mask operates on a similar principle as the Bayer mask used in colour sensitive cameras, where four colour filters comprise one pixel to capture spectral information. Our polarimetric system consists of an array of micro waveplates, a linear polarizer and a CCD matrix (Figure 4-45). Each pixel is composed of four birefringent segments (three half-wave and one quarter-wave plates). The information provided by these four segments is sufficient to calculate all four Stokes parameters, which are described as

$$S_0 = I_0 + I_{90}, \quad (4-63)$$

$$S_1 = I_0 - I_{90}, \quad (4-64)$$

$$S_2 = I_{45} - I_{-45}, \quad (4-65)$$

$$S_3 = I_l - I_r, \quad (4-66)$$

where I_0 , I_{90} , I_{45} and I_{-45} are intensities of light measured after the linear polarizer oriented at 0° , 90° , 45° and -45° respectively and I_l and I_r are intensities measured after left- or right-handed circular polarizer.

The two top segments indicated as 'a' and 'b' represent the half-wave plates with slow axis orientations at 0° and 45° (Figure 4-46, left). Combined with a linear polarizer (0° orientation) they operate as two perpendicular linear polarizers and measure the full intensity of the incident light

$$I = I_a + I_b. \quad (4-67)$$

Taking the Stokes parameter S_0 to unity ($S'_0 = 1$), the normalized parameter S'_1 can be expressed as

$$S'_1 = \frac{I_a - I_b}{I} \quad (4-68)$$

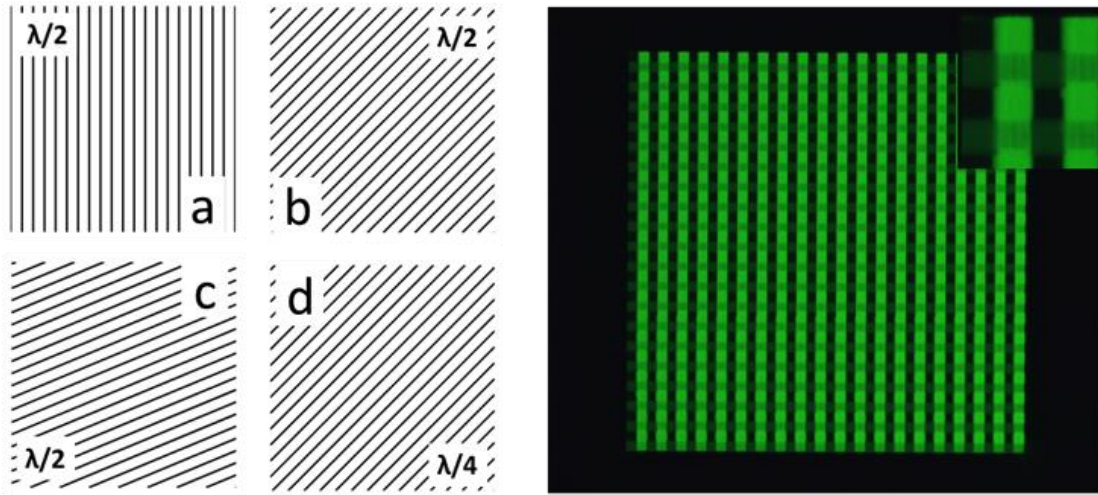


Figure 4-46 (Left) The schematic of one segment in the birefringent mask. The lines indicate direction of the imprinted nanogratings. (Right) The birefringent mask imaged in cross-polarizers (1×1 mm). The inset shows a zoomed segment of the mask.

The segment 'c' is a half-wave plate oriented at 22.5° and 'd' is a quarter-wave plate oriented at 45° . These segments combined with a linear polarizer are equivalent to a linear polarizer oriented at 45° and a circular polarizer. The normalized Stokes parameters S'_2 and S'_3 are expressed as

$$S'_2 = \frac{2 \cdot I_c - I}{I}, \quad (4-69)$$

$$S'_3 = \frac{2 \cdot I_d - I}{I}. \quad (4-70)$$

Four segments is enough to calculate Stokes parameters but in order to have good quantitative measurements, six or more segments per pixel should be fabricated as it would significantly reduce the errors [170]. Knowing the Stokes parameters, one can easily calculate the polarization degree and polarization orientation:

$$P^2 = S_1'^2 + S_2'^2 + S_3'^2, \quad (4-71)$$

$$\theta = \frac{1}{2} \arg(S_1' + iS_2'). \quad (4-72)$$

This can provide information about the object's surface and orientation of planes [156,167].

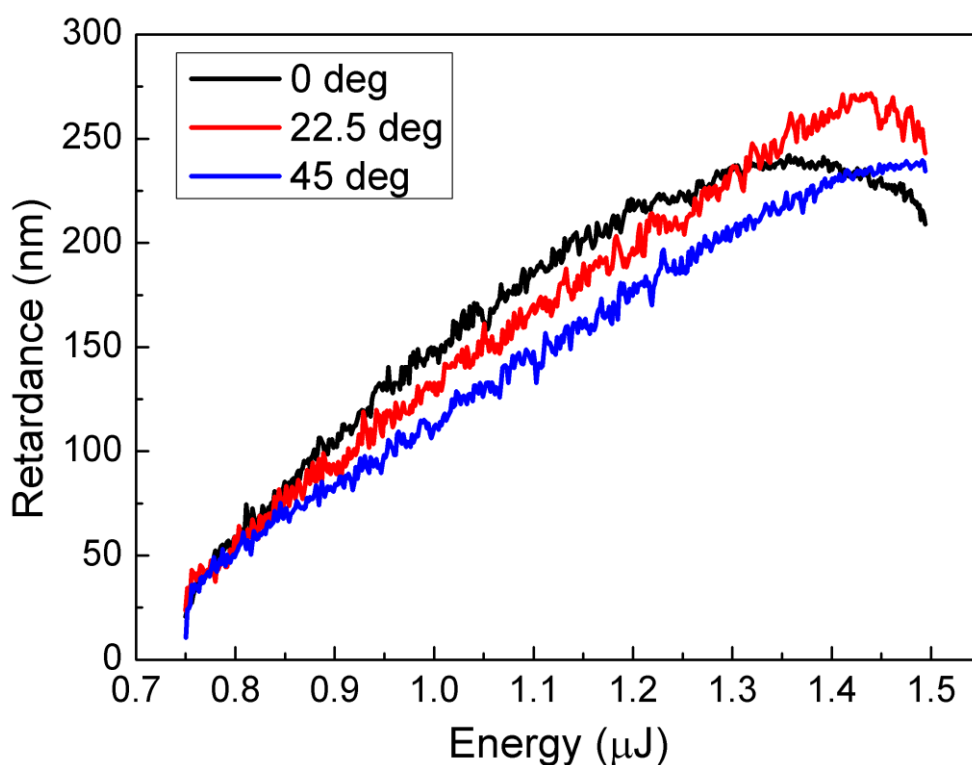


Figure 4-47 Retardance dependence on the laser pulse energy when written at different polarization orientations with respect to the writing direction.

The laser writing system is described in Chapter 3.1. The laser pulse was stretched to 700 fs. The laser beam was focused via a 0.16 NA aspheric lens into a fused silica. The optical elements were written at 200 $\mu\text{m/s}$ speed, at 200 kHz laser repetition rate.

The fabricated birefringent mask consisted of 20 \times 20 segments with each waveplate 25 \times 25 μm in size (Figure 4-46 (right)). The performance of the mask was tested by characterizing the polarization state produced by the radial polarization converter S-waveplate [67]. The mask was optimized for \sim 500 nm wavelength. Quarter- and half-wave plates were optimized for 500 nm wavelength by calibrating the retardance dependence on the laser pulse energy (Figure 4-47). The graph indicates that single layer modification is enough for half-wave plates at wavelength up to \sim 550 nm and for longer wavelength would need to fabricate two or more layers. Since the slow axis of the waveplates in the birefringent mask must be oriented in different directions (Figure 4-46 (a)) and the strength of the modification depends on the writing laser polarization direction [171], the calibration was performed for all three polarization directions (0°, 22.5° and 45°).

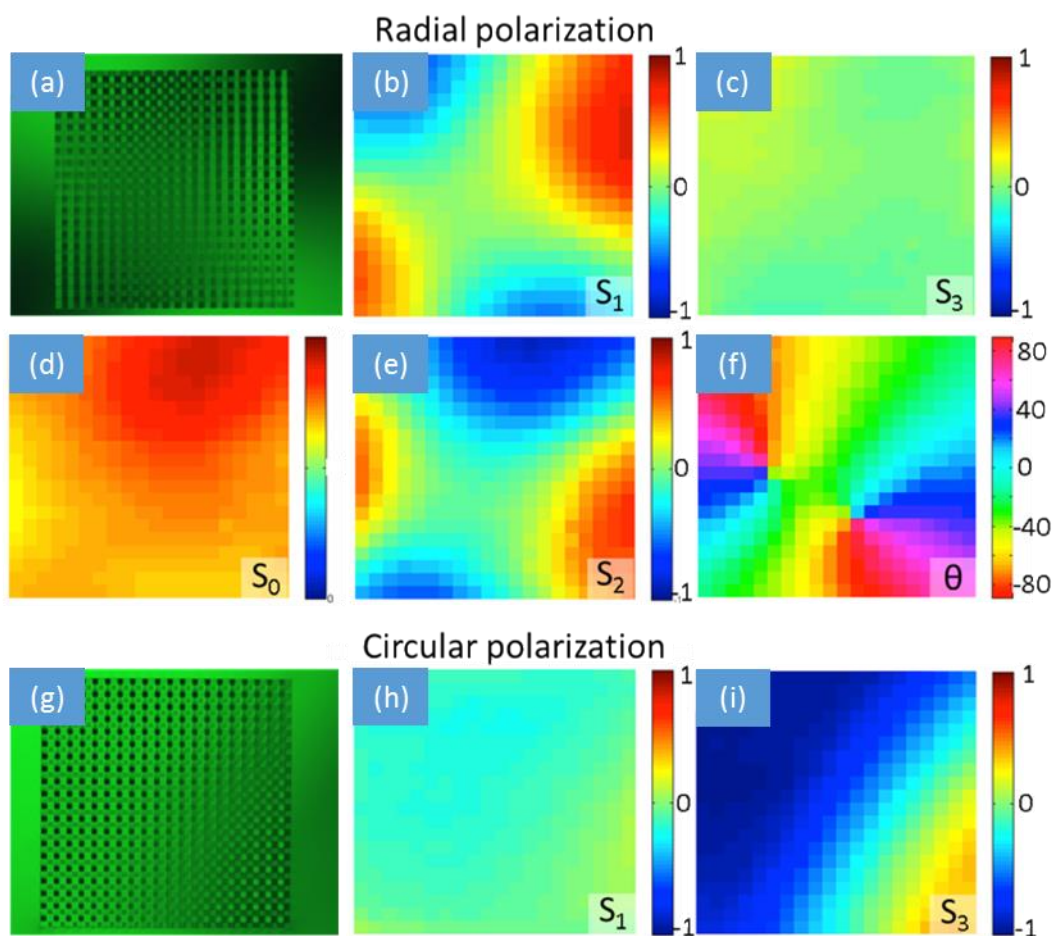


Figure 4-48 (a)-(f) The measurement of the polarization distribution in the radially polarized beam. (g)-(i) The transition of the circularly polarized light near the edge of the S-waveplate. (a) The image of the birefringent mask illuminated with the radially polarized light. (b)-(e) The distribution of the calculated Stokes parameters (S_0 , S_1 , S_2 and S_3). (f) The orientation of the linear polarization. (g) The image of the birefringent mask when it is illuminated with the circularly polarized light. (h)-(i) The distribution of the calculated Stokes parameters (S_1 and S_3).

The performance of the birefringent mask was tested with radially and circularly polarized light. The polarimetric measurements were carried out using an optical microscope BX51 (Olympus Inc.) (Figure 4-48 (a), (g)). The radial polarization was generated by inserting a band pass filter at 515 nm, a

linear polarizer and the S-waveplate into the optical path of the microscope. The values for the Stokes parameters were extracted by the algorithm developed in MATLAB (Equations (4-63)-(4-66)). The Stokes parameter S_0 (Figure 4-48 (d)) clearly shows that there is a small variation of intensity and the intensity measurement alone is not sufficient to retrieve any polarimetric information. In the radial polarization case, parameters S_1 and S_2 (Figure 4-48 (b, e)) indicate that the light is linearly polarized with electric field direction continuously varying in space. The small values of parameter S_3 (Figure 4-48 (c)) reveal the absence of the circular polarization component. Using the Stokes parameters S_1 and S_2 , the spatial distribution of the polarization plane direction was calculated (Equation 10) confirming the radial polarization of the incident light (Figure 4-48 (f)). The polarimetric camera was also successfully demonstrated for visualizing of the circularly polarized light (Figure 4-48 (h, i)). The circular polarization changes its handedness passing through the S-waveplate with the respect of circularly polarized background illumination. As a result the edge of the converter can be seen only in circular polarization (parameter S_3), whereas the distribution of the linear polarization (parameter S_1) is uniform.

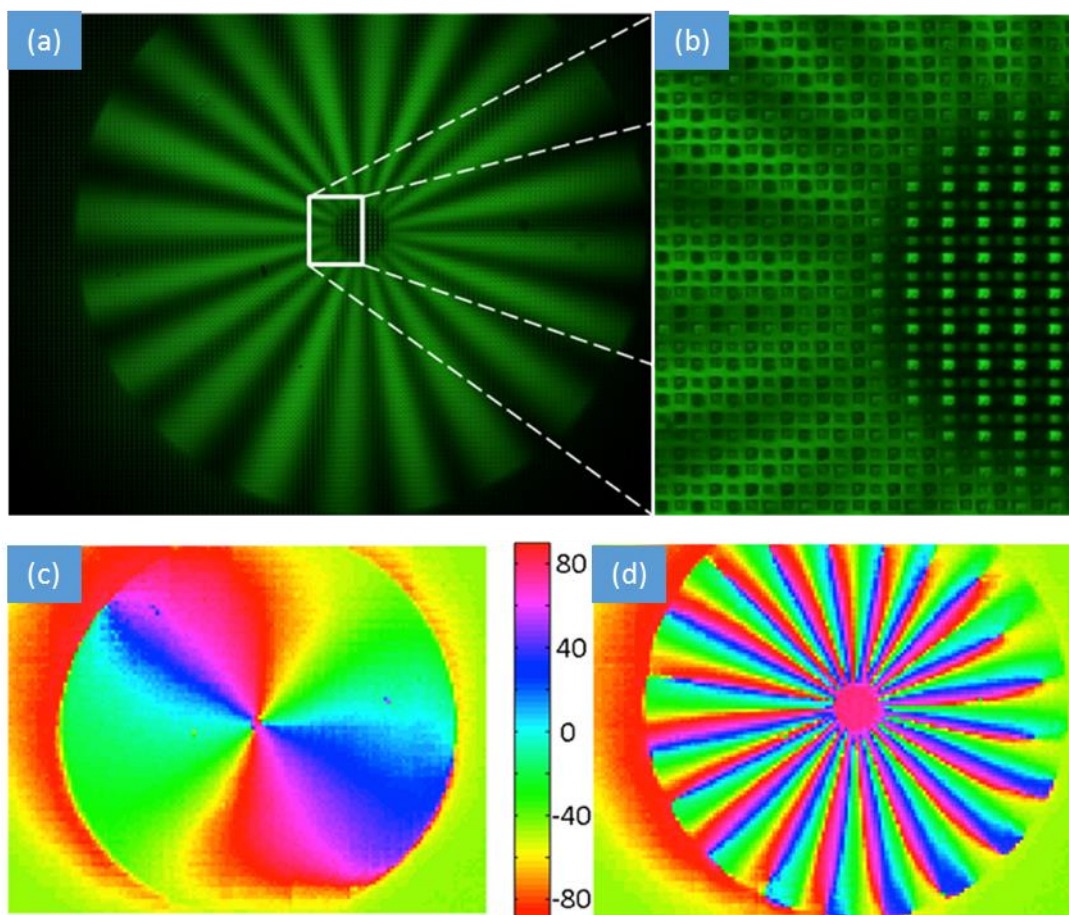


Figure 4-49 The measurement of the radially polarized light and the high order cylindrical vector (CV) beam with the high resolution waveplate mask. (a), (b) The image of the mask while illuminated with the high order CV beam. (c), (d) measured polarization distribution of the radially polarized light and the high order CV beam.

The inhomogeneity of the matrix is efficiently removed by the calibration process. In all cases, the measured polarization distribution follows the expected trend. The high quality of polarimetric images demonstrates the feasibility of the camera for polarization sensitive vision.

The polarization mask of 100×130 segments (overall size 4×5.2 mm) was fabricated for visualization of more complex polarization states. The size of the individual waveplates was reduced to 10×10 μm , with 10 μm gaps in

between eliminating the polarization cross-talk effect of the adjacent segments. There is no limitation to reduce the size of waveplates up to few microns and make them the same size as pixels in the typical CCD detector so it would not limit the resolution. In our case larger waveplates were easier to image on the detector. After the optimization of the fabrication process the writing speed was increased ten times to 2 mm/s. The total fabrication time was 4.4 hours but it could be reduced in various ways. As the fabrication does not require high average power, the same 6 W laser used in the experiments could fabricate at least 15 polarization masks during the same time. The other way to increase speed of manufacture is to use femtosecond laser to fabricate master and replicated it using micro-molding process [172].

For the high resolution imaging, the mask was projected onto the full-frame CMOS sensor of the Canon 5D Mark II camera. The radially polarized light and high order cylindrical vector beam (order number $l=10$) was successfully measured (Figure 4-49).

In conclusion, we have demonstrated a femtosecond laser written micro-waveplate array. The array with a single waveplate of a few micron size combined with a linear polarizer and a CCD sensor are combined into a polarization sensitive imaging device, which enables the real time polarimetric imaging. The imaging device can be potentially used for medical applications such as skin cancer diagnostics.

Chapter 5: Conclusions

In this theses I have reported my work related to femtosecond laser induced nanogratings: their properties and applications. Initial task was to find correct set of laser parameters which would allow fast laser fabrication (up to few mm/s) of uniform structures with high retardance values. Such fabrication parameters were found allowing the fabrication of polarization sensitive elements for wavelengths ranging from 500 nm to 1.5 micron.

For quarter-wave plate (or optical element based on micro quarter-wave plates) following parameters can be used: 700-800 fs pulse duration, 200 kHz laser repetition rate, 0.35 NA objective to focus laser beam, 1-2 mm/s fabrication speed, 140 mW average laser power. For half-wave plate: 700-800 fs pulse duration, 200 kHz laser repetition rate, 0.16 NA lens to focus laser beam, 1-2 mm/s fabrication speed, 350 mW average laser power. Elements for smaller or higher wavelength can be fabricated by adjusting average laser power. Also it was demonstrated that very high retardance values (>300 nm) can be achieved by fabricating few layers. This investigation allowed the possibility for high speed fabrication of various polarization sensitive optical elements.

By investigating laser polarization influence on the strength of induced retardance we have identified two different sources of the polarization dependence. One is related to stress induced birefringence and the other is produced by the spatio-temporal distortion of the laser pulse. Characterization of induced stress indicates that during the laser writing the material is dragged by the thermal gradient and leads chevron-shape stress distribution. Stress induced birefringence causes tilt in the front of tracks. As a result, the light polarized at 45° to the writing direction induces the highest retardance. The polarization dependence is strongly affected by the distance of laser written tracks. For overlapping tracks, this dependence is mainly defined by the stress induced birefringence. The PFT is playing the major role only for separated tracks. As a result, we demonstrate that overlapping of adjacent tracks can minimize the effect of spatio-temporal distortion. Polarization influence of the strength of retardance cannot be avoided, however the understanding of it allows us at certain conditions to overcome this effect by changing the method

of scanning. Good example of manipulation with scanning directions can be found in Figure 2-13 (3 and 6) where different sides of the structures are fabricated with perpendicular polarizations, however the strength of the retardance is same.

Stress induced retardance as high as 200 nm was observed in germanium sulphide glass because of a large photoelastic coefficient. The strength of the stress induced birefringence is very close to the values produced by self-assembled nanogratings in silica glass. The ability to control stress-induced birefringence in glasses with high photoelastic coefficients can be explored for the fabrication of birefringent optical elements such as polarization converters.

Annealing of femtosecond laser induced nanogratings experiments allowed to estimate very long the lifetime of nanogratings which is about 10^{34} years at the room temperature (pulse duration of the laser is 700 fs). Even though the number is too high to be accepted as realistic, it shows that we do not need to worry about the stability of the nanoratings. And even in the environment with higher temperatures (up to few hundreds °C) nanogratings would not lose their optical properties. The lifetimes of two quantitative properties were measured: retardance value and scattering. The same estimated lifetimes of retardance and scattering values indicates that parameters closely related and annealing cannot eliminate scattering without erasing birefringence. Also annealing can be used to control retardance value of fabricated structures, which allow reducing retardance to small values when it is difficult to do so by changing laser parameters.

Polarization converters converting Gaussian beams into cylindrical vector beams were fabricated. The technique allowed fabrication of converters for high order CV beams (up to 10th order were demonstrated) and for various wavelength (demonstrated converters from 515 nm to 1515 nm). Measurements of generated beams and comparison with theoretical modelling revealed good quality of the beams and therefore good quality of fabricated converters. These converters are very easy to use and as they are fabricated in silica glass, they exhibit very high damage threshold. However there is disadvantage of scattering losses (especially at shorter wavelength where it

reaches 50% losses). Therefore there are still space for improvement. For example preliminary results indicates that using galvano scanner (which means lower numerical aperture and much faster scanning) might solve the problem of scattering. Such technique induces smaller retardance, however as fabrication speed would be much higher it can be compensated by writing more layers. Another possible improvement on the polarization converters would be achromatic converters. This could be achieved by changing the dispersion curve of form birefringence of nanogratings. The dispersion curve depends on the periodicity and the filling factor of the nanogratings and these parameters could be potentially controlled by laser parameters such as wavelength, repetition rate and pulse energy.

Also it was demonstrated that polarization converters can be used not just for polarization control in the beam but also generating optical vortices with tuneable orbital angular momentum. OAM is tuned by simply changing ellipticity of input polarization with quarter-wave plate. This technique allow control of OAM of the photons (and therefore the torque of the beam) without changing intensity distribution of the beam. Optical trapping of silica micro spheres experiment was performed where tuneable torque of the beam is demonstrated by measuring change in the rotation speed of the trapped spheres.

Birefringence can be used not only for polarization control but also for phase control. Half-wave retarder can induce phase delay to circularly polarized light depending on the azimuth of slow axis of the retarder. Which means that optical elements based on nanogratings can be used to generate special beam instead of phase masks or SLMs. Converters were fabricated and it was demonstrated the generation of 1D and 2D Airy beams and zero and second order Bessel beams. Properties of generated beams are measured and compared with theoretical simulations. As converters are polarization sensitive, Airy beam converter had unique ability to generate a dual Airy beam where two Airy beams with opposite acceleration directions propagates together. In general this demonstrates that nanogratings can be used as alternative way to the lithography for the fabrication of phase masks. Laser fabrication method is not just faster than lithography, but laser fabricated structures have unique

abilities (as it was demonstrated with dual Airy beam) which cannot be achieved by the lithography. Generated Airy beam is also used in material modification. Thin glass laser scribing with Airy beam is demonstrated and as an outcome a simple way of cantilever fabrication is proposed based on observed self-detachment of fibre-like structure from laser modified sample.

And finally it was demonstrated a femtosecond laser written micro-waveplate array allowing real time polarization imaging. The array with a single waveplate of a few micron size combined with a linear polarizer and a CCD/CMOS sensor are combined into a polarization sensitive imaging device, which measures distribution of all four Stokes parameters. For the demonstration, the setup was used for the imaging the polarization distribution CV beams. In the setup the micro-waveplate array, the polarizer and the sensor were separated in space and lenses were used to image the array onto the sensor. The next step would be to sandwich all elements together. This would solve the problem of alignment of the array imaging and aberrations which makes the calibration of the system and the polarization imaging of complicated images very difficult. Therefore such more compact setup could be used for polarization imaging of objects.

Appendix A

Jones vectors of polarized light

Polarization	Polarization representing Jones vector
x-polarized linear polarization	$\begin{pmatrix} 1 \\ 0 \end{pmatrix}$
y-polarized linear polarization	$\begin{pmatrix} 0 \\ 1 \end{pmatrix}$
Linear polarization at 45° with x axis	$\frac{1}{\sqrt{2}} \begin{pmatrix} 1 \\ 1 \end{pmatrix}$
Linear polarization at -45° with x axis	$\frac{1}{\sqrt{2}} \begin{pmatrix} 1 \\ -1 \end{pmatrix}$
Right handed circular polarization	$\frac{1}{\sqrt{2}} \begin{pmatrix} 1 \\ -i \end{pmatrix}$
Left handed circular polarization	$\frac{1}{\sqrt{2}} \begin{pmatrix} 1 \\ i \end{pmatrix}$

Jones matrices of most common optical elements

Optical element	Element representing Jones matrix
Linear polarizer with transmission in x axis	$\begin{pmatrix} 1 & 0 \\ 0 & 0 \end{pmatrix}$
Linear polarizer with transmission in y axis	$\begin{pmatrix} 0 & 0 \\ 0 & 1 \end{pmatrix}$
Linear polarizer with transmission at 45° with x axis	$\frac{1}{2} \begin{pmatrix} 1 & 1 \\ 1 & 1 \end{pmatrix}$
Linear polarizer with transmission at -45° with x axis	$\frac{1}{2} \begin{pmatrix} 1 & -1 \\ -1 & 1 \end{pmatrix}$

Right circular polarizer	$\frac{1}{2} \begin{pmatrix} 1 & i \\ -i & 1 \end{pmatrix}$
Left circular polarizer	$\frac{1}{2} \begin{pmatrix} 1 & -i \\ i & 1 \end{pmatrix}$
Quarter wave plate with slow axis along x direction	$\begin{pmatrix} 1 & 0 \\ 0 & i \end{pmatrix}$
Half wave plate with fast axis at θ angle with x-axis	$\begin{pmatrix} \cos 2\theta & \sin 2\theta \\ \sin 2\theta & -\cos 2\theta \end{pmatrix}$
Birefringent element with phase retardation $\Delta\phi$ and the azimuth of slow axis θ	$\begin{pmatrix} \cos^2 \theta + e^{i\Delta\phi} \sin^2 \theta & (1 - e^{i\Delta\phi}) \cos \theta \sin \theta \\ (1 - e^{i\Delta\phi}) \cos \theta \sin \theta & \sin^2 \theta + e^{i\Delta\phi} \cos^2 \theta \end{pmatrix}$

Appendix B

The MATLAB code for modelling generation and propagation of CV beams

Here I present the basic MATLAB code which I have written for the modelling of the beam transformation by laser fabricated polarization converter and propagation. Main functions used in the modelling can be found here together with the main body of the example program for the radially polarized beam generation. Also there are few other examples for different beams.

The code is simple to use as optical elements or the propagation in free space can be described by single function. Therefore the situation of three optical elements (such as an half-wave plate, a polarization converter and a polarizer) and propagation in free space requires just four lines of the code.

Main function used in modelling

```
% returns theta angle rotation matrix
function y = Rot(theta)
y(1,1) = cos(theta);
y(1,2) = sin(theta);
y(2,1) = -sin(theta);
y(2,2) = cos(theta);

% returns Jones matrix for linear polarizer at angle theta
function A = Polarizer(theta)
pol = [1 0; 0 0];
A = Rot(-theta) * pol * Rot(theta);

% returns Jones matrix for half-wave plate at angle theta
function A = Half_wave_plate(theta)
A0 = [1 0; 0 -1];
A = Rot(-theta) * A0 * Rot(theta);

% returns Jones matrix for quarter-wave plate at angle theta
function A = Quarter_wave_plate(theta)
A0 = [1 0; 0 -1i];
A = Rot(-theta) * A0 * Rot(theta);

% returns Jones matrix for retarder plate with
% phase retardance phi and azimuth angle theta
function M = Retardance_plate(theta, phi)
A = cos(theta)^2 + exp(1i*phi)*sin(theta)^2;
B = (1 - exp(1i*phi))*cos(theta)*sin(theta);
D = sin(theta)^2 + exp(1i*phi)*cos(theta)^2;
```

```

M = [A B; B D];

% each point in electric field E0 is multiplied by
% Jones matrix of given polarization element 'plate'
function E = pol_converter(E0, plate)
[n_y n_x] = size(E0{1});
E = cell(2, 1);
E{1}(n_y, n_x) = 0;
E{2}(n_y, n_x) = 0;
for k = 1:n_x
    for l = 1:n_y
        e(1) = E0{1}(l,k);
        e(2) = E0{2}(l,k);
        e2 = e*plate;
        E{1}(l,k) = e2(1);
        E{2}(l,k) = e2(2);
    end;
end;

% each point in electric field E0 is multiplied by Jones matrix
% of given polarization element 'plate' which azimuth depends on
% polar angle. 'a' describes how many times the azimuth of
% the retarder rotates during the full circle.
function E = Space_variant_retarder(E0, x, y, plate, a)
[n_y n_x] = size(E0{1});
E = cell(2, 1);
E{1}(n_y, n_x) = 0;
E{2}(n_y, n_x) = 0;
for k = 1:n_x
    for l = 1:n_y
        phi = a*(faze(x(k), y(l)));
        M = Rot(-phi) * plate * Rot(phi);
        e(1) = E0{1}(l,k);
        e(2) = E0{2}(l,k);
        e2 = e*M;
        E{1}(l,k) = e2(1);
        E{2}(l,k) = e2(2);
    end;
end;

% The algorithm for Fourier propagation of the beam for distance dz.
% Polarization is not taken into the account.
function u1 = fft_propagation(u0, dx, dy, lambda, dz)
[n_y n_x] = size(u0);
U = fft2(u0);
f_x = linspace(-0.5/dx,0.5/dx,n_x);
f_y = linspace(-0.5/dy,0.5/dy,n_y);
H(n_y, n_x) = 0;
for k = 1:n_x
    for l = 1:n_y
        f_z = sqrt(1/lambda^2 - f_x(k)^2 - f_y(l)^2);
        H(l, k) = exp(-1i*2*pi*f_z*dz);
    end;
end;
shiftU = fftshift(U).*H;
U = ifftshift(shiftU);
u1 = ifft2(U);

% Propagation of polarized electric field E0 for distance dz.

```

```

% Orthogonally polarized fields propagates independently
% using function 'fft_propagation()'.
function E = Propagation_full(E0, dx, dy, lambda, dz);
E = cell(2, 1);
E{1} = fft_propagation(E0{1}, dx, dy, lambda, dz);
E{2} = fft_propagation(E0{2}, dx, dy, lambda, dz);

```

The main code

```

%% Initialization part
n_x = 256; n_y = n_x;           %the size of the matrix
max_x = 6000; max_y = max_x     %the size of simulated space in um
dx = 2*max_x/(n_x-1); dy = dx; %minimum step in xy plane

dz = 1000000; %propagation distance in um

lambda = 0.532; % wavelength

w0 = 1500; %Radii size of starting Gaussian beam
R = inf; %Wave-front radii of starting Gaussian beam

x = linspace(-max_x, max_x, n_x); % x axis
y = linspace(-max_x, max_x, n_x); % y axis

% Two matrices for the x and y polarization projection
% of the electric field is created.
% E0{1} - electric field polarized in x axis, E0{2} - y axis
E0 = cell(2, 1);
E0{1}(n_y, n_x) = 0;
E0{2}(n_y, n_x) = 0;

% Matrices E0 are filled with the Gaussian beam polarized
% in x axis (0 deg)
for k = 1:n_x
    for l = 1:n_y
        ro2 = x(k)^2 + y(l)^2;
        E0{1}(l, k) = exp(-ro2/w0^2).*exp(-i*(2*pi/lambda)*ro2/(2*R));
        E0{2}(l, k) = 0;
    end;
end;

% created Jones matrix for linear polarizer at 0 deg
poll = Polarizer(pi/180*0);
%created Jones matrix for half-wave plate at 0 deg
hwp1 = Half_wave_plate(pi/180*22.5);
%created Jones matrix for quarter-wave plate at 45 deg
qwp1 = Quarter_wave_plate(pi/180*45);

%% Beam manipulation part
%% The generation of radially polarized beam and its propagation

% the topological charge of cylindrical vector beam
% c = 1 represents radial or azimuthal polarization
c = 1;
% the electric field E0(x,y) is multiplied by the retarder which
% azimuth is varying in space (S-waveolate). In this case

```

```

% the retarded is half-wave plate and the azimuth of the
% half-wave plate rotates c/2 times in full circle. As the
% input is linearly polarized Gaussian beam, the output is
% radially polarized Gaussian shape beam. Instead of
% 'Half_wave_plate(0)' Jones matrix representing retarder or
% polarizer can be given to the function 'Space_variant_retarder()'.
% For example changing it to Jones matrix for linear polarizer
% and changing c/2 to 1, E0 would be affected by radial polarizer.
E0 = Space_variant_retarder(E0, x, y, Half_wave_plate(0), c/2);

% propagation in z direction by distance dz (in um)
E0 = Propagation_full(E0, dx, dy, lambda, dz);

% linear polarizer can be applied to analyse the distribution of
% the polarization of the generated beam.
pol2 = Polarizer(pi/180*0);
E0 = pol_converter(E0, pol1);

% Intensity distribution of the electric field is calculated
I = E0{1}.*conj(E0{1}) + E0{2}.*conj(E0{2});

% Normalised intensity of the beam is plotted
imagesc(x,y,I)

```

Some other examples

```

%% Few examples on how to change the polarization uniformly of the
%% electric field E0.

% linear polarization is changed to circular of the electric
% field E0 as E0 is multiplied by the matrix qwpl which represents
% quarter-wave plate rotaret at 45 degree.
% E0 = pol_converter(E0, qwpl);

% linear polarization is rotated by 45 deg of the electric
% field E0 as E0 is multiplied by the matrix hwpl which represents
% half-wave plate rotaret at 22.5 degree.
% E0 = pol_converter(E0, hwpl);

% linear polarizer rotated at 45 degree is applied to the
% electric field E0
% E0 = pol_converter(E0, pol1);

%% Few examples on how to generate different CV beams by playing with
%% parameters of the functions defined earlier. This text can be
%% copied/pasted after the initialization part.

% generates charge 1 circularly polarized optical vortex and
% lets it to propagate for 1 m to get donut shape
c = 1;
E0 = pol_converter(E0, Quarter_wave_plate(pi/180*45));
E0 = Space_variant_retarder(E0, x, y, Half_wave_plate(0), c/2);
E0 = Propagation_full(E0, dx, dy, lambda, dz);

```

```
% linearly polarized optical vortex
c = 1;
E0 = pol_converter(E0, Quarter_wave_plate(pi/180*45));
E0 = Space_variant_retarder(E0, x, y, Half_wave_plate(0), c/2);
E0 = pol_converter(E0, Quarter_wave_plate(pi/180*45));
E0 = Propagation_full(E0, dx, dy, lambda, dz);

% radially polarized optical vortex
c = 1;
E0 = pol_converter(E0, Quarter_wave_plate(pi/180*45));
E0 = Space_variant_retarder(E0, x, y,
    Quarter_wave_plate(pi/180*45), c);
E0 = Propagation_full(E0, dx, dy, lambda, dz);
```


Appendix C

The MATLAB code for PolScope (Abrio) numerical modelling.

Main function used in modelling

```
function I = calc_Intensity(alpha, beta, R, theta, I_max, I_min);

I = round(I_max*0.5*( 1 + cos(alpha)*sin(beta)*cos(R) -
    sin(alpha)*sin(beta)*cos(2*theta)*sin(R) +
    cos(beta)*sin(2*theta)*sin(R) ) + I_min);

function I = calc_Intensity1(alpha, beta, R, theta, I_max, I_min,
Theta_Q);

E0 = [1; 0];
M_q = Retardance_plate(Theta_Q, pi/2);
M_S = Retardance_plate(theta, R);
M_a = Retardance_plate(0, alpha);
M_b = Retardance_plate(pi/4, beta);
M_pol = [1 0; 0 0];

E1 = M_pol * M_b * M_a * M_S * M_q * E0;

I = round(I_max * E1(1).*conj(E1(1)) + E1(2).*conj(E1(2)) + I_min);
```

The main code

```
nn = 300;
lambda = 546;
R_real = linspace(0, lambda, nn);
Theta_real = pi/4 + 0*pi/180;

chi = 90*pi/180;

alpha_1 = 2*pi/2; beta_1 = 2*pi/4;
alpha_2 = 2*pi/2; beta_2 = 2*pi/4-chi;
alpha_3 = 2*pi/2; beta_3 = 2*pi/4+chi;
alpha_4 = 2*pi/2-chi; beta_4 = 2*pi/4;
alpha_5 = 2*pi/2+chi; beta_5 = 2*pi/4;

Theta_Q = -pi/4 + 0*pi/180;
R_calc(nn) = 0;
Theta_calc(nn) = 0;
I_max = 1000;
I_min = 2;
for ii = 1: nn
```

Appendix C

```
I_1 = calc_Intensity1(alpha_1, beta_1, R_real(ii)*2*pi/lambda,
    Theta_real, I_max, I_min, Theta_Q);
I_2 = calc_Intensity1(alpha_2, beta_2, R_real(ii)*2*pi/lambda,
    Theta_real, I_max, I_min, Theta_Q);
I_3 = calc_Intensity1(alpha_3, beta_3, R_real(ii)*2*pi/lambda,
    Theta_real, I_max, I_min, Theta_Q);
I_4 = calc_Intensity1(alpha_4, beta_4, R_real(ii)*2*pi/lambda,
    Theta_real, I_max, I_min, Theta_Q);
I_5 = calc_Intensity1(alpha_5, beta_5, R_real(ii)*2*pi/lambda,
    Theta_real, I_max, I_min, Theta_Q);

% Five-frame algorithm
A = (I_2 - I_3)/(I_2 + I_3 - 2*I_1)*tan(chi/2);
B = (I_5 - I_4)/(I_5 + I_4 - 2*I_1)*tan(chi/2);

if I_2 + I_3 - 2*I_1 >= 0
    R_calc(ii) = lambda/(2*pi)*(atan(sqrt(A^2+B^2)));
else
    R_calc(ii) = lambda/(2*pi)*(pi - atan(sqrt(A^2+B^2)));
end;
Theta_calc(ii) = 0.5*atan(A/B);
end;

plot(R_real, R_calc, R_real, Theta_calc/pi*180, 'LineWidth', 2)
grid on
```

List of Publications

Journal publications

- [1] **M. Gecevičius**, M. Beresna, R. Drevinskas, P. G. Kazansky
Airy beams generated by ultrafast laser-imprinted space-variant nanostructures in glass
Optics Letters, Vol. 39, Issue 24, pp. 6791-6794 (2014)
- [2] D. Lin, J. M. Daniel, **M. Gecevičius**, M. Beresna, P. G. Kazansky, W. A. Clarkson
Cladding-pumped ytterbium-doped fiber laser with radially polarized output
Optics Letters, Vol. 39, Issue 18, pp. 5359-5361 (2014)
- [3] M. Beresna, **M. Gecevičius**, P. G. Kazansky
Ultrafast laser direct writing and nanostructuring in transparent materials
Advances in Optics and Photonics, Vol. 6, Issue 3, pp. 293-339 (2014)
- [4] **M. Gecevičius**, R. Drevinskas, M. Beresna, P. G. Kazansky
Single beam optical vortex tweezers with tunable orbital angular momentum
Applied Physics Letters, Vol. 104, Issue 23, pp. 231110 (2014)
- [5] J. Zhang, **M. Gecevičius**, M. Beresna, P. G. Kazansky
Seemingly Unlimited Lifetime Data Storage in Nanostructured Glass
Physical Review Letters, Vol. 112, Issue 3, pp. 033901 (2014)
- [6] A. V. Emelyanov, M. V. Khenkin, A. G. Kazanskii, P. A. Forsh, P. K. Kashkarov, **M. Gecevičius**, M. Beresna, Peter G. Kazansky
Femtosecond laser induced crystallization of hydrogenated amorphous silicon for photovoltaic applications
Thin Solid Films, Vol. 556, pp. 410-413 (2014)
- [7] M. Khenkin, A. Emelyanov, A. Kazanskii, P. Forsh, M. Beresna, **M. Gecevičius**, Peter Kazansky
Effect of hydrogen concentration on structure and photoelectric properties of a-Si: H films modified by femtosecond laser pulses
Canadian Journal of Physics, Vol. 99, Issue 999, pp. 1-5 (2014)
- [8] **M. Gecevičius**, M. Beresna, P. G. Kazansky
Polarization sensitive camera by femtosecond laser nanostructuring
Optics Letters, Vol. 38, Issue 20, pp. 4096-4099 (2013)

- [9] M. Beresna, **M. Gecevičius**, M. Lancry, B. Poumellec, P. G. Kazansky
Broadband anisotropy of femtosecond laser induced nanogratings in fused silica
Applied Physics Letters, Vol. 103, Issue 13, pp. 131903 (2013)
- [10] **M. Gecevičius**, M. Beresna, J. Zhang, W. Yang, H. Takebe, P. G. Kazansky
Extraordinary anisotropy of ultrafast laser writing in glass
Optics Express, Vol. 21, Issue 4, pp. 3959-3968 (2013)
- [11] C. Corbari, A. Champion, **M. Gecevičius**, M. Beresna, Y. Bellouard, P. G. Kazansky
Femtosecond versus picosecond laser machining of nano-gratings and micro-channels in silica glass
Optics Express, Vol. 21, Issue 4, pp. 3946-3958 (2013)
- [12] A. V. Emelyanov, A. G. Kazanskii, M. V. Khenkin, P. A. Forsh, P. K. Kashkarov, **M. Gecevičius**, M. Beresna, P. G. Kazansky
Visible luminescence from hydrogenated amorphous silicon modified by femtosecond laser radiation
Applied Physics Letters, Vol. 101, Issue 8, pp. 081902 (2012)
- [13] Y. Bellouard, A. Champion, B. Lenssen, M. Matteucci, A. Schaap, M. Beresna, C. Corbari, **M. Gecevičius**, P. Kazansky, O. Chappuis, M. Kral, R. Clavel, F. Barrot, J-M Breguet, Y. Mabillard, S. Bottinelli, M. Hopper, C. Hoenninger, E. Mottay, J. Lopez
The Femtoprint Project
Journal of Laser Micro/Nanoengineering, Vol. 7, Issue 1, (2012)
- [14] M. Beresna, **M. Gecevičius**, P. G. Kazansky, T. Taylor, A. V. Kavokin
Exciton mediated self-organization in glass driven by ultrashort light pulses
Applied Physics Letters, Vol. 101, Issue 5, pp. 053120 (2012)
- [15] P. G. Kazansky, Y. Shimotsuma, M. Sakakura, M. Beresna, M. Gecevičius, Y. Svirko, S. Akturk, J. Qiu, K. Miura, K. Hirao
Photosensitivity control of an isotropic medium through polarization of light pulses with tilted intensity front
Optics Express, Vol. 19, Issue 21, pp. 20657-20664 (2011)
- [16] M. Beresna, **M. Gecevičius**, P. G. Kazansky
Polarization sensitive elements fabricated by femtosecond laser nanostructuring of glass [Invited]
Optical Materials Express, Vol. 1, Issue 4, pp. 783-795 (2011)
- [17] M. Beresna, **M. Gecevičius**, N. M. Bulgakova, P. G. Kazansky
Twisting light with micro-spheres produced by ultrashort light pulses
Optics Express, Vol. 19, Issue 20, pp. 18989-18996 (2011)
- [18] M. Beresna, **M. Gecevičius**, P. G. Kazansky, T. Gertus

Radially polarized optical vortex converter created by femtosecond laser nanostructuring of glass

***Applied Physics Letters*, Vol. 98, Issue 20, pp. 201101 (2011)**

[19] D. Kezys, **M. Gecevicius**, A. Piskarskas, V. Pyragaite, V. Smilgevicius, A. Stabinis

Multibeam pumping of OPA by radiation of fibre amplifiers

***Lithuanian Journal of Physics and Technical Sciences*, Vol. 51, pp. 137-142 (2011)**

Conference publications

[1] D. Lin, J. M. Daniel, **M. Gecevičius**, M. Beresna, P. G. Kazansky, W. A. Clarkson

Direct generation of radially-polarized output from an Yb-doped fiber laser

CLEO: Science and Innovations, San Jose, JW2A. 22, (2014)

[2] **M. Gecevičius**, R. Drevinskas, M. Beresna, P. G. Kazansky

Optical Tweezers with Tunable Orbital Angular Momentum

CLEO: Science and Innovations, San Jose, JTh2A. 32 (2014)

[3] J. Zhang, R. Drevinskas, M. Beresna, **M. Gecevičius**, P. G. Kazansky

Silicon Microreflector Created by Single Ultrafast Laser Pulse

CLEO: Applications and Technology, San Jose, JTh2A. 138 (2014)

[4] R. Drevinskas, **M. Gecevičius**, M. Beresna, Y. Bellouard, P. G. Kazansky

Nanotexturing of Glass Surface by Ultrafast Laser Assisted Wet Etching

CLEO: Applications and Technology, San Jose, AM1L. 2 (2014)

[5] M. Beresna, **M. Gecevičius**, P. G. Kazansky

Femtosecond Laser Nanostructuring for Polarization Sensitive Imaging

CLEO: Science and Innovations, San Jose, SF1J. 2 (2014)

[6] J. Zhang, R. Drevinskas, M. Beresna, **M. Gecevičius**, P. G. Kazansky

Polarization-Sensitive Cats Eye Structuring of Silicon by Ultrashort Light Pulses

CLEO: Science and Innovations, San Jose, STh1J. 3 (2014)

[7] P. G. Kazansky, J. Zhang, **M Gecevičius**, M Beresna

Recent advances in ultrafast laser nanostructuring: S-waveplate and eternal data storage

CLEO: Applications and Technology, San Jose, AM3L. 3 (2014)

[8] M. Khenkin, A. Emelyanov, A. Kazanskii, P. Forsh, O. Kon'kov, M. Beresna, **M Gecevičius**, P. G. Kazansky

- Post-hydrogenation of amorphous hydrogenated silicon films modified by femtosecond laser irradiation*
SPIE Photonics Europe, 914012-914012-7 (2014)
- [9] C. J. de Jong, A. Lajevardipour, **M. Gecevičius**, M. Beresna, G. Seniutinas, G. Gervinskas, R. Buividas, P. G. Kazansky, Y. Bellouard, A. H. A. Clayton, S. Juodkasis
Characterization of optical polarization converters made by femtosecond laser writing
SPIE Micro+ Nano Materials, Devices, and Applications, 89231E-89231E-8 (2013)
- [10] **M. Gecevičius**, M. Beresna, A. Kazanskii, P. Kazansky, M. V. Lomonosov
Self-Assembled Nanostructuring of a-Si:H Films with Ultrashort Light Pulses
CLEO/Europe-IQEC, Munich, CM-P.24 (2013)
- [11] J. Zhang, **M. Gecevičius**, M. Beresna, A. G. Kazanskii, P. G. Kazansky
The puzzle of longitudinal electric field interaction with transparent media
Progress in ultrafast laser modifications of materials, Corsica (2013)
- [12] A. Patel, **M. Gecevičius**, R. Drevinskas, M. Beresna, P. G. Kazansky
Unambiguous evidence of two plasmon decay during ultrafast laser writing in glass
CLEO/Europe-IQEC, Munich (2013)
- [13] J. Zhang, **M. Gecevičius**, M. Beresna, P. G. Kazansky
5D data storage by ultrafast laser nanostructuring in glass
CLEO/QELS, San Jose, CTh5D.9 (2013) (Postdeadline)
- [14] J. Zhang, **M. Gecevičius**, M. Beresna, A. G. Kazanskii, P. G. Kazansky
Anomalous interaction of longitudinal electric field with hydrogenated amorphous silicon films
CLEO/QELS, San Jose, CM4H.7 (2013)
- [15] J. Zhang, **M. Gecevičius**, M. Beresna, P. G. Kazansky
Modification of transparent materials by tightly focused annular, radially and azimuthally polarized ultrafast laser beams
CLEO/Europe-IQEC, Munich (2013)
- [16] A. Patel, **M. Gecevičius**, R. Drevinskas, M. Beresna, P. G. Kazansky
3/2 harmonic generation - the clue to the mechanism of ultrafast laser nanostructuring
CLEO/QELS, San Jose, CA, CM2M.2 (2013)
- [17] P. G. Kazansky, M. Beresna, **M. Gecevičius**, J. Zhang, A. Patel, R. Drevinskas, A. Kazanskii

Recent progress in ultrafast laser nanostructuring: from two-plasmon decay to longitudinal field puzzle

Nonlinear Optics, Kohala Coast, Hawaii, USA, NF2A.4 (2013)

[18] E.L.Lim, Q.Kang, **M.Gecevičius**, F.Poletti, S.-U.Alam, D.J.Richardson
Vector mode effects in few moded Erbium doped fiber amplifiers

Conference on Optical Fibre Communications OFC '13, Anaheim, OTu3G.2 (2013)

[19] A.V.Emelyanov, M.V.Khenkin, A.G.Kazanskii, P.A.Forsh, P.K.Kashkarov, E.V.Lyubin, A.A.Khomich, **M.Gecevičius**, M.Beresna, P.G.Kazansky

Structural and electrophysical properties of femtosecond laser exposed hydrogenated amorphous silicon films

Photonics for Solar Energy Systems IV, Proceedings of SPIE 8438, pp.843811 (2012)

[20] C.Corbari, A.V.Gladyshev, **M.Gecevičius**, M.Beresna, P.G.Kazansky
Second-harmonic vortex generation with a poled glass

BGPP, Colorado Springs USA (2012) (Postdeadline)

[21] **M.Gecevičius**, M.Beresna, J.Zhang, P.G.Kazansky

Polarization dependence of area scanning ultrafast laser machining

CLEO/QELS, San Jose, CM4K.6 (2012)

[22] **M.Gecevičius**, M.Beresna, P.G.Kazansky

Accelerating airy beams generated by ultrafast laser induced space-variant nanostructures in glass

CLEO/QELS, San Jose, JTu1K.7 (2012)

[23] C.Corbari, A.Champion, **M.Gecevičius**, M.Beresna, M.Lancry, B.Poumellec, Y.Bellouard, P.G.Kazansky

Picosecond laser machining in the bulk of transparent dielectrics: critical comparison with fs-laser direct writing

CLEO/QELS, San Jose, ATu3L.2 (2012)

[24] P.G.Kazansky, A.Kazanskii, M.Beresna, **M.Gecevičius**

Ultrafast laser half-beam writing paradox

CLEO/QELS, San Jose, CM4K.3 (2012)

[25] M.Beresna, **M.Gecevičius**, P.G.Kazansky, Y.Bellouard, A.Champion
Micromachining with femtosecond laser written radial polarization converter

CLEO/QELS, San Jose, CM4K.7 (2012)

[26] M.Beresna, **M.Gecevičius**, P.G.Kazansky

Analysis and applications of femtosecond-laser-induced nanogratings from UV telecom wavelength

CLEO/QELS, San Jose, CM4K.2 (2012)

- [27] **M.Gecevičius**, M.Beresna, P.G.Kazansky
Exploring 5th dimension of optical recording with ultrashort light pulses
CLEO/QELS, Baltimore (2011)
- [28] M.Beresna, **M.Gecevičius**, P.G.Kazansky
Polarization vortex converter imprinted by femtosecond laser nanostructuring in glass
CLEO/QELS Baltimore (2011)
- [29] P.Kazansky, M.Beresna, Y.Shimotsuma, **M.Gecevičius**, M.Sakakura, C.Corbari, K.Miura, K.Hirao, Y.Bellouard
Phase transitions induced by ultrafast laser writing in transparent materials
CLEO/QELS, Baltimore (2011)
- [30] P.G.Kazansky, M.Beresna, **M.Gecevičius**
Harnessing ultrafast laser induced nanostructures in transparent materials
Workshop on Nonlinear nanostructures for ultrafast laser applications, Berlin (2011) (Invited)
- [31] A.Champion, Y.Bellouard, **M.Gecevičius**, M.Beresna, P.G.Kazansky
Role of stress in the chemical etching of fused silica exposed to low-energy femtosecond laser pulses
Frontiers in Ultrafast Optics, Biomedical, Scientific and Industrial Applications, San Francisco, SPIE 7925 pp. 79250Z9 (2011)
- [32] M.Beresna, **M.Gecevičius**, P.G.Kazansky
Discovering new properties and applications of ultrafast laser nanostructuring in transparent materials
SPIE Smart Nano+Micro Materials and Devices, Melbourne, Proc. SPIE 8204, 820415 (2011)

Bibliography

1. D. E. Spence, P. N. Kean, and W. Sibbett, "60-fsec pulse generation from a self-mode-locked Ti:sapphire laser.," *Opt. Lett.* **16**, 42–44 (1991).
2. U. Keller, D. a Miller, G. D. Boyd, T. H. Chiu, J. F. Ferguson, and M. T. Asom, "Solid-state low-loss intracavity saturable absorber for Nd:YLF lasers: an antiresonant semiconductor Fabry-Perot saturable absorber.," *Opt. Lett.* **17**, 505–507 (1992).
3. K. M. Davis, K. Miura, N. Sugimoto, and K. Hirao, "Writing waveguides in glass with a femtosecond laser," *Opt. Lett.* **21**, 1729–1731 (1996).
4. Y. Shimotsuma, P. Kazansky, J. Qiu, and K. Hirao, "Self-Organized Nanogratings in Glass Irradiated by Ultrashort Light Pulses," *Phys. Rev. Lett.* **91**, 247405 (2003).
5. C. Schaffer, A. Brodeur, and E. Mazur, "Laser-induced breakdown and damage in bulk transparent materials induced by tightly focused femtosecond laser pulses," *Meas. Sci. Technol.* **12**, 1784–1794 (2001).
6. R. Gattass and E. Mazur, "Femtosecond laser micromachining in transparent materials," *Nat. Photonics* **2**, 219–225 (2008).
7. L. Keldysh, "Ionization in the field of a strong electromagnetic wave," *Sov. Phys. JETP* **20**, 1307–1314 (1965).
8. B. Stuart, M. Feit, A. Rubenchik, B. Shore, and M. Perry, "Laser-induced damage in dielectrics with nanosecond to subpicosecond pulses," *Phys. Rev. Lett.* **74**, 2248–2251 (1995).
9. M. D. Perry, B. C. Stuart, P. S. Banks, M. D. Feit, V. Yanovsky, and a. M. Rubenchik, "Ultrashort-pulse laser machining of dielectric materials," *J. Appl. Phys.* **85**, 6803 (1999).
10. O. Efimov, S. Juodkazis, and H. Misawa, "Intrinsic single- and multiple-pulse laser-induced damage in silicate glasses in the femtosecond-to-nanosecond region," *Phys. Rev. A* **69**, 042903 (2004).
11. A. V Smith and B. T. Do, "Bulk and surface laser damage of silica by picosecond and nanosecond pulses at 1064 nm.," *Appl. Opt.* **47**, 4812–4832 (2008).
12. L. Sudrie, a. Couairon, M. Franco, B. Lamouroux, B. Prade, S. Tzortzakis, and a. Mysyrowicz, "Femtosecond Laser-Induced Damage and Filamentary Propagation in Fused Silica," *Phys. Rev. Lett.* **89**, 186601 (2002).

13. D. G. Papazoglou, I. Zergioti, and S. Tzortzakis, "Plasma strings from ultraviolet laser filaments drive permanent structural modifications in fused silica.," *Opt. Lett.* **32**, 2055–2057 (2007).
14. K. Miura, J. Qiu, H. Inouye, T. Mitsuyu, and K. Hirao, "Photowritten optical waveguides in various glasses with ultrashort pulse laser," *Appl. Phys. Lett.* **71**, 3329 (1997).
15. E. N. Glezer, M. Milosavljevic, L. Huang, R. J. Finlay, T. H. Her, J. P. Callan, and E. Mazur, "Three-dimensional optical storage inside transparent materials," *Opt. Lett.* **22**, 422 (1997).
16. C. Hnatovsky, R. S. Taylor, P. P. Rajeev, E. Simova, V. R. Bhardwaj, D. M. Rayner, and P. B. Corkum, "Pulse duration dependence of femtosecond-laser-fabricated nanogratings in fused silica," *Appl. Phys. Lett.* **87**, 014104 (2005).
17. S. Onda, W. Watanabe, K. Yamada, K. Itoh, and J. Nishii, "Study of filamentary damage in synthesized silica induced by chirped femtosecond laser pulses," *J. Opt. Soc. Am. B* **22**, 2437 (2005).
18. B. Poumellec, M. Lancry, A. Chahid-Erraji, and P. G. Kazansky, "Modification thresholds in femtosecond laser processing of pure silica: review of dependencies on laser parameters [Invited]," *Opt. Mater. Express* **1**, 766–782 (2011).
19. J. B. Ashcom, R. R. Gattass, C. B. Schaffer, and E. Mazur, "Numerical aperture dependence of damage and supercontinuum generation from femtosecond laser pulses in bulk fused silica," *J. Opt. Soc. Am. B* **23**, 2317 (2006).
20. D. Linde and H. Schüler, "Breakdown threshold and plasma formation in femtosecond laser–solid interaction," *JOSA B* **13**, 216–222 (1996).
21. A. Marcinkevičius, V. Mizeikis, S. Juodkazis, S. Matsuo, and H. Misawa, "Effect of refractive index-mismatch on laser microfabrication in silica glass," *Appl. Phys. A Mater. Sci. Process.* **76**, 257–260 (2003).
22. R. Simmonds, P. Salter, A. Jesacher, and M. Booth, "Three dimensional laser microfabrication in diamond using a dual adaptive optics system," *Opt. Express* **19**, 24122–24128 (2011).
23. A. M. Streltsov and N. F. Borrelli, "Fabrication and analysis of a directional coupler written in glass by nanojoule femtosecond laser pulses.," *Opt. Lett.* **26**, 42–43 (2001).
24. C. B. Schaffer, A. Brodeur, J. F. García, and E. Mazur, "Micromachining bulk glass by use of femtosecond laser pulses with nanojoule energy.," *Opt. Lett.* **26**, 93–95 (2001).

25. M. Birnbaum, "Semiconductor Surface Damage Produced by Ruby Lasers," *J. Appl. Phys.* **36**, 3688 (1965).
26. A. Siegman and P. Fauchet, "Stimulated Wood's anomalies on laser-illuminated surfaces," *Quantum Electron. IEEE J.* ... 1384-1403 (1986).
27. Z. Guosheng, P. Fauchet, and A. Siegman, "Growth of spontaneous periodic surface structures on solids during laser illumination," *Phys. Rev. B* **26**, 5366-5381 (1982).
28. a. Borowiec and H. K. Haugen, "Subwavelength ripple formation on the surfaces of compound semiconductors irradiated with femtosecond laser pulses," *Appl. Phys. Lett.* **82**, 4462 (2003).
29. N. Yasumaru, K. Miyazaki, and J. Kiuchi, "Femtosecond-laser-induced nanostructure formed on hard thin films of TiN and DLC," *Appl. Phys. A Mater. Sci. Process.* **76**, 983-985 (2003).
30. G. Miyaji and K. Miyazaki, "Origin of periodicity in nanostructuring on thin film surfaces ablated with femtosecond laser pulses.," *Opt. Express* **16**, 16265-16271 (2008).
31. E. Bricchi, B. G. Klappauf, and P. G. Kazansky, "Form birefringence and negative index change created by femtosecond direct writing in transparent materials.," *Opt. Lett.* **29**, 119-121 (2004).
32. P. Kazansky, H. Inouye, T. Mitsuyu, K. Miura, J. Qiu, K. Hirao, and F. Starrost, "Anomalous Anisotropic Light Scattering in Ge-Doped Silica Glass," *Phys. Rev. Lett.* **82**, 2199-2202 (1999).
33. L. Sudrie, M. Franco, B. Prade, and A. Mysyrowicz, "Writing of permanent birefringent microlayers in bulk fused silica with femtosecond laser pulses," *Opt. Commun.* **171**, 279-284 (1999).
34. Y. Shimotsuma, K. Hirao, J. Qiu, and K. Miura, "Nanofabrication in transparent materials with a femtosecond pulse laser," *J. Non. Cryst. Solids* **352**, 646-656 (2006).
35. F. Zimmermann, A. Plech, S. Richter, A. Tünnermann, and S. Nolte, "Ultrashort laser pulse induced nanogratings in borosilicate glass," *Appl. Phys. Lett.* **104**, 211107 (2014).
36. S. Richter, C. Miese, S. Döring, F. Zimmermann, M. J. Withford, A. Tünnermann, and S. Nolte, "Laser induced nanogratings beyond fused silica - periodic nanostructures in borosilicate glasses and ULE™," *Opt. Mater. Express* **3**, 1161 (2013).
37. Y. Liao, Y. Shen, L. Qiao, D. Chen, Y. Cheng, K. Sugioka, and K. Midorikawa, "Femtosecond laser nanostructuring in porous glass with sub-50 nm feature sizes.," *Opt. Lett.* **38**, 187-189 (2013).

38. J. Gottmann, D. Wortmann, and M. Hörstmann-Jungemann, "Fabrication of sub-wavelength surface ripples and in-volume nanostructures by fs-laser induced selective etching," *Appl. Surf. Sci.* **255**, 5641–5646 (2009).
39. W. Yang, E. Bricchi, P. G. Kazansky, J. Bovatsek, and A. Y. Arai, "Self-assembled periodic sub-wavelength structures by femtosecond laser direct writing.," *Opt. Express* **14**, 10117–10124 (2006).
40. J. Canning, M. Lancry, K. Cook, a. Weickman, F. Brisset, and B. Pommellec, "Anatomy of a femtosecond laser processed silica waveguide [Invited]," *Opt. Mater. Express* **1**, 998 (2011).
41. H. Misawa and S. Juodkazis, *3D Laser Microfabrication: Principles and Applications* (Wiley-VCH Verlag GmbH & Co. KGaA, Weinheim, 2006).
42. V. Bhardwaj, E. Simova, P. Rajeev, C. Hnatovsky, R. Taylor, D. Rayner, and P. Corkum, "Optically Produced Arrays of Planar Nanostructures inside Fused Silica," *Phys. Rev. Lett.* **96**, 1–4 (2006).
43. R. Taylor, C. Hnatovsky, and E. Simova, "Applications of femtosecond laser induced self-organized planar nanocracks inside fused silica glass," *Laser Photonics Rev.* **2**, 26–46 (2008).
44. R. Buividas, L. Rosa, R. Sliupas, T. Kudrius, G. Sleky, V. Datsyuk, and S. Juodkazis, "Mechanism of fine ripple formation on surfaces of (semi)transparent materials via a half-wavelength cavity feedback," *Nanotechnology* **22**, 055304 (2011).
45. M. Beresna, M. Gecevicius, P. G. Kazansky, T. Taylor, and A. V. Kavokin, "Exciton mediated self-organization in glass driven by ultrashort light pulses," *Appl. Phys. Lett.* **101**, 053120 (2012).
46. F. Messina, E. Vella, M. Cannas, and R. Boscaino, "Evidence of Delocalized Excitons in Amorphous Solids," *Phys. Rev. Lett.* **105**, 116401 (2010).
47. E. Vella, F. Messina, M. Cannas, and R. Boscaino, "Unraveling exciton dynamics in amorphous silicon dioxide: Interpretation of the optical features from 8 to 11 eV," *Phys. Rev. B* **83**, 174201 (2011).
48. D. Grojo, M. Gertsvolf, S. Lei, T. Barillot, D. M. Rayner, and P. B. Corkum, "Exciton-seeded multiphoton ionization in bulk SiO₂," *Phys. Rev. B* **81**, 212301 (2010).
49. P. Martin, S. Guizard, P. Daguzan, G. Petite, P. D'Oliveira, P. Meynadier, and M. Perdrix, "Subpicosecond study of carrier trapping dynamics in wide-band-gap crystals," *Phys. Rev. B* **55**, 5799–5810 (1997).
50. L. Bressel and D. De Ligny, "Observation of O₂ inside voids formed in GeO₂ glass by tightly-focused fs-laser pulses," *Opt. Mater. Express* **1**, 416–424 (2011).

51. E. Bricchi and P. G. Kazansky, "Extraordinary stability of anisotropic femtosecond direct-written structures embedded in silica glass," *Appl. Phys. Lett.* **88**, 111119 (2006).
52. R. S. Taylor, C. Hnatovsky, E. Simova, P. P. Rajeev, D. M. Rayner, and P. B. Corkum, "Femtosecond laser erasing and rewriting of self-organized planar nanocracks in fused silica glass," *Opt. Lett.* **32**, 2888–2890 (2007).
53. Y. Shimotsuma, M. Sakakura, P. G. Kazansky, M. Beresna, J. Qiu, K. Miura, and K. Hirao, "Ultrafast manipulation of self-assembled form birefringence in glass.," *Adv. Mater.* **22**, 4039–4043 (2010).
54. M. Beresna, M. Gecevicius, M. Lancry, B. Poumellec, and P. G. Kazansky, "Broadband anisotropy of femtosecond laser induced nanogratings in fused silica," *Appl. Phys. Lett.* **103**, 131903 (2013).
55. L. P. R. Ramirez, M. Heinrich, S. Richter, F. Dreisow, R. Keil, A. V. Korovin, U. Peschel, S. Nolte, and A. Tünnermann, "Tuning the structural properties of femtosecond-laser-induced nanogratings," *Appl. Phys. A* **100**, 1–6 (2010).
56. H. Kikuta, Y. Ohira, and K. Iwata, "Achromatic quarter-wave plates using the dispersion of form birefringence.," *Appl. Opt.* **36**, 1566–72 (1997).
57. N. F. Borrelli, C. M. Smith, J. J. Price, and D. C. Allan, "Polarized excimer laser-induced birefringence in silica," *Appl. Phys. Lett.* **80**, 219 (2002).
58. M. Ams, G. D. Marshall, and M. J. Withford, "Study of the influence of femtosecond laser polarisation on direct writing of waveguides.," *Opt. Express* **14**, 13158–13163 (2006).
59. S. Eaton, H. Zhang, P. Herman, F. Yoshino, L. Shah, J. Bovatsek, and A. Arai, "Heat accumulation effects in femtosecond laser-written waveguides with variable repetition rate.," *Opt. Express* **13**, 4708–4716 (2005).
60. R. R. Gattass, L. R. Cerami, and E. Mazur, "Micromachining of bulk glass with bursts of femtosecond laser pulses at variable repetition rates.," *Opt. Express* **14**, 5279–84 (2006).
61. F. Zimmermann, a. Plech, S. Richter, S. Döring, a. Tünnermann, and S. Nolte, "Structural evolution of nanopores and cracks as fundamental constituents of ultrashort pulse-induced nanogratings," *Appl. Phys. A* **114**, 75–79 (2013).
62. E. Bricchi, J. D. Mills, P. G. Kazansky, B. G. Klappauf, and J. J. Baumberg, "Birefringent Fresnel zone plates in silica fabricated by femtosecond laser machining.," *Opt. Lett.* **27**, 2200–2202 (2002).
63. E. Bricchi, "Femtosecond laser micro-machining and consequent self-assembled nano-structures in transparent materials," (2005).

64. J. D. Mills, P. G. Kazansky, E. Bricchi, and J. J. Baumberg, "Embedded anisotropic microreflectors by femtosecond-laser nanomachining," *Appl. Phys. Lett.* **81**, 196 (2002).
65. D. Papazoglou and M. Loulakis, "Embedded birefringent computer-generated holograms fabricated by femtosecond laser pulses," *Opt. Lett.* **31**, 1441-1443 (2006).
66. W. Cai, A. Libertun, and R. Piestun, "Polarization selective computer-generated holograms realized in glass by femtosecond laser induced nanogratings," *Opt. Express* **14**, 3785-3791 (2006).
67. M. Beresna, M. Gecevičius, and P. G. Kazansky, "Polarization sensitive elements fabricated by femtosecond laser nanostructuring of glass [Invited]," *Opt. Mater. Express* **1**, 10117-10124 (2011).
68. M. Beresna and P. G. Kazansky, "Polarization diffraction grating produced by femtosecond laser nanostructuring in glass.," *Opt. Lett.* **35**, 1662-1664 (2010).
69. E. Hasman, Z. Bomzon, A. Niv, G. Biener, and V. Kleiner, "Polarization beam-splitters and optical switches based on space-variant computer-generated subwavelength quasi-periodic structures," **209**, 45-54 (2002).
70. J. Zhang, M. Gecevičius, M. Beresna, and P. G. Kazansky, "Seemingly Unlimited Lifetime Data Storage in Nanostructured Glass," *Phys. Rev. Lett.* **112**, 033901 (2014).
71. M. Shribak and R. Oldenbourg, "Techniques for fast and sensitive measurements of two-dimensional birefringence distributions," *Appl. Opt.* **42**, 3009-3017 (2003).
72. C. Corbari, A. Champion, M. Gecevičius, M. Beresna, Y. Bellouard, and P. G. Kazansky, "Femtosecond versus picosecond laser machining of nanogratings and micro-channels in silica glass.," *Opt. Express* **21**, 3946-58 (2013).
73. K. Venkatakrishnan, B. Tan, P. Stanley, and N. R. Sivakumar, "The effect of polarization on ultrashort pulsed laser ablation of thin metal films," *J. Appl. Phys.* **92**, 1604 (2002).
74. M. Beresna, M. Gecevičius, P. G. Kazansky, and T. Gertus, "Radially polarized optical vortex converter created by femtosecond laser nanostructuring of glass," *Appl. Phys. Lett.* **98**, 201101 (2011).
75. M. Gecevičius, M. Beresna, and P. G. Kazansky, "Polarization sensitive camera by femtosecond laser nanostructuring.," *Opt. Lett.* **38**, 4096-9 (2013).
76. V. G. Niziev and a V Nesterov, "Influence of beam polarization on laser cutting efficiency," *J. Phys. D. Appl. Phys.* **32**, 1455-1461 (1999).

77. P. G. Kazansky, W. Yang, E. Bricchi, J. Bovatsek, A. Arai, Y. Shimotsuma, K. Miura, and K. Hirao, "“Quill” writing with ultrashort light pulses in transparent materials," *Appl. Phys. Lett.* **90**, 151120 (2007).
78. D. N. Vitek, E. Block, Y. Bellouard, D. E. Adams, S. Backus, D. Kleinfeld, C. G. Durfee, and J. A. Squier, "Spatio-temporally focused femtosecond laser pulses for nonreciprocal writing in optically transparent materials Abstract :," **18**, 24673–24678 (2010).
79. S. Akturk, X. Gu, E. Zeek, and R. Trebino, "Pulse-front tilt caused by spatial and temporal chirp.," *Opt. Express* **12**, 4399–410 (2004).
80. P. G. Kazansky, Y. Shimotsuma, M. Sakakura, M. Beresna, M. Gecevičius, Y. Svirko, S. Akturk, J. Qiu, K. Miura, and K. Hirao, "Photosensitivity control of an isotropic medium through polarization of light pulses with tilted intensity front.," *Opt. Express* **19**, 20657–20664 (2011).
81. A. Champion and Y. Bellouard, "Direct volume variation measurements in fused silica specimens exposed to femtosecond laser," *Opt. Mater. Express* **2**, 789–798 (2012).
82. W. Primak and D. Post, "Photoelastic Constants of Vitreous Silica and Its Elastic Coefficient of Refractive Index," *J. Appl. Phys.* **30**, 779 (1959).
83. W. Yang, P. G. Kazansky, and Y. P. Svirko, "Non-reciprocal ultrafast laser writing," *Nat. Photonics* **2**, 99–104 (2008).
84. D. J. Stokes, *Principles and Practice of Variable Pressure/Environmental Scanning Electron Microscopy (VP-ESEM)* (John Wiley & Sons, Ltd, 2008).
85. M. Beresna, "Polarization engineering with ultrafast laser writing in transparent media," (2012).
86. S. Quabis, R. Dorn, M. Eberler, O. Glockl, and G. Leuchs, "Focusing light to a tighter spot," *Opt. Commun.* 1–7 (2000).
87. R. Dorn, S. Quabis, and G. Leuchs, "Sharper Focus for a Radially Polarized Light Beam," *Phys. Rev. Lett.* **91**, 1–4 (2003).
88. B. Hao and J. Leger, "Experimental measurement of longitudinal component in the vicinity of focused radially polarized beam.," *Opt. Express* **15**, 3550–6 (2007).
89. D. P. Biss and T. G. Brown, "Polarization-vortex-driven second-harmonic generation.," *Opt. Lett.* **28**, 923–5 (2003).
90. S. Carrasco, B. E. A. Saleh, M. C. Teich, and J. T. Fourkas, "Second-and third-harmonic generation with vector Gaussian beams," *JOSA B* **23**, 2134–2141 (2006).

91. D. P. Biss, K. S. Youngworth, and T. G. Brown, "Dark-field imaging with cylindrical-vector beams.," *Appl. Opt.* **45**, 470–9 (2006).
92. Q. Zhan, "Evanescent Bessel beam generation via surface plasmon resonance excitation by a radially polarized beam.," *Opt. Lett.* **31**, 1726–8 (2006).
93. Q. Zhan and J. Leger, "Focus shaping using cylindrical vector beams.," *Opt. Express* **10**, 324–31 (2002).
94. W. Chen and Q. Zhan, "Three-dimensional focus shaping with cylindrical vector beams," *Opt. Commun.* **265**, 411–417 (2006).
95. H. Wang, L. Shi, B. Lukyanchuk, C. Sheppard, and C. T. Chong, "Creation of a needle of longitudinally polarized light in vacuum using binary optics," *Nat. Photonics* **2**, 501–505 (2008).
96. K. Yonezawa, Y. Kozawa, and S. Sato, "Generation of a radially polarized laser beam by use of the birefringence of a c-cut Nd:YVO₄ crystal.," *Opt. Lett.* **31**, 2151–3 (2006).
97. V. G. Niziev, R. S. Chang, and a V Nesterov, "Generation of inhomogeneously polarized laser beams by use of a Sagnac interferometer.," *Appl. Opt.* **45**, 8393–9 (2006).
98. Q. Zhan and J. R. Leger, "Microellipsometer with radial symmetry.," *Appl. Opt.* **41**, 4630–7 (2002).
99. Q. W. L. J. R. Zhan, "Interferometric measurement of the geometric phase in space-variant polarization manipulations," *Opt. Commun.* **213**, 241–245 (2002).
100. G. Machavariani, Y. Lumer, I. Moshe, a. Meir, and S. Jackel, "Spatially-variable retardation plate for efficient generation of radially- and azimuthally-polarized beams," *Opt. Commun.* **281**, 732–738 (2008).
101. Z. Bomzon, G. Biener, V. Kleiner, and E. Hasman, "Radially and azimuthally polarized beams generated by space-variant dielectric subwavelength gratings.," *Opt. Lett.* **27**, 285–7 (2002).
102. D. G. Hall, "Vector-beam solutions of Maxwell ' s wave equation," *Opt. Lett.* **21**, 9–11 (1996).
103. Q. Zhan, "Cylindrical vector beams: from mathematical concepts to applications," *Adv. Opt. Photonics* **1**, 1 (2009).
104. L. Marrucci, C. Manzo, and D. Paparo, "Optical Spin-to-Orbital Angular Momentum Conversion in Inhomogeneous Anisotropic Media," *Phys. Rev. Lett.* **96**, 163905 (2006).

105. Y. Zhao, J. Edgar, G. Jeffries, D. McGloin, and D. Chiu, "Spin-to-Orbital Angular Momentum Conversion in a Strongly Focused Optical Beam," *Phys. Rev. Lett.* **99**, 073901 (2007).
106. C. Hnatovsky, V. Shvedov, W. Krolikowski, and A. Rode, "Revealing Local Field Structure of Focused Ultrashort Pulses," *Phys. Rev. Lett.* **106**, 123901 (2011).
107. A. Ashkin, J. M. Dziedzic, J. E. Bjorkholm, and S. Chu, "Observation of a single-beam gradient force optical trap for dielectric particles," *Opt. Lett.* **11**, 288–290 (1987).
108. A. Ashkin, J. Dziedzic, and T. Yamane, "Optical trapping and manipulation of single cells using infrared laser beams," *Nature* **330**, 769–771 (1987).
109. S. Smith, Y. Cui, and C. Bustamante, "Overstretching B-DNA: the elastic response of individual double-stranded and single-stranded DNA molecules," *Science* (80-.). **271**, 795–798 (1996).
110. M. P. MacDonald, L. Paterson, K. Volke-Sepulveda, J. Arlt, W. Sibbett, and K. Dholakia, "Creation and manipulation of three-dimensional optically trapped structures.," *Science* (80-.). **296**, 1101–1103 (2002).
111. D. G. Grier, "A revolution in optical manipulation.," *Nature* **424**, 810–6 (2003).
112. J. Berthelot, S. S. Aćimović, M. L. Juan, M. P. Kreuzer, J. Renger, and R. Quidant, "Three-dimensional manipulation with scanning near-field optical nanotweezers.," *Nat. Nanotechnol.* (2014).
113. R. Beth, "Mechanical detection and measurement of the angular momentum of light," *Phys. Rev.* **50**, 115–125 (1936).
114. L. Allen, M. W. Beikersbergen, R. J. C. Spreeuw, and J. P. Woerdman, "Orbital angular momentum of light and the transformation of Laguerre-Gaussian laser modes," *Phys. Rev. A* **45**, 8185–8189 (1992).
115. a. O'Neil, I. MacVicar, L. Allen, and M. Padgett, "Intrinsic and Extrinsic Nature of the Orbital Angular Momentum of a Light Beam," *Phys. Rev. Lett.* **88**, 053601 (2002).
116. H. He, M. Friese, N. Heckenberg, and H. Rubinsztein-Dunlop, "Direct observation of transfer of angular momentum to absorptive particles from a laser beam with a phase singularity," *Phys. Rev. Lett.* **75**, 826–829 (1995).
117. N. B. Simpson, K. Dholakia, L. Allen, and M. J. Padgett, "Mechanical equivalence of spin and orbital angular momentum of light: an optical spanner.," *Opt. Lett.* **22**, 52–54 (1997).

118. M. Friese, T. Nieminen, N. R. Heckenberg, and H. Rubinsztein-Dunlop, "Optical alignment and spinning of laser-trapped microscopic particles," *Nature* **394**, 348–350 (1998).
119. E. Higurashi, R. Sawada, and T. Ito, "Optically induced angular alignment of trapped birefringent micro-objects by linearly polarized light," *Phys. Rev. E* **59**, 3676–3681 (1999).
120. K. T. Gahagan and G. a Swartzlander, "Optical vortex trapping of particles.," *Opt. Lett.* **21**, 827–9 (1996).
121. T. Kuga, Y. Torii, N. Shiokawa, T. Hirano, Y. Shimizu, and H. Sasada, "Novel Optical Trap of Atoms with a Doughnut Beam," *Phys. Rev. Lett.* **78**, 4713–4716 (1997).
122. K.-P. Marzlin, W. Zhang, and E. Wright, "Vortex Coupler for Atomic Bose-Einstein Condensates," *Phys. Rev. Lett.* **79**, 4728–4731 (1997).
123. G. Molina-Terriza, J. Torres, and L. Torner, "Management of the Angular Momentum of Light: Preparation of Photons in Multidimensional Vector States of Angular Momentum," *Phys. Rev. Lett.* **88**, 013601 (2001).
124. A. Vaziri, J.-W. Pan, T. Jennewein, G. Weihs, and A. Zeilinger, "Concentration of Higher Dimensional Entanglement: Qutrits of Photon Orbital Angular Momentum," *Phys. Rev. Lett.* **91**, 227902 (2003).
125. L. Paterson, M. P. MacDonald, J. Arlt, W. Sibbett, P. E. Bryant, and K. Dholakia, "Controlled rotation of optically trapped microscopic particles.," *Science (80-.)*. **292**, 912–914 (2001).
126. M. Funk, S. J. Parkin, A. B. Stilgoe, T. a Nieminen, N. R. Heckenberg, and H. Rubinsztein-Dunlop, "Constant power optical tweezers with controllable torque.," *Opt. Lett.* **34**, 139–141 (2009).
127. M. Friese, J. Enger, H. Rubinsztein-Dunlop, and N. Heckenberg, "Optical angular-momentum transfer to trapped absorbing particles.," *Phys. Rev. A* **54**, 1593–1596 (1996).
128. T. Galstyan and V. Drnoyan, "Light-Driven Molecular Motor," *Phys. Rev. Lett.* **78**, 2760–2763 (1997).
129. E. Brasselet and T. Galstian, "Optical control of molecular orientational dynamics in liquid crystals," *Opt. Commun.* **186**, 291–302 (2000).
130. C. H. J. Schmitz, K. Uhrig, J. P. Spatz, and J. E. Curtis, "Tuning the orbital angular momentum in optical vortex beams," *Opt. Express* **14**, 6604–6612 (2006).
131. S. Tao, X.-C. Yuan, J. Lin, X. Peng, and H. Niu, "Fractional optical vortex beam induced rotation of particles.," *Opt. Express* **13**, 7726–7731 (2005).

132. Y. Roichman, B. Sun, Y. Roichman, J. Amato-Grill, and D. Grier, "Optical Forces Arising from Phase Gradients," *Phys. Rev. Lett.* **100**, 013602 (2008).
133. "S-waveplate," <http://www.wophotonics.com/products/accessories/radial-polarization-converter/>.
134. E. Karimi, S. Slussarenko, B. Piccirillo, L. Marrucci, and E. Santamato, "Polarization-controlled evolution of light transverse modes and associated Pancharatnam geometric phase in orbital angular momentum," *Phys. Rev. A* **81**, 053813 (2010).
135. J. Durnin, J. J. Miceli, and J. H. Eberly, "Diffraction-free beams," *Phys. Rev. Lett.* **58**, 1499–1501 (1987).
136. J. C. Gutiérrez-Vega, M. D. Iturbe-Castillo, and S. Chávez-Cerda, "Alternative formulation for invariant optical fields: Mathieu beams.," *Opt. Lett.* **25**, 1493–5 (2000).
137. J. Gutiérrez-Vega and M. Iturbe-Castillo, "Experimental demonstration of optical Mathieu beams," *Opt. Commun.* **195**, 35–40 (2001).
138. M. a Bandres, J. C. Gutiérrez-Vega, and S. Chávez-Cerda, "Parabolic nondiffracting optical wave fields.," *Opt. Lett.* **29**, 44–46 (2004).
139. G. Siviloglou, J. Broky, a. Dogariu, and D. Christodoulides, "Observation of Accelerating Airy Beams," *Phys. Rev. Lett.* **99**, 23–26 (2007).
140. J. Broky, G. a Siviloglou, A. Dogariu, and D. N. Christodoulides, "Self-healing properties of optical Airy beams.," *Opt. Express* **16**, 12880–91 (2008).
141. J. Baumgartl, M. Mazilu, and K. Dholakia, "Optically mediated particle clearing using Airy wavepackets," *Nat. Photonics* **2**, 675–678 (2008).
142. P. Polynkin, M. Kolesik, J. V Moloney, G. A. Siviloglou, and D. N. Christodoulides, "Curved plasma channel generation using ultraintense Airy beams.," *Science* **324**, 229–32 (2009).
143. P. Polynkin, M. Kolesik, and J. Moloney, "Filamentation of Femtosecond Laser Airy Beams in Water," *Phys. Rev. Lett.* **103**, 123902 (2009).
144. A. Mathis, F. Courvoisier, L. Froehly, L. Furfaro, M. Jacquot, P. a. Lacourt, and J. M. Dudley, "Micromachining along a curve: Femtosecond laser micromachining of curved profiles in diamond and silicon using accelerating beams," *Appl. Phys. Lett.* **101**, 071110 (2012).
145. G. a Siviloglou and D. N. Christodoulides, "Accelerating finite energy Airy beams.," *Opt. Lett.* **32**, 979–81 (2007).

146. D. Abdollahpour, S. Suntsov, D. Papazoglou, and S. Tzortzakis, "Spatiotemporal Airy Light Bullets in the Linear and Nonlinear Regimes," *Phys. Rev. Lett.* **105**, 253901 (2010).
147. N. K. Efremidis and D. N. Christodoulides, "Abruptly autofocusing waves.," *Opt. Lett.* **35**, 4045–7 (2010).
148. Y. Hu, P. Zhang, C. Lou, S. Huang, J. Xu, and Z. Chen, "Optimal control of the ballistic motion of Airy beams.," *Opt. Lett.* **35**, 2260–2 (2010).
149. T. Ellenbogen and N. Voloch-Bloch, "Nonlinear generation and manipulation of Airy beams," *Nat. Photonics* **3**, 395–398 (2009).
150. D. Papazoglou, S. Suntsov, D. Abdollahpour, and S. Tzortzakis, "Tunable intense Airy beams and tailored femtosecond laser filaments," *Phys. Rev. A* **81**, 061807 (2010).
151. M. Gecevičius and M. Beresna, "Airy beams generated by ultrafast laser-imprinted space-variant nanostructures in glass," *Opt. Lett.* **39**, 6791–6794 (2014).
152. C.-Y. Hwang, D. Choi, K.-Y. Kim, and B. Lee, "Dual Airy beam.," *Opt. Express* **18**, 23504–16 (2010).
153. J. Chen and Z. Wu, "Laser cutting of ultra-thin glasses based on a nonlinear laser interaction effect," in *Proc. SPIE 8786, Pacific Rim Laser Damage 2013: Optical Materials for High Power Lasers* (2013).
154. F. Gaebler, "Laser glass cutting in flat panel display production," *Ind. Laser Solut.* **23**, 14 (2008).
155. F. He, Y. Cheng, Z. Xu, Y. Liao, J. Xu, and H. Sun, "Direct fabrication of homogeneous microfluidic channels embedded in fused silica using a femtosecond laser," *Opt. Lett.* **35**, 282–284 (2010).
156. J. S. Tyo, D. L. Goldstein, D. B. Chenault, and J. a Shaw, "Review of passive imaging polarimetry for remote sensing applications.," *Appl. Opt.* **45**, 5453–5469 (2006).
157. G. Yao and L. V Wang, "Two-dimensional depth-resolved Mueller matrix characterization of biological tissue by optical coherence tomography.," *Opt. Lett.* **24**, 537–539 (1999).
158. J. F. de Boer, T. E. Milner, M. J. van Gemert, and J. S. Nelson, "Two-dimensional birefringence imaging in biological tissue by polarization-sensitive optical coherence tomography.," *Opt. Lett.* **22**, 934–936 (1997).
159. K. Schoenenberger, B. W. Colston, D. J. Maitland, L. B. Da Silva, and M. J. Everett, "Mapping of Birefringence and Thermal Damage in Tissue by use of Polarization-Sensitive Optical Coherence Tomography.," *Appl. Opt.* **37**, 6026–6036 (1998).

160. B. Cense, T. C. Chen, B. H. Park, M. C. Pierce, and J. F. De Boer, "In vivo depth-resolved birefringence measurements of the human retinal nerve fiber layer by polarization-sensitive optical coherence tomography," **27**, 1610–1612 (2002).
161. M. G. Ducros, J. F. De Boer, H. Huang, L. C. Chao, Z. Chen, J. S. Nelson, T. E. Milner, H. G. Rylander, and A. Member, "Polarization Sensitive Optical Coherence Tomography of the Rabbit Eye," **5**, 1159–1167 (1999).
162. M. Anastasiadou, a. De Martino, D. Clement, F. Liège, B. Laude-Boulesteix, N. Quang, J. Dreyfuss, B. Huynh, a. Nazac, L. Schwartz, and H. Cohen, "Polarimetric imaging for the diagnosis of cervical cancer," *Phys. Status Solidi* **5**, 1423–1426 (2008).
163. A. Pierangelo, A. Benali, M.-R. Antonelli, T. Novikova, P. Validire, B. Gayet, and A. De Martino, "Ex-vivo characterization of human colon cancer by Mueller polarimetric imaging.," *Opt. Express* **19**, 1582–1593 (2011).
164. D. Lara and C. Dainty, "Double-pass axially resolved confocal Mueller matrix imaging polarimetry," *Opt. Lett.* **30**, 2879–2881 (2005).
165. M. Fridman, E. Grinvald, A. Godel, M. Nixon, A. a. Friesem, and N. Davidson, "Real time achromatic measurement of space-variant polarizations," *Appl. Phys. Lett.* **98**, 141107 (2011).
166. J. Guo and D. Brady, "Fabrication of thin-film micropolarizer arrays for visible imaging polarimetry.," *Appl. Opt.* **39**, 1486–1492 (2000).
167. F. Sadjadi and C. Chun, "Application of a passive polarimetric infrared sensor in improved detection and classification of targets," *Int. J. Infrared Millimeter Waves* **19**, 1541–1559 (1998).
168. Z. Bomzon, V. Kleiner, and E. Hasman, "Formation of radially and azimuthally polarized light using space-variant subwavelength metal stripe gratings," *Appl. Phys. Lett.* **79**, 1587 (2001).
169. J. Ford, F. Xu, K. Urquhart, and Y. Fainman, "Polarization-selective computer-generated holograms," *Opt. Lett.* **18**, 456–458 (1993).
170. J. S. Tyo, "Design of optimal polarimeters: maximization of signal-to-noise ratio and minimization of systematic error," **41**, 619–630 (2002).
171. M. Gecevičius, M. Beresna, J. Zhang, W. Yang, H. Takebe, and P. G. Kazansky, "Extraordinary anisotropy of ultrafast laser writing in glass.," *Opt. Express* **21**, 3959–3968 (2013).
172. A. Schaap and Y. Bellouard, "Molding topologically-complex 3D polymer microstructures from femtosecond laser machined glass," *Opt. Mater. Express* **3**, 1428 (2013).